STUDIES ON DYNAMICS OF SUCTION PILES

DURING THEIR LOWERING OPERATIONS

A Thesis

by

LIQING HUANG

Submitted to the Office of Graduate Studies of
Texas A&M University
in partial fulfillment of the requirements for the degree of

MASTER OF SCIENCE

August 2010

Major Subject: Ocean Engineering

STUDIES ON DYNAMICS OF SUCTION PILES

DURING THEIR LOWERING OPERATIONS

A Thesis

by

LIQING HUANG

Submitted to the Office of Graduate Studies of
Texas A&M University
in partial fulfillment of the requirements for the degree of

MASTER OF SCIENCE

Approved by:

Chair of Committee,	Jun Zhang
Committee Members,	Moo-Hyun Kim
	Ping Chang
Head of Department,	John M. Niedzwecki

August 2010

Major Subject: Ocean Engineering

ABSTRACT

Studies on Dynamics of Suction Piles during Their Lowering Operations. (August 2010)

Liqing Huang, B.S., Harbin Institute of Technology, P.R. China

Chair of Advisory Committee: Dr. Jun Zhang

Suction piles are used for anchoring the mooring lines at the seafloor. One of the challenges of their installing is the occurrence of the heave resonance of the pile-cable system and possibly the heave induced pitch resonance during the lowering process. When the heave and/or pitch frequency of the vessel which operates the lowering of the pile matches the heave natural frequency of the pile-cable system, the heave resonance may occur, resulting in large heave oscillations of the pile and thus significantly increasing loads on the lowering cable and lowering devices. Furthermore, the large heave may resonantly induce the pitch of a pile. To predict and possibly mitigate the heave/pitch resonance of the pile-cable system during the lowering process, it is crucial to under the mechanism of heave induced pitch resonance and estimate the added-mass and damping coefficients of the pile-cable system accurately.

The model tests of the forced heave excitation of pile models were first conducted to investigate the added-mass coefficient for a pile model with different opening area ratios at its top cap at the Haynes Coastal Engineering Laboratory of Texas A&M University. In the model tests, it was observed that the resonant heave may occur if the heave

excitation frequency matches the related heave natural frequency and the pitch resonance may be induced by the heave resonance.

The results of the following theoretical analysis and numerical simulation of the heave excitation of the pile-cable system are found to be consistent with the related measurements, which is helpful to further understand the physics of lowering a pile-cable system. The results of this study may be used to determine the magnitudes of total heave added-mass and damping coefficient of a pile and the heave natural frequency of the pile-cable system based upon its main characteristics. The heave induced resonant pitch is found to occur when 1) the pitch natural frequency is roughly equal to one half of the heave natural frequency and 2) the heave excitation frequency is approximately equal to the heave natural frequency. If only one of the two conditions is satisfied, no significant pitch resonance will occur. These results may have important implications to the operation of lowering offshore equipment to the seafloor in deep water.

DEDICATION

This is dedicated to my parents, who encourage me to study in graduate school.

ACKNOWLEDGEMENTS

I would like first to express my gratitude to Dr. Jun Zhang, my advisor and committee chair, for his encouragement, guidance and support throughout the course of this research. Sincere thanks are expressed to Dr. Moo-Hyun Kim and Dr. Ping Chang for serving as my committee members. I would also like to thank Dr. Alejandro H. Orsi for attending my thesis defense and giving some useful suggestions.

The experimental study was sponsored by InterMoor Inc. and conducted at Haynes Coastal Engineering Laboratory at Texas A&M University. I gratefully acknowledge the approval of use and publication of the experimental data by InterMoor Inc. Special thanks go to Dr. Robert E. Randall and his graduate student, Dustin Young, for their cooperation and help in conducting the model tests. I also thank Premium Solutions Inc. for building the excellent actuator and testing models, and laboratory technician John Reed and graduate student John Henrikson for technical help with electronic equipment.

I extend my gratitude to Mr. Bob Wilde, chief engineer at InterMoor Inc., who took time to modify the related report and paper and to provide useful information for our further study. I also acknowledge New Industries Inc. as well for providing the photos of suction piles. My thanks are expressed to the graduate students Xiaochuan Yu and Zhiyong Su at Texas A&M University as well for sharing their numerical techniques of MATLAB and their review and discussions of my theoretical formulation.

Finally, thanks also go to my friends and colleagues and the department faculty and staff for making my time at Texas A&M University a great experience.

TABLE OF CONTENTS

Page

Page

CHAPTER

Page

LIST OF FIGURES

FIGURE Page

FIGURE Page

FIGURE Page

FIGURE Page

FIGURE Page

FIGURE Page

FIGURE Page

FIGURE Page

FIGURE Page

FIGURE Page

LIST OF TABLES

TABLE Page

TABLE Page

TABLE Page

CHAPTER I

INTRODUCTION

1.1 Background

Suction piles or suction anchors are used for anchoring mooring lines of floating exploration and production platforms at the seafloor, particularly in a soft to intermediate cohesive soil. They were introduced into deepwater applications where alternative foundation concepts may prove to be much more costly or probably require the usage of a large derrick barge. Suction piles usually consists of a hollow steel cylinder, almost completely open at the bottom but closed at the top except for some vent valves and a suction port, which is located somewhere near the top through which water is pumped out to "suck" the pile into the seafloor (see Fig. 1). Suction piles have been installed in the engineering cases with water depths varying from as shallow as 40 m to as deep as 2500 m. Its diameters range from 3.5 m to 7 m, and its penetration into soils may be up to 20 m. The choice of the installation vessel depends on the size of the suction pile and other operations taking place during the installation operations. In deep water mooring installations, a suction pile is often installed at the same time as the related mooring line, thus avoiding the need to connect those two components under water. There are also connectors which can be used to connect mooring lines to a pre-installed suction pile (Diab and Tahan 2005).

This thesis follows the style and format of Ocean Engineering.

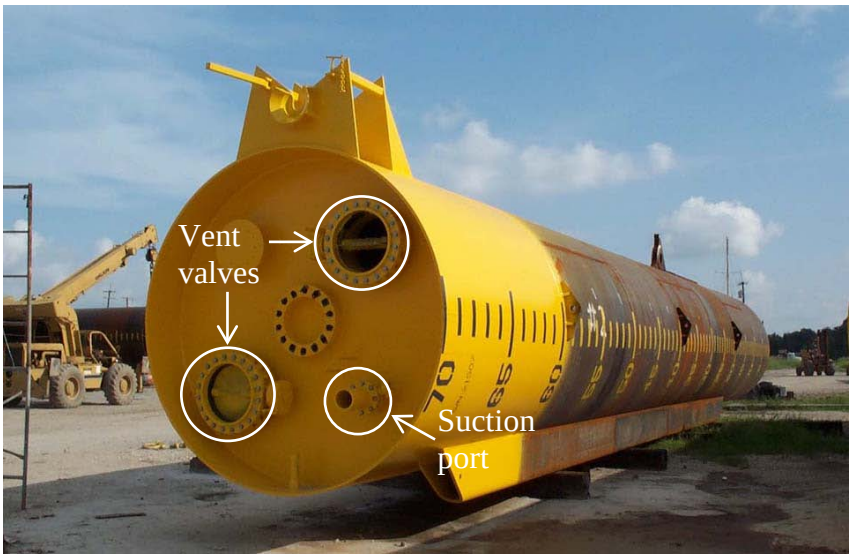

Fig. 1. Picture of a suction pile. *Courtesy of New Industries Inc.*

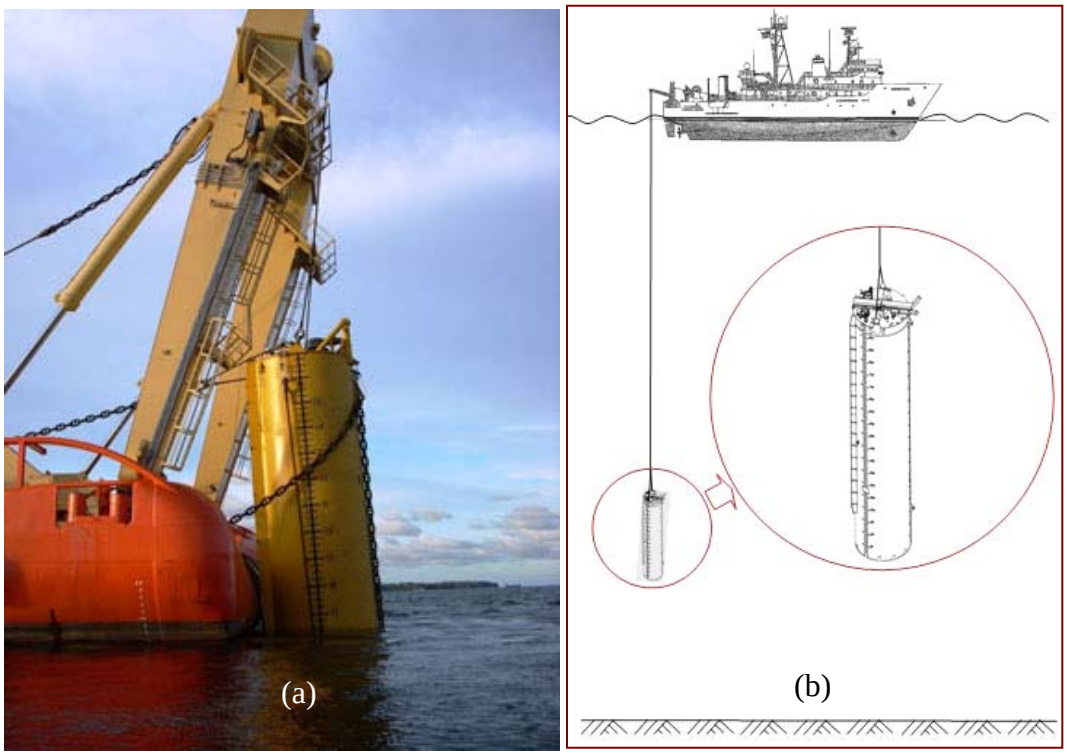

Fig. 2. Suction pile installation process: (a) Over-boarding; (b) Lowering operation. *Courtesy of InterMoor Inc.*

Suction piles can be lifted or skidded onto the deck of an anchor handling tug (AHT) which transports them directly to the offshore installation location. The installation process consists of the following stages: (a) Over-boarding, (b) Lowering to the seafloor (see Fig. 2), (c) Penetration into the seabed. Deploying suction piles over-board the installation vessel can be carried out by using a crane or an A-frame, which is depending on the size of the pile. Once in water, the pile can be lowered to the seafloor by a vessel crane or the deck-mounted winch.

There are two serious engineering problems with the lowering operations. The first is the heave “resonance” when the heave and/or pitch frequency of the vessel matches the natural frequency of the pile-cable system during the lowering operation. The heave resonance of the system may result in the large amplitude oscillation of the pile then the slackening and snapping of the lowering cable, which significantly increases the tensile loads on the lowering cable and vessel devices. To predict and possibly mitigate the resonance of the pile-cable system during the lowering process, it is crucial to estimate the natural frequency and damping coefficient of the pile-cable system accurately, which in turn needs to estimate the mass of entrapped water inside the pile as well as the added-mass water outside the pile. The model tests of the forced heave of pile models were conducted to investigate the total added-mass coefficient for different pile models with different opening area ratio of the top cap at the Haynes Coastal Engineering Laboratory at Texas A&M University. In the model tests, we were also able to find that the heave induced pitch amplification may possibly occur along with the heave resonance, with the pitch amplitude as large as 2° ~ 3° (Huang et al. 2010).

The second critical problem is the ‘hovering’ when the suction pile is suspended several meters above the seafloor. During the ‘hovering’, successive heave cycles cause the pile to partially penetrate and then retract from the seabed. As the pile approaching the seabed, the water escapes below the lower rim and the entrapped water through the suction port on top, thus resulting in a damping force on the pile. It is important to ensure at this stage that the damping loads and the seafloor resistance to penetration do not cause slackening of the cables and subsequently resulting in subsequent snap loads. Heave compensators fitted to the crane or the winch can help making these two problems much more manageable. Especially in some specific situations, the heave induced pitch motions were also observed along with the heave resonance in the “hovering” stage. For example, the pitch amplitude as large as 9° ~ 10° was observed by the subsea camera in the lowering project of SEPLA suction follower of 14 ft (4.27 m) in diameter and 90 ft (27.43 m) in length with a T1-A-28 SEPLA anchor in Angola (InterMoor Inc.).

An accurate means of predicting the cable tensions, accounting for the transition between taut and slack cable conditions, is required for the proper design of marine cable systems. Snap loads can be several times larger than the normal static and dynamic loading and are the dominant design consideration (Niedzwecki and Thampi 1991). Because of the strong nonlinear nature of the snap phenomenon, which is characterized by a sudden loss of cable stiffness in the slack regime, time domain simulations are the most appropriate means of predicting the snap loads.

A number of researchers investigated the snap loading of marine cables in the past. Goeller and Laura (1971) conducted analytical and experimental investigations on the dynamic response of vertically hanging segmented cable systems, where the upper portion is a stranded steel cable and the lower segment is a nylon rope, for the purposes of salvage recovery of objects embedded in ocean sediments or handling structures placed on the bottom of the ocean. They provided four mathematical models to study the problem of snap loading, including distributed mass Voigt model, parameter viscoelastic model, analog model and Slic model. Liu (1973) used a two-dimensional, multi-degree-of-freedom (MDOF) model to determine snap loads in lifting and mooring lines. Later, Yoshida and Oka (1978) studied snap loads in taut moored platforms through model tests and theoretical analysis. Niedzwecki and Thampi (1991) investigated the snap load behavior in marine cable systems in the case of the deep ocean coring activities. By using a simple SDOF model of a cable-body system, they provided a dimensionless curve for the preliminary assessment of snap loading occurrence. Besides, a complex MDOF model of the complete drill string/cable/package system was introduced by them for predicting the snap loading qualitatively when it occurs. Milgram et al. (1988) and Shin (1991) considered 2-D cases and simplified the governing equations using various assumptions and solved them by a spectrum method with the Newmark's method for the time integration. Huang and Vassalos (1993) considered 3-D modeling based upon a lumped-mass-and-spring scheme with modifications to take into account of the bi-linear axial stiffness of the cable. They developed a numerical approach using the modified Euler method for the time integration to predict the snap loading of marine cables

operating in alternating taut-slack conditions. Driscoll et al. (2000) developed a finite-element lumped-mass scheme to model a vertically tethered ROV system by applying Galerkin's method to a continuous representation of the tether. Hennessey, Pearson and Plaut (2005) experimentally investigated the snap loading of synthetic ropes by repeated drop tests to examining the effects of the type of rope, drop height, drop weight, whether the rope has been subjected to static precycling, and the number of dynamic tests.

However, almost all investigations mentioned above focused on the snap loading of the cable and the heave motion of the attached weight, and none of them considered the heave induced pitch motion of the attached slender body. During the lowering operation of suction piles, the heave motion are dominant almost all the process, while the heave induced pitch motions were also observed by underwater cameras sometime when the pile-cable system experiences the "resonance" or "hovering" stage. The mechanism of heave induced pitch motion and the relation between the heave motion and the pitch motion are required to be investigated in great needs for lowering fragile objects with light weight and complicated shape to the seafloor, such as a Christmas tree. After we have conducted the analytical formulation and numerical simulations, it is found that the heave induced pitch motion can be predicted by a Mathieu instability diagram described by a damped Mathieu equation, and the unstable scenarios are located in the principle unstable region. That is, if the heave and/or pitch frequency of the vessel happens to be twice of the pitch natural frequency of the pile, the heave induced pitch amplification may also occur along with the heave resonance.

Although the Mathieu instability have been well studied mathematically and some researcher have also investigated the Mathieu instability of the ocean surface floating structures, such as SPAR platforms (Haslum and Faltinsen 1999, Rho et al. 2002, Zhang et al. 2002, Koo et al. 2004), but the Mathieu instability of totally submerged subsea structures during lowering or recovering operations has not been well studied so far.

1.2 Objectives

The primary interest of this study is to conduct experimental, analytic and numerical investigations on the dynamic responses of suction piles during lowering operations, including the dominant heave motion and the heave induced pitch motion, under the heave excitations by a surface vessel. The effects of current and payout rate of cable are ignored in this study. The objectives of the present research are:

1. To determine the total added-mass coefficient of a model suction pile (including the mass of entrapped water inside and added mass of water outside the pile) with different opening area ratio on the top plate through model tests.
2. To formulate the governing equations of the heave-pitch coupled motion for the model suction piles considering the slackening of the cables, develop a numerical scheme in the time domain and conduct the numerical simulation.
3. To compare the numerical results with the related measurements of model tests, and understand the mechanism of heave induced pitch motion and the relation between the dominant heave motion and the induced resonant pitch.

CHAPTER II

EXPERIMENT

In this chapter the total added mass coefficients of a model suction pile with different opening area ratio on the top plate are deduced by identifying the heave resonance frequency of the pile-cable system. The model tests employ an electric motor (actuator) to induce the heave excitation of a pile-cable model in water at certain range of frequencies which cover the resonance frequency of the model. Within the range of frequencies, we determine the heave natural frequency of the pile-cable system by searching at which frequency the model experiences the largest heave. Since the stiffness of the cable (spring) and the mass of the model pile are known, the natural frequency of the system can be used to calculate the added-mass coefficient of the pile.

2.1 Test Tank Facility

The dredge/towing tank in the Haynes Coastal Engineering Laboratory at Texas A&M University was used for the testing. The tank shown in Fig. 3 is 149.5 ft (45.57 m) long, 12 ft (3.66 m) wide, and 10 ft (3.05) maximum water depth. The sediment pit is an additional 5 ft (1.52) deep and is 24.8 ft (7.56 m) long located about 41 ft (12.5 m) from the weir end of the tank. There is an observation well with view windows for motion observation and video recording. Fig. 4 shows the dredge/tow carriage and Fig. 5 shows the model suction pile actuator attached to the front of the dredge/tow carriage.

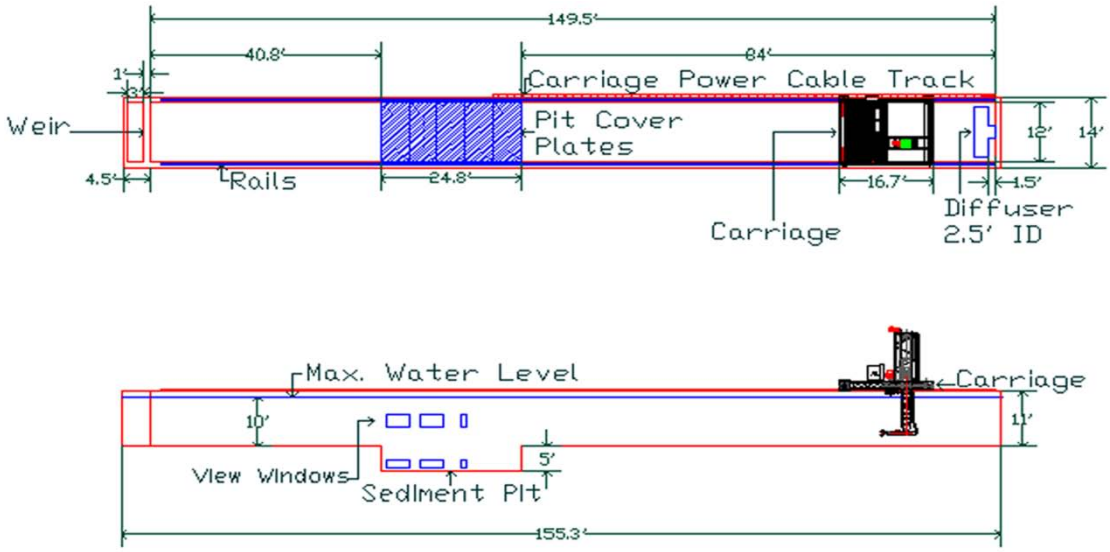

Fig. 3. Elevation and plan view of dredge/tow tank in the Haynes Coastal Engineering Laboratory at Texas A&M University.

Fig. 4. Dredge/tow carriage and tank in front of sediment pit filled with water.

2.2 Experimental Setup

The actuator built by Premium Solutions Inc. was used for heave excitation of the models while in the tank. As shown in Fig. 5 it consists of a 220 volt variable speed electric motor, a 20:1 reduction gearbox and the actuating spindle that is attached to the gearbox. The spindle has holes for adjusting the heave stroke to 3 in (7.6 cm), 4 in (10.2 cm), 5 in (12.7 cm), 6 in (15.2 cm), 7 in (17.8 cm), 8 in (20.3 cm), and 9 in (22.9 cm). The actuator assembly was supported by the frame attached to the dredge carriage.

To control the variable speed motor, a voltage regulator was employed. It is a Lenze (AC Tech) SCM Series Sub-Micro drive provided by InterMoor Inc. and shown in Fig. 6 (lower right). The voltage controller was mounted on a bracket that was situated on the dredge carriage for easy access. The sub-micro drive is equipped with a remote; the drive system has the ability to slowly ramp up the motor.

The cable assembly contains an upper and lower force transducer, upper and lower accelerometer and a spring. The force transducers are 250 lb (1,112 N) in-line strain gauges and waterproof. The accelerometers are single directional. The first force transducer was placed close to the actuating arm and the second was placed right above the model suction pile cap as shown in Fig. 7. This setup was used to determine the different loads in the cable above and below the spring.

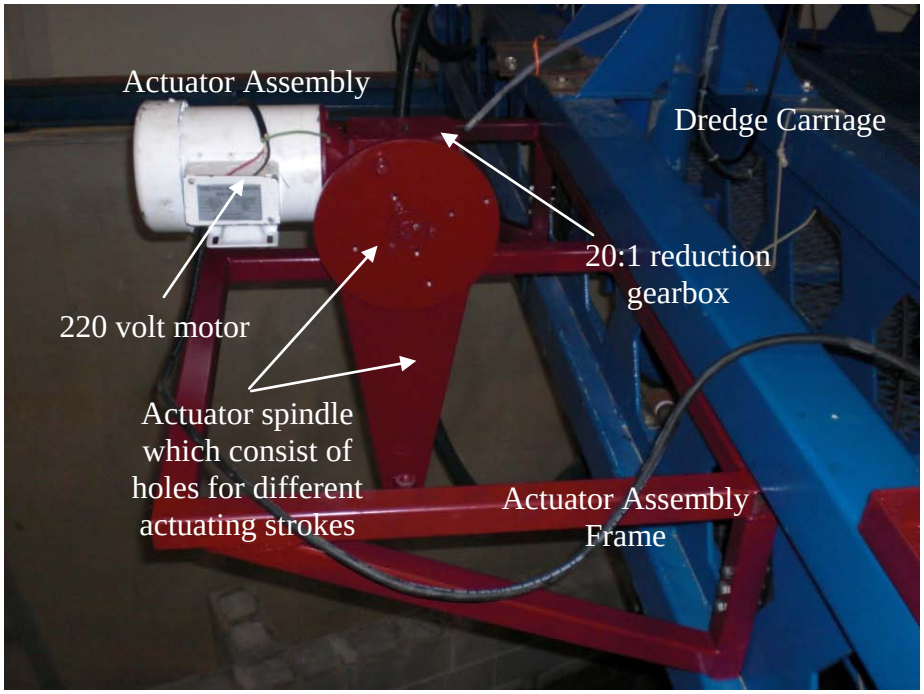

Fig. 5. Setup of actuator for suction pile tests.

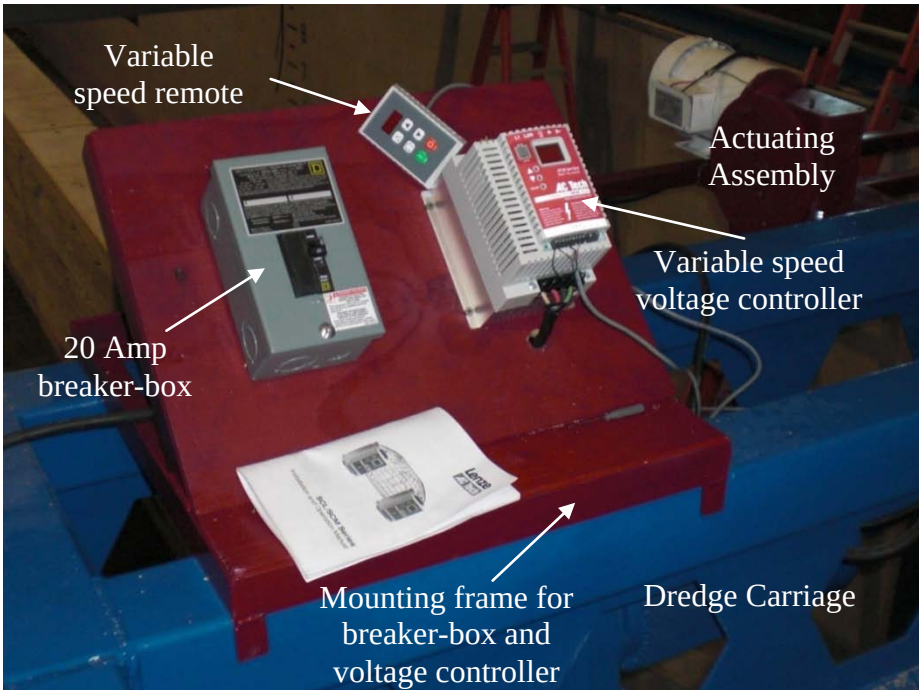

Fig. 6. Variable speed motor controls.

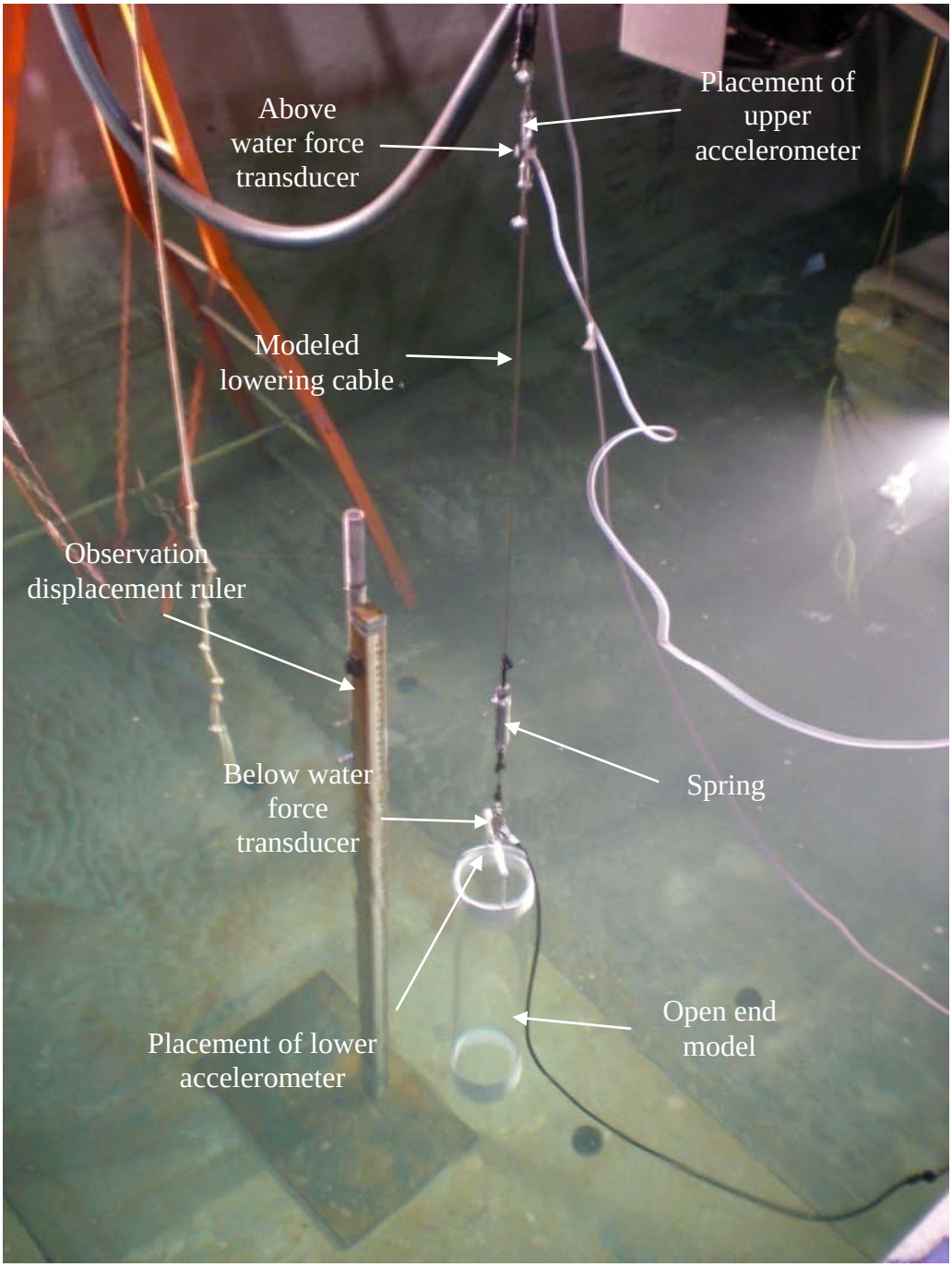

Fig. 7. Model pile with the cable assembly.

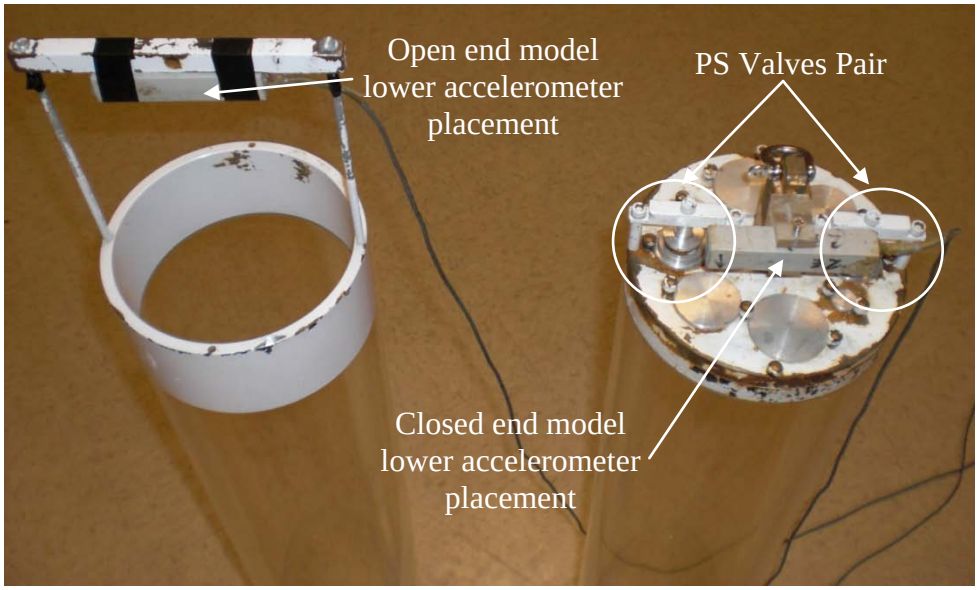

Fig. 8. Accelerometer placements on model suction piles.

Fig. 9. Data acquisition system and amplifier setup.

A spring was inserted in the middle of the cable to approximately simulate the stiffness of a prototype 6,562 ft (2,000 m) cable used for lowering a suction pile to the sea floor so that the model pile may have the equivalent resonant heave period following the Froude number similarity.

For the two accelerometers, the first was placed at the force transducers U-bolt connection and the second at the top of the model suction piles, as shown in Fig. 7. The purpose for the two accelerometers placed at these two locations is to measure the acceleration above the spring and the acceleration of the model suction pile below the spring, which are different as anticipated. In Fig. 8, the placement of the lower accelerometer can be seen in the cases of the open and closed end models. For the open ended model the accelerometer was attached by using electrical tape on the connection bar for the cable assembly, and for the closed ended model, the accelerometer was attached by using a fabricated acrylic bracket that was attached to the connection for the cable assembly.

Lastly, an observation ruler was put in the tow tank for visually observing the displacement of the model suction pile while it was undergoing oscillation. This visual observation is accomplished by looking through the observation glass window of the tank. The oscillation of the model suction pile was videoed to make sure that the accelerometers were recording correctly.

The force transducers and accelerometers were powered and the output signal amplified to render good signals. This was done using a strain gauge amplifier shown in Fig. 9. The strain gauge amplifier is also capable of filtering the high-frequency noise.

To record the output signal from the two force transducers and accelerometers, a program called Lab-View was used which recorded the voltage reading into a text file.

2.3 Model Parameters

The two suction pile models are shown in Fig. 10 (left) and their basic parameters listed in Table 1. The model scale is 1:32, thus the prototype pile size is 16 ft (4.88 m) in diameter and 96 ft (29.26 m) in length. The main difference between the two models is one with the cap and the other without the cap (open end). The cap may have up to six pairs of valves with different diameters and different types located on the cap. When all valves are completely sealed, the model is referred as the closed end model. When some or all of these valves are open, the model is referred as partially open end model. For the purpose description, the valve pairs are numbered ranging from the smallest to the largest in diameter and shown in the Fig. 10 (right). The specifications of these valves are summarized in the Table 2. It is noted that a pair of ring reducers can be mounted on the pair of #2 valves to decrease the valve diameter from 1 in (2.5 cm) to 3/4 in (1.9 cm). The latter are named #2' valves. Also modeled was a simulation of a new generation vent valves called the PS valves. The closure plates for this type valve were mounted above the pair of #2' valves as shown in the Fig. 8. In the standard configuration, the orifices in the pile’s top plate are meant to simulate butterfly valves.

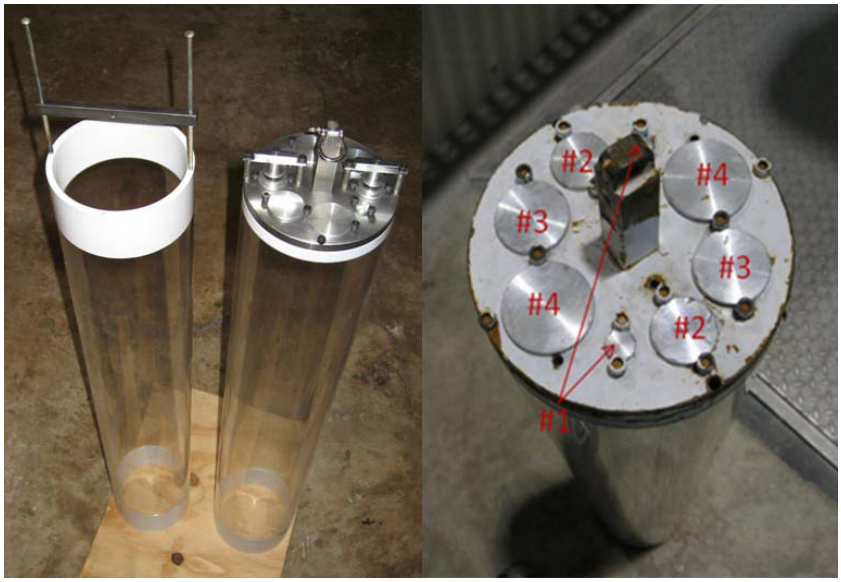

Fig. 10. Two pile models (left) and valve pair number for the closed end model (right).

Table 1. Model parameters of the two suction pile models.

Model parameters	Open end model	Closed end model
Cylinder length	3 ft (0.91 m)	3 ft (0.91 m)
External diameter	6 in (15.2 cm)	6 in (15.2 cm)
Wall thickness	0.25 in (0.635cm)	0.25 in (0.635cm)
External area	28.274 in^2 (182.4 cm^2)	28.274 in^2 (182.4 cm^2)
Internal area	23.758 in^2 (153.3 cm^2)	23.758 in^2 (153.3 cm^2)
External volume	1017.9 in^3 (16,680.4 cm^3)	1017.9 in^3 (16,680.4 cm^3)
Internal volume	855.3 in^3 (14,015.9 cm^3)	855.3 in^3 (14,015.9 cm^3)
Weight of water inside pile	30.9 lb (137.45 N)	30.9 lb (137.45 N)
Weight of water displaced by pile	5.9 lb (26.24 N)	5.9 lb (26.24 N)
Dry weight	14.5 lb (64.50 N)	16.0 lb (71.17 N)
Wet weight	8.5 lb (37.81 N)	9.6 lb (42.70 N)
Weight of model accessories*	1.06 lb (4.72 N)	1.06 lb (4.72 N)
Total dry weight	15.57 lb (69.26 N)	17.06 lb (75.89 N)
Gravity center from top	1.29 ft (0.393 m)	1.27 ft (0.387 m)
Buoyancy center from top	1.50 ft (0.457 m)	1.40 ft (0.427 m)

* Model accessories include a spring, an underwater force transducer, an underwater accelerometer, a section of cable and connections between the spring and the model.

Table 2. Specifications of the valves on the cap of the closed end model.

Model valve pair No.	Prototype valve diameter	Model valve diameter	Area of model valve pair	Note
#1	12 in (30.48 cm)	0.375 (0.95 cm)	0.221 in^2 (1.426 cm^2)	Smallest in diameter
#2	32 in (81.28 cm)	1.000 in (2.54 cm)	1.571 in^2 (10.135 cm^2)	
#2'	24 in (60.96 cm)	0.750 in (1.91 cm)	0.884 in^2 (5.703 cm^2)	With ring reducers on #2 valves
PS Valves	24 in (60.96 cm)	0.750 in (1.91 cm)	0.884 in^2 (5.703 cm^2)	With closure plates over #2' valves
#3	40 in (101.60 cm)	1.250 in (3.18 cm)	2.454 in^2 (15.832 cm^2)	
#4	48 in (121.92 cm)	1.500 in (3.81 cm)	3.534 in^2 (22.780 cm^2)	Largest in diameter

Fig. 11. Calibration procedure for the spring.

2.4 Spring Stiffness and Sensor Calibration

An extension spring is used throughout all the model tests, and the stiffness of the spring is the key parameter for determining the total added-mass coefficients and for the later numerical simulations. The elongation of the spring was measured for adding 1 kg weight increment at a time, as illustrated in Fig. 11. This procedure rendered a five point calibration shown in Table 3. It is found from linear regression in Fig. 12 that the spring stiffness is 1.5063 lb/in (2.638 N/cm) with the initial (minimum) tension of 2.222 lb (9.884 N).

The force transducers and accelerometers were calibrated before the tests. The calibration of the force transducers is illustrated in Fig. 13 (left). A segment of cable was attached to the overhead crane and five different weights in 1 kg increments were used in the calibration. The calibration of the accelerometers was accomplished by using a turn table device as shown in Fig. 13 (right). The accelerometers were calibrated by turning them at zero degree to get a reading for zero gravity, and then at positive and negative ninety degrees to get a reading for positive and negative reading of one “g”. Finally, a reading was taken at positive and negative thirty degrees. This procedure rendered a five point calibration for the accelerometers.

Table 3. Calibration results of the spring used through the model tests.

Weight added in each step (kg)	(lb)	Accumulative load (lb)	Deformation of spring (mm)	(in)
0	0	0	152	5.984
1.001	2.207	2.207	154	6.063
1.001	2.207	4.414	187	7.362
1.003	2.211	6.625	225	8.858
1.001	2.207	8.832	263	10.354
1.001	2.207	11.038	302	11.890
Initial Tension		2.222 lb	(9.884 N)	
Spring Stiffness		1.5063 lb/in	(2.638 N/cm)	

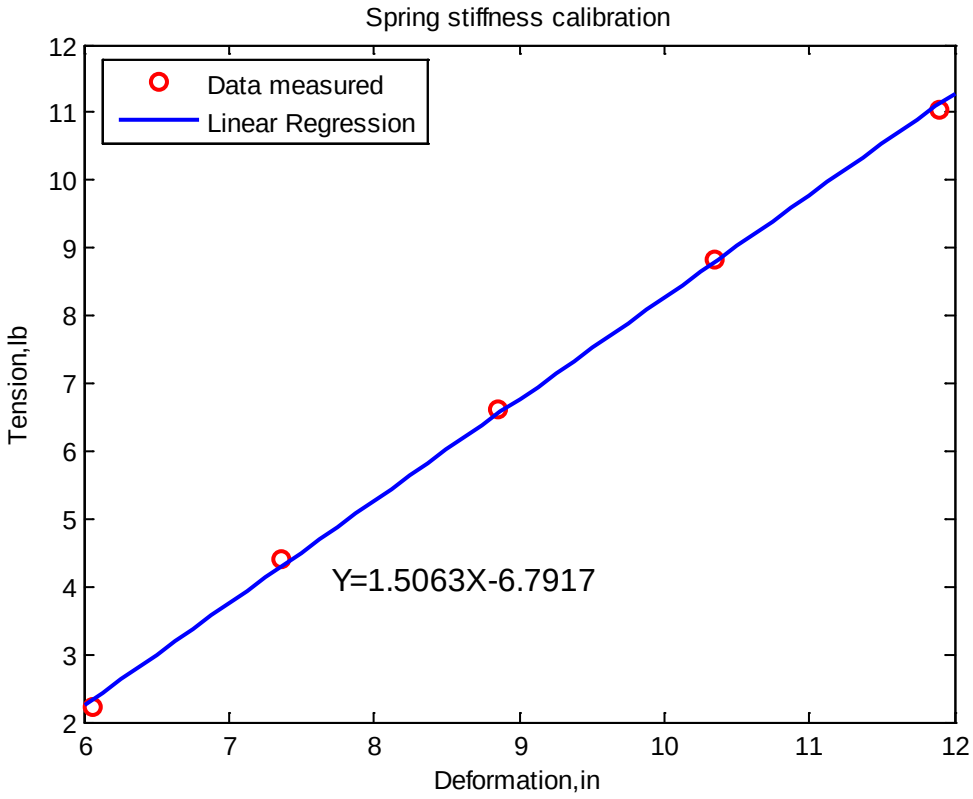

Fig. 12. Linear regression of the calibration results for the spring stiffness.

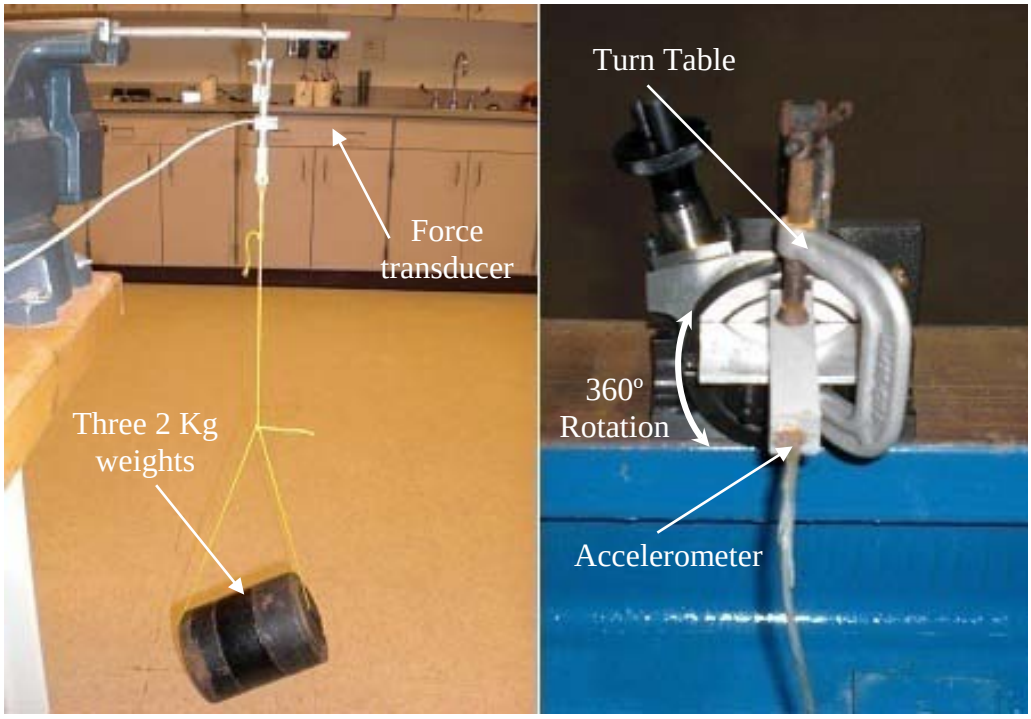

Fig. 13. Force transducer (left) and accelerometer (right) calibration procedure.

2.5 Dye Injection Procedure and Flow Visualization

The purpose of the dye injection is to visualize whether or not and how fast the water inside the suction pile model moved with the model while it oscillates. The dye was injected through a ¼ inch (0.635cm) plastic hose and a syringe was used to pump the dye from a storage vessel into the plastic hose, as shown in Fig. 14. During all tests, dye was released from the end of the hose which was attached to the inside wall of the pile model, as shown in Fig. 15. In the case of the closed end and partially open end models, in addition to the hose attached the inside wall, there was an additional hose also placed inside the model but near the upper cap. The locations of the two hoses in the closed ended model suction pile are shown in Fig. 15 (right).

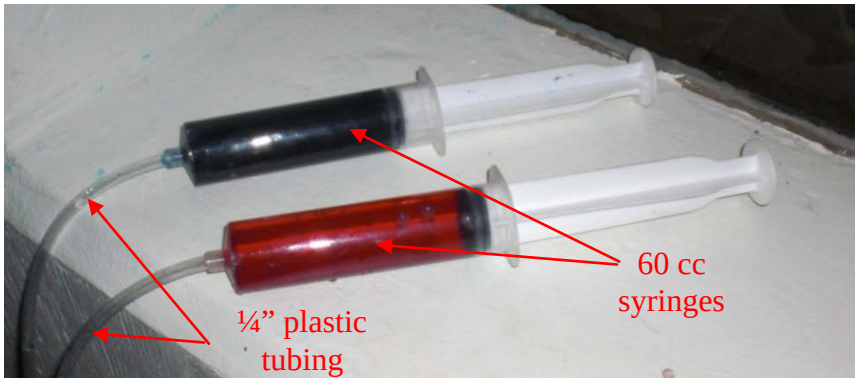

Fig. 14. Equipments for injecting dye.

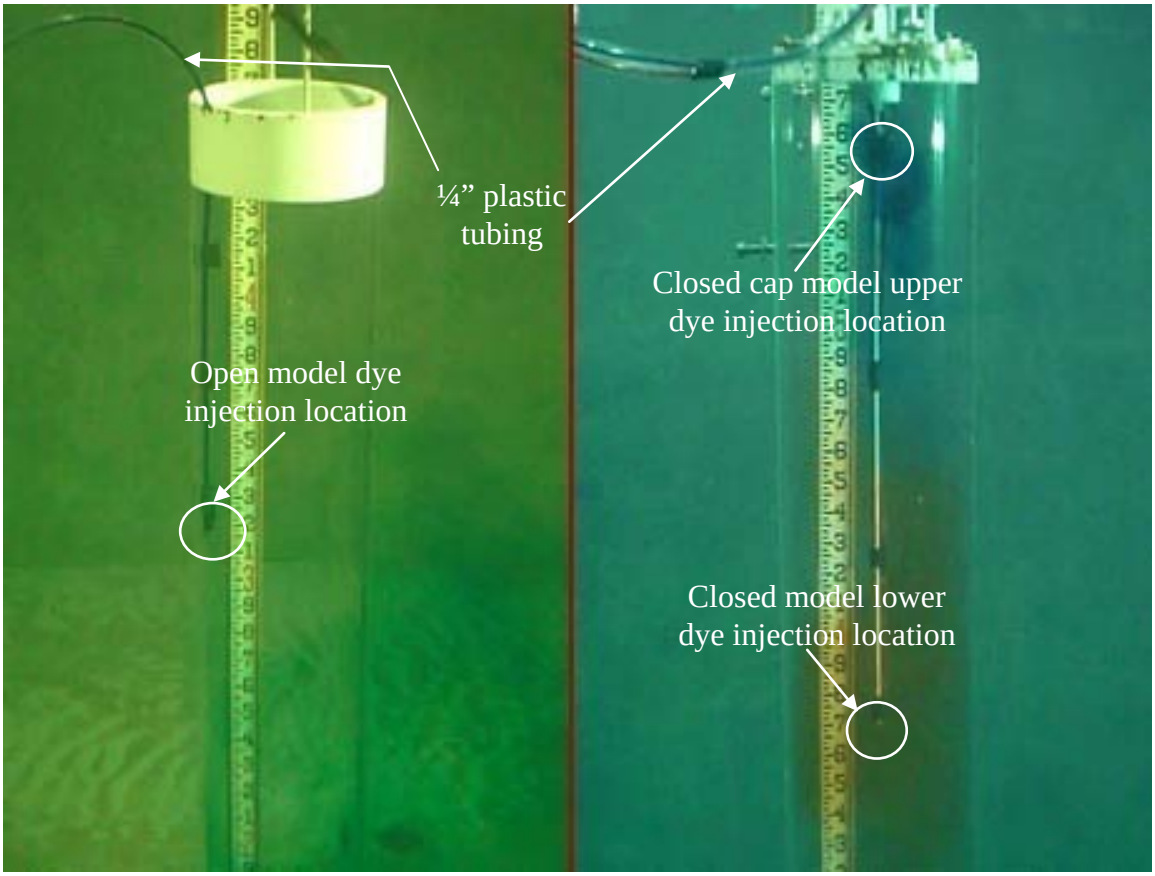

Fig. 15. Open (left) and closed (right) model dye injection procedure.

In the case of the open-ended model, a streak of dye from the open end of the plastic hose was observed. Since the open end of the hose was attached the pile model, the dye streak indicates the water inside the pile did not move with the model. However, in the case of the closed end model, no dye streak was observed inside the model, indicating the water moves at the same velocity of the model. In all cases of model testing, the inside of a pile model was always filled with water and no cavitations were observed.

2.6 Analysis of Measurements

The procedures of measurement analyzing for each model pile are virtually the same and described as follows. When the heave responses of the model pile reach the steady state, the signals of four sensors (two force transducers and two accelerometers) were recorded for a period of 120 sec. Before applying Fast Fourier Transform (FFT) to the time series of measurements, it is multiplied by a unit (height) trapezoidal window function with a ramp of 15 sec at both ends. Fig. 16 to Fig. 19 show the measurements of the four sensors at the far below resonance frequency $f = 0.3751\text{Hz}$ for the closed end model in both time and frequency domains. We integrate the measured heave acceleration time history over time once to obtain the heave velocity history and twice to obtain the heave displacements, which are depicted in Fig. 20 and Fig. 21 respectively. Fig. 22 to Fig. 25 show the measurements of the four sensors at the near resonance frequency $f = 0.5502\text{Hz}$ for the closed end model in both time and frequency domain. Similarly, we integrate the measured heave acceleration time history over time once to

obtain the heave velocity history and twice to obtain the heave displacements, which are depicted in Fig. 26 and Fig. 27, respectively.

The dynamic tension amplitude above the spring is similar to but slightly greater than the corresponding one below the spring. It is because the tension above the spring includes the weight and initial force of the spring. However, the acceleration above the spring is significantly smaller than the corresponding one below the spring, especially when the excitation frequency of the actuator is very close to the natural frequency. As expected, the heave amplitude of the model is greatly amplified near its natural frequency.

It is observed in Fig. 22 that the measured acceleration at the above water accelerometer is asymmetric (higher positive magnitude and relatively lower negative magnitude) in time domain. The asymmetry of measured acceleration results in several super-harmonic peaks in frequency domain, which is located at the frequencies of integral times of that of the major peak. The asymmetry in the above water acceleration is caused by the ‘push up’ of the pile model, which occurs when the pile model moves up much more than the cable above the spring and the tension in spring reaches its minimum tension. The ‘push up’ may result in greater heave amplitude at the location of the above water accelerometer than that at the actuator. Because of the ‘push up’, the cables above and below the spring can be slack at the moment, which was visually observed during the tests.

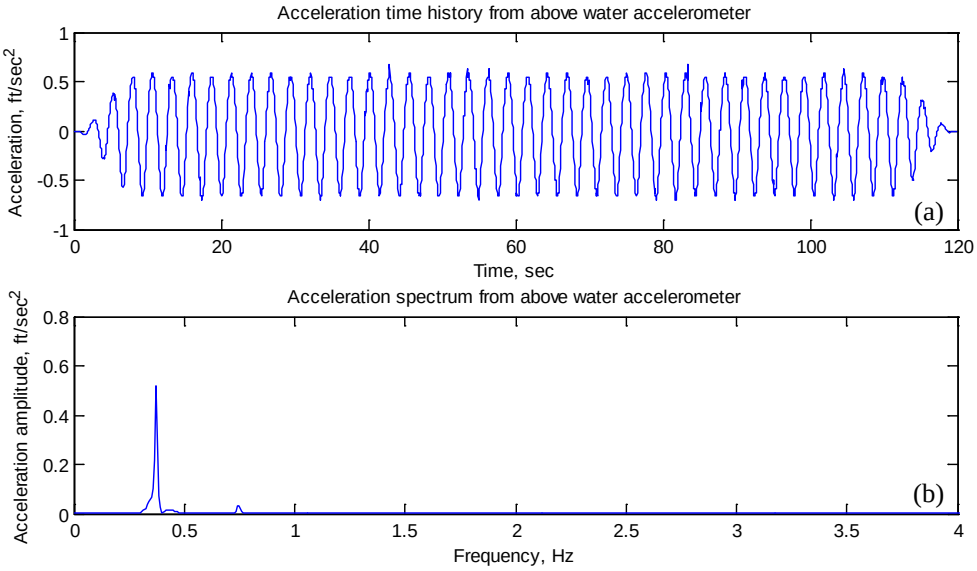

Fig. 16. An acceleration measurement of the upper accelerometer at the far below resonance frequency f = 0.3751 Hz for the closed end model: (a) Acceleration time history; (b) Acceleration spectrum.

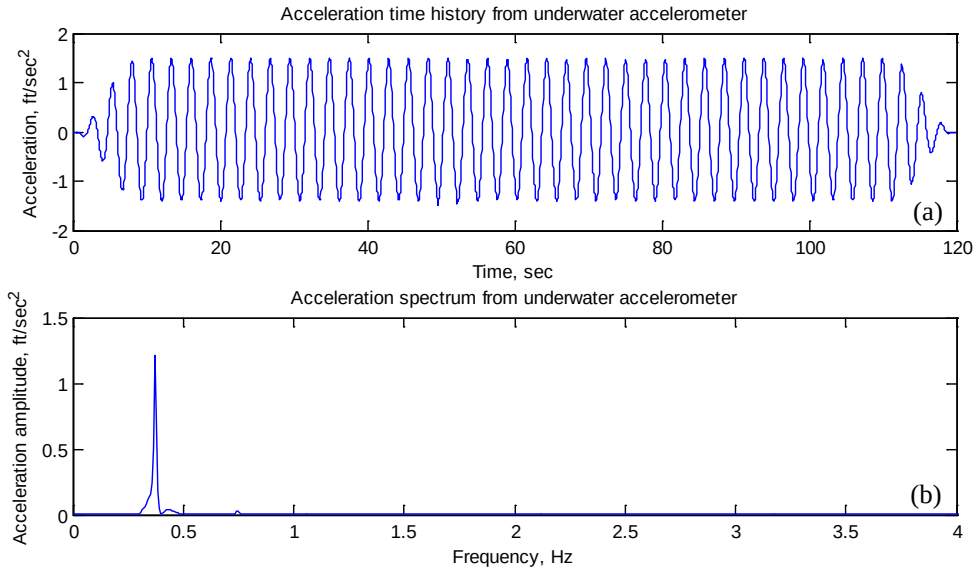

Fig. 17. An acceleration measurement of the lower accelerometer at the far below resonance frequency f = 0.3751 Hz for the closed end model: (a) Acceleration time history; (b) Acceleration spectrum.

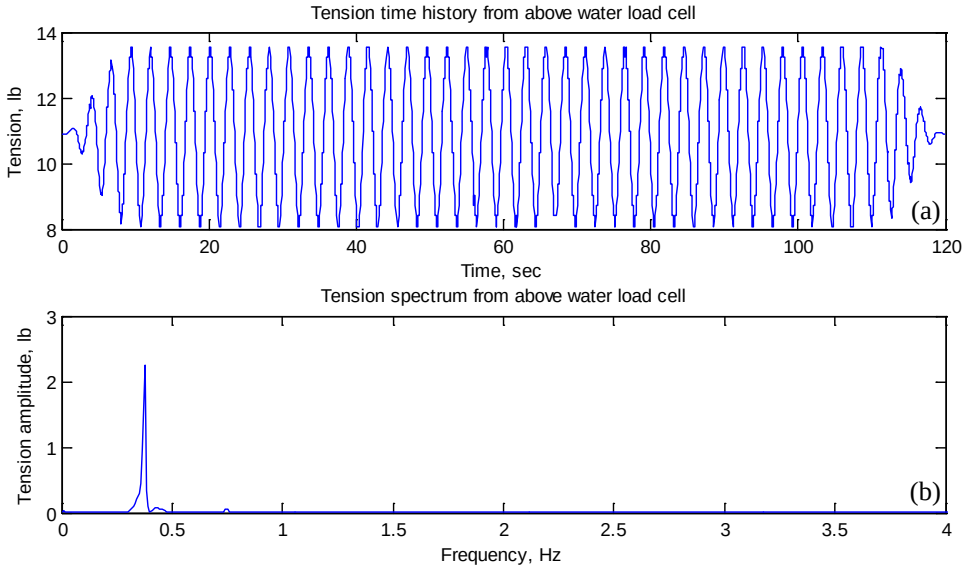

Fig. 18. A tension measurement of the upper force transducer at the far below resonance frequency f = 0.3751 Hz for the closed end model: (a) Tension time history; (b) Tension spectrum.

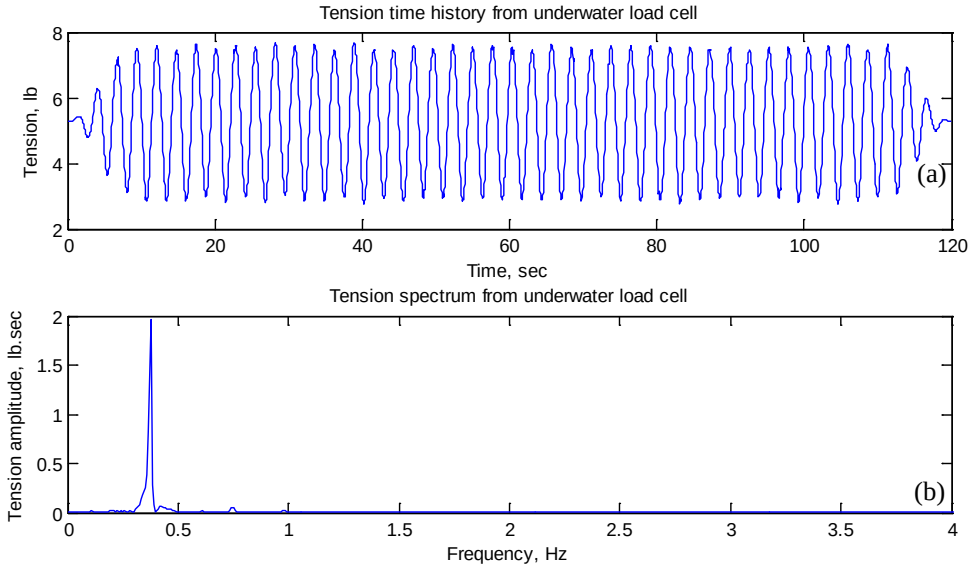

Fig. 19. A tension measurement of the lower force transducer at the far below resonance frequency f = 0.3751 Hz for the closed end model: (a) Tension time history; (b) Tension spectrum.

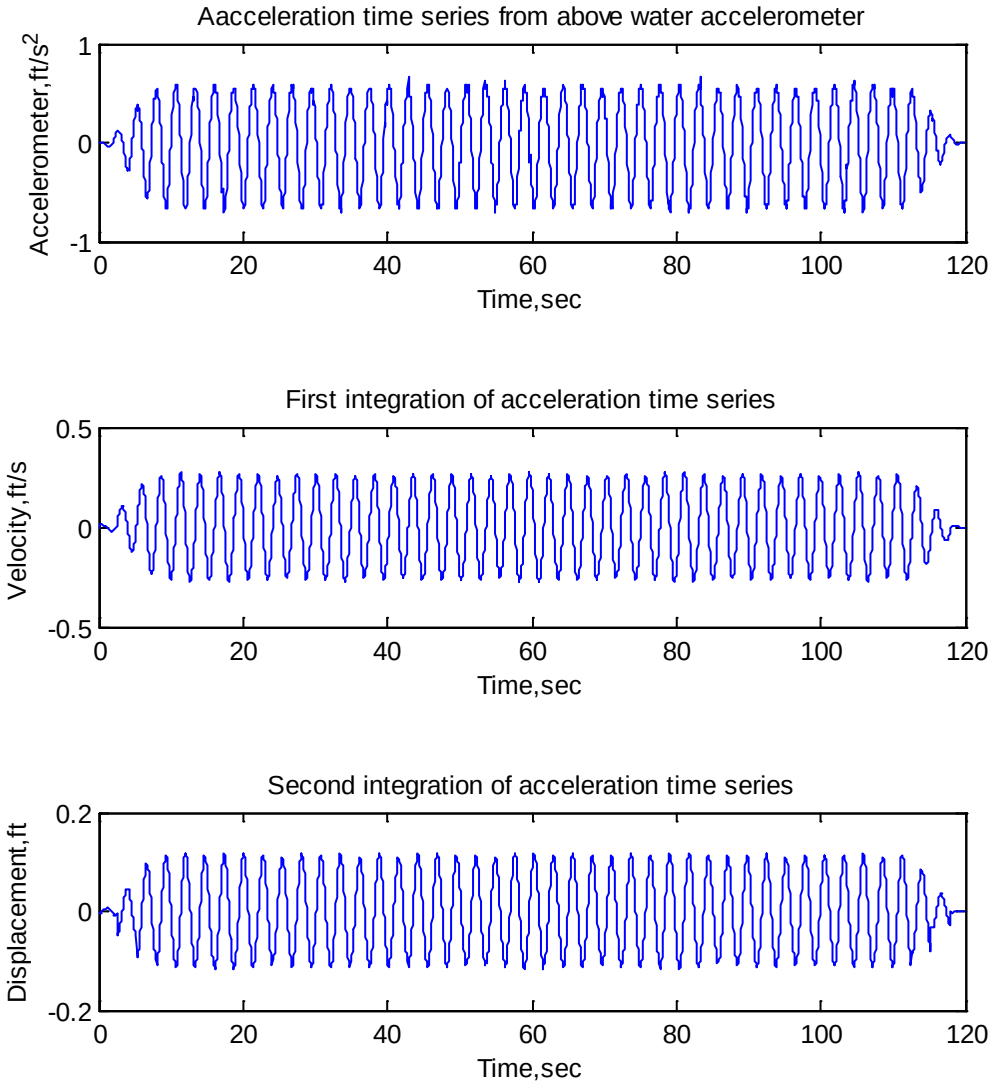

Fig. 20. Integrations of the acceleration time history of the upper accelerometer at the far below resonance frequency f = 0.3751 Hz for the closed end model.

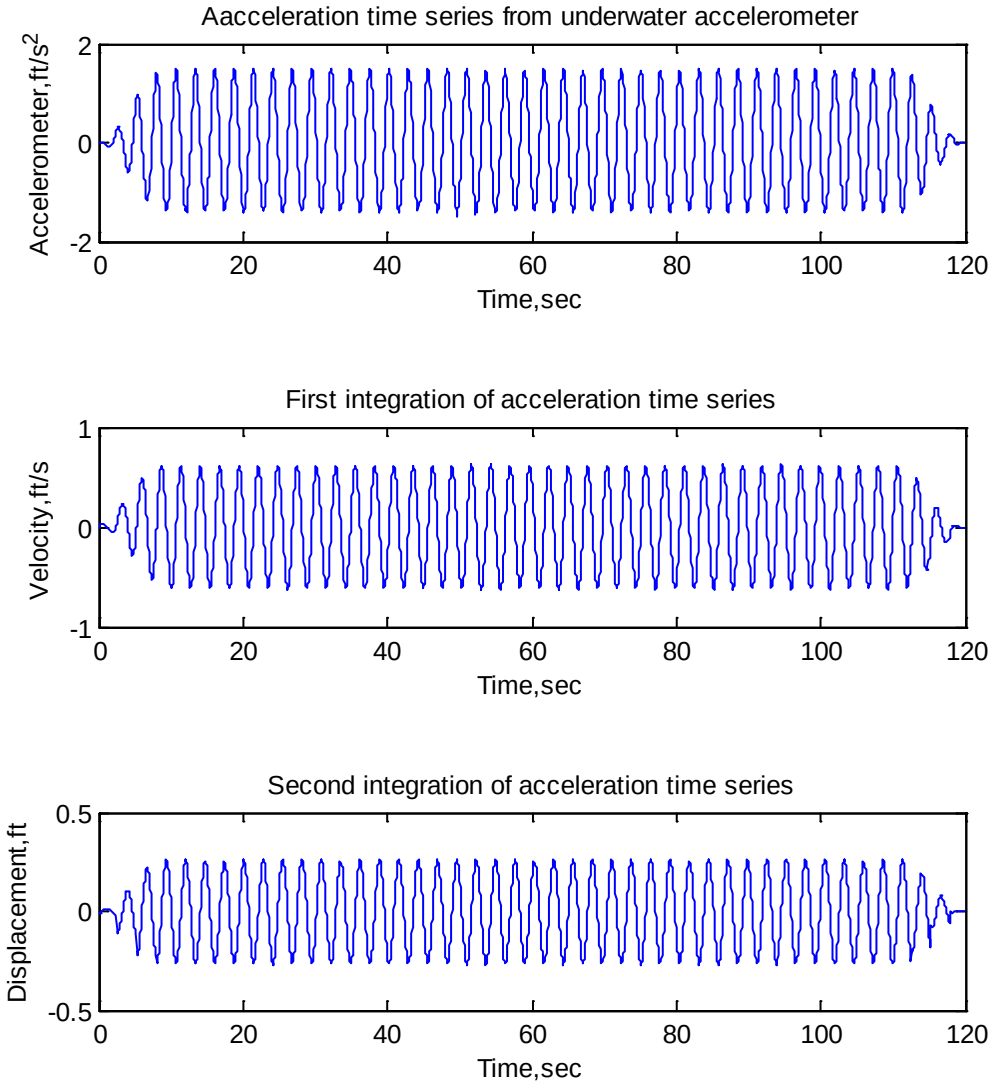

Fig. 21. Integrations of the acceleration time history of the lower accelerometer at the far below resonance frequency f = 0.3751 Hz for the closed end model.

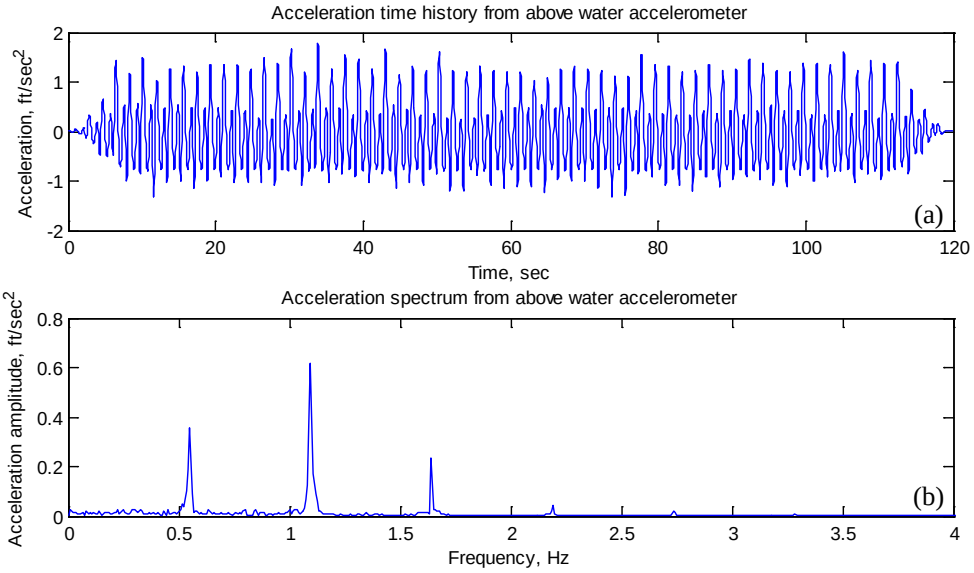

Fig. 22. An acceleration measurement of the upper accelerometer at the near resonance frequency f = 0.5502 Hz for the closed end model: (a) Acceleration time history; (b) Acceleration spectrum.

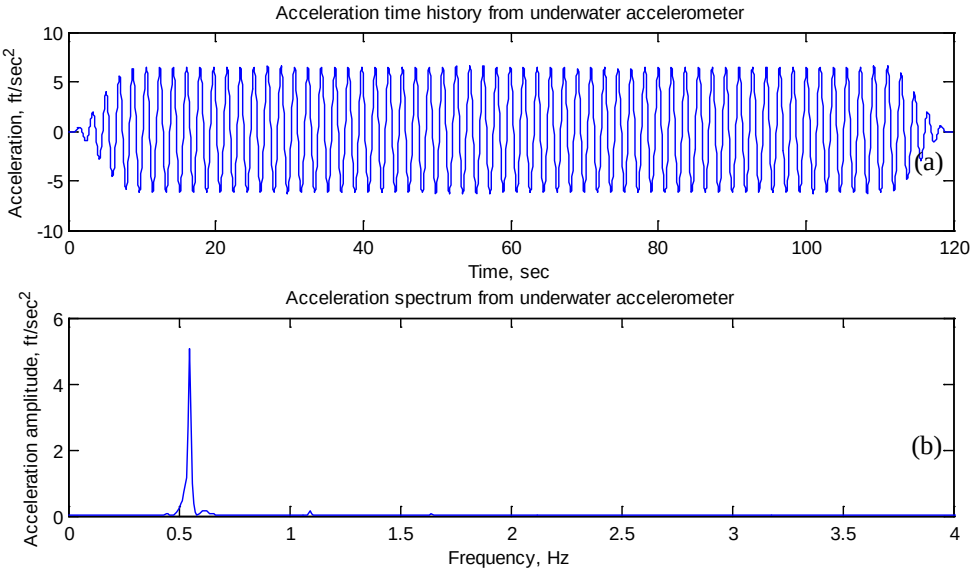

Fig. 23. An acceleration measurement of the lower accelerometer at the near resonance frequency f = 0.5502 Hz for the closed end model: (a) Acceleration time history; (b) Acceleration spectrum.

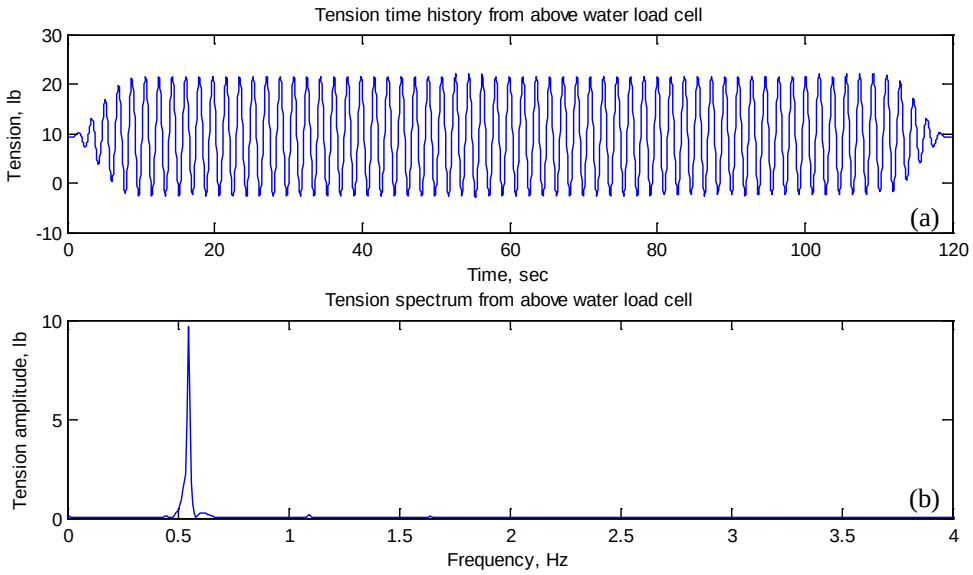

Fig. 24. A tension measurement of the upper force transducer at the near resonance frequency f = 0.5502 Hz for the closed end model: (a) Tension time history; (b) Tension spectrum.

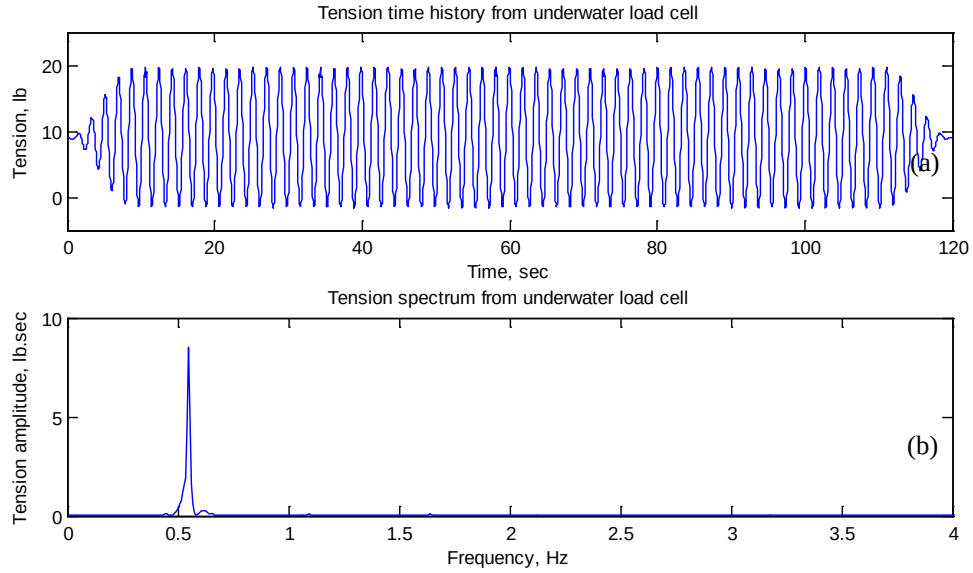

Fig. 25. A tension measurement of the lower force transducer at the near resonance frequency f = 0.5502 Hz for the closed end model: (a) Tension time history; (b) Tension spectrum.

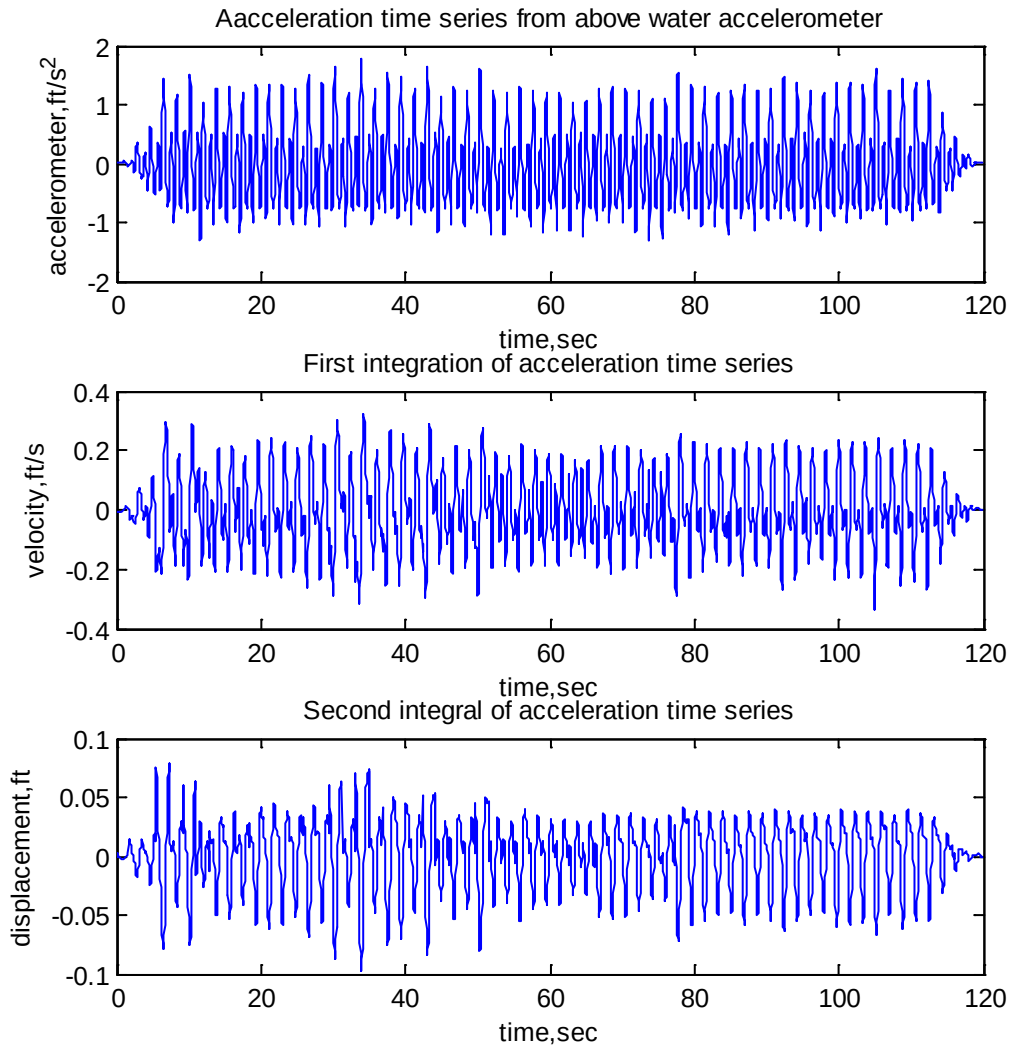

Fig. 26. Integrations of the acceleration time history of the upper accelerometer at the near resonance frequency f = 0.5502 Hz for the closed end model.

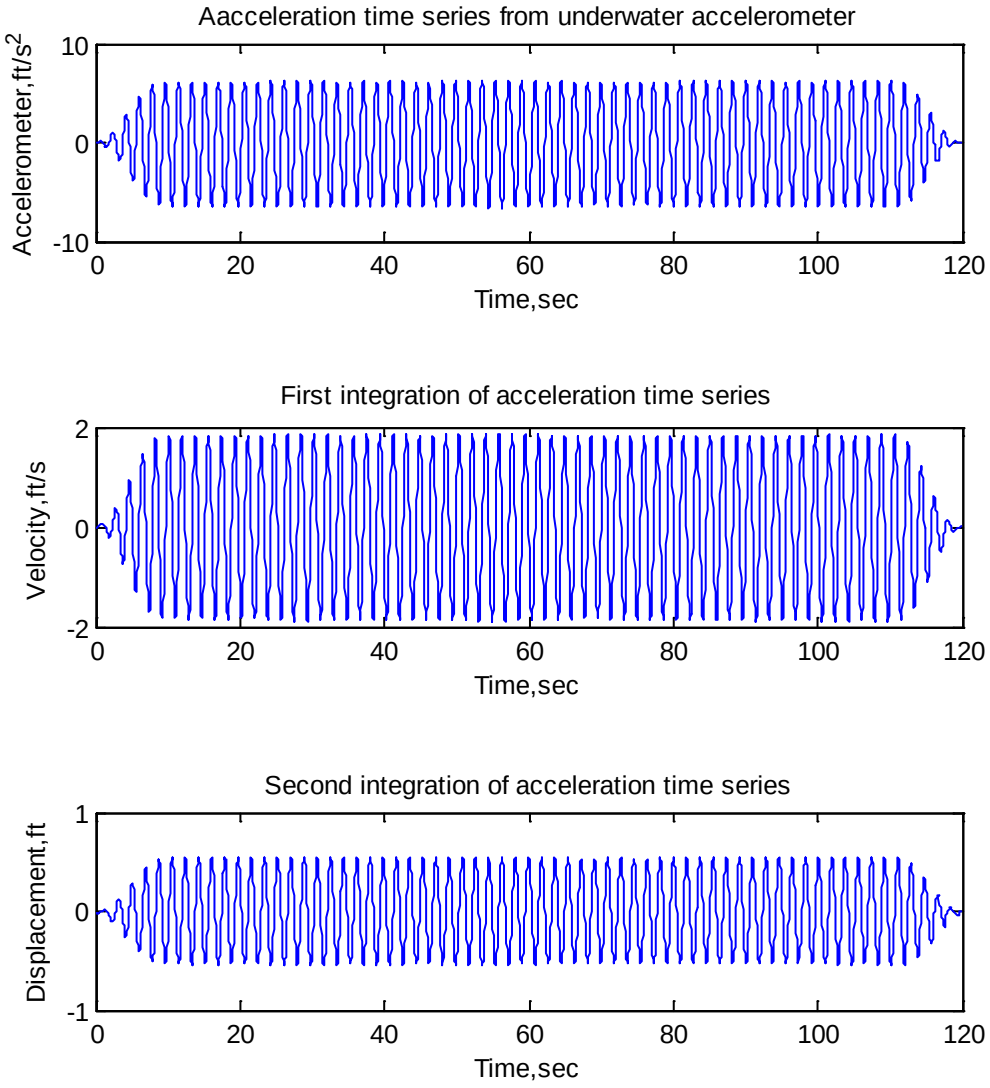

Fig. 27. Integrations of the acceleration time history of the lower accelerometer at the near resonance frequency f = 0.5502 Hz for the closed end model.

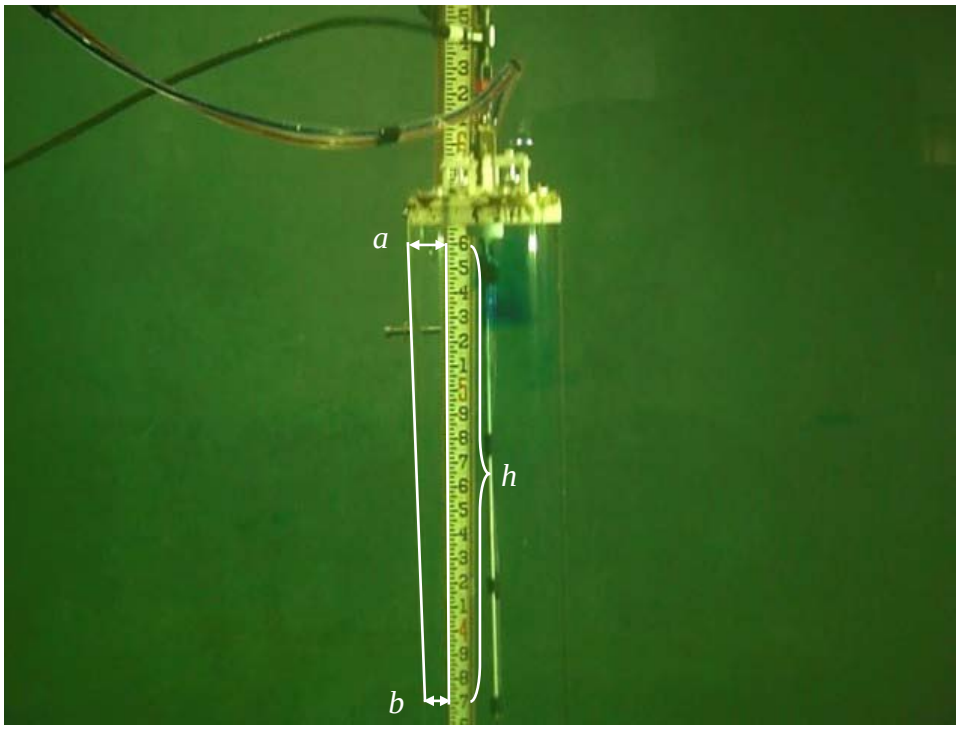

Fig. 28. Measurement method for the maximum pitch angle.

Besides, also observed in the model tests is the heave induced pitch resonance when heave is relatively large. The maximum pitch angle (pitch amplitude) is roughly determined based on the video records. Fig. 28 schematically shows how to measure the pitch amplitude. The maximum pitch angle is determined by identifying the maximum $|b-a|$,

$$\beta_{\max} = \beta_{\text{video}} \pm \beta_{\text{error}} = \tan^{-1}\left(\frac{|b-a|}{h}\right) \pm \beta_{\text{error}} \tag{2.1}$$

where β_{error} is error of the measured pitch amplitude and roughly equal to 0.5° (0.087 rad) for this method. The error results from the measurements of a and b due to limited resolution in the picture and limited sampling rate (30 Hz).

2.7 Analysis of Results

2.7.1 Closed end model

Table 4 summarizes the time domain results of the tests conducted for the closed end model. The first column (*f*) is the excitation frequency of the prescribed heave motion applied at the top of the cable (input frequency). The second column (ST1) and third columns (ST2) are the dynamic tension strokes (the differences between the maximum and minimum tensions) measured by the above and under water force transducers, respectively. The fourth column (ST2/ST1) is the ratio of the under-water tension stroke to the above water one, which is slightly smaller than one in most cases as expected. The fifth (SD3) and sixth column (SD2) are the heave strokes (the differences between the maximum and minimum heave displacement), which are obtained by integration twice of the heave acceleration with respect to time from the above and under water accelerometers, respectively. SD1 is the nominal strokes (excitation stroke) of the prescribed heave motion applied at the top of the cable. It remains constant (SD1 = 3 in = 0.0762 m) and independent of the excitation frequency throughout all the model tests. Since the under-water accelerometer is rigidly attached to the model pile, SD2 is also the heave stroke (output stroke) of the pile. It is shown that the heave stroke at the pile model (SD2) is much greater than that at the above water accelerometer (SD3), especially when the excitation frequency is close to the heave natural frequency. The heave stroke above water (SD3) gradually decreases with the increase in frequency, especially when the excitation frequency is slightly greater than the resonance frequency. However, the heave stroke at frequencies very close to the natural frequency

can be greater than that at the actuator because of the ‘pushing up’ by the pile. The seventh column (SD2/SD3), eighth column (SD2/SD1) and ninth column (SD3/SD1) are of the ratios between SD1, SD2 and SD3. The ratio SD2/SD1 (output stroke/excitation stroke) is also known as heave transmissibility (*TR*) of the pile-cable system. Fig. 29 shows that the heave transmissibility at the frequency near the natural is much greater than that at frequencies far from the natural frequency. Since the largest heave transmissibility indicates that the related excitation frequency is closest to the natural frequency, thus the natural frequency is approximately equal to 0.500 Hz in this case, and the largest *TR* is about 6. The heave induced pitch amplification is observed in this case at the frequency near heave resonance, and the pitch amplitude is roughly equal to 2.5° ± 0.5° (0.0436 rad ± 0.0087 rad).

Table 4. Time domain results for the closed end mode tests.

f (Hz)	ST1 (lb)	ST2 (lb)	ST2/ST1	SD3 (ft)	SD2 (ft)	SD2/SD3	SD2/SD1	SD3/SD1
0.3001	2.5652	2.4603	0.9591	0.2498	0.3772	1.5100	1.5088	0.9992
0.3251	3.0098	2.9024	0.9643	0.2256	0.4049	1.7948	1.6196	0.9024
0.3501	4.0767	3.9041	0.9577	0.2257	0.4561	2.0208	1.8244	0.9028
0.3751	5.3593	5.1542	0.9617	0.2279	0.5369	2.3559	2.1476	0.9116
0.4001	7.0866	6.8510	0.9668	0.2331	0.6632	2.8451	2.6528	0.9324
0.4251	10.2741	9.8385	0.9576	0.2289	0.7824	3.4181	3.1296	0.9156
0.4501	14.4177	14.1304	0.9801	0.2407	1.0534	4.3764	4.2136	0.9628
0.4751	19.5945	19.9400	1.0176	0.2448	1.1994	4.8995	4.7976	0.9792
0.5002	26.2636	25.6617	0.9771	0.2748	1.4841	5.4007	5.9364	1.0992
0.5252	26.3299	26.4451	1.0044	0.2275	1.2726	5.5938	5.0904	0.9100
0.5502	24.0869	24.2014	1.0048	0.2264	1.0786	4.7641	4.3144	0.9056
0.5752	21.8771	21.6808	0.9910	0.2252	0.9006	3.5992	3.6024	0.9008
0.6002	16.6341	16.5848	0.9970	0.2274	0.7350	2.5858	2.9400	0.9096
0.6252	12.8459	12.7207	0.9903	0.2261	0.4812	2.1283	1.9248	0.9044

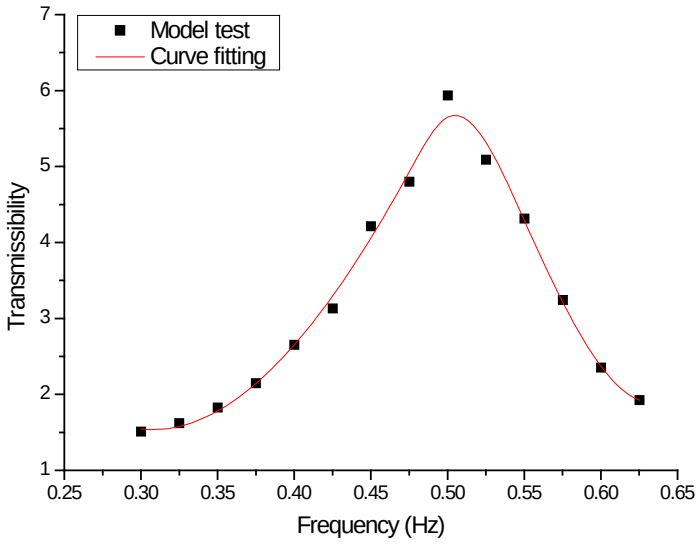

Fig. 29. Determining of the heave resonance frequency by the transmissibility curve for the closed end model.

2.7.2 Open end model

Table 5 summarizes the time domain results for the open end model. Similarly, the largest heave transmissibility indicates that the resonance frequency is approximately equal to 0.90 Hz based on Fig. 30, and the largest *TR* is about 6.4. Near the resonance frequency (0.90 Hz), the heave stroke of the upper sensors above the spring is slightly greater than that at the actuator, which is caused by the 'pushing up' of the pile model. However, there is no heave induced pitch resonance observed throughout the testing frequencies in this case.

Table 5. Time domain results for the open end model tests.

f (Hz)	ST1 (lb)	ST2 (lb)	ST2/ST1	SD3 (ft)	SD2 (ft)	SD2/SD3	SD2/SD1	SD3/SD1
0.7002	6.8913	6.3923	0.9276	0.2223	0.5819	2.6175	2.3275	0.8892
0.7252	7.5533	7.4899	0.9916	0.2216	0.6344	2.8630	2.5378	0.8864
0.7502	8.4780	8.4081	0.9918	0.2195	0.7600	3.4623	3.0399	0.8780
0.7752	9.6016	9.5866	0.9984	0.2153	0.8893	4.1304	3.5571	0.8612
0.8003	11.4883	11.4640	0.9979	0.2105	1.0408	4.9445	4.1632	0.8420
0.8253	12.6437	12.5016	0.9888	0.2068	1.1870	5.7396	4.7478	0.8272
0.8503	13.4707	13.4197	0.9962	0.2061	1.3065	6.3392	5.2261	0.8244
0.8753	14.8910	14.7369	0.9897	0.2142	1.3978	6.5257	5.5912	0.8568
0.9003	15.6676	15.2920	0.9760	0.2610	1.5984	6.1242	6.3936	1.0440
0.9253	15.6013	15.2127	0.9751	0.2360	1.5741	6.6699	6.2964	0.9440
0.9503	15.3743	15.3548	0.9987	0.2264	1.4057	6.2089	5.6228	0.9056
0.9753	15.0810	15.0753	0.9996	0.2139	1.2265	5.7340	4.9060	0.8556
1.0003	14.9213	14.8139	0.9928	0.2138	1.0943	5.1184	4.3773	0.8552
1.0253	14.2953	14.1581	0.9904	0.2198	0.9979	4.5399	3.9915	0.8792
1.0503	11.3030	10.3805	0.9184	0.2234	0.8538	3.8218	3.4151	0.8936
1.0753	13.3120	13.2214	0.9932	0.2261	0.7697	3.4044	3.0790	0.9044
1.1003	12.3210	12.1627	0.9872	0.2266	0.6459	2.8505	2.5837	0.9064
1.1254	12.1310	11.0251	0.9088	0.2273	0.5624	2.4741	2.2495	0.9092
1.1504	11.9477	11.8288	0.9900	0.2117	0.3912	1.8480	1.5649	0.8468
1.1754	11.4207	11.1903	0.9798	0.2111	0.3453	1.6359	1.3814	0.8444
1.2004	10.9577	10.6711	0.9738	0.2121	0.2869	1.3527	1.1476	0.8484
1.2254	10.3633	10.0717	0.9719	0.2193	0.2542	1.1592	1.0169	0.8772
1.2504	8.9667	8.9524	0.9984	0.2109	0.2119	1.0046	0.8475	0.8436

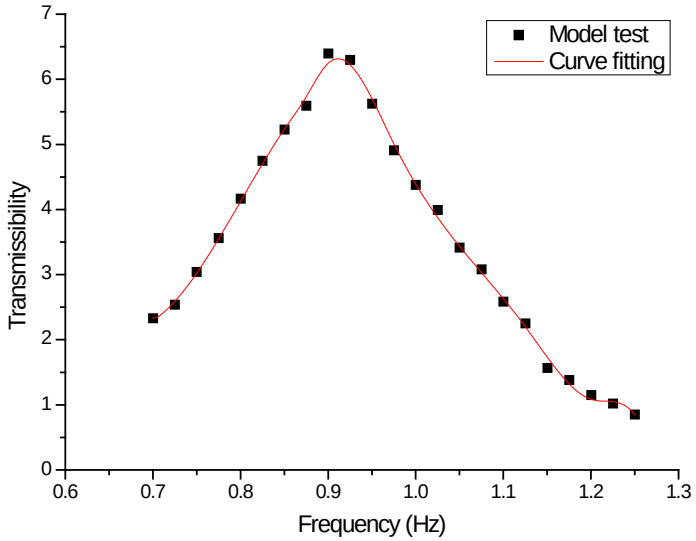

Fig. 30. Determining of the heave resonance frequency by the transmissibility curve for the open end model.

2.7.3 Partially open end models

By selecting a combination of various opening pairs of valves, there are nine partially open end models (with different total opening areas) tested in this study. Table 6 summarizes the details of these cases. The most important factor to distinguish these partially open models is the total opening area of the cap presented in the third column. Their ratios (γ) of the total opening area to the inner cross section area of the pile A_c = 23.758 in^2 (153.277 cm^2) are given in the fourth column. For brevity, only the results of Case 3, Case 5 and Case 9 are presented here. The results of the remaining cases are given in the Appendix A.

Table 6. Nine testing cases of partially open end model conducted in the laboratory.

Case No.	Valve pair opening	Total opening area	Opening area ratio, γ
Case 1	#1	0.221 in^2 (1.426 cm^2)	0.9%
Case 2	#2'	0.884 in^2 (5.703 cm^2)	3.7%
Case 3	PS Valves	0.884 in^2 (5.703 cm^2)	3.7%
Case 4	#3	2.454 in^2 (15.832 cm^2)	10.3%
Case 5	#4	3.534 in^2 (22.780 cm^2)	14.9%
Case 6	#1, #2, #3	4.246 in^2 (27.393 cm^2)	17.9%
Case 7	#2, #4	5.105 in^2 (32.935 cm^2)	21.5%
Case 8	#1, #3, #4	6.210 in^2 (40.064 cm^2)	26.1%
Case 9	#1, #2, #3, #4	7.780 in^2 (50.193 cm^2)	32.7%

2.7.3.1 PS valves opening model

Table 7 summarizes the time domain results of the tests conducted for the PS valves opening model. Similarly, the largest heave transmissibility indicates that the resonance frequency is approximately equal to 0.505 Hz based on Fig. 31, and the largest *TR* is about 5.5. The dynamics of the PS valves opening model is quite similar to that of the

closed end model. Near the resonance frequency (0.505 Hz), the heave stroke of the upper sensors above the spring is slightly greater than that at the actuator, which is caused by the 'pushing up' of the pile model. The heave induced pitch resonance is also observed in this case at the frequency near the heave natural frequency, and the pitch amplitude is roughly equal to $2.5^\circ \pm 0.5^\circ$ $(0.0436\text{rad} \pm 0.0087\text{rad})$. The difference between the two models is that the PS valves opening model has a larger damping due to the water flows through the opening valves and the vortices shed alternatively upwards and downwards from the PS valves.

Table 7. Time domain results for the PS valves opening mode tests.

f (Hz)	ST1 (lb)	ST2 (lb)	ST2/ST1	SD3 (ft)	SD2 (ft)	SD2/SD3	SD2/SD1	SD3/SD1
0.3751	4.4297	4.3121	0.9735	0.2467	0.5188	2.1030	2.0752	0.9868
0.4001	5.9500	5.6694	0.9528	0.2486	0.6022	2.4223	2.4087	0.9944
0.4251	8.1310	7.7053	0.9476	0.2476	0.7648	3.0890	3.0593	0.9904
0.4501	11.8986	11.2979	0.9495	0.2489	0.9942	3.9943	3.9767	0.9956
0.4751	15.9980	15.1309	0.9458	0.2464	1.1768	4.7759	4.7071	0.9856
0.5002	21.9466	21.7577	0.9914	0.2564	1.3665	5.3295	5.4660	1.0256
0.5252	21.4173	20.0407	0.9357	0.2269	1.2727	5.6091	5.0908	0.9076
0.5502	20.2273	18.9631	0.9375	0.2256	1.0462	4.6374	4.1848	0.9024
0.5752	18.3103	17.1267	0.9354	0.2286	0.8598	3.7612	3.4392	0.9144
0.6002	13.6843	13.2544	0.9686	0.2277	0.5970	2.6219	2.3880	0.9108
0.6252	11.5670	10.9389	0.9457	0.2257	0.4657	2.0634	1.8628	0.9028
0.6502	10.5110	9.9006	0.9419	0.2254	0.3976	1.7640	1.5904	0.9016
0.6752	9.5186	9.1026	0.9563	0.2282	0.3404	1.4917	1.3616	0.9128
0.7002	8.5276	7.9849	0.9364	0.2293	0.2795	1.2189	1.1180	0.9172

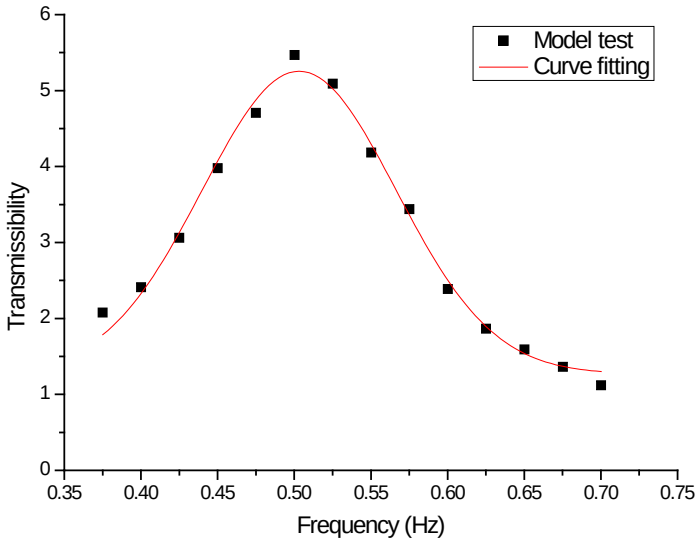

Fig. 31. Determining of the heave resonance frequency by the transmissibility curve for the PS valves opening model.

2.7.3.2 # 4 valves opening model

Table 8 summarizes the time domain results of the tests conducted for the #4 valves opening model. Similarly, the largest heave transmissibility indicates that the resonance frequency is approximately equal to 0.555 Hz based on Fig. 32, and the largest *TR* is about 3.6. There is no 'pushing up' occur for this case throughout the testing frequencies. However, the heave induced pitch resonance is still observed in this case at the frequency near the heave resonance, and the pitch amplitude is roughly equal to 1.0° ± 0.5° (0.0175 rad ± 0.0087 rad).

Table 8. Time domain results for the # 4 valves opening model tests.

f (Hz)	ST1 (lb)	ST2 (lb)	ST2/ST1	SD3 (ft)	SD2 (ft)	SD2/SD3	SD2/SD1	SD3/SD1
0.4501	7.5257	7.0475	0.9365	0.2477	0.6384	2.5773	2.5536	0.9908
0.4751	9.4892	9.0240	0.9510	0.2460	0.7074	2.8757	2.8297	0.9840
0.5002	11.7787	12.7784	1.0849	0.2446	0.7832	3.2018	3.1326	0.9784
0.5252	14.3967	13.5043	0.9380	0.2413	0.8567	3.5502	3.4266	0.9652
0.5502	15.5722	14.7895	0.9497	0.2399	0.8942	3.7273	3.5767	0.9596
0.5752	16.1625	15.1502	0.9374	0.2360	0.8732	3.6999	3.4927	0.9440
0.6002	15.8570	15.2282	0.9603	0.2324	0.8086	3.4795	3.2346	0.9296
0.6252	15.1715	14.3124	0.9434	0.2283	0.7225	3.1649	2.8902	0.9132
0.6502	14.3795	13.5938	0.9454	0.2284	0.6031	2.6404	2.4123	0.9136
0.6752	12.5870	11.8496	0.9414	0.2294	0.4821	2.1015	1.9283	0.9176
0.7002	11.8458	11.2337	0.9483	0.2209	0.4033	1.8255	1.6130	0.8836
0.7252	10.8872	10.3480	0.9505	0.2200	0.3503	1.5922	1.4011	0.8800
0.7502	9.7959	9.8617	1.0067	0.2182	0.2992	1.3712	1.1968	0.8728
0.7752	9.2820	9.0305	0.9729	0.2126	0.2686	1.2634	1.0744	0.8504
0.8003	8.6801	8.4596	0.9746	0.2122	0.2427	1.1437	0.9708	0.8488
0.8253	8.1644	7.9920	0.9789	0.2056	0.2216	1.0778	0.8864	0.8224

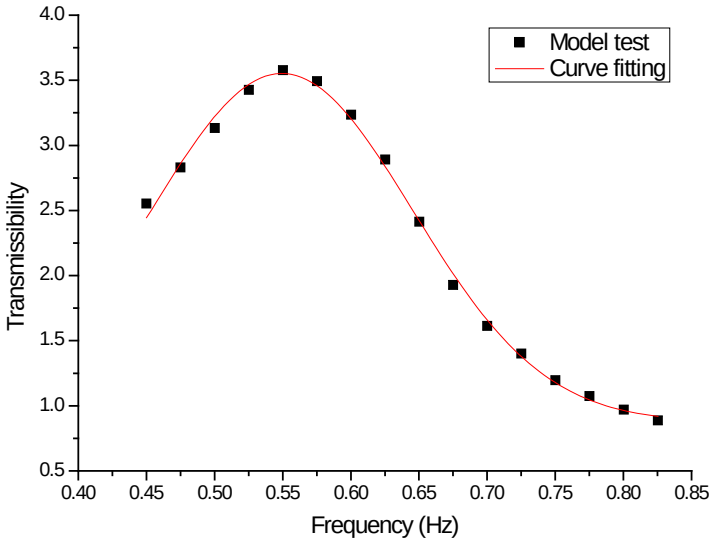

Fig. 32. Determining of the heave resonance frequency by the transmissibility curve for the # 4 valves opening model.

2.7.3.3 #1, #2, #3, #4 valves opening model

Table 9 summarizes the time domain results of the tests conducted for the #1, #2, #3, #4 valves opening model. Similarly, the largest heave transmissibility indicates that the resonance frequency is approximately equal to 0.710 Hz based on Fig. 33, and the largest *TR* is about 3.0. There are no 'pushing up' and no heave induced pitch resonance observed in this case.

The trends observed in Table 8 and Table 9 in general are similar to those observed in the cases of open and closed models. However, there are two unique trends shown in. Because of these pile top openings representing vent valves, the flow through these openings induces vortices near the cap which significantly dampen the heave of the pile model, especially near their corresponding natural frequencies. The *TR* in these two tables is about 3 to 3.6. Because the heave strokes of the pile model in these two cases are small in comparison with those in the previous two cases, the 'push up' from the pile model to the spring no longer occurs. Consequently, the heave strokes of the upper sensors above the spring decreases with the increase of the excitation frequency.

Table 9. Time domain results for the #1, #2, #3, #4 valves opening model tests.

f (Hz)	ST1 (lb)	ST2 (lb)	ST2/ST1	SD3 (ft)	SD2 (ft)	SD2/SD3	SD2/SD1	SD3/SD1
0.5002	4.1565	4.1009	0.9866	0.2434	0.4599	1.8894	1.8395	0.9736
0.5252	4.9753	4.7518	0.9551	0.2388	0.4841	2.0273	1.9365	0.9552
0.5502	5.9508	5.6057	0.9420	0.2380	0.5337	2.2422	2.1346	0.9520
0.5752	7.2846	6.6738	0.9161	0.2368	0.5844	2.4677	2.3374	0.9472
0.6002	8.5397	8.3437	0.9770	0.2328	0.6347	2.7262	2.5387	0.9312
0.6252	9.6716	8.7227	0.9019	0.2291	0.6759	2.9502	2.7036	0.9164
0.6502	11.0529	10.3928	0.9403	0.2254	0.7102	3.1509	2.8409	0.9016
0.6752	12.1847	11.5300	0.9463	0.2315	0.7400	3.1966	2.9600	0.9260
0.7002	13.4374	12.2881	0.9145	0.2220	0.7597	3.4219	3.0386	0.8880
0.7252	14.0630	12.8510	0.9138	0.2197	0.7544	3.4339	3.0177	0.8788
0.7502	14.5540	13.6648	0.9389	0.2169	0.7311	3.3707	2.9244	0.8676
0.7752	14.9195	13.8115	0.9257	0.2162	0.6957	3.2179	2.7828	0.8648
0.8003	14.7969	13.8857	0.9384	0.2117	0.6500	3.0705	2.6001	0.8468
0.8253	13.4844	12.6917	0.9412	0.2061	0.5922	2.8734	2.3688	0.8244
0.8503	12.4789	11.6259	0.9316	0.2016	0.5249	2.6036	2.0995	0.8064
0.8753	12.0587	11.4978	0.9535	0.2031	0.4568	2.2489	1.8270	0.8124
0.9003	11.7403	11.0502	0.9412	0.2081	0.3994	1.9191	1.5974	0.8324
0.9253	11.3179	10.7310	0.9481	0.2097	0.3507	1.6723	1.4027	0.8388
0.9503	10.6810	10.2195	0.9568	0.2128	0.3185	1.4965	1.2738	0.8512
0.9753	10.1547	9.6453	0.9498	0.2141	0.2826	1.3199	1.1304	0.8564
1.0003	9.6240	9.5144	0.9886	0.2253	0.2603	1.1552	1.0410	0.9012
1.0253	9.0976	8.6864	0.9548	0.2251	0.2435	1.0819	0.9742	0.9004
1.0503	8.5669	8.1762	0.9544	0.2256	0.2157	0.9562	0.8628	0.9024

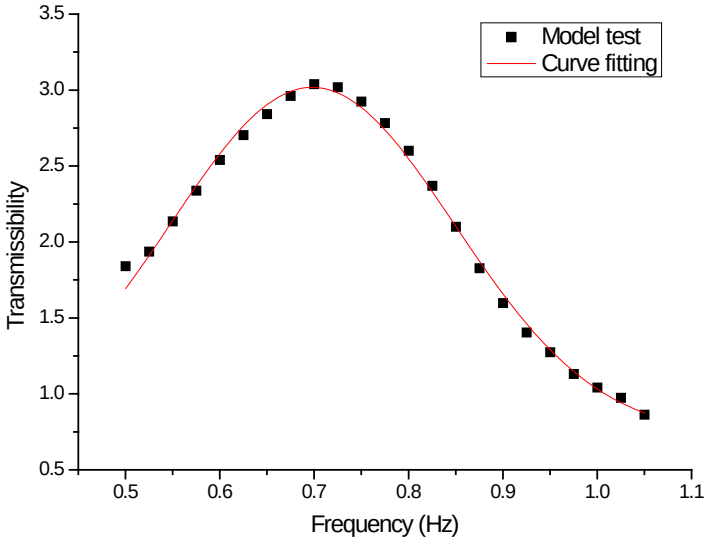

Fig. 33. Determining of the heave resonance frequency by the transmissibility curve for the #1, #2, #3, #4 valves opening model.

2.7.4 Summary of all cases

The open end and closed end models can be viewed as two special cases among the partially open end models. That is, $\gamma = 1$ for the open end model and $\gamma = 0$ for the closed end model. All results of the eleven cases are summarized in Table 10. The resonance (natural) frequency (f_{res}) and the related circular frequency ($\omega_{res} = 2\pi f_{res}$) for partially open end models are determined in the same manner as illustrated in open and closed end cases. Total mass of the system (M') and consequently total weight of the system (W'), are calculated from the resonance frequency using the following relationship:

$$M' = \frac{K}{\omega_{res}^2} \tag{2.2}$$

Weight of model pile (W_{pile}), weight of water inside model pile (W_{in}), and weight of water displaced by pile plus interior entrapped water (W_0) are identical except for the open end model. The total added water weight ($W_a = W' - W_{pile}$), and total added-mass coefficient ($C_a = W_a / W_0$) are given in Column 9 and Column 10. The exterior added water weight ($W_{a,ex} = W' - W_{pile} - W_{in}$), and exterior added-mass coefficient ($C_{a,ex} = W_{a,ex} / W_0$) are given in Column 11 and Column 12. Assume $C_{a,ex}$ are constant for closed end model and partially open end models. The interior entrapped water weight ($W_E = W' - W_{pile} - W_{a,ex}$), and entrainment ($E = W_{a,in} / W_{in}$) are given in Column 13 and Colume14. If E is less than zero, then E is set to be zero and the exterior added mass coefficient is recalculated.

The last column lists the Transmissibility (TR) at resonance defined as the ratio of the heave strokes of the pile at resonance observed from video records to the nominal

heave strokes at the actuator (3.0 inches heave stroke throughout all the tests). The last row lists the results of the case of the PS valves opening model. Although the opening PS valve ratio ($\gamma = 0.037$) is greater than that of the case of opening Valve #1 ($\gamma = 0.009$), their natural frequencies and so the added-mass coefficient are identical. This is because the PS valves have covers hanging about one inch above the hole. The covers hinder the flow through the hole and effectively reduce the opening area ratio. In general, the larger the opening area ratio is, the smaller the added-mass coefficient is, and consequently, the larger the natural (resonance) frequency is. The related results are plotted in Fig. 34 to Fig. 36, respectively. The trends observed in these two figures are expected. That is, a larger opening ratio results in less mass of water moving with the same velocity as the pile model.

Table 10. Summary of all the model test results and calculation of added-mass coefficients.

γ	f_{res}(Hz)	W'	W_a	C_a	$W_{a,ex}$	$C_{a,ex}$	W_E	E	TR	Note
0.000	0.500	58.91 lb (262.04 N)	41.85 lb (186.16 N)	1.14	10.95 lb (48.71 N)	0.298	30.900 lb (137.45 N)	1.000	5.4	Closed end
0.009	0.505	57.75 lb (256.88 N)	40.69 lb (181.00 N)	1.11	10.95 lb (48.71 N)	0.298	29.739 lb (132.29 N)	0.962	5.0	Case 1
0.037	0.510	56.62 lb (251.86 N)	39.56 lb (175.97 N)	1.08	10.95 lb (48.71 N)	0.298	28.612 lb (127.27 N)	0.926	4.8	Case 2
0.103	0.540	50.51 lb (224.68 N)	33.45 lb (148.79 N)	0.91	10.95 lb (48.71 N)	0.298	22.496 lb (100.07 N)	0.728	4.2	Case 4
0.149	0.555	47.81 lb (212.67 N)	30.75 lb (136.78 N)	0.84	10.95 lb (48.71 N)	0.298	19.803 lb (88.09 N)	0.641	3.2	Case 5
0.179	0.585	43.03 lb (191.41 N)	25.97 lb (115.52 N)	0.71	10.95 lb (48.71 N)	0.298	15.025 lb (66.83 N)	0.486	3.0	Case 6
0.215	0.610	39.58 lb (176.06 N)	22.52 lb (100.17 N)	0.61	10.95 lb (48.71 N)	0.298	11.570 lb (51.47 N)	0.374	2.9	Case 7
0.261	0.640	35.96 lb (159.96 N)	18.90 lb (84.07 N)	0.51	10.95 lb (48.71 N)	0.298	7.946 lb (35.35 N)	0.257	2.85	Case 8
0.327	0.710	29.22 lb (129.98 N)	12.16 lb (54.09 N)	0.33	10.95 lb (48.71 N)	0.298	1.206 lb (5.36 N)	0.039	2.8	Case 9
1.000	0.905	17.98 lb (79.98 N)	2.41 lb (10.72 N)	0.07	2.41 lb (10.72 N)	0.066	0.000 lb (0.00 N)	0.000	6.4	Open end
0.037	0.505	57.75 lb (256.88 N)	40.69 lb (181.00 N)	1.11	10.95 lb (48.71 N)	0.298	29.739 lb (132.29 N)	0.962	5.0	Case 3

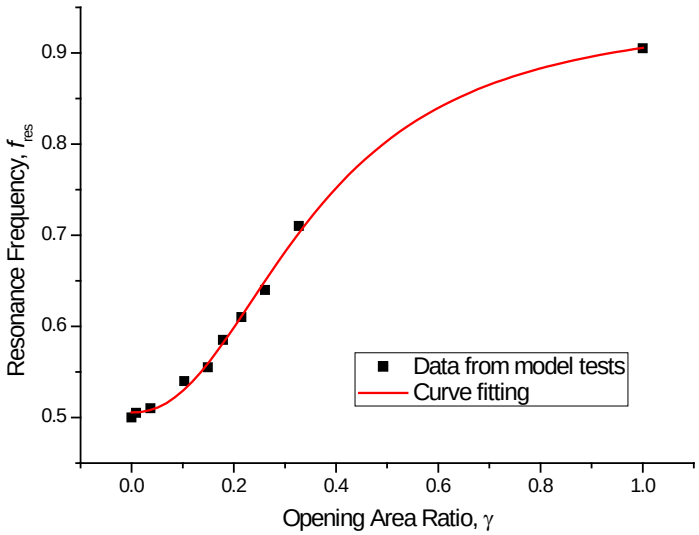

Fig. 34. Relation of resonance frequency to opening area ratio.

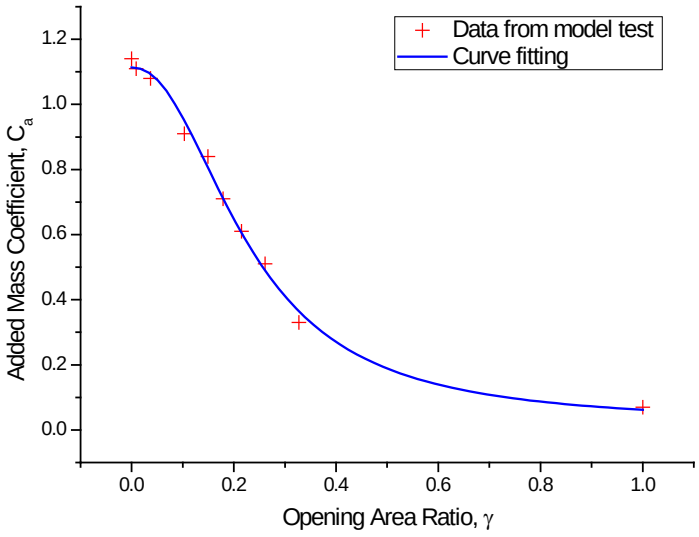

Fig. 35. Relation of total added mass coefficient to opening area ratio.

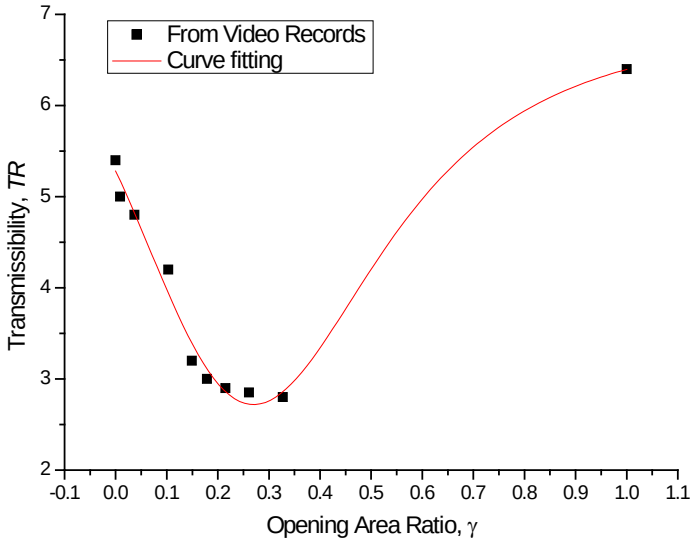

Fig. 36. Relation of opening area ratio to transmissibility at resonance.

CHAPTER III

FOMULATION

In this chapter we first derive the governing equations for the motions of the pile-cable system described in Chapter II. Based on the measurements and the bilinear stiffness of cable and spring, we distinguish the taut and slack phases of the cable for modeling the dynamic mechanism of the observed “pushing up” phenomenon near the heave resonance frequency regions. The governing equations of the surge-heave-pitch coupled motion of the suction pile models are then derived to investigate the heave induced pitch resonance. In addition, damped Mathieu Equation is employed to study the “Mathieu Instability” when the heave excitation frequency is approximately equal to twice of the pitch natural frequency.

3.1 Governing Equations of Decoupled Heave Motion

In this section, we simplify the heave motion of the pile-cable system as 1-D motion problem and derive the governing equations using the *D’Alembert’s Principle*. Only the heave motions of the model pile and the upper sensors are consider in the derivation. The taut and slack phases of the cable are considered in four different sets of equations.

The experimental setup of the suction pile model tests is sketched in Fig. 37. In order to describe the heave motions of the model pile and the upper sensors in the space-fixed coordinates relative to the static equilibrium positions, the heave displacement, velocity and acceleration at the top of the cable are denoted as z_1, $\dot{z}_1$ and $\ddot{z}_1$ respectively.

Similarly, those at the top of the suction pile as z_2, $\dot{z}_2$ and $\ddot{z}_2$, and those at the upper sensors as z_3, $\dot{z}_3$ and $\ddot{z}_3$. Note that the overhead dot and double dots respectively denote the first derivative and second derivative with respect to time.

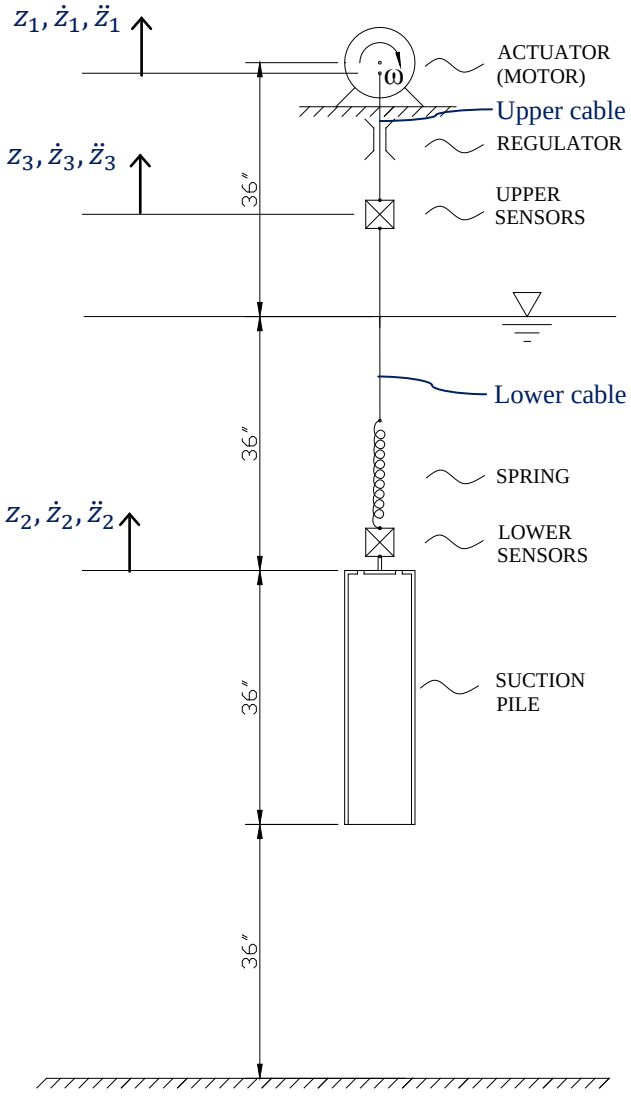

Fig. 37. Schematic layout of the suction pile model tests.

To force the pile model to have periodic heave motion, a sinusoidal heave excitation $z_1(t)$ at frequency f is applied to the top end of the cable by an electric actuator (motor) with 15 seconds ramping at the very beginning,

$$z_1(t) = A\sin(\omega t + \theta)\left(1 - e^{-st}\right) \tag{3.1}$$

where A, ω and θ are the heave amplitude, circular frequency and initial phase of the prescribed harmonic excitation respectively, and $\left(1 - e^{-st}\right)$ is a ramp function with the index s (Given in Chapter V, s = 0.3).

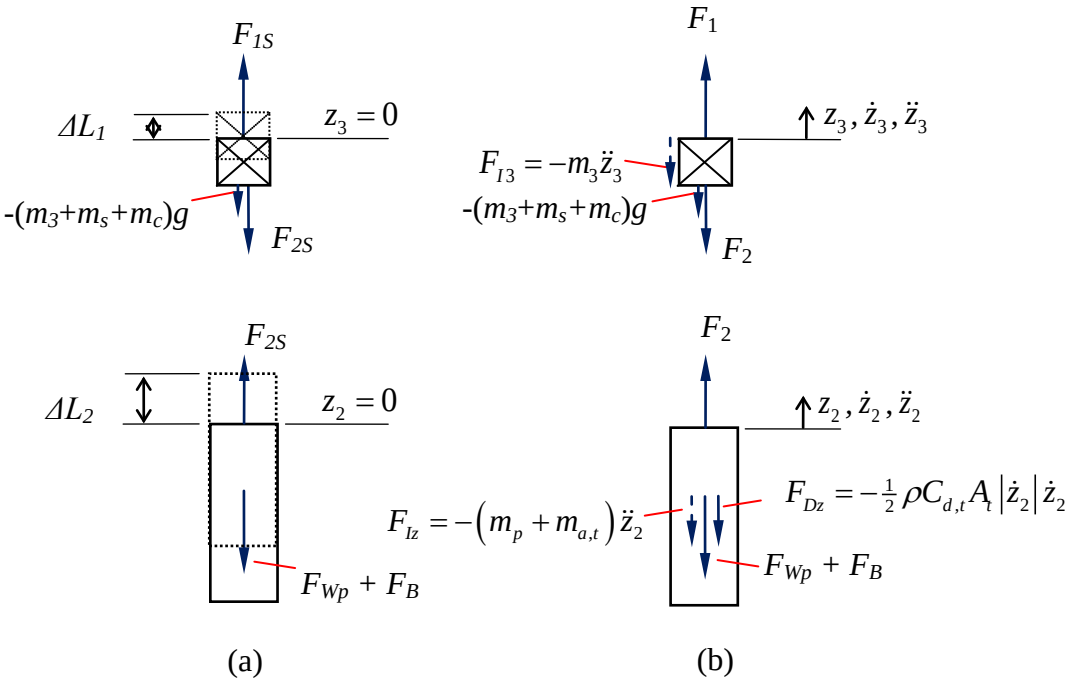

Fig. 38. Free body diagrams for the model suction pile and the upper sensors: (a) Static equilibrium; (b) Dynamic equilibrium.

Following the static equilibrium of the model pile and the upper sensors shown in Fig. 38 (a), and ignoring the structural damping of the pile-cable system, the static tensions in the upper cable and lower cable are given below,

$$\begin{cases} F_{1S} = k_1 \Delta L_1 = k_2 \Delta L_2 + (m_3 + m_s + m_c) g \\ F_{2S} = k_2 \Delta L_2 = -(F_{Wp} + F_B) \end{cases} \tag{3.2}$$

$$F_{Wp} = -m_p g \tag{3.3}$$

$$F_B = \rho g V_{disp} \tag{3.4}$$

where k_1 and k_2 are respectively the linear tensile stiffness of the upper cable and lower cable when the related cables are taut; ΔL_1 and ΔL_2 are respectively the static elongation of the upper cable and lower cable when the pile-cable is static and totally submerged in water; The notations, m_p, m_3, m_s and m_c, represent the masses of the model pile, the upper sensors, the spring and the lower cable; F_B is the buoyancy force of the model pile and g the gravitational acceleration; ρ is the density of water and V_{disp} the total volume of displaced water by the model pile.

According to the dynamic equilibrium of the model pile and the upper sensors shown in Fig. 38 (b), the governing equations of the heave motions can be written as

$$\begin{cases} F_{Iz} + F_{Dz} + F_{Wp} - F_B = F_2 \\ m_3 \ddot{z}_3 + F_2 + (m_3 + m_s + m_c) g = F_1 \end{cases} \tag{3.5}$$

where

$$F_{Iz} = -m_z \ddot{z}_G = -\left(m_p + C_{a,t} m_0 \right) \ddot{z}_2 \tag{3.6}$$

$$F_{Dz} = -\frac{1}{2}\rho C_{d,t} A_t \left|\dot{z}_2\right| \dot{z}_2 \tag{3.7}$$

$$\begin{cases} F_1 = k_{(1)} \Delta l_1 \\ F_2 = k_{(2)} \Delta l_2 \end{cases} \tag{3.8}$$

$$k_{(1)} = \begin{cases} k_1, \text{ for } \Delta l_1 \geq 0 \\ k_1', \text{ for } \Delta l_1 < 0 \end{cases} \tag{3.9}$$

$$k_{(2)} = \begin{cases} k_2, \text{ for } \Delta l_2 \geq \Delta L_{s0} \\ k_2', \text{ for } \Delta l_2 < \Delta L_{s0} \end{cases} \tag{3.10}$$

$$m_{a,t} = C_{a,t} m_0 \tag{3.11}$$

$$\Delta L_{s0} = T_{s0} / k_2 \tag{3.12}$$

F_{Iz} is the inertial force applied at the GC of the model pile for the heave motion in water; F_{Dz} is the drag force applied on the model pile against the heave motion in water; F_{Wp} is the dry weight of the model pile; F_1 and F_2 are the total tensions in the upper cable and the lower cable respectively; Δl_1 and Δl_2 are the total elongation from stress-free states of the upper cable and the lower cable respectively; $k_{(1)}$ and $k_{(2)}$ are the bilinear stiffness of the upper cable and lower cable, and the nonlinear vibration mechanism is derived from the bilinear stiffness of the cable system, which had been proved theoretically by Huang et al. (1989); k_1' and k_2' are the linear compressive stiffness of the upper cable and lower cable when the related cables are slack; m_z is the virtual (total) mass of the heave motion of the model pile; $m_{a,t}$ is the total added-mass of the model pile in the axial direction of the cylinder including the exterior added mass

and interior entrapped water mass moving at the same acceleration with the model pile; m_0 is the total mass of the water filling inside the model pile and the water displaced by the model pile; $C_{a,t}$ is the total added-mass coefficient of the model pile in the axial direction of the cylinder; $C_{d,t}$ is the drag coefficient of the model pile in the axial direction of the cylinder; A_t is the area of the submerged model pile projected onto a plane normal to the axial direction of the cylinder; ΔL_{s0} is the equivalent elongation of an ideal spring[1] under the load equal to the minimum tension of the extension spring used in the model tests.

During the excitation of the system, the upper cable and/or the lower cable may be alternatively in taut and slack phase when the heave amplitude of the model pile becomes very large. There are four possible scenarios for the vibration states of the pile-cable system: (a) Both cables are taut; (b) Only the lower cable goes slack; (c) Only the upper cables goes slack; (d) Both cables go slack together.

Scenario (a): Both cables are taut

When the excitation frequency is far from the heave natural frequency of the pile-cable system, both cables remain taut and satisfy the following conditions

[1] An idea spring is a spring with the minimum tension being equal to zero.

$$\begin{cases} k_2\left[\Delta L_2 + \left(z_3 - z_2\right)\right] \geq T_{s0} \\ k_1\left[\Delta L_1 + \left(z_1 - z_3\right)\right] \geq 0 \end{cases} . \tag{3.13}$$

Denoting the dynamic tensions in the upper cable and lower cable respectively by

$$\begin{cases} F_{1D} = k_1\left(z_1 - z_3\right) \\ F_{2D} = k_2\left(z_3 - z_2\right) \end{cases}, \tag{3.14}$$

the total tensions in upper and lower cables are respectively given by

$$\begin{cases} F_1 = F_{1S} + F_{1D} = k_1\left[\Delta L_1 + \left(z_1 - z_3\right)\right] \\ F_2 = F_{2S} + F_{2D} = k_2\left[\Delta L_2 + \left(z_3 - z_2\right)\right] \end{cases}. \tag{3.15}$$

Substituting Eqn. (3.12) into Eqn. (3.13), the conditions can be simplified to,

$$\begin{cases} \Delta l_1 = \Delta L_1 + \left(z_1 - z_3\right) \geq 0 \\ \Delta l_2 = \Delta L_2 + \left(z_3 - z_2\right) \geq \Delta L_{s0} \end{cases} . \tag{3.16}$$

Substituting Eqn. (3.15) into the Eqn. (3.5), the heave governing equations for the model pile and the upper sensors become,

$$\begin{cases} \left(m_p + C_{a,t} m_0\right)\ddot{z}_2 + \frac{1}{2}\rho C_{d,t} A_t \left|\dot{z}_2\right| \dot{z}_2 + \left(m_p g - F_B\right) = k_2\left[\Delta L_2 + \left(z_3 - z_2\right)\right] \\ m_3 \ddot{z}_3 + k_2\left[\Delta L_2 + \left(z_3 - z_2\right)\right] + \left(m_3 + m_s + m_c\right) g = k_1\left[\Delta L_1 + \left(z_1 - z_3\right)\right] \end{cases} . \tag{3.17}$$

Using Eqn. (3.2), Eqn. (3.17) can be simplified to,

$$\begin{cases} \left(m_p + C_{a,t} m_0\right)\ddot{z}_2 + \frac{1}{2}\rho C_{d,t} A_t \left|\dot{z}_2\right| \dot{z}_2 = k_2\left(z_3 - z_2\right) \\ m_3 \ddot{z}_3 + k_2\left(z_3 - z_2\right) = k_1\left(z_1 - z_3\right) \end{cases} . \tag{3.18}$$

Scenario (b): Only the lower cable goes slack

When the total tension in the lower cable reduces to less than the minimum tension in the spring and the total tension in the upper cable still keeps greater than or equal to zero, that is,

$$\begin{cases} \Delta l_1 = \Delta L_1 + \left(z_1 - z_3 \right) \geq 0 \\ \Delta l_2 = \Delta L_2 + \left(z_3 - z_2 \right) < \Delta L_{s0} \end{cases}, \tag{3.19}$$

the lower cable goes slack only. In this scenario, the expression of the total tensions of the upper cable and the lower cable in Eqn. (3.15) become

$$\begin{cases} F_1 = k_1 \left[\Delta L_1 + \left(z_1 - z_3 \right) \right] \\ F_2 = k_2 ' \left[\Delta L_2 + \left(z_3 - z_2 \right) \right] \end{cases}, \tag{3.20}$$

where $k_2 '$ is the linear compressive stiffness of the lower cable, which is assumed to be a very small value or zero (Given in Chapter V, $k_2 '$=0.05lb/in=0.0876N/cm).

Substituting Eqn. (3.20) into Eqn. (3.5), the heave governing equations for the model pile and the upper sensors becomes,

$$\begin{cases} \left(m_p + C_{a,t} m_0 \right) \ddot{z}_2 + \frac{1}{2} \rho C_{d,t} A_t \left| \dot{z}_2 \right| \dot{z}_2 + \left(m_p g - F_B \right) = k_2 ' \left[\Delta L_2 + \left(z_3 - z_2 \right) \right] \\ m_3 \ddot{z}_3 + k_2 ' \left[\Delta L_2 + \left(z_3 - z_2 \right) \right] + (m_3 + m_s + m_c) g = k_1 \left[\Delta L_1 + \left(z_1 - z_3 \right) \right] \end{cases}. \tag{3.21}$$

Scenario (c): Only the upper cable goes slack

When the total tension in the upper cable becomes less than zero, and the total tension of the lower cable still keeps greater than or equal to the minimum tension of the spring, that is,

$$\begin{cases} \Delta l_1 = \Delta L_1 + (z_1 - z_3) < 0 \\ \Delta l_2 = \Delta L_2 + (z_3 - z_2) \geq \Delta L_{s0} \end{cases}, \tag{3.22}$$

only the upper cable goes slack. In this scenario, the expression of the total tensions of the upper cable and the lower cable in Eqn. (3.11) become

$$\begin{cases} F_1 = k_1'\left[\Delta L_1 + (z_1 - z_3)\right] \\ F_2 = k_2\left[\Delta L_2 + (z_3 - z_2)\right] \end{cases}, \tag{3.23}$$

where k_1' is the linear compressive stiffness of the upper cable, which is assumed to be a very small value or zero (Given in Chapter V, k_1'=0.05lb/in=0.0876N/cm).

Substituting Eqn. (3.23) into Eqn. (3.5), the heave governing equations for the model pile and the upper sensors becomes,

$$\begin{cases} \left(m_p + C_{a,t} m_0\right)\ddot{z}_2 + \frac{1}{2}\rho C_{d,t} A_t \left|\dot{z}_2\right| \dot{z}_2 + \left(m_p g - F_B\right) = k_2\left[\Delta L_2 + (z_3 - z_2)\right] \\ m_3 \ddot{z}_3 + k_2\left[\Delta L_2 + (z_3 - z_2)\right] + (m_3 + m_s + m_c) g = k_1'\left[\Delta L_1 + (z_1 - z_3)\right] \end{cases}. \tag{3.24}$$

Scenario (d): Both cables go slack together

When the total tension in the lower cable becomes less than the minimum tension of the spring and the total tension in the upper cable less than zero, that is,

$$\begin{cases} \Delta l_1 = \Delta L_1 + (z_1 - z_3) < 0 \\ \Delta l_2 = \Delta L_2 + (z_3 - z_2) < \Delta L_{s0} \end{cases}, \tag{3.25}$$

both cables go slack. In this scenario, the expression of the total tensions in the upper cable and the lower cable in Eqn. (3.11) become,

$$\begin{cases} F_1 = k_1'\left[\Delta L_1 + \left(z_1 - z_3\right)\right] \\ F_2 = k_2'\left[\Delta L_2 + \left(z_3 - z_2\right)\right] \end{cases}. \tag{3.26}$$

Substituting Eqn. (3.26) into Eqn. (3.5), the heave governing equations for the model pile and the upper sensors becomes,

$$\begin{cases} \left(m_p + C_{a,t} m_0\right)\ddot{z}_2 + \frac{1}{2}\rho C_{d,t} A_t \left|\dot{z}_2\right| \dot{z}_2 + \left(m_p g - F_B\right) = k_2'\left[\Delta L_2 + \left(z_3 - z_2\right)\right] \\ m_3 \ddot{z}_3 + k_2'\left[\Delta L_2 + \left(z_3 - z_2\right)\right] + \left(m_3 + m_s + m_c\right) g = k_1'\left[\Delta L_1 + \left(z_1 - z_3\right)\right] \end{cases}. \tag{3.27}$$

3.2 Governing Equations of Surge-Heave-Pitch Coupled Motion

In this section, we derive the governing equations the surge-heave-pitch coupled motion for the suction pile using the *D'Alembert's Principle*. In order to simplify the derivation, we make several assumptions based on the experimental setup and observations as follows:

(1) Because of the axial symmetry of the model pile, we can simplify the 3-D motion of the pile to a 2-D motion. Hence, only the surge, heave and pitch motions and their couplings are taken into consideration in the derivation.

(2) Based on the observation during the model tests, the pitch angle is assumed to be relatively small, and the directions of axial forces applied at the eye bolts of the model piles by the connected cables are assumed to be always in the vertical directions.

(3) The heave induced pitch motion of the pile is assumed to be initiated by some perturbations or disturbances, such as the vortex shedding from the pile, the slackening

of the lowering cables and so on. Therefore, we set a small initial pitch angle β_0 (Given in Chapter V, β_0 =0.001rad) is assumed.

In Fig. 39, two coordinate systems are used to describe the motions of the model pile in the formulation: one is the *global coordinates* (*Earth-fixed coordinates*), which is fixed on the earth, with the x-axis in the horizontal direction pointing to the right and z-direction in the vertical direction pointing upward; the other is the *local coordinates* (*body-fixed coordinates*), located at the eye bolts of the model piles, with the ζ-direction in the axial direction of pointing outward and ξ-direction is normal to the ζ-direction and initially pointing to the right.

The free body diagrams of the closed end model and the open end model are shown in Fig. 39 and Fig. 40 respectively. Taking the static positions of the model piles in water as the references, (x_G, z_G), (x_B, z_B) and (x_2, z_2) denote the displacements of the center of gravity (GC), the center of buoyancy (BC) and the origin of the body-fixed coordinates (point O') respectively in the global coordinate system. (ξ_G, ζ_G), (ξ_B, ζ_B) and (ξ_2, ζ_2) are the local coordinates of GC, BC and O' of the model pile.

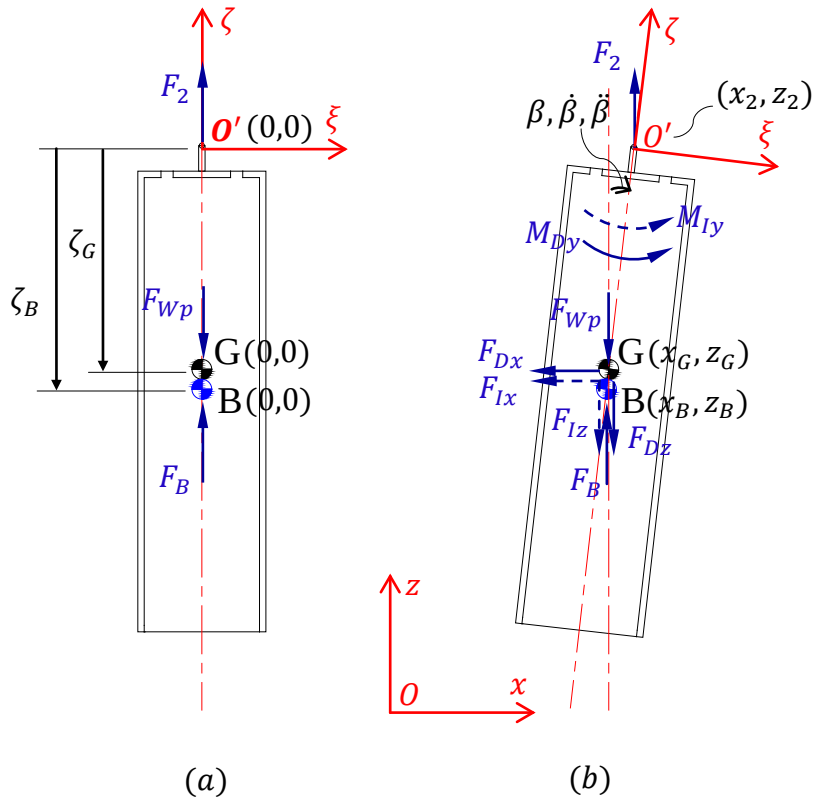

Fig. 39. Free body diagrams of the closed end model: (a) Static equilibrium state; (b) Dynamic equilibrium state

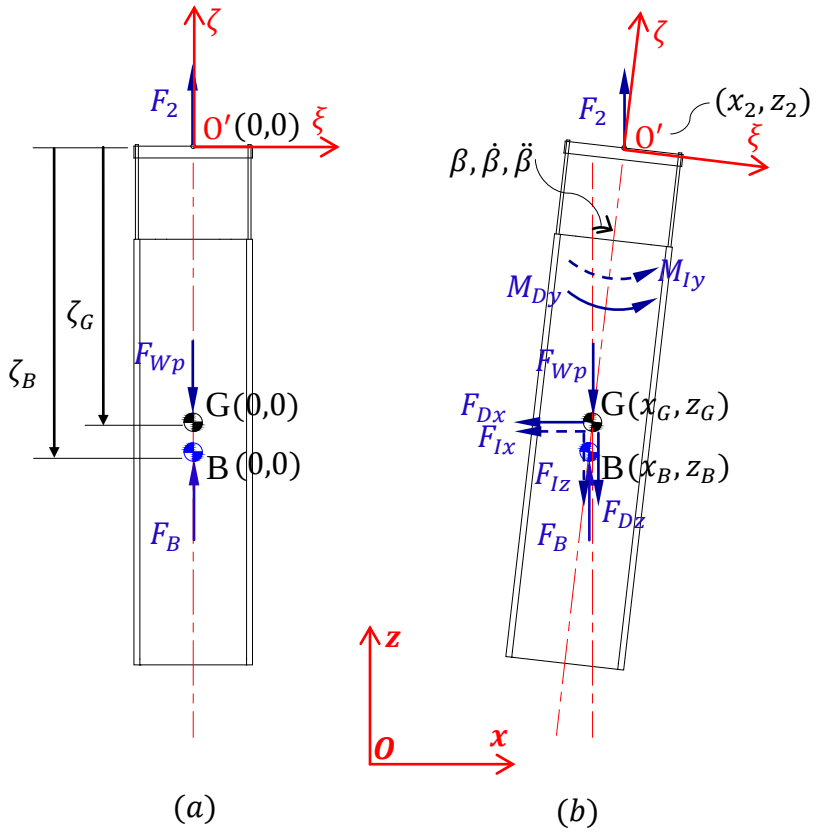

Fig. 40. Free body diagrams of the open end model: (a) Static equilibrium state; (b) Dynamic equilibrium state.

For a certain pitch angle $(\beta$, clockwise "+"$)$, the displacements, velocities and accelerations between GC and point O' are correlated as follows:

$$\begin{cases} x_G = x_2 + \zeta_G \sin\beta \\ z_G = z_2 - \zeta_G (1 - \cos\beta) \end{cases} \tag{3.28}$$

$$\begin{cases} \dot{x}_G = \dot{x}_2 + \zeta_G \dot{\beta} \cos\beta \\ \dot{z}_G = \dot{z}_2 - \zeta_G \dot{\beta} \sin\beta \end{cases} \tag{3.29}$$

$$\begin{cases} \ddot{x}_G = \ddot{x}_2 + \zeta_G \left(\ddot{\beta} \cos\beta - \dot{\beta}^2 \sin\beta \right) \\ \ddot{z}_G = \ddot{z}_2 - \zeta_G \left(\ddot{\beta} \sin\beta - \dot{\beta}^2 \cos\beta \right) \end{cases} \tag{3.30}$$

It should be noted that ζ_G is negative because the origin O' is located at the eye bolt.

Based on the video records, it is observed that heave induced pitch occurs only in certain cases and at certain frequencies. That is, they occurs in the cases of the frequencies near heave resonance for the closed end model and PS valves opening model, whose opening area ratio are relatively small.

The observed largest amplitude of the pitch angle is around 3°. Thus, a small pitch motion $\left(\beta \sim O(\varepsilon), \varepsilon << 1\right)$ is valid and the following approximations are used,

$$\begin{cases} \sin\beta \approx \beta \\ \cos\beta \approx 1 - \beta^2/2 \end{cases} \tag{3.31}$$

Substituting Eqn. (3.31) into Eqns. (3.28), (3.29) and (3.30), and omitting the terms of $O\left(\varepsilon^3\right)$ and higher, we can obtain,

$$\begin{cases} x_G \approx x_2 + \zeta_G \beta \\ z_G \approx z_2 + \zeta_G \beta^2/2 \end{cases} \tag{3.32}$$

$$\begin{cases} \dot{x}_G \approx \dot{x}_2 + \zeta_G \dot{\beta} \\ \dot{z}_G \approx \dot{z}_2 - \zeta_G \beta \dot{\beta} \end{cases} \tag{3.33}$$

$$\begin{cases} \ddot{x}_G \approx \ddot{x}_2 + \zeta_G \ddot{\beta} \\ \ddot{z}_G \approx \ddot{z}_2 - \zeta_G \left(\beta \ddot{\beta} - \dot{\beta}^2 \right) \end{cases} \tag{3.34}$$

Similarly, we have the similar relations of the displacements, velocities and accelerations between BC and point O' as follows,

$$\begin{cases} x_B \approx x_2 + \zeta_B \beta \\ z_B \approx z_2 + \zeta_B \beta^2 / 2 \end{cases} \tag{3.35}$$

$$\begin{cases} \dot{x}_B \approx \dot{x}_2 + \zeta_B \dot{\beta} \\ \dot{z}_B \approx \dot{z}_2 - \zeta_B \beta \dot{\beta} \end{cases} \tag{3.36}$$

$$\begin{cases} \ddot{x}_B \approx \ddot{x}_2 + \zeta_B \ddot{\beta} \\ \ddot{z}_B \approx \ddot{z}_2 - \zeta_B \left(\beta \ddot{\beta} - \dot{\beta}^2 \right) \end{cases} \tag{3.37}$$

Making the three assumptions described early and the approximations in Eqns. (3.32) - (3.37) , we can straightforwardly extend the governing equation of heave motion for the model pile presented in Section 3.1 to the governing equations for describing the surge-heave-pitch coupled motion for the model pile. Since the governing equations of the upper sensors remain the same, for brevity, we drop out the governing equations of the upper sensors in the following derivation.

For the dynamic equilibrium of the forces in the *x*-direction, we obtain the equation for the surge motion,

$$\sum F_x = F_{Ix} + F_{Dx} = 0 \tag{3.38}$$

$$F_{Ix} = -m_x \ddot{x}_G = -\left(m_p + C_{a,n} m_0 \right) \left(\ddot{x}_2 + \zeta_G \ddot{\beta} \right) \tag{3.39}$$

$$F_{Dx} = -C_{Dx} \left| \dot{x}_G \right| \dot{x}_G = -\frac{1}{2} \rho C_{d,n} A_n \left| \dot{x}_2 + \zeta_G \dot{\beta} \right| \left(\dot{x}_2 + \zeta_G \dot{\beta} \right) \tag{3.40}$$

where F_{Ix} is the horizontal component of the inertia force (D'Alembert force) applied at the GC of the model pile; F_{Dx} is the horizontal component of the drag force applied at the geometric center of the model pile. Because the GC is very close to the geometric center of the model pile and the simulation shows that the results are virtually the same

by moving the drag force from the geometric center to the GC, thus, the drag force is applied at the GC in the derivation; $C_{a,n}$ and $C_{d,n}$ are respectively the total added-mass coefficient and the drag coefficient of the model pile in the normal direction (radial direction) of the cylinder; m_x is the virtual mass of the surge motion of the model pile and $m_{a,n}$ the total added-mass of the model pile in the normal direction (radial direction) of the cylinder including the exterior added mass and interior entrapped water mass moving at the same acceleration with the model pile; A_n is the area of the submerged model pile projected onto a plane normal to the normal direction of the cylinder; C_{Dx} is the damping coefficient of the surge motion of model pile.

Based on the dynamic equilibrium of the forces in the *z*-direction, we get the equation for the heave motion of the model pile,

$$\sum F_z = F_{Iz} + F_{Dz} + F_{Wp} + F_B + F_2 = 0 \tag{3.41}$$

$$F_{Iz} = -m_z \ddot{z}_G = -\left(m_p + C_{a,t} m_0\right)\left(\ddot{z}_2 - \zeta_G \beta \ddot{\beta} + \zeta_G \dot{\beta}^2\right) \tag{3.42}$$

$$F_{Dz} = -C_{Dz}\left|\dot{z}_G\right|\dot{z}_G = -\frac{1}{2}\rho C_{d,t} A_n \left|\dot{z}_2 - \zeta_G \beta \dot{\beta}\right|\left(\dot{z}_2 - \zeta_G \beta \dot{\beta}\right) \tag{3.43}$$

Based on the dynamic equilibrium of the moments about the *y*-axis through the origin O' (clockwise "+" for the moments), we get the equations for the pitch motion of the model pile,

$$\sum M_y = M_{Iy} + M_{Dy} + M_{Wpy} + M_{By} + M_{F2y} = 0 \tag{3.44}$$

$$M_{Iy} = -I_\beta \ddot{\beta} + F_{Ix}\zeta_G - F_{Iz}\beta\zeta_G \tag{3.45}$$

$$M_{Dy} = -C_{D\beta}\left|\dot{\beta}\right|\dot{\beta} + F_{Dx}\zeta_G - F_{Dz}\beta\zeta_G \tag{3.46}$$

$$M_{Wpy} = -F_{Wp}\beta\zeta_G \tag{3.47}$$

$$M_{By} = -F_B\beta\zeta_B \tag{3.48}$$

$$M_{F2y} = F_2\beta\zeta_2 \tag{3.49}$$

where M_{Iy} is the total moment contributed from the inertia forces; M_{Dy} the total moment from the drag forces; M_{Wpy} the moment from the dry weight of the model pile; M_{By} the moment of the buoyancy force of the model pile; M_{F2y} the moment of the axial force applied at the eye bolt of the model pile by the cable. I_β is the total moment of inertia with respect to the *y*-axis through GC, which includes the moment of inertia for the decoupled pitch motion in air $\left(I_{\beta p}\right)$ and the added moment of inertia of the model pile in water $\left(I_{\beta a}\right)$. $C_{D\beta}$ is the coefficient for the hydrodynamic damping moment term. The calculations of $I_{\beta a}$ and $C_{D\beta}$ are based on the *Strip Theory* given in Appendix B.

Assuming that the initial pitch results from the disturbances, the pitch initial condition is given by

$$\begin{cases} \beta(0) = \beta_0 \\ \dot{\beta}(0) = 0 \\ \ddot{\beta}(0) = 0 \end{cases} \tag{3.50}$$

where β_0 = 0.001 rad is used in our numerical simulations (Given in Chapter V).

3.3 Pitch Resonance and Mathieu Equation

In order to understand the resonant pitch of the model pile induced by its heave, the pitch dynamic equation (3.44) is simplified to Mathieu equation. The solution for the Mathieu equation will reveal the relation between the heave and pitch natural frequency and qualitatively examine the numerical simulations to be presented in Chapter V.

Substituting Eqns. (3.45) - (3.49) into Eqn. (3.44), we have the governing equation for the heave induced pitch motion,

$$I_\beta \ddot{\beta} + C_{D\beta} \left|\dot{\beta}\right| \dot{\beta} + \left[\left(F_{Iz} + F_{Dz} + F_{Wp}\right)\zeta_G + F_B \zeta_B\right]\beta - \left(F_{Ix} + F_{Dx}\right)\zeta_G = 0 \tag{3.51}$$

By using the surge governing equation (3.38) and the heave governing equation (3.41), the above equation becomes,

$$I_\beta \ddot{\beta} + C_{D\beta} \left|\dot{\beta}\right| \dot{\beta} + \left[\left(-F_B - F_2\right)\zeta_G + F_B \zeta_B\right]\beta = 0 \tag{3.52}$$

The above equation indicates that the pitch resonance can be induced only by the heave excitation. That is, the surge motion has no contribution to the heave induced pitch motion. Hence, we will neglect the surge motion in the numerical schemes in Chapter IV. Further introducing the following substitutions and linearizing the pitch damping,

$$\begin{cases} \overline{GB} = \zeta_G - \zeta_B \\ \overline{O'G} = \zeta_{O'} - \zeta_G \\ C_\beta = C_{D\beta}\left|\dot{\beta}\right| \approx \dfrac{8\omega}{3\pi} C_{D\beta} \mathrm{B} \end{cases} \tag{3.53}$$

where B is the steady-state response of the pitch motion for the model pile defined as

$$\mathrm{B} = \frac{\beta_0}{\sqrt{\left(1-\Lambda^2\right)^2 + \left(2\chi\Lambda\right)^2}} \tag{3.54}$$

where $\Lambda = \omega \big/ \left(2\omega_p\right)$ is the heave excitation frequency nondimensionalized by $2\omega_p$ and $\chi = C_\beta \big/ \left(2I_\beta \omega_p\right)$ is the dimensionless damping ratio of the pitch motion; ω_p is the pitch natural frequency of the model pile in water and defined as

$$\omega_p = \sqrt{\frac{-F_B \cdot \overline{GB} + F_{2S}\overline{O'G}}{I_\beta}} \tag{3.55}$$

For non-resonance case, the maximum pitch for the model pile is the initial pitch disturbance (β_0); for the pitch resonance case, the maximum steady state response of the pitch motion is several times of the initial pitch disturbance. Using Eqn. (3.53), Eqn. (3.52) can be linearized as,

$$I_\beta \ddot{\beta} + C_\beta \dot{\beta} + \left[-F_B \cdot \overline{GB} + F_2 \overline{O'G}\right] = 0 \tag{3.56}$$

For simplicity, we only considering F_2 related to the no slack scenario of the heave motion. Using Eqn. (3.15), Eqn. (3.56) reduced to,

$$I_\beta \ddot{\beta} + C_\beta \dot{\beta} + \left[\left(-F_B \cdot \overline{GB} + F_{2S}\overline{O'G}\right) + F_{2D}\overline{O'G}\right] = 0 \tag{3.57}$$

where

$$\begin{aligned} F_{2D} &= k_2\left(z_3 - z_2\right) \approx k_2\left(z_1 - z_2\right) \\ &= k_2\left|A - A_p\right|\cos\left(\omega t + \theta'\right) \\ &= k_2 A\left|1 - TR\right|\cos\left(\omega t + \theta'\right) \end{aligned} \tag{3.58}$$

$$TR = \frac{A_p}{A} = \frac{1}{\sqrt{\left(1-\psi^2\right)^2 + \left(2\kappa\psi\right)^2}} \tag{3.59}$$

θ' is the phase difference between z_1 and z_2; A_p and $\omega_n = \sqrt{k_2/m_z}$ are the heave amplitude and natural frequency of the model pile; $\psi = \omega/\omega_n$ is the dimensionless heave excitation frequency ratio and $\kappa = C_z/(2m_z\omega_n)$ the dimensionless damping ratio of the heave motion; *TR* is the heave transmissibility of the pile-cable system, when $0 \le \psi \le \sqrt{2}$ we have $TR \ge 1$, when $\psi > \sqrt{2}$ we have $0 < TR < 1$; C_z is the linearized damping coefficient of the heave motion,

$$C_z = C_{Dz}\left|\dot{z}_2\right| \approx \frac{8\omega}{3\pi} C_{Dz} A_p \tag{3.60}$$

Dividing the Eqn. (3.57) by I_β and replacing $(\omega t + \theta')$ by τ, Eqn. (3.56) can be written in the standard form of a damped Mathieu's equation,

$$\frac{d^2\beta}{d\tau^2} + \mu\frac{d\beta}{d\tau} + (\alpha + \gamma\cos\tau)\beta = 0 \tag{3.61}$$

the parameters in the above equation are defined below,

$$\alpha = \frac{-F_B \cdot \overline{GB} + F_{2S}\overline{O'G}}{I_\beta\omega^2} = \frac{\omega_p^2}{\omega^2} = \frac{1}{4\Lambda^2} \tag{3.62}$$

$$\gamma = \frac{k_2 A \cdot \overline{O'G}}{I_\beta\omega^2}\left|TR - 1\right| \tag{3.63}$$

$$\mu = \frac{C_\beta}{I_\beta\omega} = \frac{8C_{D\beta}\mathrm{B}}{3\pi I_\beta} \tag{3.64}$$

In Eqn. (3.61), the second term represents the damping force and the last term $(\gamma\beta\cos\tau)$ the forcing term contributed from the heave motion. The boundaries between the stability and instability regions for the heave induced pitch resonance can be

obtained by applying the perturbation method and the Hill's infinite determinant method to Eqn. (3.61). Here, only the Hill's determinant method is employed to determine the damped Mathieu stability diagram. For brevity, the procedure of applying Hill's infinite determinant to the damped Mathieu equation is presented in Appendix C.

The boundaries dividing the stable and the unstable regions obtained are plotted in Fig. 41. It shows that the damping to the pitch renders the separation of the unstable region from the α -axis, and the unstable regions shrink owing to the increasing damping effect. However, the principle unstable region (I) is significantly less influenced by the damping than the second unstable region (II) and the former is the dominant unstable region for the heave induced pitch resonance in our model tests. When the natural pitch frequency $\left(\omega_p\right)$ is one half of the heave excitation frequency $\left(\omega\right)$, $\omega_p = \frac{1}{2}\omega$, so $\Lambda = 1$ (or $\alpha = \frac{\omega_p^2}{\omega^2} = \frac{1}{4}$), where the principle unstable region touches the α-axis. Because the principle unstable region is less influenced by the damping effect, we always observe the heave induced pitch amplification at this situation even through the value of γ is relatively small. The value of γ defined in Eqn. (3.63) increases with the increase of the heave transmissibility (*TR*) and is inversely proportional the square of the heave excitation frequency. The larger value of γ, the wider of the heave excitation frequency range for the significant pitch instability to occur. It was observed in Section 2.7, the large heave transmissibility occurs when the heave excitation frequency is close to the heave natural frequency. Hence, the significant pitch resonance can be induced by the heave motion when 1) the pitch natural frequency

is roughly one half of the heave excitation frequency and 2) the heave excitation frequency is approximately equal to the heave natural frequency. If only condition 1) is satisfied, the range of the heave excitation frequency for the pitch resonance to occur is significantly narrowed; If only condition 2) is satisfied, the pitch resonance will be eventually damped away even though the existence of the initial pitch disturbance.

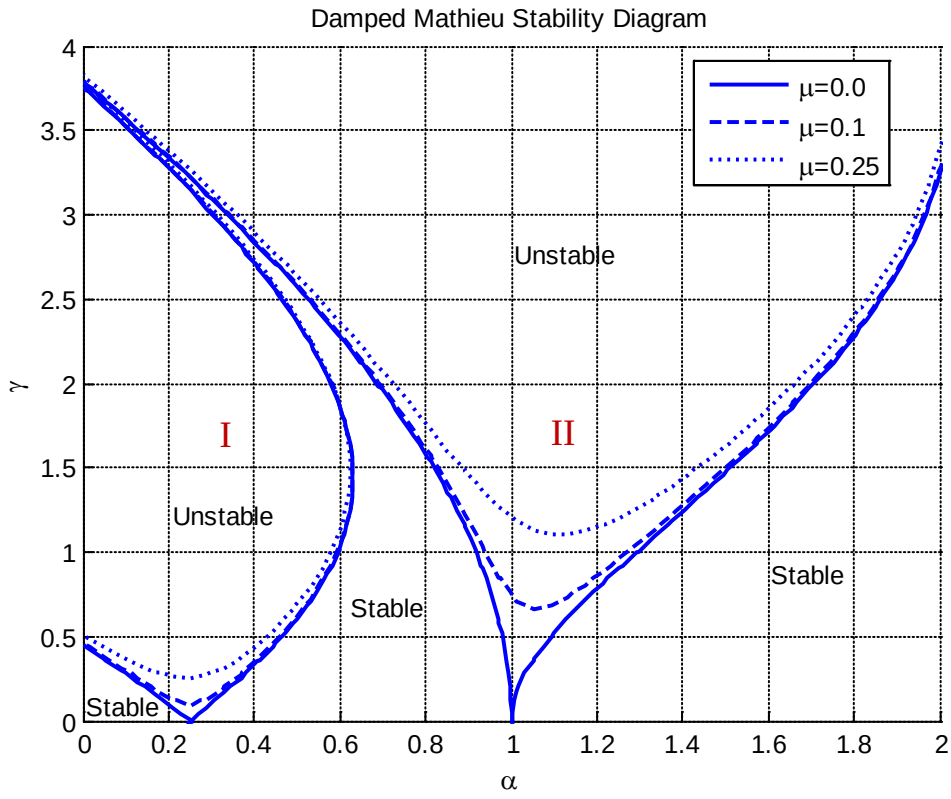

Fig. 41. Stability diagram described by the damped Mathieu's Equation.

CHAPTER IV

NUMERICAL SCHEMES

In this Chapter, two numerical schemes are developed sequentially to carry out the numerical simulations based on the theoretical formulations presented in Chapter III. The first one is the numerical scheme for the decoupled heave motion of the model pile and the second one is the numerical scheme for the heave-pitch coupled motion of the model pile. In both schemes, the heave motion of the upper sensors and the alternatively taut and slack phases of the cable system (bilinear stiffness) are considered.

4.1 Numerical Scheme for the Decoupled Heave Motion

The flowchart of the numerical scheme for the decoupled heave motion is shown in Fig. 42. The initial condition for the simulation is the static equilibrium state. At each time step (from t_{i-1} to t_i), the stiffness of the upper and lower cables related to different taut and slack phases are examined at the beginning of each step to determine which set of governing equations of motion for the model pile and the upper sensors should be chosen to be solved for the responses at the end of this time step. The second-order differential equations presented in Chapter III are transformed to two first-order differential equations and then solved by a Runge-Kutta method. The solver we utilized to solve the state-space equations is the "ODE45" ($4^{th}/5^{th}$-order Runge-Kutta method) provided in MATLAB (MathWorks Inc.). The solutions given by the "ODE45" are displacements and velocities at each time step (time instance t_i). A linear backward

difference scheme is employed to calculate the accelerations using the two recent time steps' results of velocity. All the responses (z_i, $\dot{z}_i$ and $\ddot{z}_i$) obtained at end of the previous time step are set as the initial conditions for the next time step from t_i to t_{i-1} and iteration is required until the tolerance of relative error ($\varepsilon < 10^{-3}$) is satisfied. For convenience, this numerical scheme is referred to as "decoupled motion scheme" hereafter.

4.2 Numerical Scheme for Heave-Pitch Coupled Motion

The flowchart of the numerical scheme for the heave-pitch coupled motion is shown in Fig. 43. The logic blocks and procedure are almost the same as the first numerical scheme. The differences are 1) the governing equations for the heave-pitch coupled motion and 2) the employment of a under-relaxation technique in calculating the nonlinear coupling terms of the governing equations presented in Chapter III. That is, the nonlinear terms are initially calculated using the results of the previous step and then the governing equations is solved using "ODE45" for the first time; After the governing equations is solved, the nonlinear terms are recalculated using a under-relaxation parameter (Given in Chapter V, $\lambda = 0.8$) to get the current values and solve the governing equations again by "ODE45" for the second time. For convenience, this numerical scheme is referred to as "coupled motion scheme" hereafter.

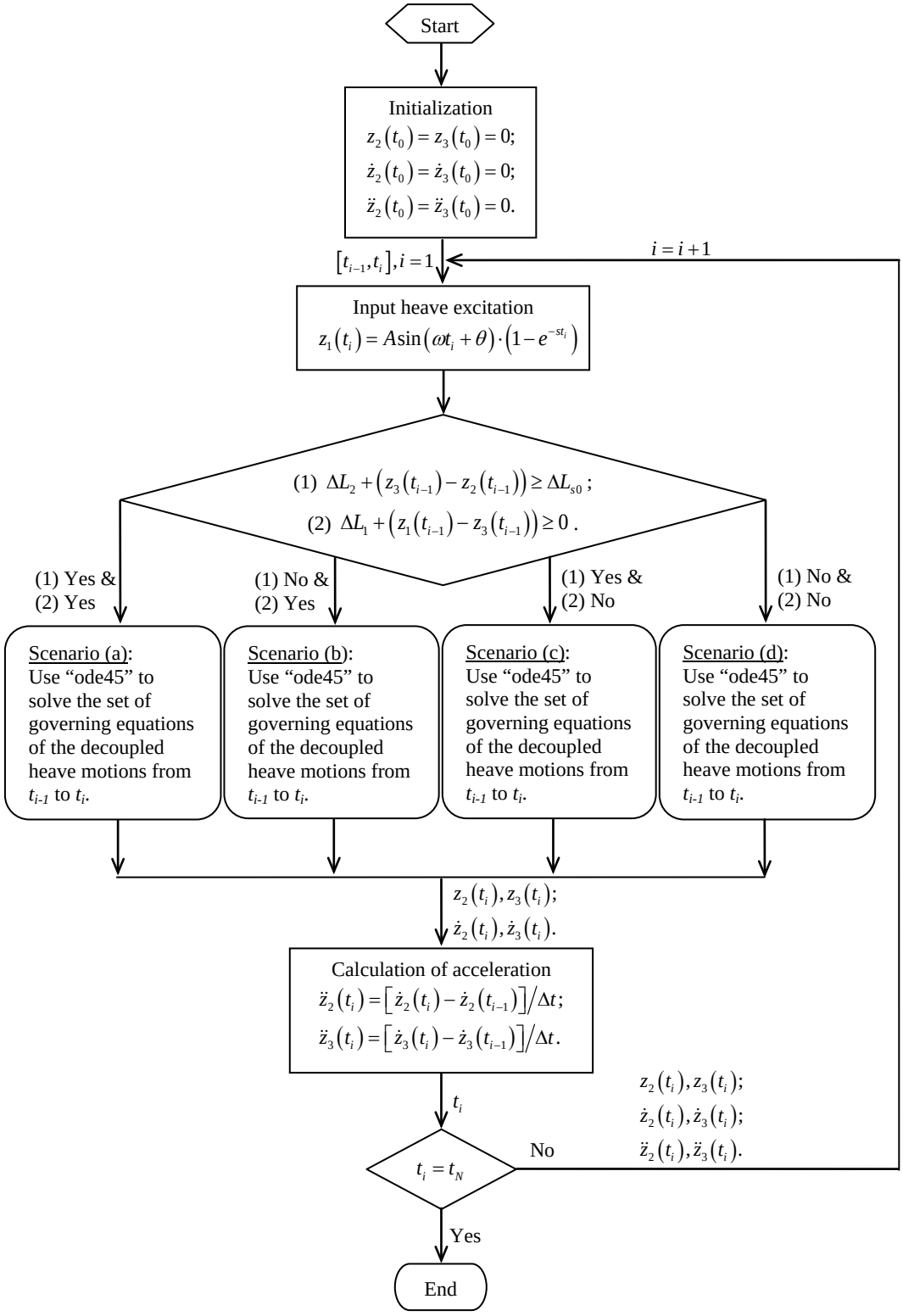

Fig. 42. Flowchart of the numerical scheme for the decoupled heave motion.

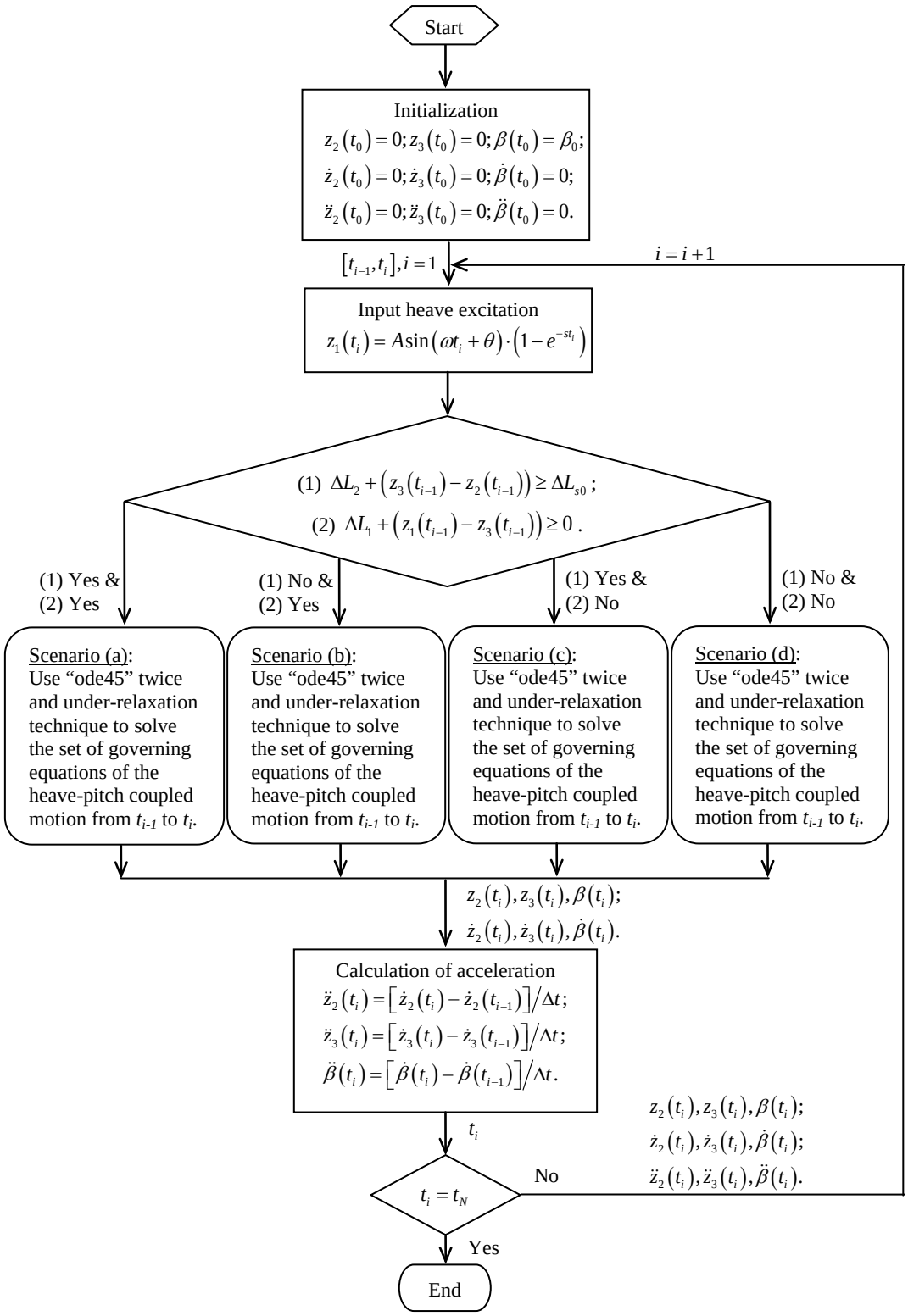

Fig. 43. Flowchart of the numerical scheme for the heave-pitch coupled motion.

CHAPTER V

NUMERICAL RESULTS AND COMPARISONS

In this Chapter, the numerical results from the two numerical schemes described in Chapter IV are compared with the measurements of the model tests in time domain. The hydrodynamic parameters used in the numerical simulation, such as added-mass coefficients and drag coefficients of the model suction piles are examined by existing empirical results (DNV-RP-H103 Modeling and Analysis of Marine Operations).

5.1 Hydrodynamic Parameters

5.1.1 Comparison of the added mass coefficients

Fig. 44 presents the relation between the added-mass reduction factors to the opening area ratios from the model tests. The added-mass reduction factor is defined as the ratio of the total axial added-mass coefficient for a model with an opening area ratio (γ) to the total axial added-mass coefficient for the closed end model. It is clearly shown that the added-mass reduction factor curve from the suction pile model tests is located between the DNV recommended curve (4.6.4, DNV-RP-H103) and the $\exp(-\gamma/0.28)$ curve (4.6.4 Guidance note, DNV-RP-H103). Both are considered applicable for opening area ratios below 50%. Hence, the total axial added-mass coefficients from the model tests are valid and will be utilized in the numerical simulations.

The recommended DNV-curve shown in Fig. 44, as a function of the opening area ratio γ (perforation *p* is used in the original reference) is described by,

$$\begin{cases} A_{33} = A_{33S}, & \text{if } 0 \le \gamma \le 0.05 \\ A_{33} = A_{33S}\left\{0.7 + 0.3\cos\left[\dfrac{\pi(\gamma - 0.05)}{0.34}\right]\right\}, & \text{if } 0.05 < \gamma < 0.34 \\ A_{33} = A_{33S} e^{\frac{0.10-\gamma}{0.28}}, & \text{if } 0.34 \le \gamma \le 0.50 \end{cases} \tag{5.1}$$

where A_{33S} =solid added-mass (added-mass in heave for a non-perforated structure). This curve is considered to be overestimated.

The $\exp(-\gamma / 0.28)$ curve is derived from the numerical simulations based on potential flow theory of perforated plates. Since it neglected the viscous effect, it may give underestimated values. Hence, the comparison in Fig. 44 indicates the added-mass coefficients derived based on our measurement in Chapter III are consistent with the related existing results.

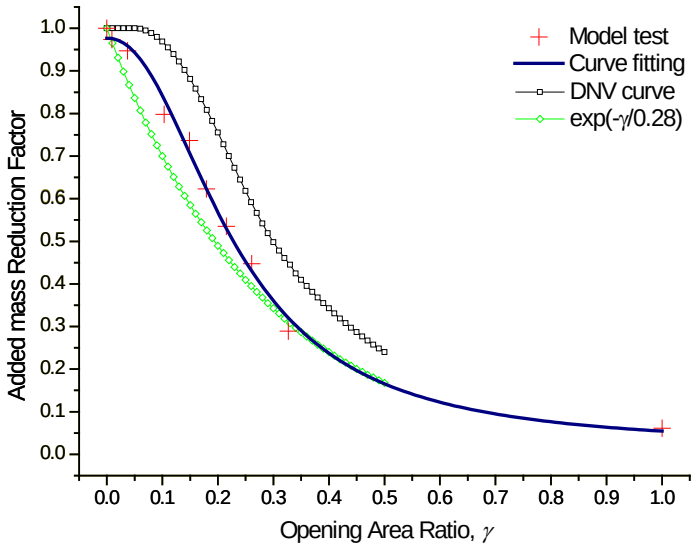

Fig. 44. Relation of total added-mass reduction factor to opening area ratio.

5.1.2 Determining the drag coefficients and comparison

Fig. 45 summarizes the relation between the axial drag coefficient and the opening area ratio. The axial drag coefficient ($C_{d,t}$) is defined as

$$C_{d,t} = \frac{F_{Dz}}{\frac{1}{2}\rho \dot{z}_2^2 A_t} \tag{5.2}$$

where A_t is the area of the submerged model pile projected onto a plane normal to the axial direction of the cylinder. For all models except the open end model, A_t is given by

$$A_t = A_0(1-\gamma) + A_w \tag{5.3}$$

where A_w is the projected area of the wall of the pile cylinder and A_0 the inner cross section area of the pile cylinder. In the case of the open end model A_t is equal to the sum of A_w and the projected area of steel-hanging bar in the axial direction.

The axial drag coefficient of each model is determined by fitting the results of the numerical simulations. By varying the value of the axial drag coefficient in equal increments, we can obtain a group of transmissibility curves as a function of frequency and the axial drag coefficients. In comparing with the measured transmissibility curve obtained in Chapter II, we can find a simulated *TR* curve of a given axial drag coefficient matching measured *TR* curve the best. Hence, the corresponding value of the axial drag coefficient is chosen as the true value of the axial drag coefficient. The method will be revisited in the following section in details. It shows that the axial drag coefficient for the model pile is greater or equal to 2.5, and peaks at 7.75 in the case with the opening area ratio round 25% at the pile top cap.

As recommended in DNV code (4.6.2.4, DNV-RP-H103) concerning the lowering operations of subsea structures, the drag coefficient in oscillatory flow $C_{d,t}$ (notation C_D is used in the original reference) vary with Keulegan-Carpenter (KC) number and can be typically two to three times larger than the steady flow drag coefficient C_{DS}. Unless specific CFD studies or model tests have been performed, the drag coefficient on typical subsea structures in oscillatory flow is given,

$$C_{d,t} \geq 2.5 \tag{5.4}$$

In model tests and CFD analyses (4.6.2.6 Guidance note, DNV-RP-H103) of complex subsea structures at relevant KC numbers, oscillatory flow drag coefficients is suggested to be in the range 4 to 8 when wake wash-out due to wave, current or lowering speed is neglected. The axial drag coefficients given in Fig. 45 are hence consistent with the related results suggested by the DNV code (4.6.2.4, DNV-RP-H103).

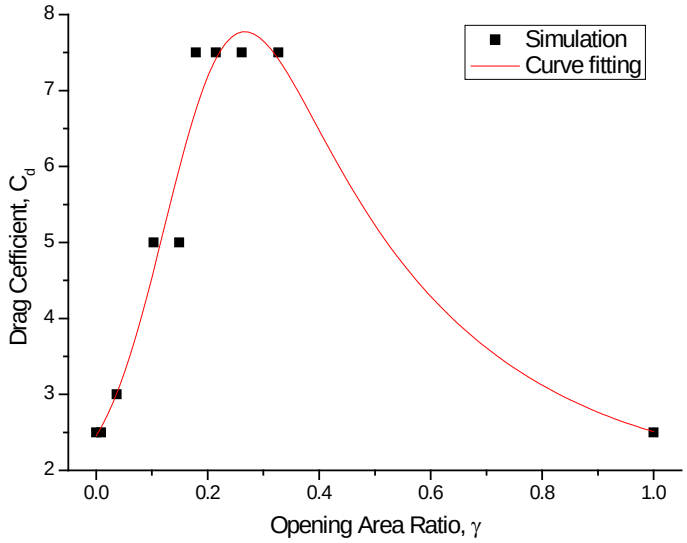

Fig. 45. Relation of axial drag coefficient to opening area ratio.

5.2 Comparison of the Closed End Model

The comparison between the results obtained using the two numerical scheme described in Chapter IV and the related measurements presented in Chapter II is detailed in this section for the case of the closed end model. The comparisons for the other cases are similar and will be briefly made in the following section.

5.2.1 Comparison of the heave motion

We can directly get the simulated response time histories of the heave displacements, heave velocities, heave accelerations and total tensions for both the upper sensors and the lower sensors, while only the response time histories of the heave accelerations and total tensions for both the upper sensors and the lower sensors are measured in the model tests. The so called ‘measured’ heave velocity and displacement were obtained by integrating the measured heave acceleration.

The common parameters used in all the simulations are listed in Table 11, and the specific parameters for the closed end model are in Table 12. The comparisons between the simulations made by two different numerical scheme and measurements are made in time domain for five different heave excitation frequencies: 1) far below resonance frequency; 2) far above resonance frequency; 3), 4) and 5) near resonance frequency.

Table 11. Common parameters for all numerical simulations.

Parameters	Notation	Value	Note
Excitation parameters			
Heave amplitude	A	0.125 ft (0.038 m)	
Initial phase	θ	0 rad	
Ramp index	s	0.3	About 15 sec ramping time
Simulation parameters			
Time step	Δt	0.04 sec	
Time span	t_N	360 sec	
Relaxation parameter	λ	0.8	Under-relaxation
Tolerance of relative error	ε	10^{-3}	
Pitch disturbance	β_0	0.001 rad	No effect on stable pitch amplitude
Cable assembly			
Upper cable tensile stiffness	k_1	2.0E+05 lb/ft (2.92E+06 N/m)	Steel cable
Upper cable compressive stiffness	k'_1	0.05 lb/ft (0.73 N/m)	Consider cable weight/length
Lower cable tensile stiffness	k_2	18.08 lb/ft (263.86 N/m)	Spring inserted
Lower cable compressive stiffness	k'_2	0.05 lb/ft (0.730 N/m)	Consider cable weight/length
Upper cable weight	W_{c1}	0.169 lb (0.752 N)	
Lower cable weight	W_{c2}	0.174 lb (0.774 N)	
Upper sensors weight	W_3	0.43 lb (1.913 N)	
Lower sensors weight	W_r	0.43 lb (1.913 N)	
Spring weight	W_s	0.456 lb (2.028N)	
Spring stiffness	k_s	18.0756 lb/ft (263.794 N/m)	
Spring initial tension	T_{s0}	2.222 lb (9.884 N)	
Minimum tension equivalent elongation	ΔL_{s0}	0.123 ft (0.037 m)	

Table 12. Closed end model parameters for numerical simulations.

Model parameters	Notation	Value	Note
Length	L	3 ft (0.914 m)	
Outer diameter	D	6 in (15.24 cm)	
Wall thickness	t	0.25 in (0.64 cm)	
Opening area ratio	γ	0.00%	Perforation for the top plate
Normal added-mass coef.	$C_{a,n}$	1.2	
Normal drag coef.	$C_{d,n}$	1.0	
Axial added-mass coef.	$C_{a,t}$	1.14	From model test
Axial drag coef.	$C_{d,t}$	2.5	
Coef. of pitch damping term	$C_{D\beta}$	9.8236	Refer to Appendix B
Weight in air	W	16.0 lb (71.172 N)	
Weight in water	W'	9.6 lb (42.703 N)	
Weight of water inside pile plus water displaced by pile	W_0	36.8 lb (163.695 N)	
Buoyancy	F_B	6.729 lb (29.932 N)	
Moment of inertia in air	$I_{\beta p}$	1.5780 slug·ft^2 (2.139 kg/m^2)	Refer to Appendix B
Added moment of inertia in water	$I_{\beta a}$	4.1176 slug·ft^2 (5.583 kg/m^2)	Refer to Appendix B
Moment of inertia in water	I_{β}	5.6956 slug·ft^2 (7.722 kg/m^2)	
Gravity center from eye bolt	$O'G$	1.44 ft (0.439 m)	Including hanging bar height 2”
Buoyancy center from eye bolt	$O'B$	1.57 ft (0.479 m)	Including hanging bar height 2”
Heave natural frequency	f_n	0.5000 Hz	From model test
Pitch natural frequency	f_p	0.2400 Hz	Hand calculation

The comparisons in time domain are given in Fig. 46 to Fig. 50, in which the results are in the time span [90, 100] sec for clear contrast. For the convenience of description, the figures are arranged following the same sequence for all five figures: (a) response heave displacement of the upper sensors; (b) response heave displacement of the lower sensors; (c) response heave velocity of the upper sensors; (d) response heave velocity of the lower sensors; (e) response heave acceleration of the upper sensors; (f) response heave acceleration of the lower sensors; (g) tension at the upper load cell; and (h) tension at the lower load cell.

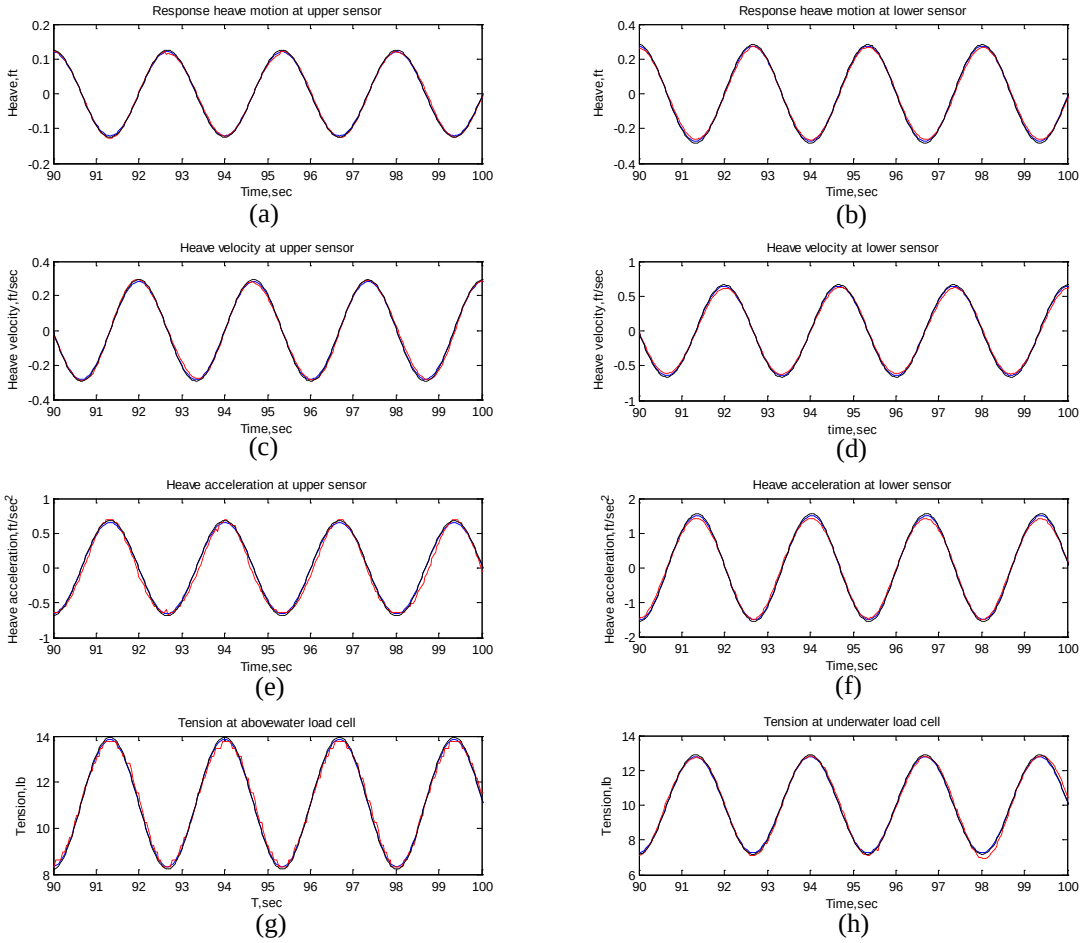

Fig. 46. Time domain comparisons of results from coupled motion scheme $(-)$ and decoupled motion scheme $(---)$ with the measurements of model tests $(-\cdot-)$ for the closed end model at excitation frequency far below resonance (f = 0.375 Hz, $C_{a,t}$ = 1.14, $C_{d,t}$ = 2.5).

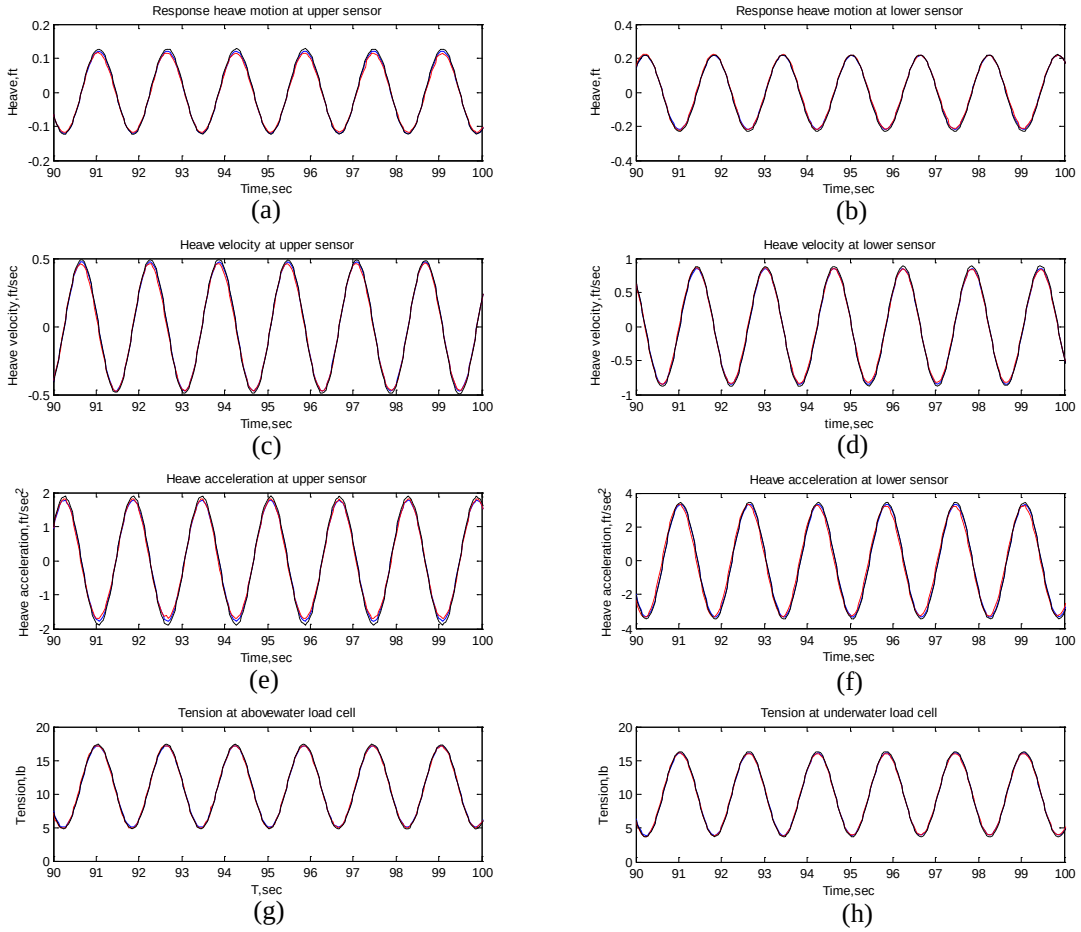

Fig. 47. Time domain comparisons of results from coupled motion scheme $(-)$ and decoupled motion scheme $(---)$ with the measurements of model tests $(-\cdot-)$ for the closed end model at excitation frequency far above resonance (f = 0.625 Hz, $C_{a,t}$ = 1.14, $C_{d,t}$ = 2.5).

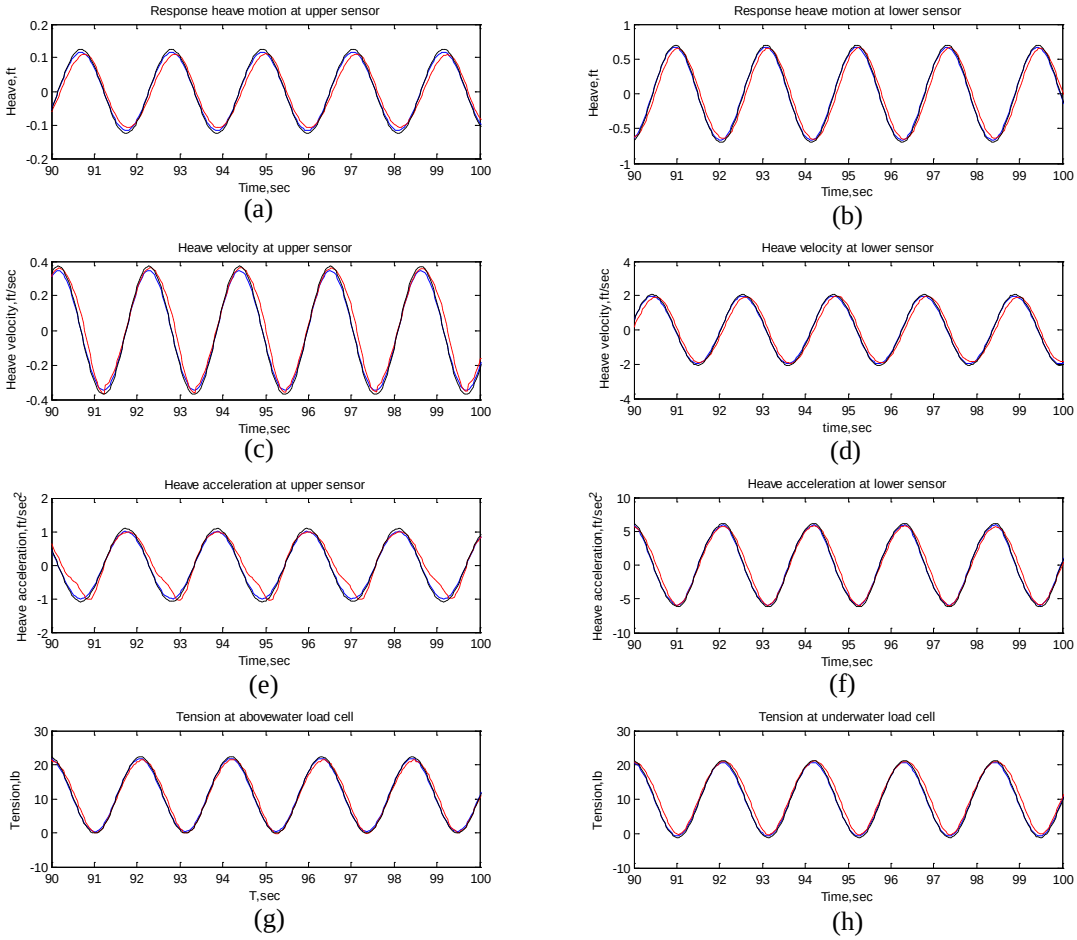

Fig. 48. Time domain comparisons of results from coupled motion scheme $(-)$ and decoupled motion scheme $(---)$ with the measurements of model tests $(-\cdot-)$ for the closed end model at excitation frequency near below resonance (f = 0.475 Hz, $C_{a,t}$ = 1.14, $C_{d,t}$ = 2.5).

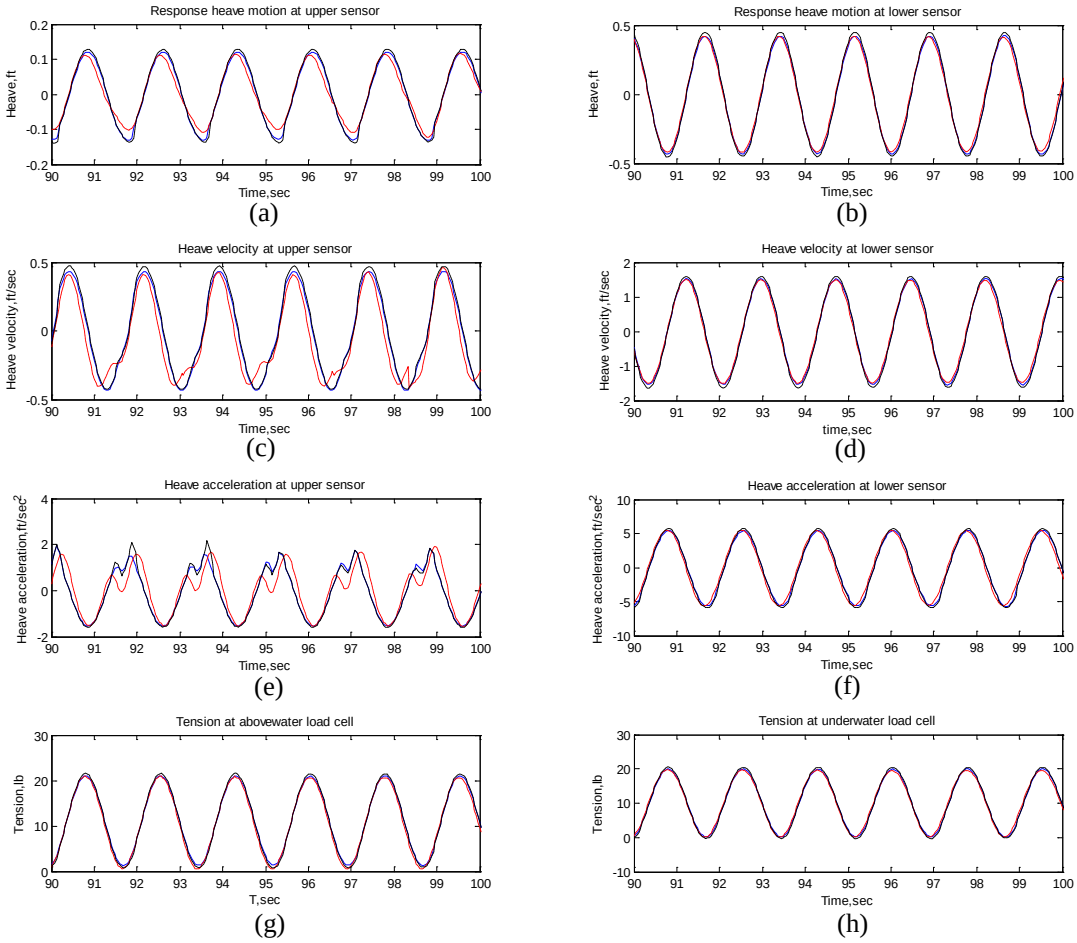

Fig. 49. Time domain comparisons of results from coupled motion scheme (–) and decoupled motion scheme (---) with the measurements of model tests (-·-) for the closed end model at excitation frequency near above resonance (f = 0.575 Hz, $C_{a,t}$ = 1.14, $C_{d,t}$ = 2.5).

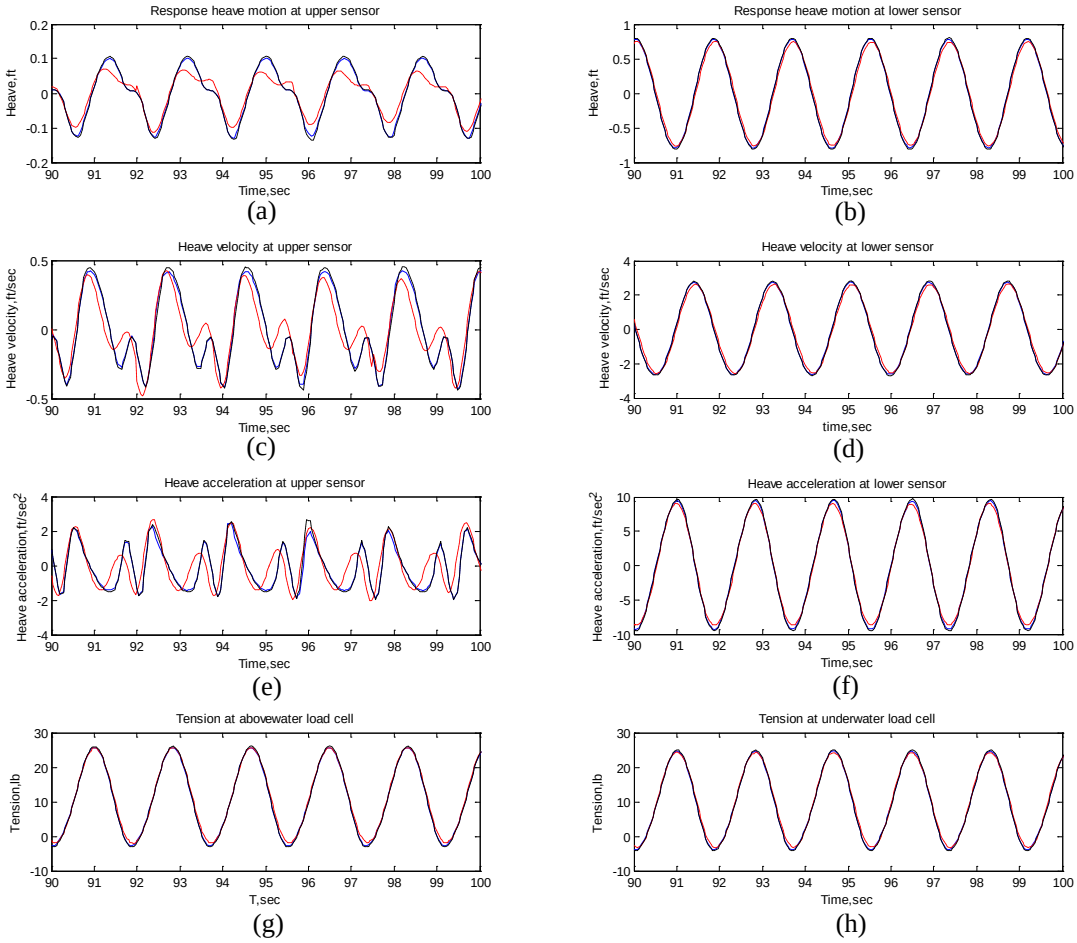

Fig. 50. Time domain comparisons of results from coupled motion scheme (–) and decoupled motion scheme (---) with the measurements of model tests (-·-) for the closed end model at excitation frequency near above resonance (f = 0.550 Hz, $C_{a,t}$ =1.14, $C_{d,t}$ =2.5).

When the excitation frequency is far below or above the resonance frequency, the simulations made by either the coupled motion scheme (–) or the decoupled motion scheme (---) agree very well with the measurements (-··-) of the model tests, as shown in Fig. 46 and Fig. 47. No slack phase of cables is observed when the excitation frequency is either far below or far above resonance frequencies. The tensions in the upper load cell and lower load cell are always greater than the minimum tensions in the related cables. Hence, the governing equations of oscillation scenario (a) are solely utilized in calculating the dynamics of the pile-cable system, and the measurement at the upper sensors is exactly the same as the heave excitation at the top end of the cable. It is also observed that the response of the suction pile is virtually in phase with the heave excitation at the top end of the cable in the frequency far below resonance frequency and out of phase by 180° in the frequency far above resonance frequency, which is as expected.

The heave natural frequency of the closed end model was determined to be about 0.500 Hz in Chapter II. In the frequency near the heave resonance frequency, the simulations of the coupled motion scheme (–) and the decoupled motion scheme (---) also agree satisfactorily with the measurement (-··-), as shown in Fig. 48, Fig. 49 and Fig. 50. No slack phase of the upper cables is observed by examining the heave acceleration at the upper accelerometer in the case of the excitation frequency is near but below resonance frequency. Double peaks are observed in the heave acceleration at the upper accelerometer in the case of the excitation frequency is near but above the

resonance frequency, indicating the occurrence of the slackening of upper cables. Because of the slack of the upper cable, the measured upper acceleration is different from that at the top end of the upper cable. In the frequency near but above the heave resonance frequency (f = 0.575 Hz, Fig. 49), the tensions in the lower load cell can be less than the minimum tension of the spring but always positive, indicating the governing equations of the slack oscillation scenario (b) is invoked in the duration between the double peaks as shown in Fig. 49(e). In the frequency much nearer the heave resonance frequency (f = 0.550 Hz, Fig. 50), the tensions in both upper and lower load cells can be negative, indicating the slack oscillation scenario (d) occurs during the longer time span between the double peaks, as shown in Fig. 50(a), (c) and (e). It should be noted that when the oscillation scenario (d) occurs, all the three slack oscillation scenarios will occur in the sequence from scenario (b) to scenario (d) and then scenario (c). When the tensions in both upper and lower load cells are in phase with each other, they have almost the same magnitudes. Before the tension in the upper load cell becomes negative, the tension in the lower load cell becomes less than the minimum tension of the spring. That is why the slack oscillation scenario (b) should go before the slack vibration scenario (d). After the occurrence of the slack oscillation scenario (d), the pile is dropping down freely in water, only subjected to the gravity force, buoyancy force and resistance from the water, and moving down with the lower cable together, which is the case of the slack oscillation scenario (c). After the upper cable regains the positive tension, the oscillation recovers the case of taut oscillation scenario (a).

The method of determining the axial (heave) drag coefficient for the heave motion of the closed end model is demonstrated in Fig. 51 and described briefly as follows. By varying the axial drag coefficient from 1.0 to 3.0 in equal increment of 0.5, the simulated transmissibility curves as a function of frequency and axial drag coefficient were obtained and plotted in Fig. 51. In comparison with the measured transmissibility curve presented in Chapter II, it is found that the *TR* curve for $C_{d,t}$=2.5 matches the measured curve the best. Thus in our numerical simulation for the case of the closed end model, we let $C_{d,t}$=2.5. The summary of the simulated results for this case are given in Table 13, and the meaning of each column is the same as described in Chapter II. It is noted that the axial drag coefficient $C_{d,t} \geq 2.5$ is also recommended by DNV for the lowering operation of subsea structures (4.6.2, DNV-RP-H103).

Table 13. Numerical results of heave motion for the closed end model simulations using the heave-pitch coupling scheme ($C_{a,t}$=1.14, $C_{d,t}$=2.5).

f (Hz)	ST1 (lb)	ST2 (lb)	ST2/ST1	SD3 (ft)	SD2 (ft)	SD2/SD3	SD2/SD1	SD3/SD1
0.3000	2.3693	2.3571	0.9949	0.2491	0.3804	1.5271	1.5216	0.9964
0.3250	3.0178	3.0035	0.9953	0.2282	0.4163	1.8243	1.6652	0.9128
0.3500	3.9174	3.9001	0.9956	0.2302	0.4659	2.0239	1.8636	0.9208
0.3750	5.2147	5.1950	0.9962	0.2322	0.5375	2.3148	2.1500	0.9288
0.4000	6.9780	6.9575	0.9971	0.2453	0.6350	2.5887	2.5400	0.9812
0.4250	9.6623	9.6391	0.9976	0.2294	0.7827	3.4119	3.1308	0.9176
0.4500	14.6726	14.6462	0.9982	0.2384	1.0570	4.4337	4.2280	0.9536
0.4750	20.2562	20.2371	0.9991	0.2424	1.2956	5.3449	5.1824	0.9696
0.5000	25.7474	25.7396	0.9997	0.2275	1.4780	6.4967	5.9120	0.9100
0.5250	27.1005	27.1054	1.0002	0.2135	1.4186	6.6445	5.6744	0.8540
0.5500	24.4911	24.5111	1.0008	0.2254	1.1732	5.2050	4.6928	0.9016
0.5750	21.8576	21.8963	1.0018	0.2605	0.9662	3.7090	3.8648	1.0420
0.6000	16.6206	16.6652	1.0027	0.2495	0.6728	2.6966	2.6912	0.9980
0.6250	13.7442	13.7927	1.0035	0.2496	0.5128	2.0545	2.0512	0.9984

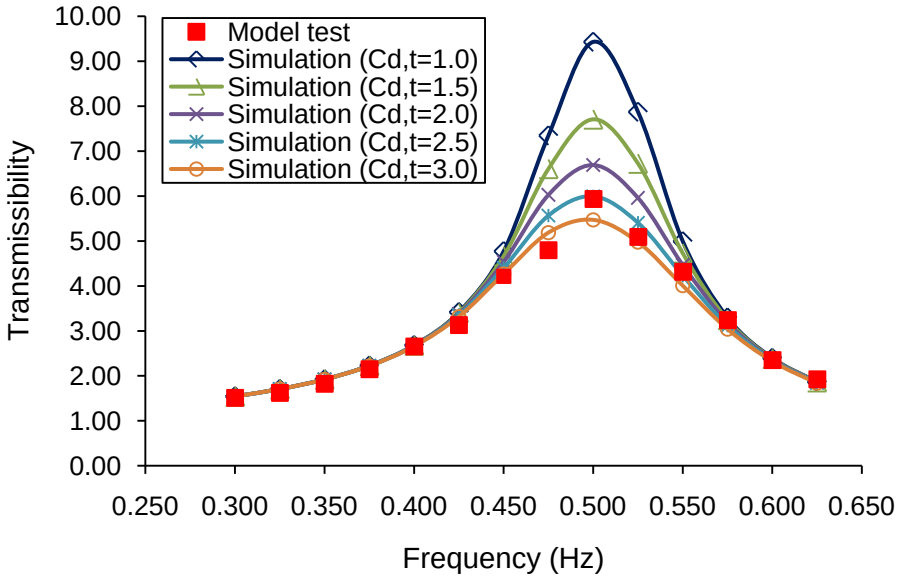

Fig. 51. Matching the heave amplitude transmissibility curves from the model tests by the simulations with different drag coefficients (heave-pitch coupling, $C_{a,t}$ =1.14) for the closed end model.

By comparing with the measured *TR* curve in Fig. 52, the simulated TR curves for $C_{d,t}$ =2.5 obtained respectively by the two numerical schemes agree well with the measurements in all frequency range (0.300 Hz ~ 0.625 Hz), not only in the non-resonance cases but also in the near resonance cases. Thus, it validates the two numerical schemes presented in Chapter IV. The results of the decoupled motion scheme are slightly larger than those of the coupled motion scheme near the heave natural frequency. That is because the resonance pitch draws energy from the heave energy and thus slightly reduces the heave amplitude. In the resonance cases, there are still certain discrepancies of the heave displacement, velocity and acceleration at the upper sensors between calculated and measured response time histories, which is probably due to the inaccuracy in determining the quantity of compressive stiffness (k_1' and k_2') of cables

during the slackening cases, and the miner errors in measured acceleration due to limited resolution of the accelerometers.

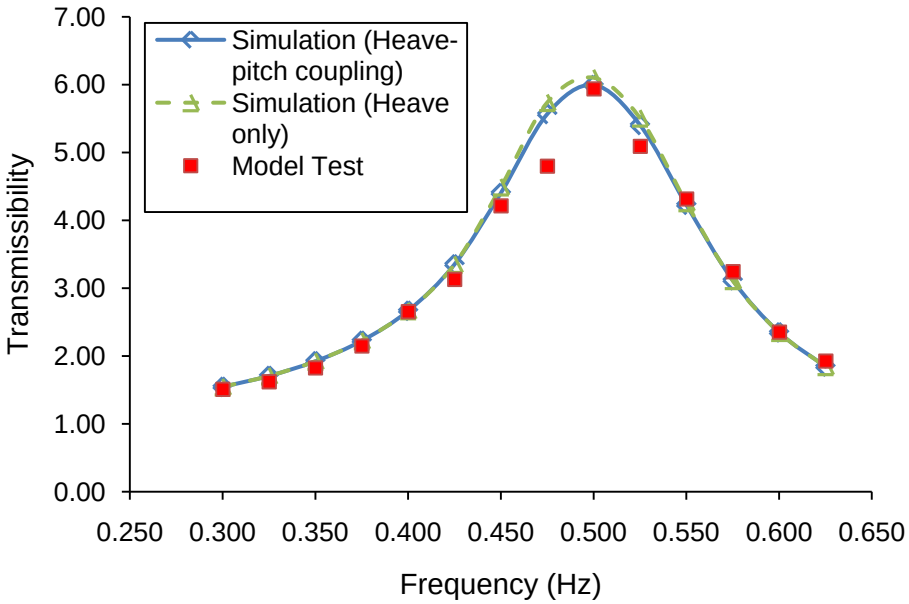

Fig. 52. Comparison of the heave amplitude transmissibility curves obtained using different numerical schemes ($C_{a,t}$ =1.14, $C_{d,t}$ =2.5) for the closed end model.

5.2.2 Comparison of the heave induced pitch motion

Table 14 summarizes the simulated results for the heave induced pitch motion for the closed end model simulations ($C_{a,t}$ =1.14, $C_{d,t}$ =2.5) based on the heave-pitch coupled motion scheme. The first column of the table is the heave excitation frequency applied at the top of the lowering cable, and the excitation frequency increment is refined near the pitch natural frequency to capture the maximum pitch angle (pitch amplitude in resonance). The second column is the pitch natural frequency of the pile-cable system obtained by applying FFT to the simulated pitch displacement time series. The third

column is the difference frequency between the heave excitation frequency and the simulated pitch natural frequency. The fourth column is the ratio of the simulated pitch natural frequency to the heave excitation frequency. The fifth column is the maximum pitch angle (pitch amplitude) observed during the 360 sec simulation, and the pitch amplitude is independent of the initial pitch disturbance (β_0=0.001 rad, see Table 11), which has been confirmed by the simulations using different initial pitch disturbance. The last two columns are the measured pitch amplitude β_{video} and error amplitude β_{error} from video records for the closed end model test, whose measuring method was described in the Section 2.6.

Table 14. Numerical results of heave induced pitch motion for the close end model simulations using the heave-pitch coupling scheme ($C_{a,t}$ =1.14, $C_{d,t}$ =2.5).

f (Hz)	f_β (Hz)	$f - f_\beta$ (Hz)	f_β/f	Pitch amplitude (rad)	β_{video} (rad)	β_{error} (rad)
0.3000	0.2333	0.0667	0.7777	0.0009	-	-
0.3250	0.2333	0.0917	0.7178	0.0009	-	-
0.3500	0.2333	0.1167	0.6666	0.0010	-	-
0.3750	0.2333	0.1417	0.6221	0.0010	0.0017	0.0017
0.4000	0.2333	0.1667	0.5833	0.0010	-	-
0.4250	0.2333	0.1917	0.5489	0.0011	-	-
0.4500	0.2306	0.2194	0.5124	0.0024	-	-
0.4550	0.2278	0.2272	0.5007	0.0156	-	-
0.4600	0.2306	0.2294	0.5013	0.0378	-	-
0.4650	0.2333	0.2317	0.5017	0.0460	-	-
0.4700	0.2361	0.2339	0.5023	0.0485	-	-
0.4750	0.2389	0.2361	0.5029	0.0466	0.0436	0.0087
0.4800	0.2389	0.2411	0.4977	0.0399	-	-
0.4850	0.2417	0.2433	0.4984	0.0254	-	-
0.4900	0.2417	0.2483	0.4933	0.0019	-	-
0.4950	0.2389	0.2561	0.4826	0.0014	-	-
0.5000	0.2389	0.2611	0.4778	0.0013	-	-
0.5250	0.2361	0.2889	0.4497	0.0012	-	-
0.5500	0.2361	0.3139	0.4293	0.0011	-	-
0.5750	0.2333	0.3417	0.4057	0.0010	-	-
0.6000	0.2333	0.3667	0.3888	0.0010	-	-
0.6250	0.2333	0.3917	0.3733	0.0009	0.0017	0.0017

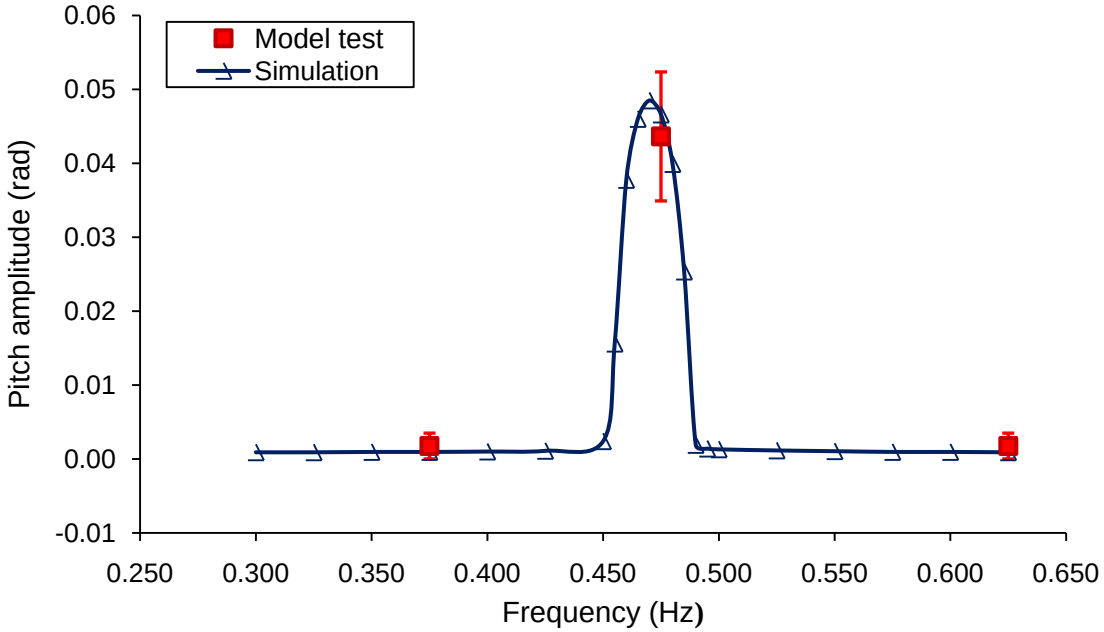

Fig. 53. Comparison of pitch amplitudes of the close end model pile between simulations (heave-pitch coupling, $C_{a,t}$=1.14, $C_{d,t}$=2.5) and model tests.

In the model test, only three cases with different frequencies are recorded for each model. However, Fig. 53 shows satisfactory agreement in the comparison between the simulated pitch amplitude with measured pitch amplitude. The heave excitation frequency range for the heave induced pitch resonance to occur for the closed end model is relatively broad (0.450~0.500 Hz) comparing with that for the open end model presented later. The reason for this is due to the heave natural frequency is quite close the twice of the pitch natural frequency for the closed end model, and the heave

amplitude of the model pile is relatively large when the excitation frequency is approaching one half of the pitch natural frequency. Since the value γ in Eqn. (3.63) increases with the increase of the heave transmissibility (*TR*), thus, the primary unstable region governed by the damped Mathieu equation is relatively broad, as shown in Fig. 41.

Fig. 54 to Fig. 69 show the simulated pitch in time domain and frequency domain at the heave excitation frequency f = 0.400 Hz to f = 0.575 Hz for the case of the closed end model ($C_{a,t}$ =1.14, $C_{d,t}$ =2.5). From these figures, we can clearly see that when the difference frequency is approaching the pitch natural frequency (That is, the ratio of the pitch natural frequency to the heave excitation frequency is close to one half), the heave induced pitch motion is amplified significantly. However, the instability pitch motion finally ends up to be stable motion with the much larger pitch amplitude due to the damping effect. That is, when the heave excitation frequency is twice of the pitch natural frequency, the pitch motion experience damped Mathieu instability, which can be described by the damped Mathieu equation (3.61) discussed in Section 3.3.

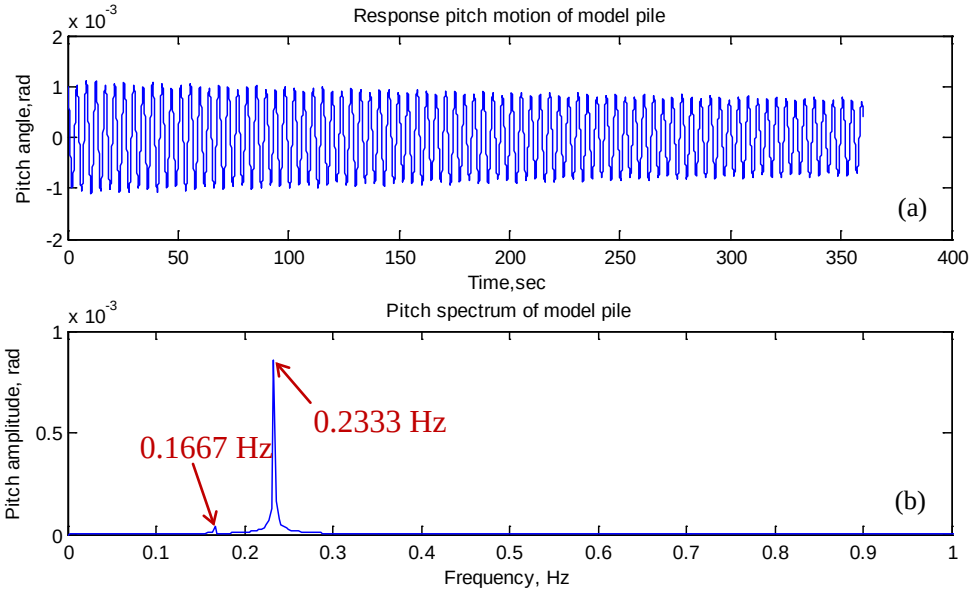

Fig. 54. The heave induced pitch motion at heave excitation frequency f = 0.400 Hz for the closed end model: (a) Pitch angle of the model pile; (b) Pitch spectrum of the model pile.

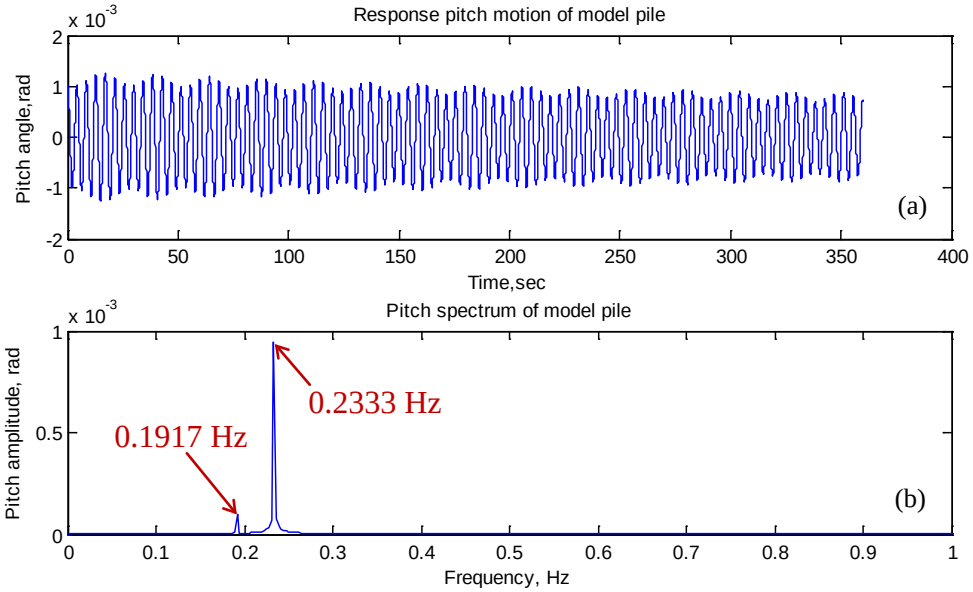

Fig. 55. The heave induced pitch motion at heave excitation frequency f = 0.425 Hz for the closed end model: (a) Pitch angle of the model pile; (b) Pitch spectrum of the model pile.

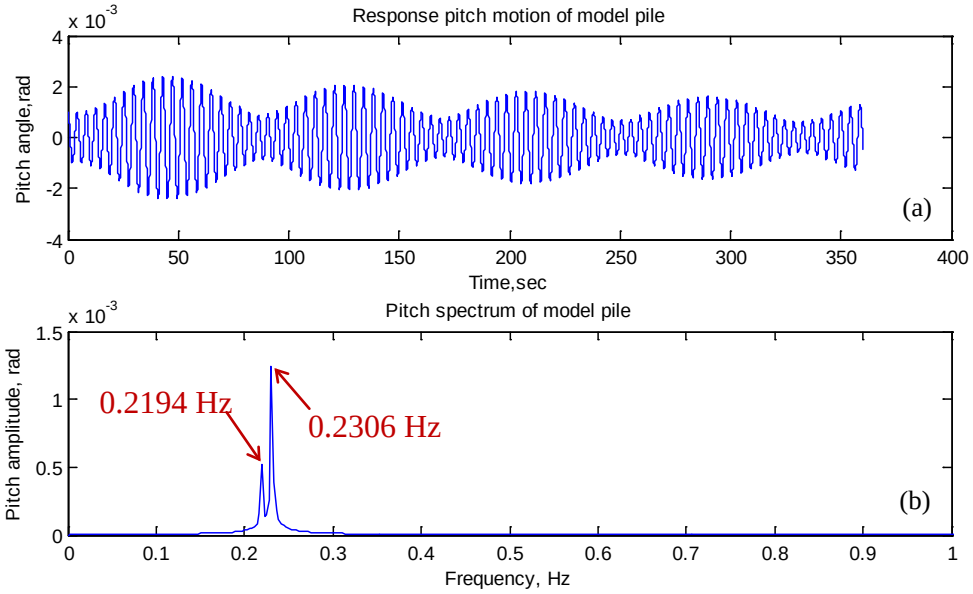

Fig. 56. The heave induced pitch motion at heave excitation frequency f = 0.450 Hz for the closed end model: (a) Pitch angle of the model pile; (b) Pitch spectrum of the model pile.

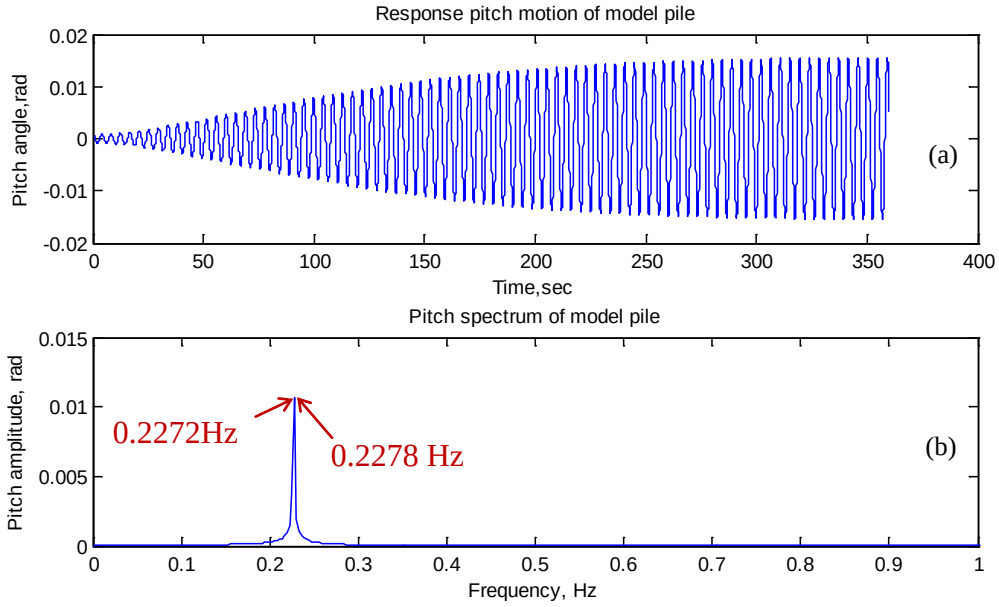

Fig. 57. The heave induced pitch motion at heave excitation frequency *f* = 0.455 Hz for the closed end model: (a) Pitch angle of the model pile; (b) Pitch spectrum of the model pile.

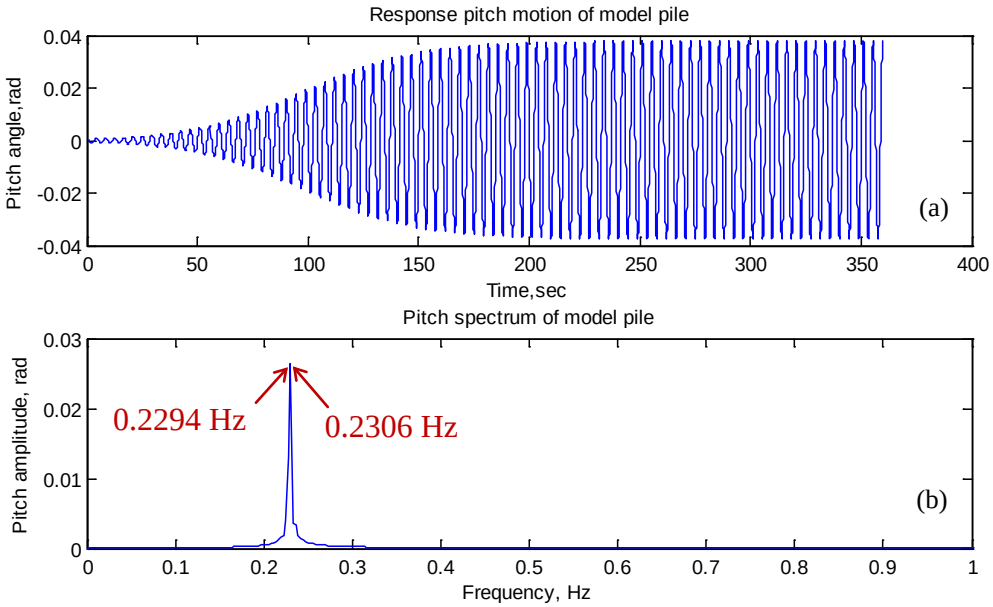

Fig. 58. The heave induced pitch motion at heave excitation frequency f = 0.460 Hz for the closed end model: (a) Pitch angle of the model pile; (b) Pitch spectrum of the model pile.

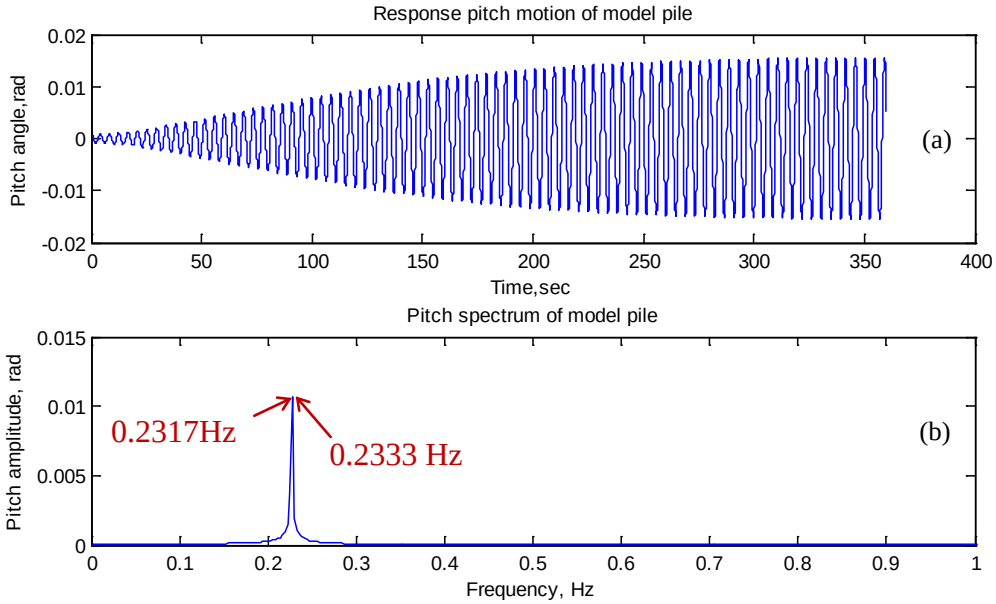

Fig. 59. The heave induced pitch motion at heave excitation frequency f = 0.465 Hz for the closed end model: (a) Pitch angle of the model pile; (b) Pitch spectrum of the model pile.

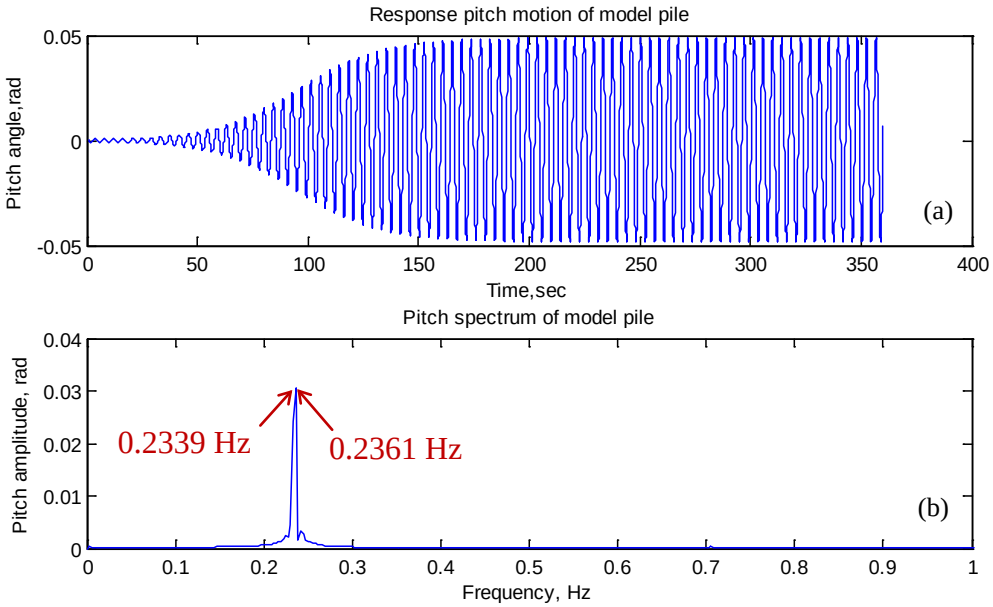

Fig. 60. The heave induced pitch motion at heave excitation frequency f = 0.470 Hz for the closed end model: (a) Pitch angle of the model pile; (b) Pitch spectrum of the model pile.

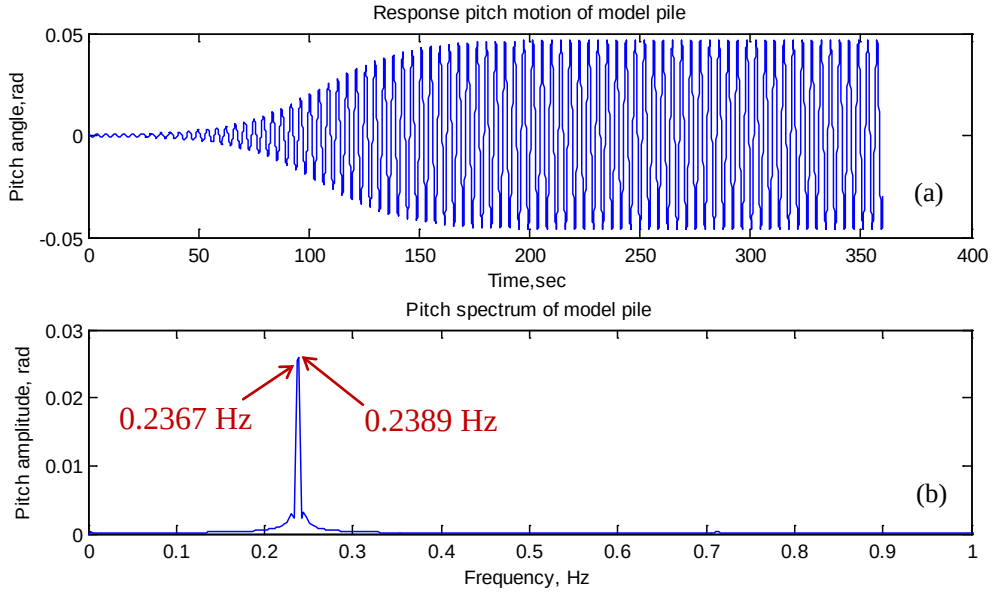

Fig. 61. The heave induced pitch motion at heave excitation frequency f = 0.475 Hz for the closed end model: (a) Pitch angle of the model pile; (b) Pitch spectrum of the model pile.

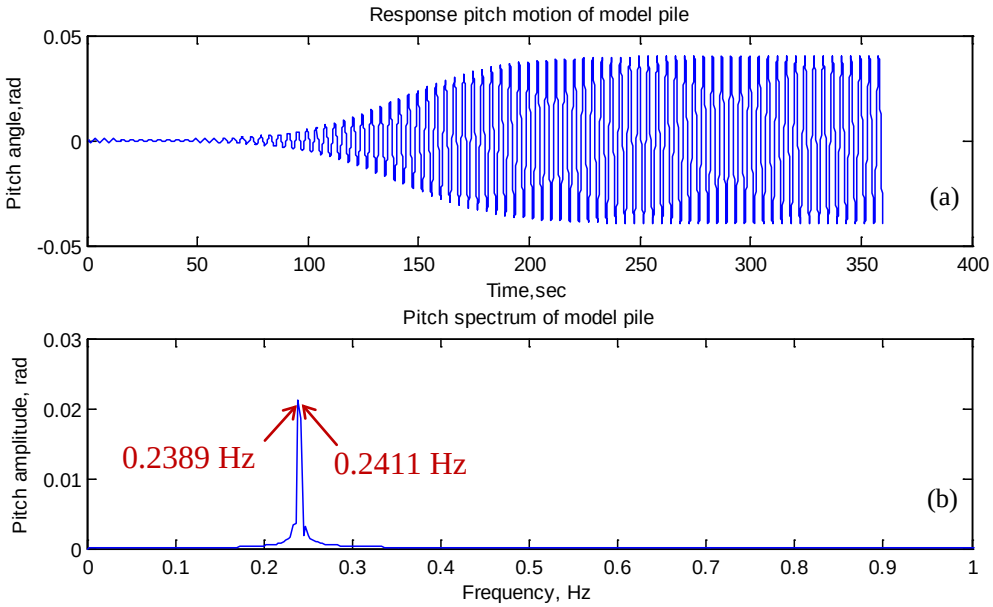

Fig. 62. The heave induced pitch motion at heave excitation frequency f = 0.480 Hz for the closed end model: (a) Pitch angle of the model pile; (b) Pitch spectrum of the model pile.

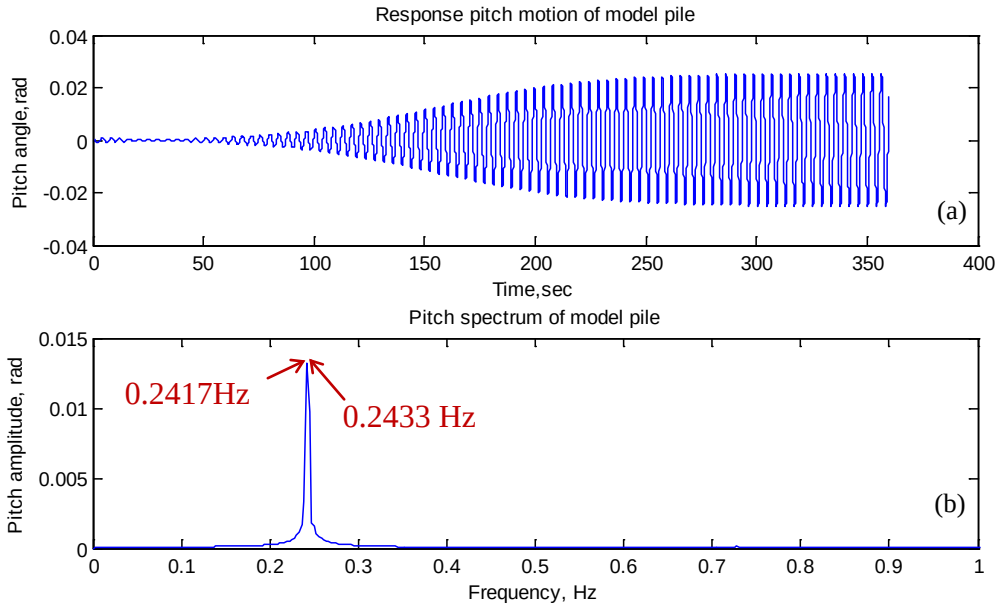

Fig. 63. The heave induced pitch motion at heave excitation frequency f = 0.485 Hz for the closed end model: (a) Pitch angle of the model pile; (b) Pitch spectrum of the model pile.

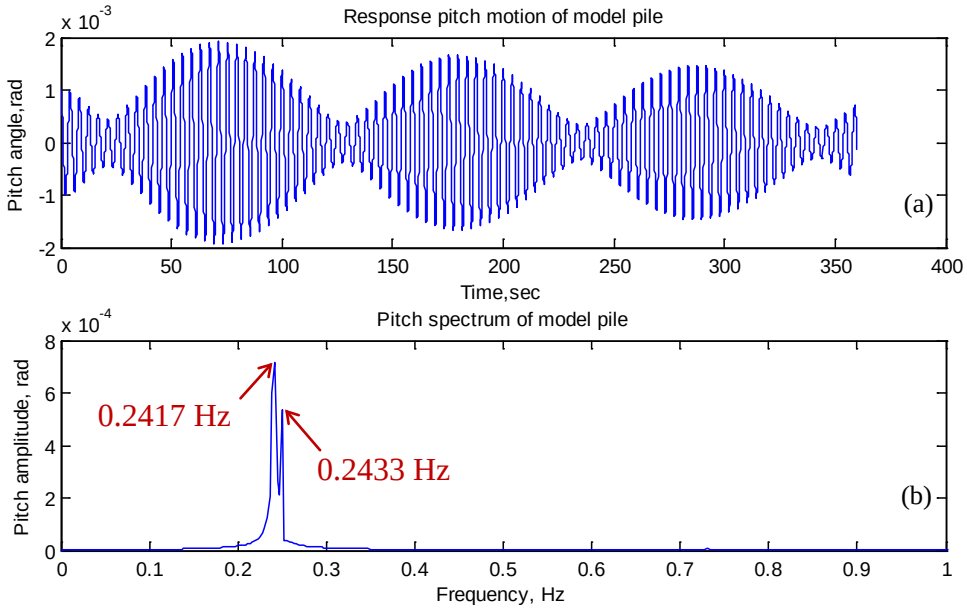

Fig. 64. The heave induced pitch motion at heave excitation frequency f = 0.490 Hz for the closed end model: (a) Pitch angle of the model pile; (b) Pitch spectrum of the model pile.

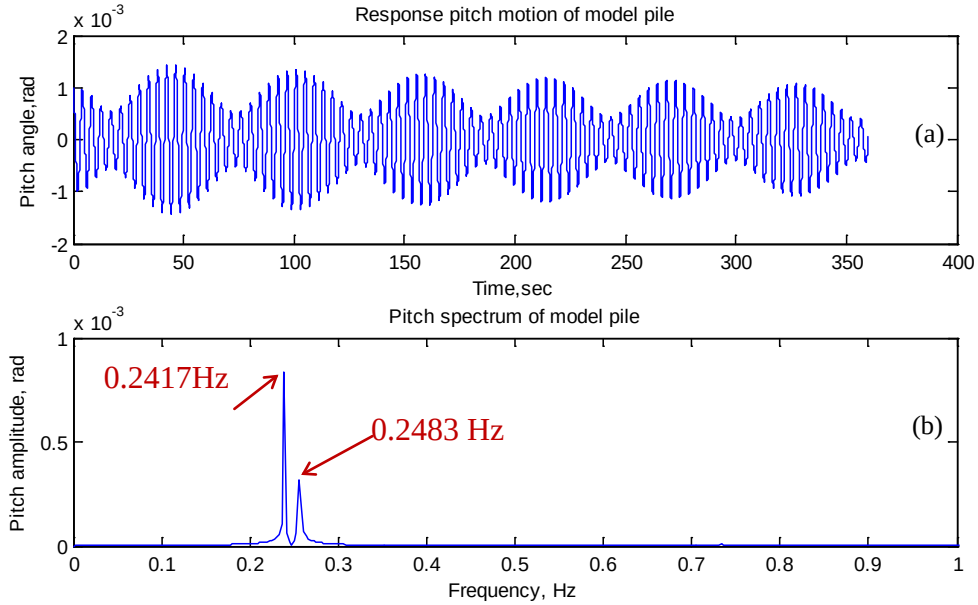

Fig. 65. The heave induced pitch motion at heave excitation frequency f = 0.495 Hz for the closed end model: (a) Pitch angle of the model pile; (b) Pitch spectrum of the model pile.

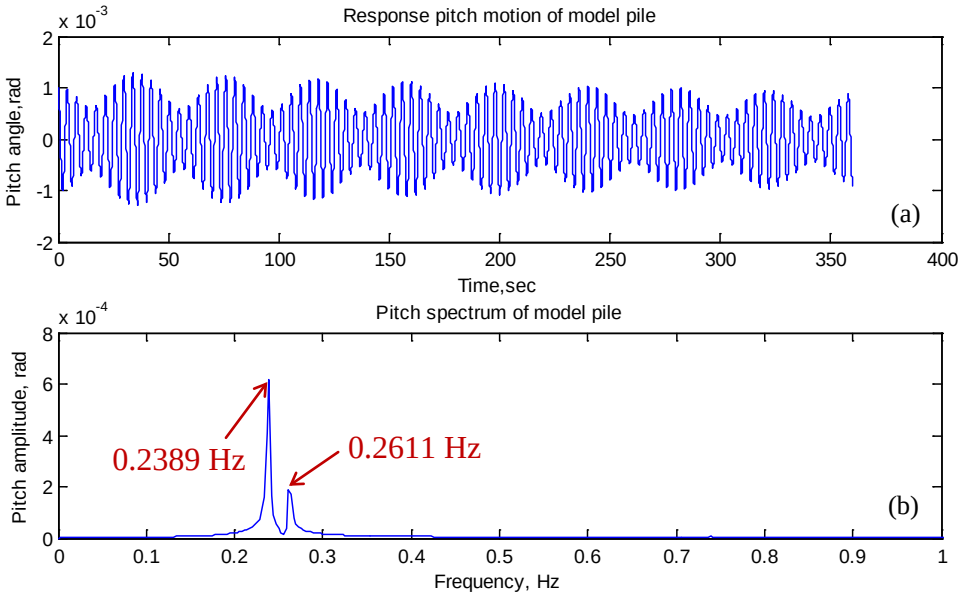

Fig. 66. The heave induced pitch motion at heave excitation frequency f = 0.500 Hz for the closed end model: (a) Pitch angle of the model pile; (b) Pitch spectrum of the model pile.

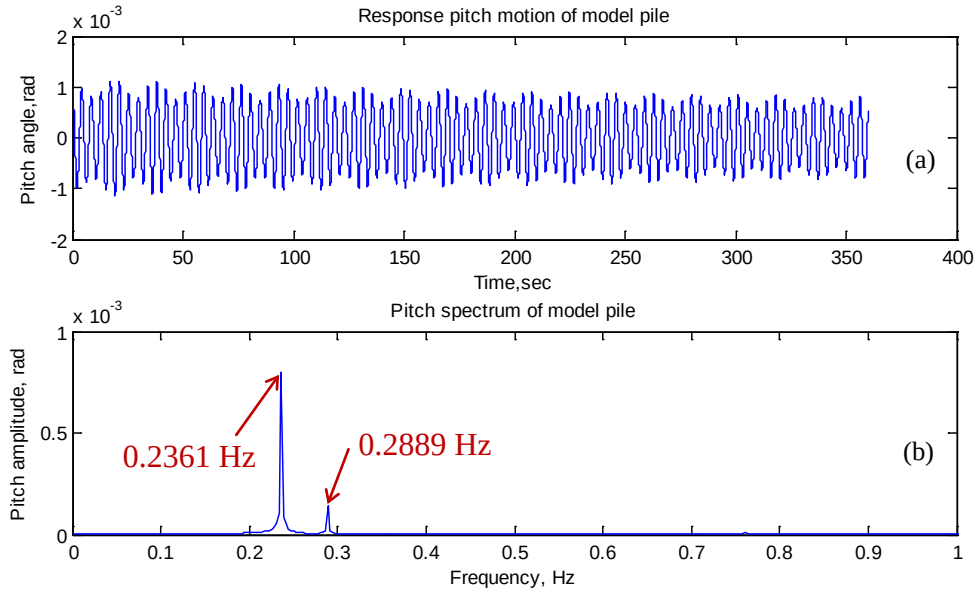

Fig. 67. The heave induced pitch motion at heave excitation frequency f = 0.525 Hz for the closed end model: (a) Pitch angle of the model pile; (b) Pitch spectrum of the model pile.

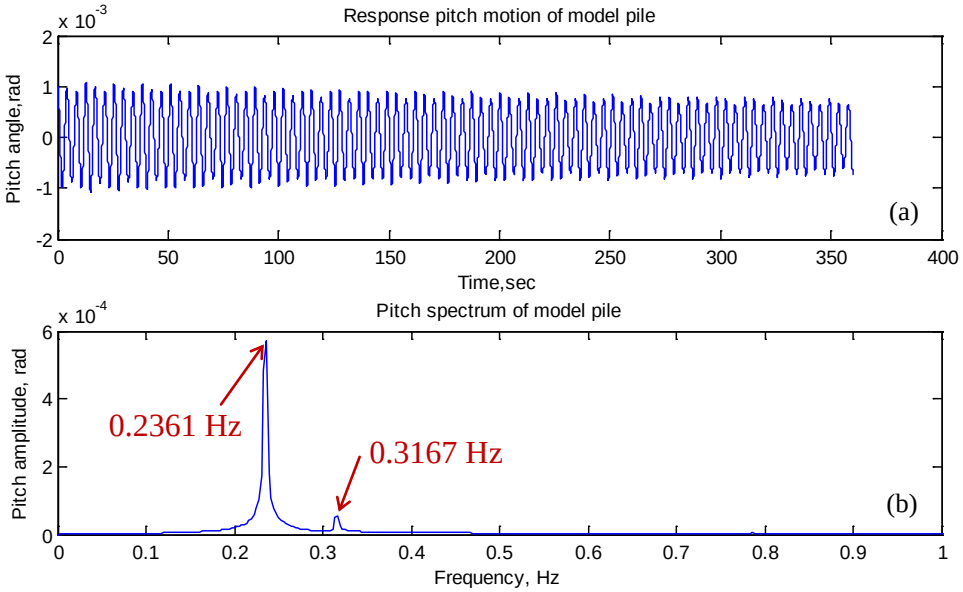

Fig. 68. The heave induced pitch motion at heave excitation frequency f = 0.550 Hz for the closed end model: (a) Pitch angle of the model pile; (b) Pitch spectrum of the model pile.

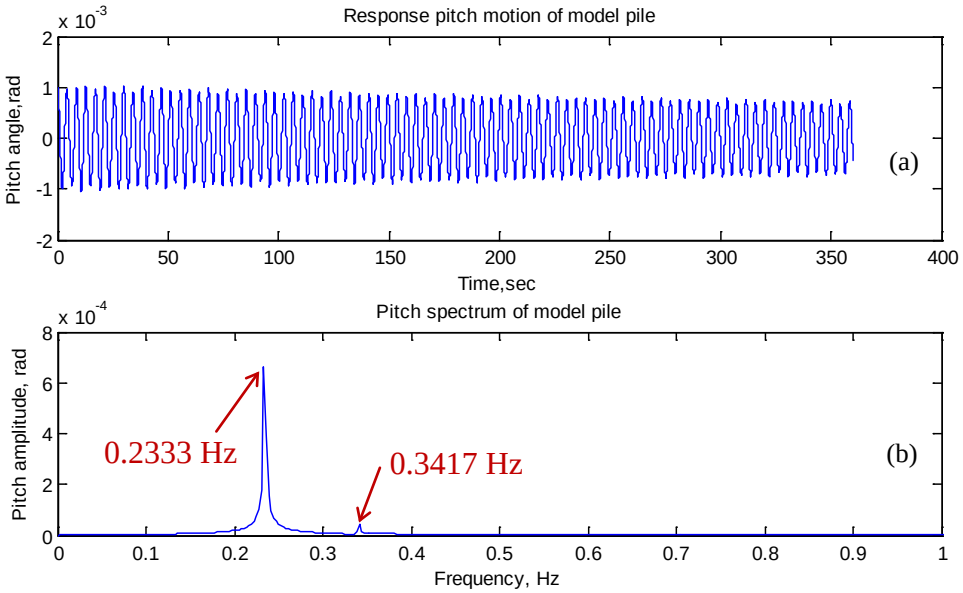

Fig. 69. The heave induced pitch motion at heave excitation frequency f = 0.575 Hz for the closed end model: (a) Pitch angle of the model pile; (b) Pitch spectrum of the model pile.

From Table 15 and Fig. 70, we know that the amplitude of the initial pitch perturbation (β_0) has no effect on the final stable pitch amplitude but the time duration has some effect for the pitch motion to reach the final steady state. The large the amplitude of the initial perturbation the sooner for the pitch motion to reach steady state; however, it has no effect on the pitch amplitudes of the finial steady state as long as the time duration is long enough for the pitch motion to reach steady state.

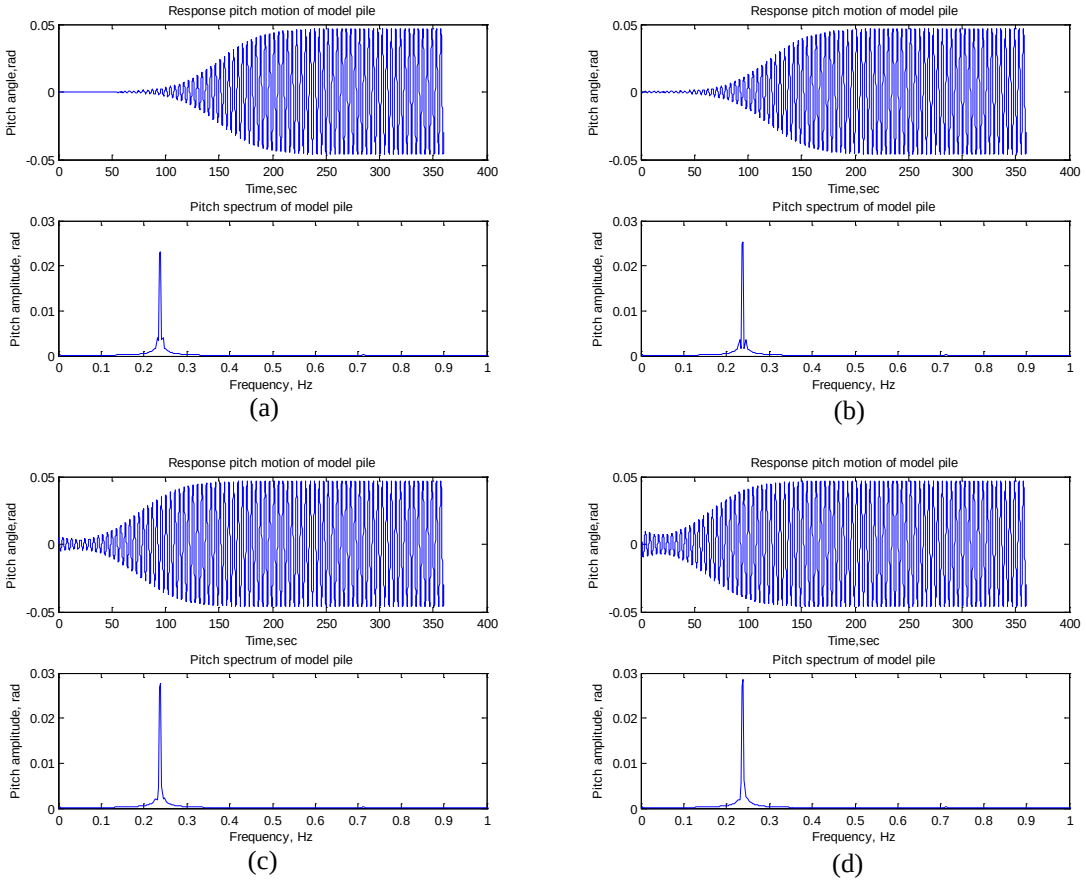

Fig. 70. The effects of the initial pitch perturbation (β_0) on the heave induced pitch motion at heave excitation frequency f = 0.475 Hz for the closed end model: (a) $\beta_0 = 0.0001$ rad ; (b) $\beta_0 = 0.0005$ rad ; (c) $\beta_0 = 0.005$ rad ; (d) $\beta_0 = 0.01$ rad .

Table 15. Initial pitch angle effect on the pitch angle at the end of 360 sec simulation.

f (Hz)	f_β (Hz)	Steady state pitch amplitude (rad)				
		β_0=0.0001 rad	β_0=0.0005 rad	β_0=0.001 rad	β_0=0.005 rad	β_0=0.01 rad
0.3000	0.2333	0.0001	0.0004	0.0008	0.0017	0.0021
0.3250	0.2333	0.0001	0.0004	0.0008	0.0017	0.0021
0.3500	0.2333	0.0001	0.0004	0.0008	0.0017	0.0021
0.3750	0.2333	0.0001	0.0005	0.0008	0.0018	0.0022
0.4000	0.2333	0.0001	0.0005	0.0008	0.0018	0.0022
0.4250	0.2333	0.0001	0.0005	0.0009	0.0020	0.0024
0.4500	0.2306	0.0002	0.0008	0.0014	0.0025	0.0028
0.4750	0.2389	0.0466	0.0465	0.0466	0.0465	0.0466
0.5000	0.2389	0.0001	0.0005	0.0010	0.0021	0.0026
0.5250	0.2361	0.0001	0.0005	0.0009	0.0019	0.0024
0.5500	0.2361	0.0001	0.0004	0.0008	0.0017	0.0022
0.5750	0.2333	0.0001	0.0004	0.0008	0.0018	0.0022
0.6000	0.2333	0.0001	0.0004	0.0008	0.0017	0.0022
0.6250	0.2333	0.0001	0.0004	0.0008	0.0017	0.0021

5.3 Comparison of the PS Valves Opening Model

5.3.1 Comparison of the heave motion

The specific parameters for the PS valves opening model are listed in Table 16. The comparisons between the simulations and measurements in time domain in four cases are given in Fig. 71 to Fig. 74. That is, the heave excitation frequency is a) far below the heave resonance frequency; b) far above the heave resonance frequency; c) and d) close to the heave resonance frequency. The comparisons are given in the time span [90, 100] sec. Since the results from the decoupled motion scheme is quite close to the coupled motion scheme, we drop out the results of the decoupled pitch motion scheme and focus on the comparisons between the simulations by the coupled motion scheme with the measurements for the PS valves opening model.

Table 16. PS valves opening model parameters for numerical simulations.

Model parameters	Notation	Value	Note
Length	L	3 ft (0.914 m)	
Outer diameter	D	6 in (15.24 cm)	
Wall thickness	t	0.25 in (0.64 cm)	
Opening area ratio (Perforation)	γ	3.70%	For the top cap
Normal added-mass coef.	$C_{a,n}$	1.2	
Normal drag coef.	$C_{d,n}$	1.0	
Axial added-mass coef.	$C_{a,t}$	1.11	From model test
Axial drag coef.	$C_{d,t}$	3.0	
Coef. of pitch damping term	$C_{D\beta}$	9.8236	Refer to Appendix B
Weight in air	W	16.0 lb (71.172 N)	
Weight in water	W'	9.6 lb (42.703 N)	
Weight of water inside pile plus water displaced by pile	W_0	36.8 lb (163.695 N)	
Buoyancy	F_B	6.729 lb (29.932 N)	
Moment of inertia in air	$I_{\beta p}$	1.5780 slug·ft^2 (2.139 kg/m^2)	Refer to Appendix B
Added moment of inertia in water	$I_{\beta a}$	4.1176 slug·ft^2 (5.583 kg/m^2)	Refer to Appendix B
Moment of inertia in water	I_{β}	5.6956 slug·ft^2 (7.722 kg/m^2)	
Gravity center from eye bolt	$O'G$	1.44 ft (0.439 m)	Including hanging bar height 2"
Buoyancy center from eye bolt	$O'B$	1.57 ft (0.479 m)	Including hanging bar height 2"
Heave natural frequency	f_n	0.5050 Hz	From model test
Pitch natural frequency	f_p	0.2400 Hz	Hand calculation

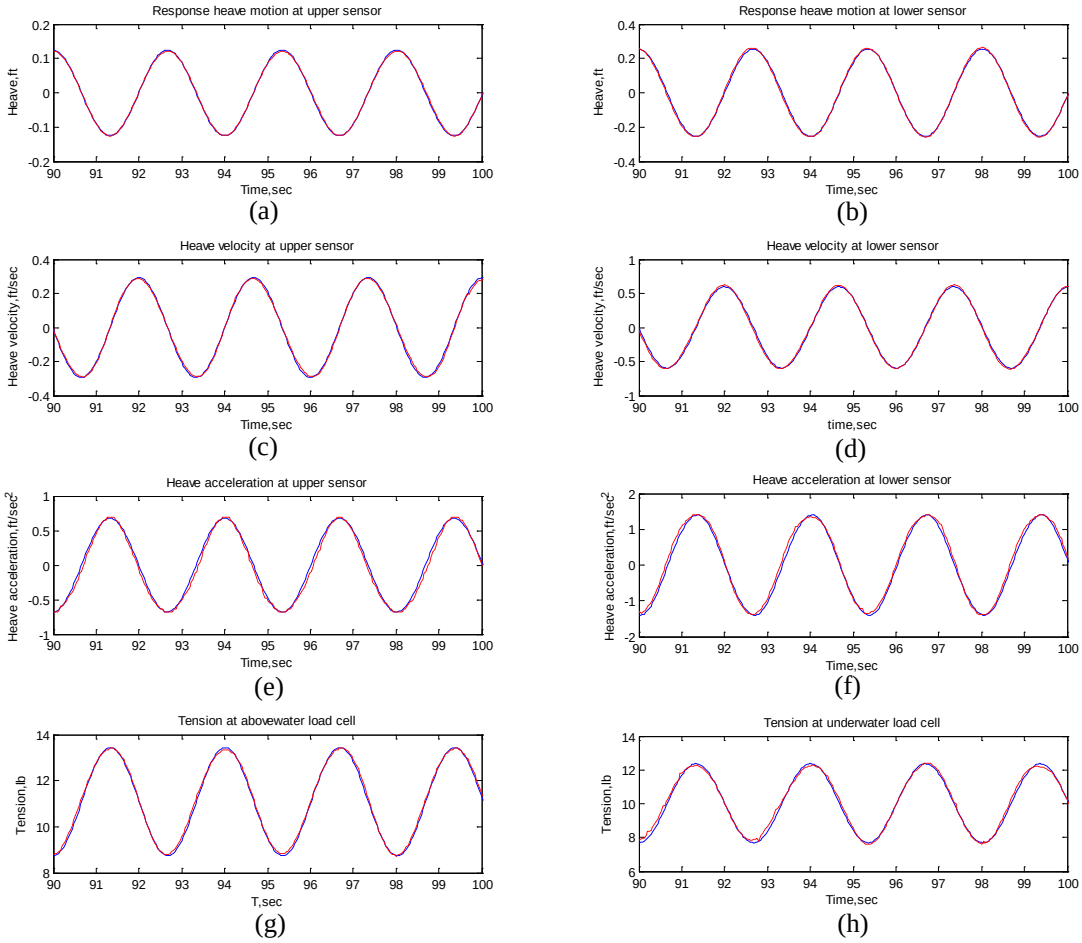

Fig. 71. Time domain comparisons of results from coupled motion scheme $(-)$ with the measurements of model tests $(-\cdot-)$ for the PS valves opening model at excitation frequency far below resonance (f = 0.375 Hz, $C_{a,t}$ =1.11, $C_{d,t}$ =3.0).

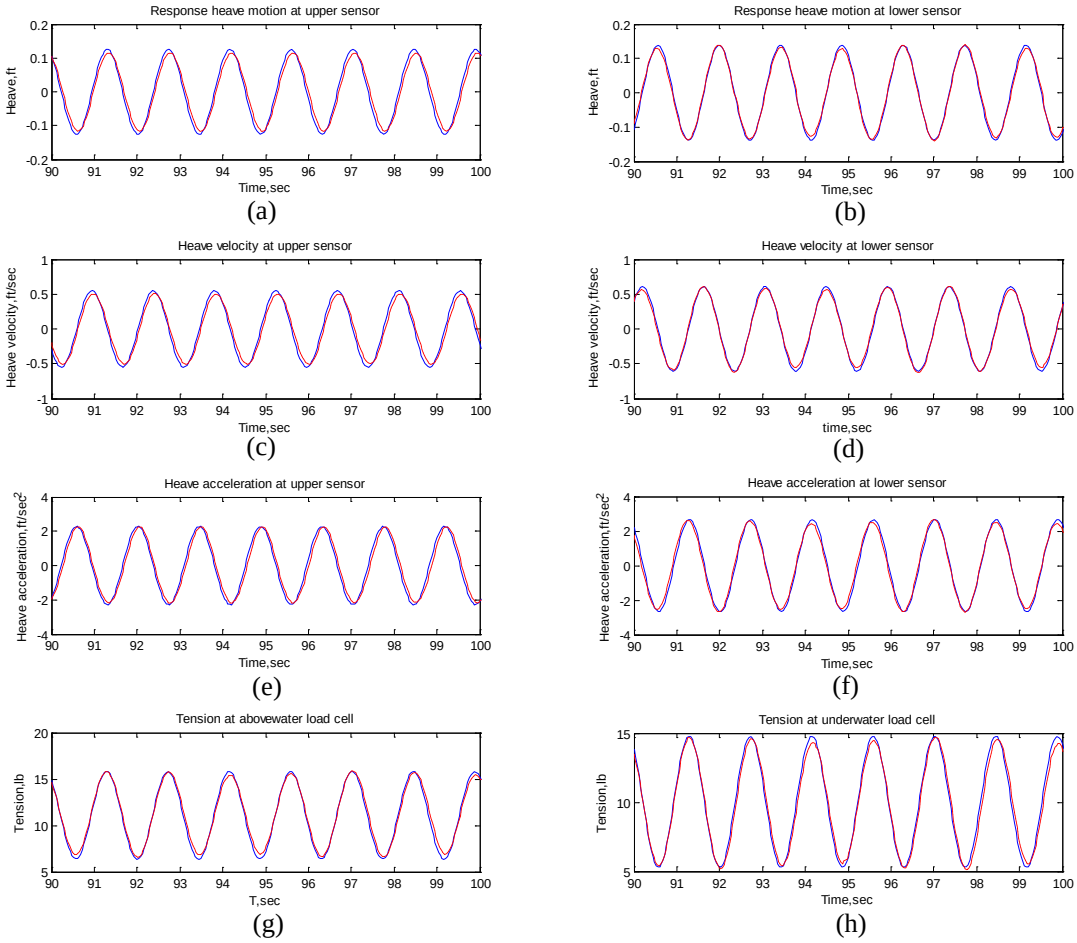

Fig. 72. Time domain comparisons of results from coupled motion scheme $(-)$ with the measurements of model tests $(-\cdot-)$ for the PS valves opening model at excitation frequency far above resonance (f = 0.625 Hz, $C_{a,t}$ =1.11, $C_{d,t}$ =3.0).

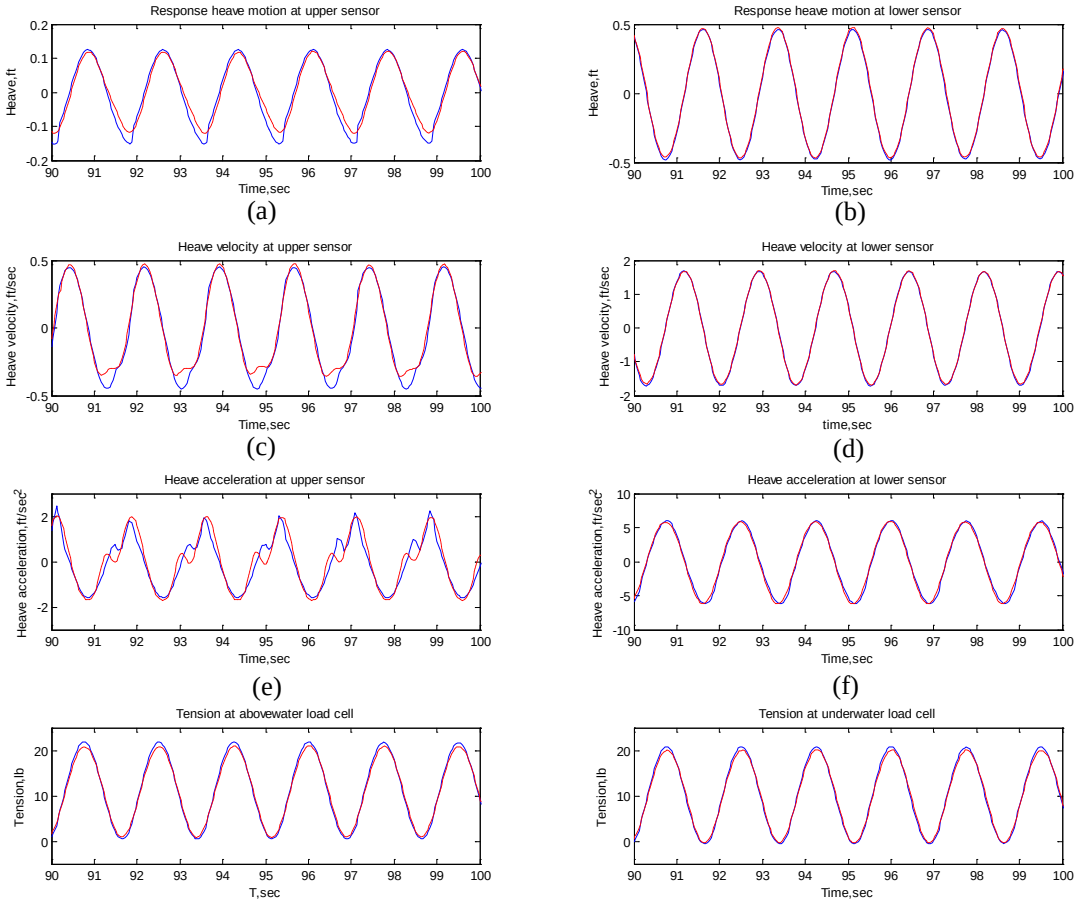

Fig. 73. Time domain comparisons of results from coupled motion scheme $(-)$ with the measurements of model tests $(-\cdot-)$ for the PS valves opening model at excitation frequency near above resonance (f = 0.575 Hz, $C_{a,t}$ =1.11, $C_{d,t}$ =3.0).

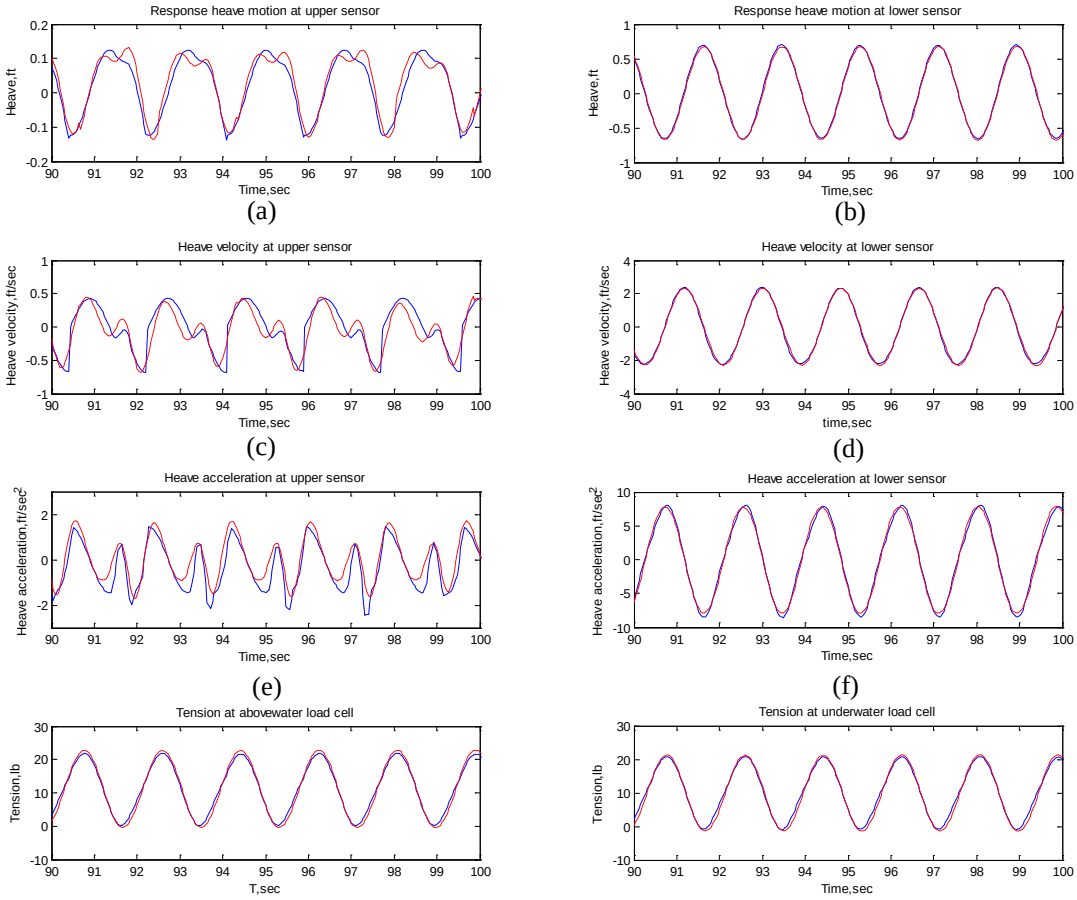

Fig. 74. Time domain comparisons of results from coupled motion scheme $(-)$ with the measurements of model tests $(- \cdot -)$ for the PS valves opening model at excitation frequency near above resonance (f = 0.550 Hz, $C_{a,t}$ =1.11, $C_{d,t}$ =3.0).

Table 17. Numerical results of heave motion for the PS valves opening model simulations using the heave-pitch coupling scheme ($C_{a,t}$=1.11, $C_{d,t}$=3.0).

f (Hz)	ST1 (lb)	ST2 (lb)	ST2/ST1	SD3 (ft)	SD2 (ft)	SD2/SD3	SD2/SD1	SD3/SD1
0.3750	4.3471	4.3286	0.9957	0.2478	0.5105	2.0601	2.0420	0.9912
0.4000	5.1818	5.1613	0.9960	0.2522	0.6064	2.4044	2.4256	1.0088
0.4250	8.8278	8.8066	0.9976	0.2438	0.7308	2.9975	2.9232	0.9752
0.4500	11.3429	11.3227	0.9982	0.2504	0.9239	3.6897	3.6956	1.0016
0.4750	15.9539	15.9161	0.9976	0.2516	1.1458	4.5541	4.5832	1.0064
0.5000	21.2985	21.2983	1.0000	0.2423	1.3742	5.6715	5.4968	0.9692
0.5250	20.9604	20.9641	1.0002	0.2318	1.3524	5.8343	5.4096	0.9272
0.5500	19.9547	19.9785	1.0012	0.2228	1.1829	5.3092	4.7316	0.8912
0.5750	18.9566	18.9843	1.0015	0.2305	0.8273	3.5892	3.3092	0.9220
0.6000	14.7404	14.7785	1.0026	0.2327	0.5842	2.5105	2.3368	0.9308
0.6250	11.8446	11.8940	1.0042	0.2295	0.4709	2.0519	1.8836	0.9180
0.6500	10.4329	10.4727	1.0038	0.2235	0.3880	1.7360	1.5520	0.8940
0.6750	9.3342	9.3807	1.0050	0.2291	0.3258	1.4221	1.3032	0.9164
0.7000	8.5106	8.5555	1.0053	0.2247	0.2788	1.2408	1.1152	0.8988

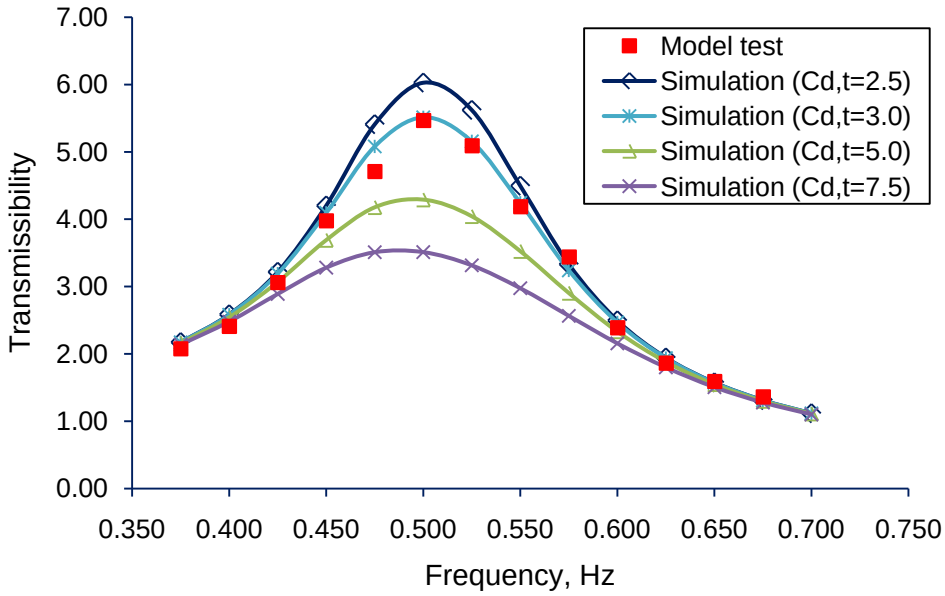

Fig. 75. Matching the heave amplitude transmissibility curves from the model tests by the simulations with different drag coefficients (heave-pitch coupling, $C_{a,t}$=1.11) for the PS valves opening model.

The dynamics of the PS valves opening model is quite similar to the closed end model, and the results in Fig. 71 to Fig. 74 show the similar characteristics with those of the closed end model. For brevity, we drop out the detail discussions of the vibration scenarios for each case. Fig. 75 presents the searching of the axial drag coefficient for the heave motion of the PS valves opening model, and the axial drag coefficient for this case is roughly determined as $C_{d,t}$ =3.0. Table 17 presents numerical results for the heave-pitch coupled motion ($C_{a,t}$ =1.11, $C_{d,t}$ =3.0) for the PS valves opening model.

5.3.2 Comparison of the heave induced pitch motion

Table 18 summarizes numerical results of the heave induced pitch motion for the PS valves opening model simulations ($C_{a,t}$ =1.11, $C_{d,t}$ =3.0) based on the heave-pitch coupled motion scheme, and each columns have the same meaning as presented in the closed end model simulation. Fig. 76 shows satisfactory agreement in the comparison between the simulated pitch amplitude with measured pitch amplitude for the PS valves opening model. The heave excitation frequency range for the heave induced pitch amplification is also relatively broad (0.450~0.500 Hz) as for the closed end model.

Fig. 77 to Fig. 87 show the time domain and frequency domain results of the heave induced pitch motion at the heave excitation frequency f = 0.450 Hz to f = 0.500 Hz for the PS valves opening model simulations ($C_{a,t}$ =1.11, $C_{d,t}$ =3.0). From these figures, we can clearly obtain the similar conclusion as those of the closed end model.

Table 18. Numerical results of heave induced pitch motion for the PS valves opening model simulations using the heave-pitch coupling scheme ($C_{a,t}$=1.11, $C_{d,t}$=3.0).

f (Hz)	f_β (Hz)	$f - f_\beta$ (Hz)	f_β/f	Pitch amplitude (rad)	β_{video} (rad)	β_{error} (rad)
0.3750	0.2333	0.1417	0.6221	0.0010	0.0017	0.0017
0.4000	0.2333	0.1667	0.5833	0.0010	-	-
0.4250	0.2333	0.1917	0.5489	0.0011	-	-
0.4500	0.2306	0.2194	0.5124	0.0022	-	-
0.4550	0.2278	0.2272	0.5007	0.0071	-	-
0.4600	0.2306	0.2294	0.5013	0.0345	-	-
0.4650	0.2333	0.2317	0.5017	0.0432	-	-
0.4700	0.2361	0.2339	0.5023	0.0458	-	-
0.4750	0.2389	0.2361	0.5029	0.0438	0.0436	0.0087
0.4800	0.2389	0.2411	0.4977	0.0368	-	-
0.4850	0.2417	0.2433	0.4984	0.0209	-	-
0.4900	0.2389	0.2511	0.4876	0.0018	-	-
0.4950	0.2389	0.2561	0.4826	0.0015	-	-
0.5000	0.2389	0.2611	0.4778	0.0014	-	-
0.5250	0.2361	0.2889	0.4497	0.0011	-	-
0.5500	0.2361	0.3139	0.4293	0.0011	-	-
0.5750	0.2333	0.3417	0.4057	0.0010	-	-
0.6000	0.2333	0.3667	0.3888	0.0010	-	-
0.6250	0.2333	0.3917	0.3733	0.0009	-	-
0.6500	0.2333	0.4167	0.3589	0.0009	-	-
0.6750	0.2333	0.4417	0.3456	0.0009	-	-
0.7000	0.2333	0.4667	0.3333	0.0009	0.0017	0.0017

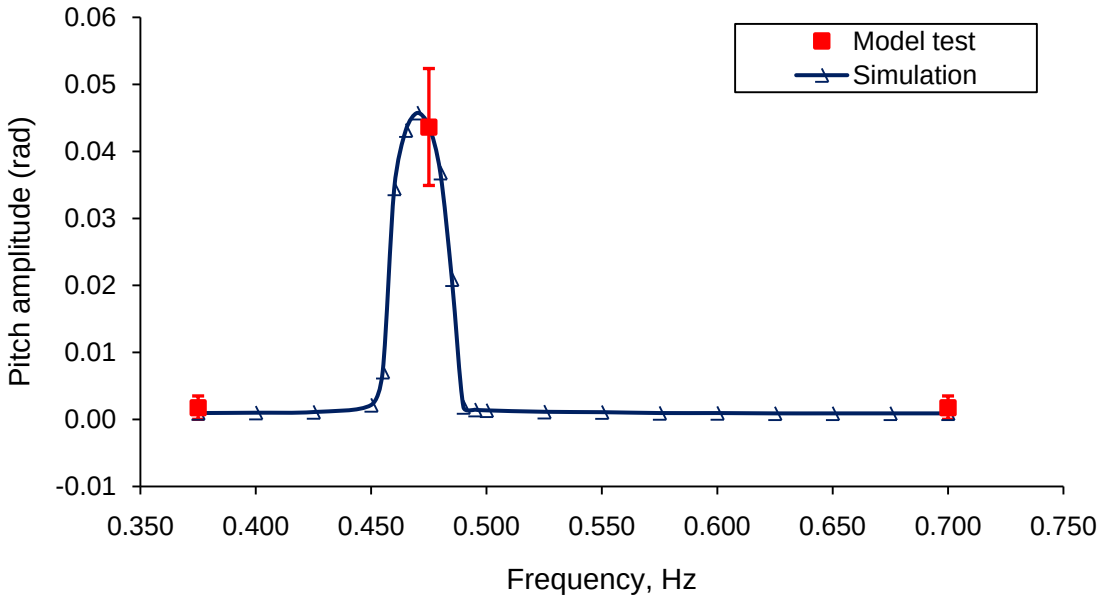

Fig. 76. Comparison of pitch amplitudes of the PS valves opening model pile between simulations (heave-pitch coupling, $C_{a,t}$=1.11, $C_{d,t}$=3.0) and model tests.

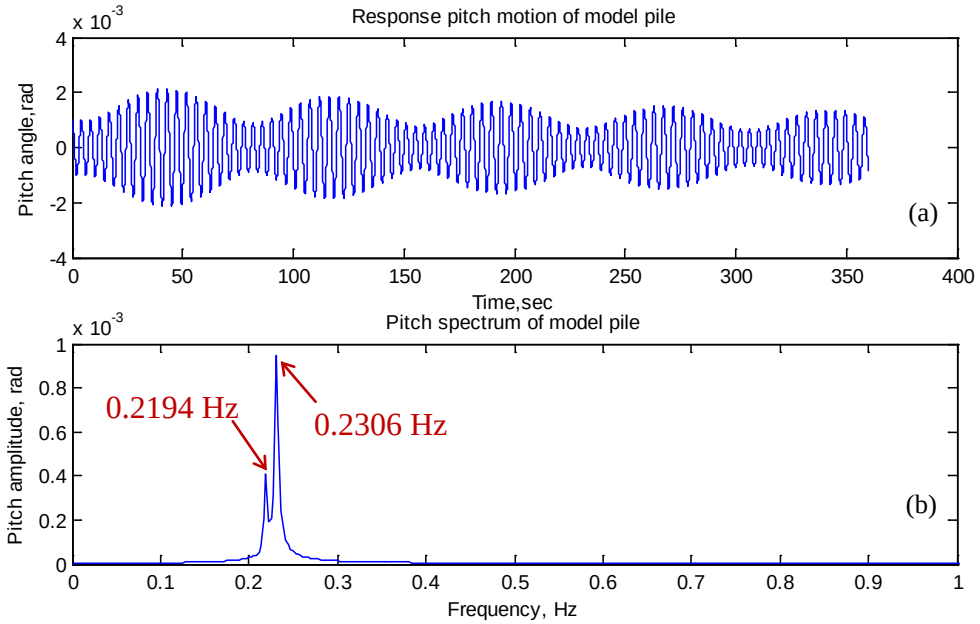

Fig. 77. The heave induced pitch motion at heave excitation frequency f = 0.450 Hz for the PS valves opening model: (a) Pitch angle of the model pile; (b) Pitch spectrum of the model pile.

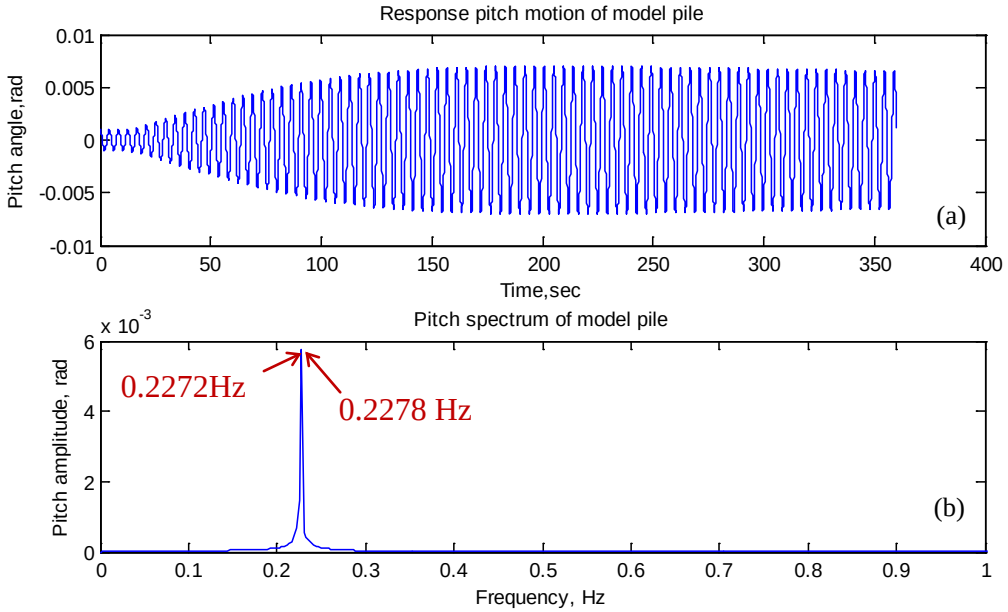

Fig. 78. The heave induced pitch motion at heave excitation frequency f = 0.455 Hz for the PS valves opening model: (a) Pitch angle of the model pile; (b) Pitch spectrum of the model pile.

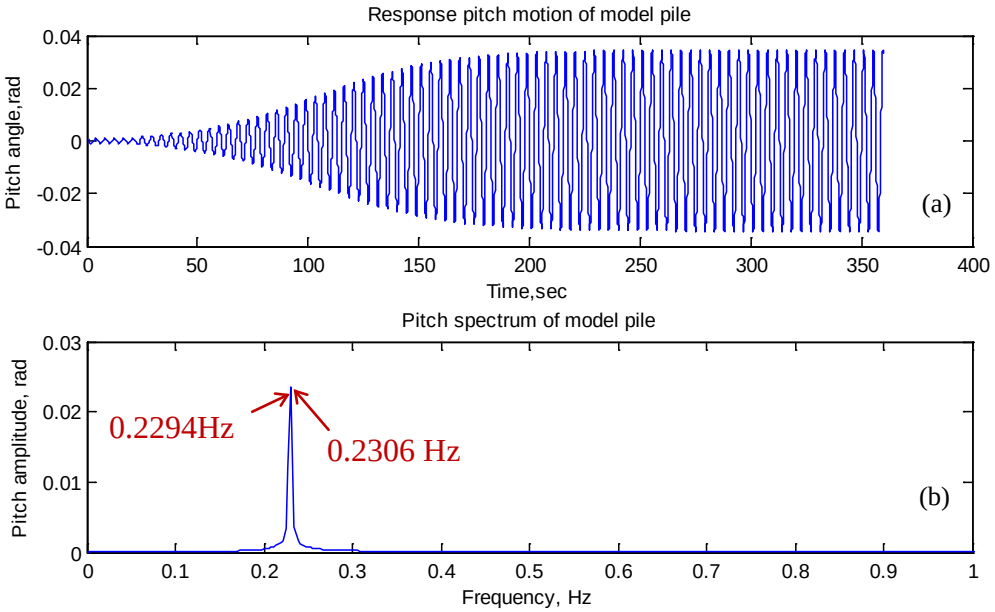

Fig. 79. The heave induced pitch motion at heave excitation frequency f = 0.460 Hz for the PS valves opening model: (a) Pitch angle of the model pile; (b) Pitch spectrum of the model pile.

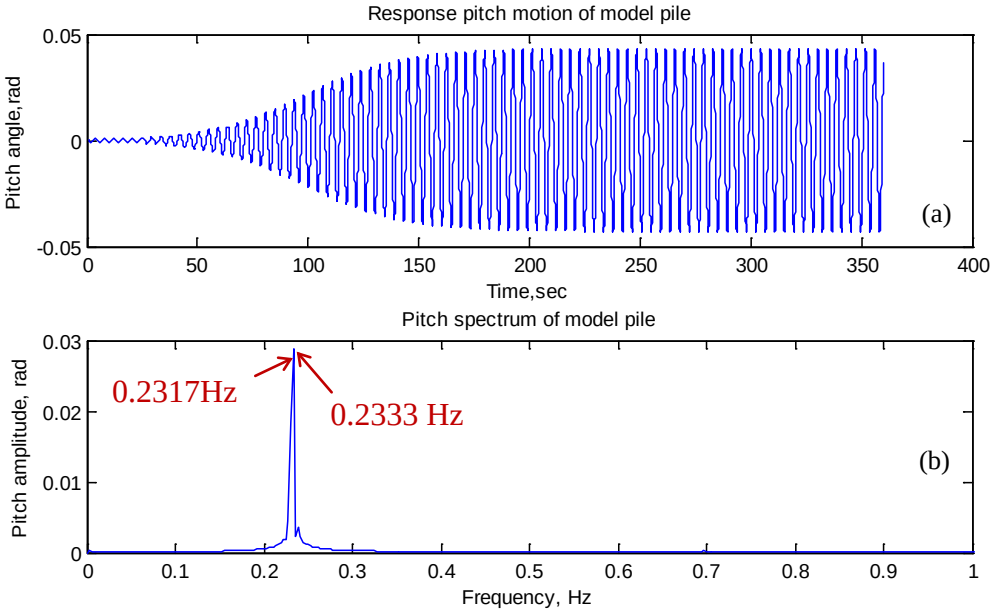

Fig. 80. The heave induced pitch motion at heave excitation frequency f = 0.465 Hz for the PS valves opening model: (a) Pitch angle of the model pile; (b) Pitch spectrum of the model pile.

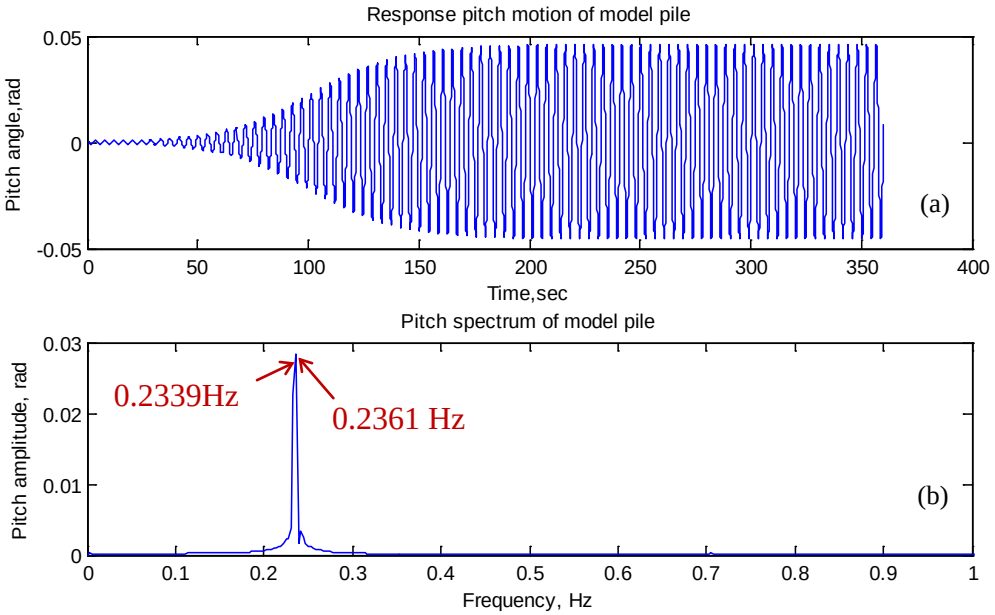

Fig. 81. The heave induced pitch motion at heave excitation frequency f = 0.470 Hz for the PS valves opening model: (a) Pitch angle of the model pile; (b) Pitch spectrum of the model pile.

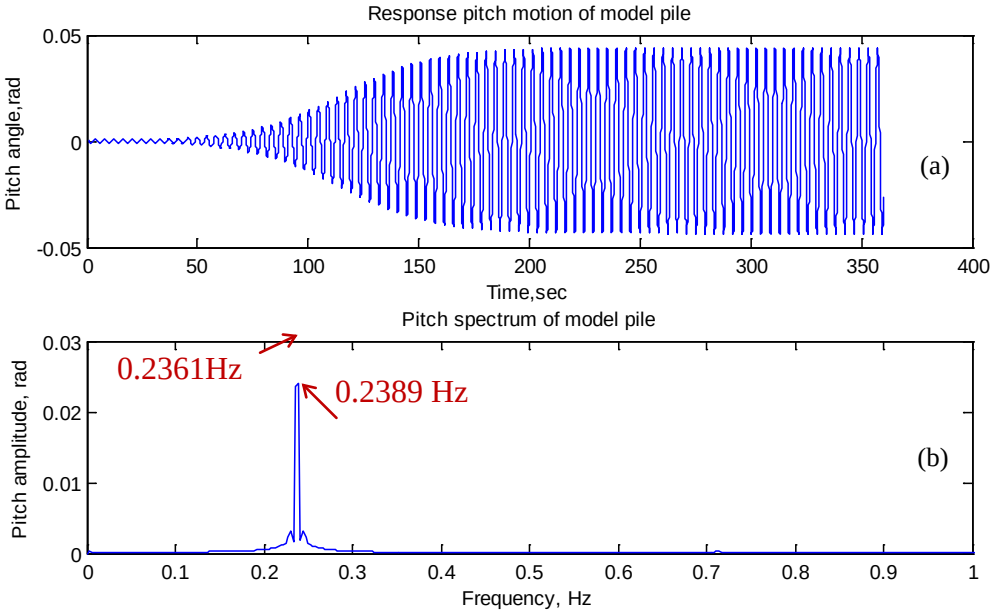

Fig. 82. The heave induced pitch motion at heave excitation frequency f = 0.475 Hz for the PS valves opening model: (a) Pitch angle of the model pile; (b) Pitch spectrum of the model pile.

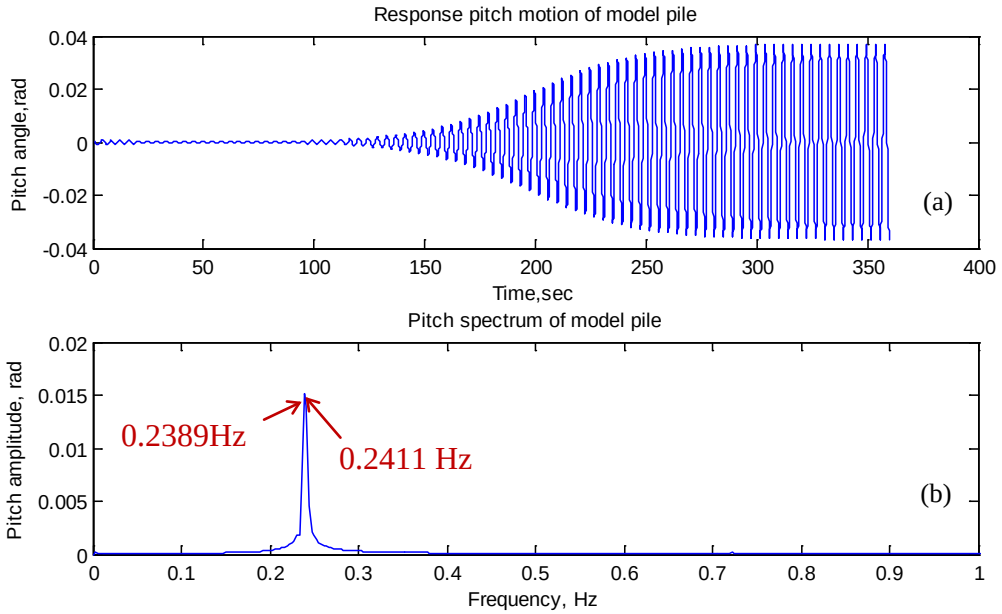

Fig. 83. The heave induced pitch motion at heave excitation frequency f = 0.480 Hz for the PS valves opening model: (a) Pitch angle of the model pile; (b) Pitch spectrum of the model pile.

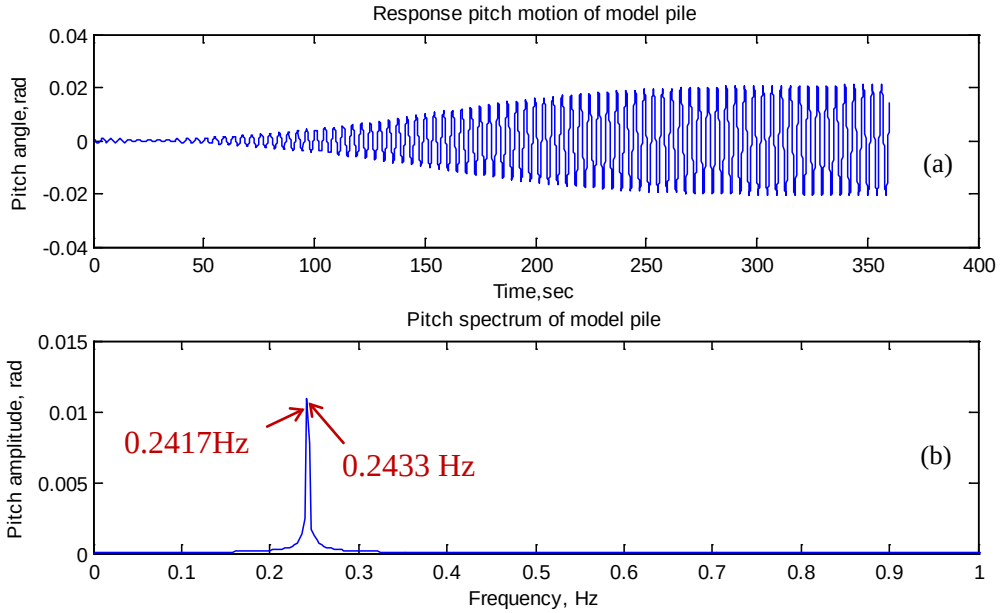

Fig. 84. The heave induced pitch motion at heave excitation frequency f = 0.485 Hz for the PS valves opening model: (a) Pitch angle of the model pile; (b) Pitch spectrum of the model pile.

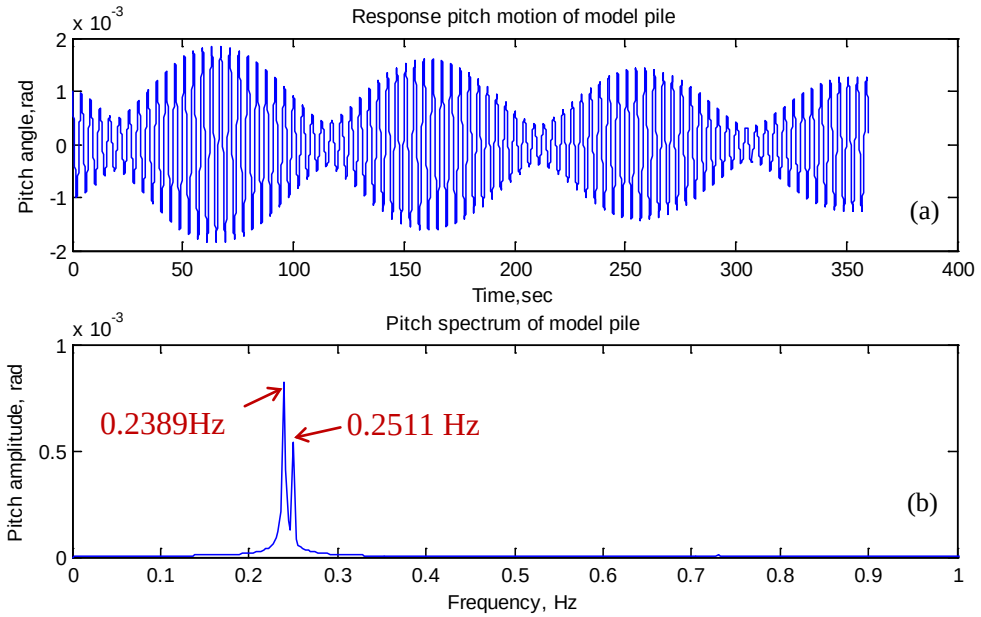

Fig. 85. The heave induced pitch motion at heave excitation frequency f = 0.490 Hz for the PS valves opening model: (a) Pitch angle of the model pile; (b) Pitch spectrum of the model pile.

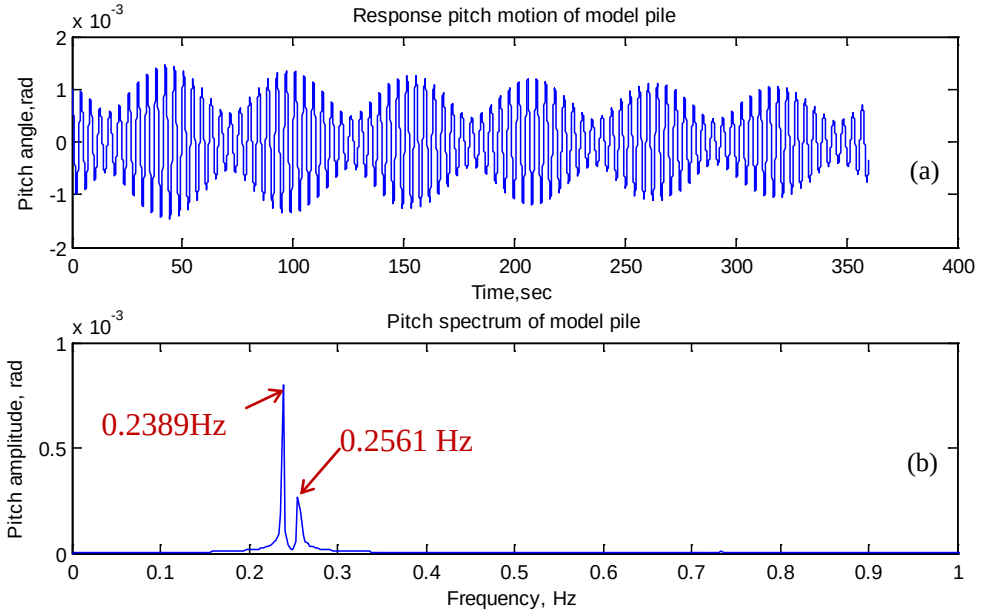

Fig. 86. The heave induced pitch motion at heave excitation frequency f = 0.495 Hz for the PS valves opening model: (a) Pitch angle of the model pile; (b) Pitch spectrum of the model pile.

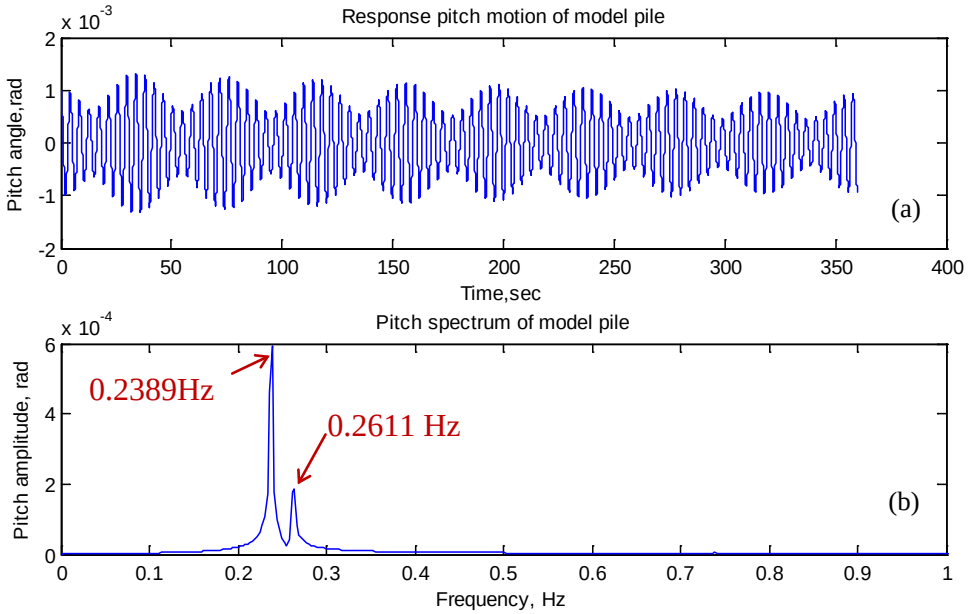

Fig. 87. The heave induced pitch motion at heave excitation frequency f = 0.500 Hz for the PS valves opening model: (a) Pitch angle of the model pile; (b) Pitch spectrum of the model pile.

5.4 Comparison of the Open End Model

5.4.1 Comparison of the heave motion

The specific parameters for the open end model are listed in Table 19. The comparisons between the simulations and measurements in time domain in four cases are given in Fig. 88 to Fig. 91. That is, the heave excitation frequency is a) far below the heave resonance frequency; b) far above the heave resonance frequency; c) and d) close to the heave resonance frequency. The comparisons are given in the time span [90, 100] sec. For the results from the decoupled motion scheme is quite close to those of the coupled motion scheme, we drop out the results of the decoupled pitch scheme and focus

on the comparisons between the simulations using the coupled motion scheme with the measurements for the open end model.

Table 19. Open end model parameters for numerical simulations.

Model parameters	Notation	Value	Note
Length	L	3 ft (0.914 m)	
Outer diameter	D	6 in (15.24 cm)	
Wall thickness	t	0.25 in (0.64 cm)	
Opening area ratio	γ	100.00%	Perforation for the top cap
Normal added-mass coef.	$C_{a,n}$	1.2	
Normal drag coef.	$C_{d,n}$	1.0	
Axial added-mass coef.	$C_{a,t}$	0.07	From model test
Axial drag coef.	$C_{d,t}$	2.5	
Coef. of pitch damping term	$C_{D\beta}$	9.8236	Refer to Appendix B
Weight in air	W	14.5 lb (64.499 N)	
Weight in water	W'	8.5 lb (37.810 N)	
Weight of water inside pile plus water displaced by pile	W_0	36.8 lb (163.695 N)	
Buoyancy	F_B	6.8646 lb (30.535 N)	
Moment of inertia in air	$I_{\beta p}$	1.6416 slug·ft^2 (2.226 kg/m^2)	Refer to Appendix B
Added moment of inertia in water	$I_{\beta a}$	4.1176 slug·ft^2 (5.583 kg/m^2)	Refer to Appendix B
Moment of inertia in water	I_{β}	5.7592 slug·ft^2 (7.808 kg/m^2)	
Gravity center from eye bolt	$O'G$	1.79 ft (0.546 m)	Including hanging bar height 6"
Buoyancy center from eye bolt	$O'B$	2.00 ft (0.610 m)	Including hanging bar height 6"
Heave natural frequency	f_n	0.9000 Hz	From model test
Pitch natural frequency	f_p	0.2460 Hz	Hand calculation

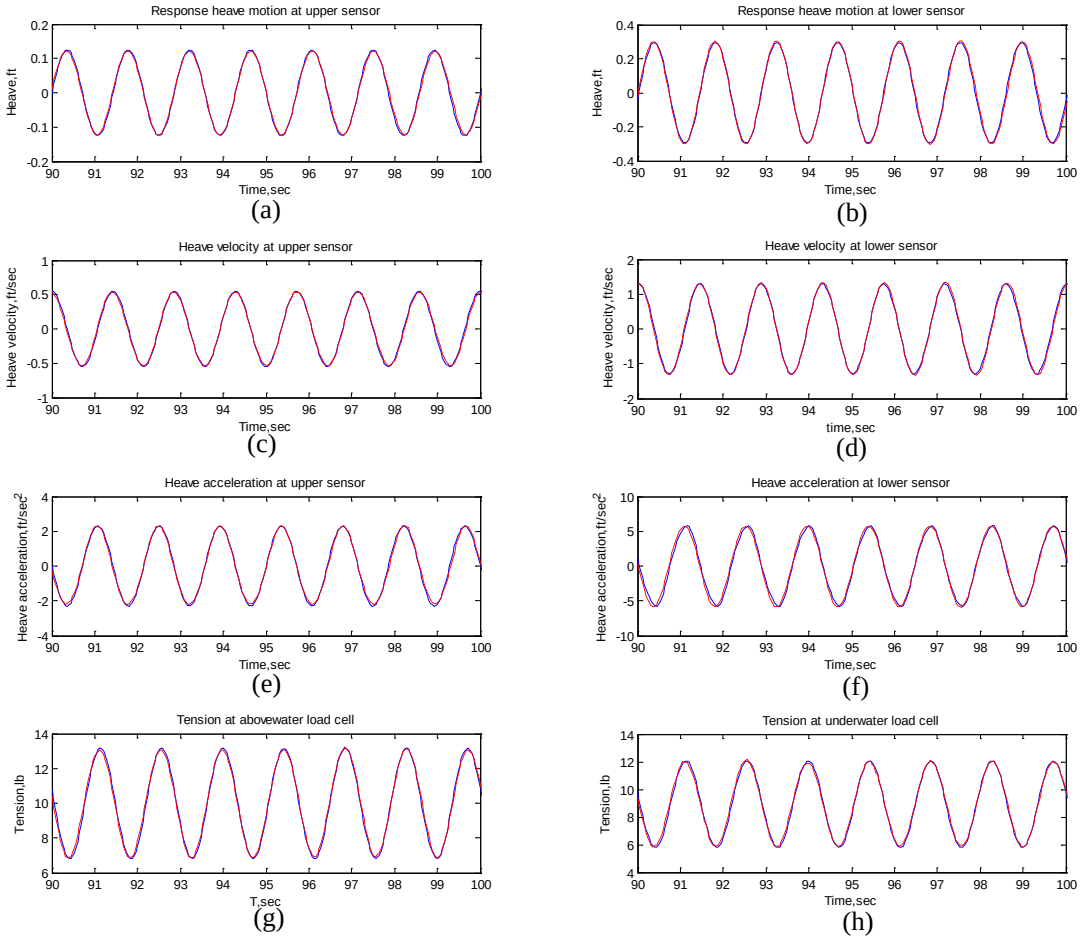

Fig. 88. Time domain comparisons of results from heave-pitch coupled motion scheme $(-)$ with the measurements of model tests $(-\cdot-)$ for the open end model at excitation frequency far below resonance (f = 0.700 Hz, $C_{a,t}$ =0.07, $C_{d,t}$ =2.5).

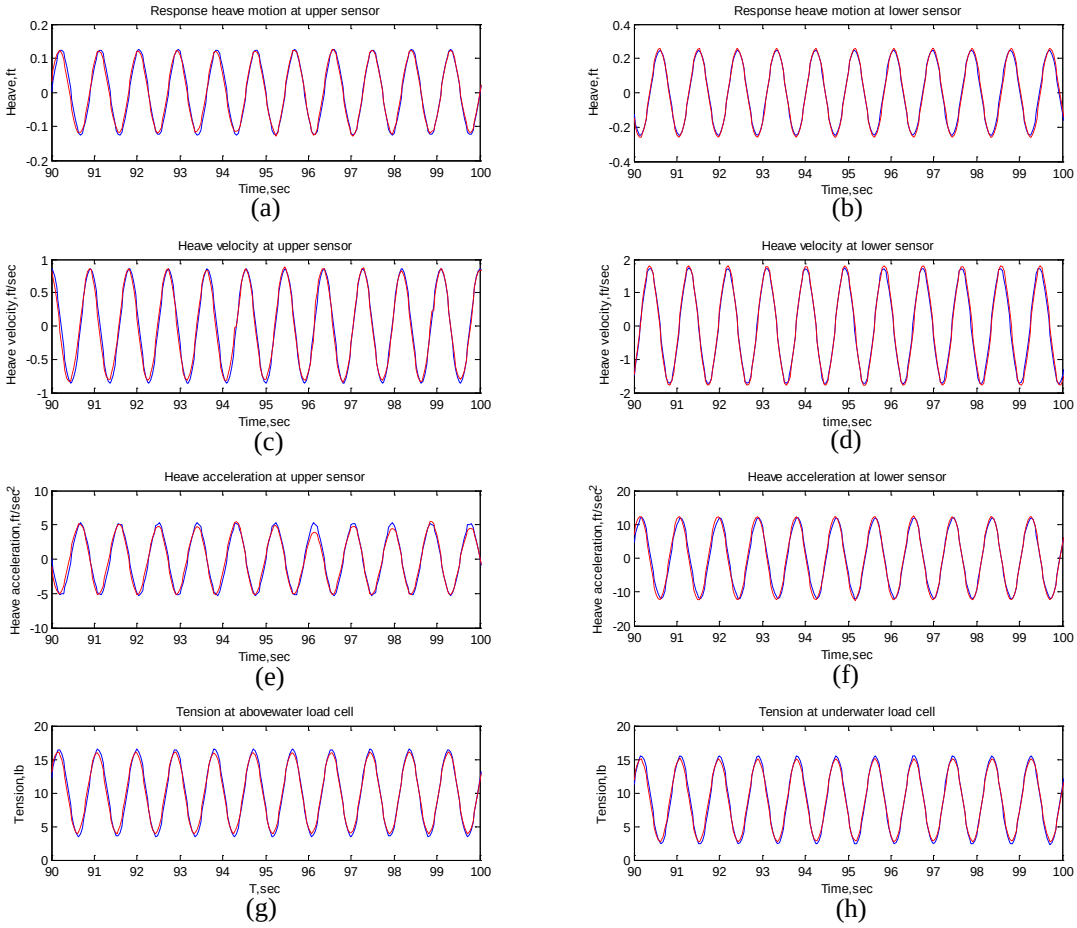

Fig. 89. Time domain comparisons of results from heave-pitch coupled motion scheme (–) with the measurements of model tests (- · -) for the open end model at excitation frequency far above resonance (f = 1.100 Hz, $C_{a,t}$ =0.07, $C_{d,t}$ =2.5).

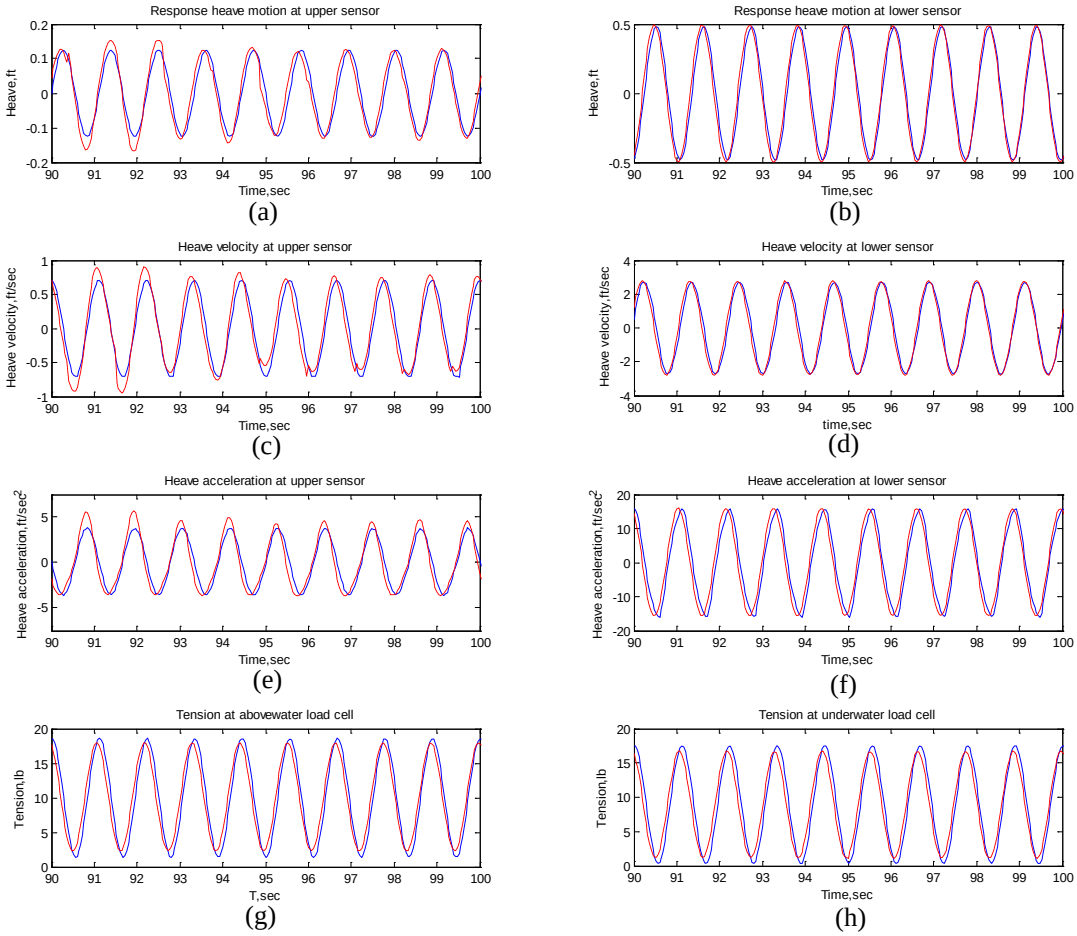

Fig. 90. Time domain comparisons of results from heave-pitch coupled motion scheme $(-)$ with the measurements of model tests $(-\cdot-)$ for the open end model at excitation frequency near above resonance (f = 0.900 Hz, $C_{a,t}$ =0.07, $C_{d,t}$ =2.5).

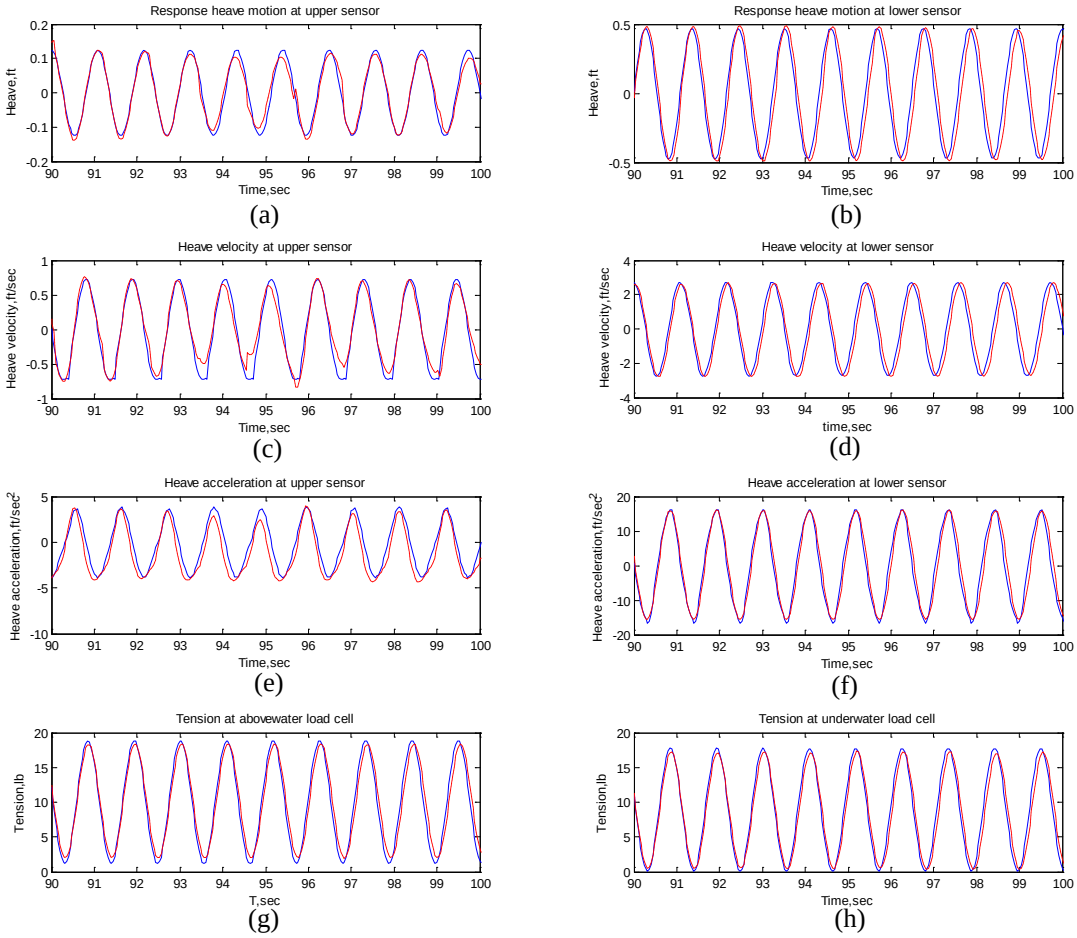

Fig. 91. Time domain comparisons of results from heave-pitch coupled motion scheme $(-)$ with the measurements of model tests $(-\cdot-)$ for the open end model at excitation frequency near above resonance (f = 0.925 Hz, $C_{a,t}$ =0.07, $C_{d,t}$ =2.5).

The dynamics of the open end model is different from the closed end model and the PS valves opening model, and the results in Fig. 88 to Fig. 91 show the different characteristics with those of the closed end model and the PS valves opening model in the near resonance cases. The slackening of cables/spring is not as remarkable as the closed end model and the PS valves opening model, and even no double peak occur in the near above resonance cases. Fig. 92 presents the searching of the axial drag coefficient for the heave motion of the open end model, and the axial drag coefficient for this case is roughly determined as $C_{d,t}$=2.5. Table 20 presents the time domain results for the heave-pitch coupled motion ($C_{a,t}$=0.07, $C_{d,t}$=2.5) for the open end model.

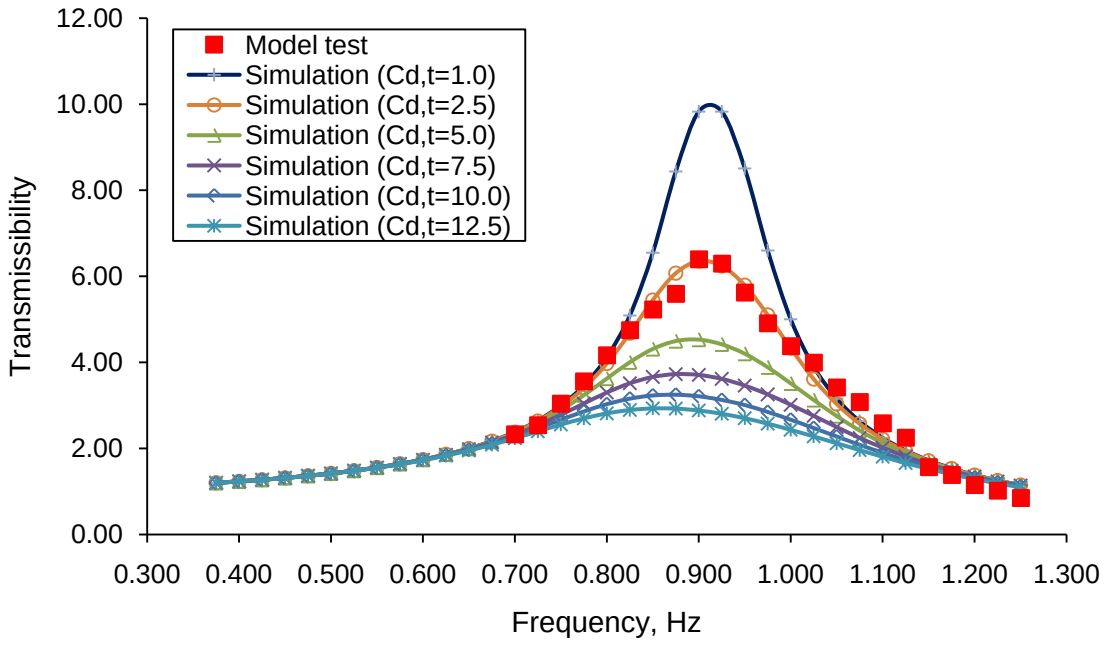

Fig. 92. Matching the heave amplitude transmissibility curves from the model tests by the simulations with different drag coefficients (heave-pitch coupling, $C_{a,t}$ = 0.07) for the open end model pile.

Table 20. Numerical results of heave motion for the open end model simulations using the heave-pitch coupling scheme ($C_{a,t}$=0.07, $C_{d,t}$=2.5).

f (Hz)	ST1 (lb)	ST2 (lb)	ST2/ST1	SD3 (ft)	SD2 (ft)	SD2/SD3	SD2/SD1	SD3/SD1
0.3750	0.9494	0.9289	0.9784	0.2503	0.3001	1.1990	1.2004	1.0012
0.4000	1.1006	1.0785	0.9799	0.2502	0.3086	1.2334	1.2344	1.0008
0.4250	1.2783	1.2524	0.9797	0.2503	0.3182	1.2713	1.2728	1.0012
0.4500	1.4831	1.4520	0.9790	0.2504	0.3291	1.3143	1.3164	1.0016
0.4750	1.7122	1.6789	0.9805	0.2504	0.3414	1.3634	1.3656	1.0016
0.5000	1.9679	1.9315	0.9815	0.2504	0.3554	1.4193	1.4216	1.0016
0.5250	2.2669	2.2270	0.9824	0.2505	0.3715	1.4830	1.4860	1.0020
0.5500	2.6089	2.5634	0.9826	0.2506	0.3900	1.5563	1.5600	1.0024
0.5750	3.0011	2.9531	0.9840	0.2506	0.4114	1.6417	1.6456	1.0024
0.6000	3.4612	3.4103	0.9853	0.2506	0.4364	1.7414	1.7456	1.0024
0.6250	3.9887	3.9340	0.9863	0.2502	0.4657	1.8613	1.8628	1.0008
0.6500	4.6266	4.5667	0.9870	0.2508	0.5012	1.9984	2.0048	1.0032
0.6750	5.3826	5.3111	0.9867	0.2508	0.5433	2.1663	2.1732	1.0032
0.7000	6.2677	6.1919	0.9879	0.2509	0.5962	2.3762	2.3848	1.0036
0.7250	7.2729	7.2097	0.9913	0.2510	0.6618	2.6367	2.6472	1.0040
0.7500	8.4900	8.4076	0.9903	0.2510	0.7458	2.9713	2.9832	1.0040
0.7750	9.7395	9.6665	0.9925	0.2512	0.8548	3.4029	3.4192	1.0048
0.8000	11.0175	10.9676	0.9955	0.2511	0.9972	3.9713	3.9888	1.0044
0.8250	12.2709	12.2160	0.9955	0.2513	1.1760	4.6797	4.7040	1.0052
0.8500	13.3498	13.3019	0.9964	0.2514	1.3701	5.4499	5.4804	1.0056
0.8750	14.2709	14.2244	0.9967	0.2515	1.5271	6.0720	6.1084	1.0060
0.9000	16.8959	16.8745	0.9986	0.2516	1.5988	6.3545	6.3952	1.0064
0.9250	16.2133	16.2315	1.0012	0.2515	1.5695	6.2406	6.2780	1.0060
0.9500	15.3824	15.4072	1.0016	0.2516	1.4578	5.7941	5.8312	1.0064
0.9750	15.3077	15.3446	1.0024	0.2518	1.2852	5.1041	5.1408	1.0072
1.0000	14.9900	15.0448	1.0037	0.2511	1.0879	4.3325	4.3516	1.0044
1.0250	14.5719	14.6520	1.0055	0.2524	0.9116	3.6117	3.6464	1.0096
1.0500	14.0096	14.1109	1.0072	0.2519	0.7641	3.0333	3.0564	1.0076
1.0750	13.3844	13.4934	1.0081	0.2523	0.6487	2.5711	2.5948	1.0092
1.1000	12.7221	12.8408	1.0093	0.2524	0.5592	2.2155	2.2368	1.0096
1.1250	12.0439	12.1782	1.0111	0.2525	0.4887	1.9354	1.9548	1.0100
1.1500	11.4415	11.5763	1.0118	0.2525	0.4324	1.7125	1.7296	1.0100
1.1750	10.8674	11.0183	1.0139	0.2525	0.3866	1.5311	1.5464	1.0100
1.2000	10.3414	10.5131	1.0166	0.2525	0.3487	1.3810	1.3948	1.0100
1.2250	9.8851	10.0593	1.0176	0.2528	0.3168	1.2532	1.2672	1.0112
1.2500	9.4502	9.6332	1.0194	0.2510	0.2885	1.1494	1.1540	1.0040

5.3.2 Comparison of the heave induced pitch motion

Table 21 summarizes the numerical results for the heave induced pitch motion for the open end model simulations ($C_{a,t}$ =0.07, $C_{d,t}$ =2.5) based on the heave-pitch coupled motion scheme, and each columns have the same meaning as presented in the closed end model simulation. Fig. 93 shows satisfactory agreement in the comparison between the simulated pitch amplitude with measured pitch amplitude for the open end model. Compared with the results of the heave induced pitch motion for the closed end model, the heave excitation frequency range for the heave induced pitch amplification is greatly narrowed to a very small region (0.475~0.480 Hz). The reason for this is due to the heave natural frequency is far above the twice of the pitch natural frequency for the open end model, and the heave amplitude of the model pile is relatively small when the excitation frequency is approaching one half of the pitch natural frequency. Since the value γ in Eqn. (3.63) is quite close to zero, thus, the primary unstable region governed by the damped Mathieu equation is relatively narrow, as shown in Fig. 41.

Table 21. Numerical results of heave induced pitch motion for the open end model simulations using the heave-pitch coupling scheme ($C_{a,t}$=0.07, $C_{d,t}$=2.5).

f (Hz)	f_β (Hz)	$f - f_\beta$ (Hz)	f_β/f	Pitch amplitude (rad)	β_{video} (rad)	β_{error} (rad)
0.3750	0.2389	0.1361	0.6371	0.0007	-	-
0.4000	0.2389	0.1611	0.5973	0.0007	-	-
0.4250	0.2389	0.1861	0.5621	0.0008	-	-
0.4500	0.2389	0.2111	0.5309	0.0008	-	-
0.4550	0.2389	0.2161	0.5251	0.0009	-	-
0.4600	0.2389	0.2211	0.5193	0.0011	-	-
0.4650	0.2389	0.2261	0.5138	0.0009	-	-
0.4700	0.2389	0.2311	0.5083	0.0013	-	-
0.4750	0.2389	0.2361	0.5029	0.0055	-	-
0.4800	0.2389	0.2411	0.4977	0.0101	-	-
0.4850	0.2389	0.2461	0.4926	0.0014	-	-
0.4900	0.2389	0.2511	0.4876	0.0009	-	-
0.4950	0.2389	0.2561	0.4826	0.0011	-	-
0.5000	0.2389	0.2611	0.4778	0.0008	-	-
0.5250	0.2389	0.2861	0.4550	0.0008	-	-
0.5500	0.2389	0.3111	0.4344	0.0007	-	-
0.5750	0.2389	0.3361	0.4155	0.0007	-	-
0.6000	0.2389	0.3611	0.3982	0.0007	-	-
0.6250	0.2389	0.3861	0.3822	0.0007	-	-
0.6500	0.2389	0.4111	0.3675	0.0007	-	-
0.6750	0.2389	0.4361	0.3539	0.0007	-	-
0.7000	0.2389	0.4611	0.3413	0.0007	-	-
0.7250	0.2389	0.4861	0.3295	0.0007	-	-
0.7500	0.2389	0.5111	0.3185	0.0007	0.0017	0.0017
0.7750	0.2389	0.5361	0.3083	0.0007	-	-
0.8000	0.2389	0.5611	0.2986	0.0007	-	-
0.8250	0.2389	0.5861	0.2896	0.0007	-	-
0.8500	0.2389	0.6111	0.2811	0.0007	-	-
0.8750	0.2389	0.6361	0.2730	0.0007	-	-
0.9000	0.2389	0.6611	0.2654	0.0007	0.0017	0.0017
0.9250	0.2389	0.6861	0.2583	0.0007	-	-
0.9500	0.2389	0.7111	0.2515	0.0007	-	-
0.9750	0.2389	0.7361	0.2450	0.0007	-	-
1.0000	0.2389	0.7611	0.2389	0.0007	-	-
1.0250	0.2389	0.7861	0.2331	0.0007	-	-
1.0500	0.2389	0.8111	0.2275	0.0007	-	-
1.0750	0.2389	0.8361	0.2222	0.0007	-	-
1.1000	0.2389	0.8611	0.2172	0.0007	0.0017	0.0017
1.1250	0.2389	0.8861	0.2124	0.0007	-	-
1.1500	0.2389	0.9111	0.2077	0.0007	-	-
1.1750	0.2389	0.9361	0.2033	0.0007	-	-
1.2000	0.2389	0.9611	0.1991	0.0007	-	-
1.2250	0.2389	0.9861	0.1950	0.0007	-	-
1.2500	0.2389	1.0111	0.1911	0.0007	-	-

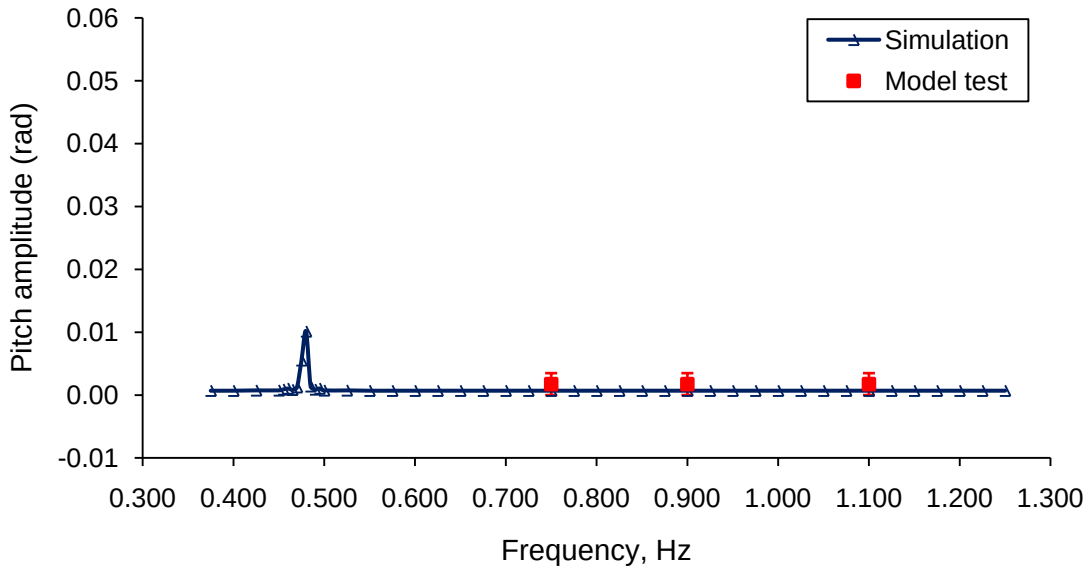

Fig. 93. Comparison of pitch amplitudes of the open end model pile between simulations (heave-pitch coupling, $C_{a,t}$ =0.07, $C_{d,t}$ =2.5) and model tests.

Fig. 94 and Fig. 95 show the simulated pitch in time domain and frequency domain at the heave excitation frequency f = 0.475 Hz and f = 0.480 Hz for the case of the open end model simulations ($C_{a,t}$ =0.07, $C_{d,t}$ =2.5). From these figures, we know that it takes relatively longer time duration for the heave induced pitch motion to reach the steady state and the final pitch amplitude is also relatively small.

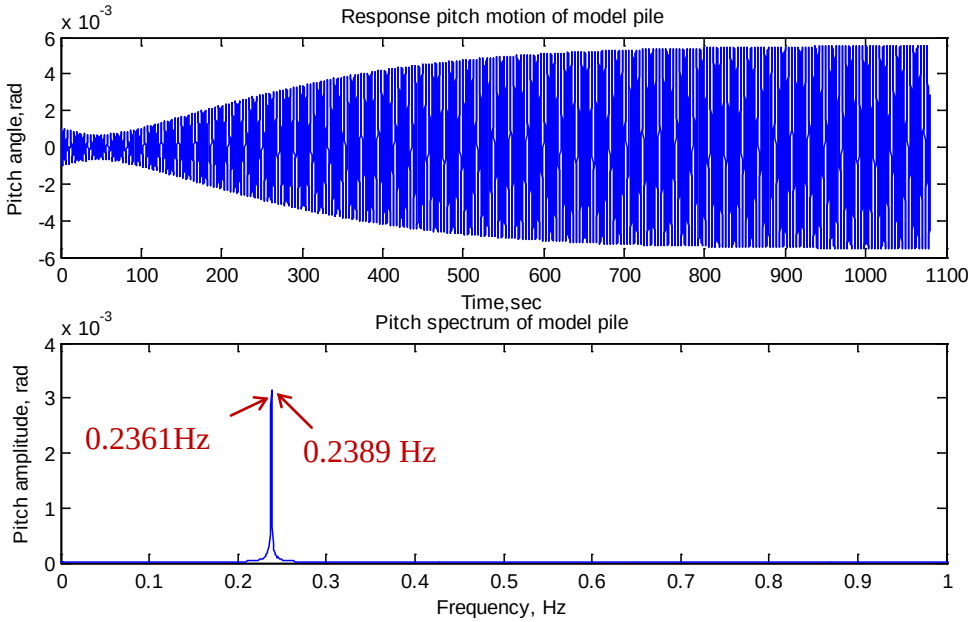

Fig. 94. The heave induced pitch motion at heave excitation frequency f = 0.475 Hz for the open end model: (a) Pitch angle of the model pile; (b) Pitch spectrum of the model pile.

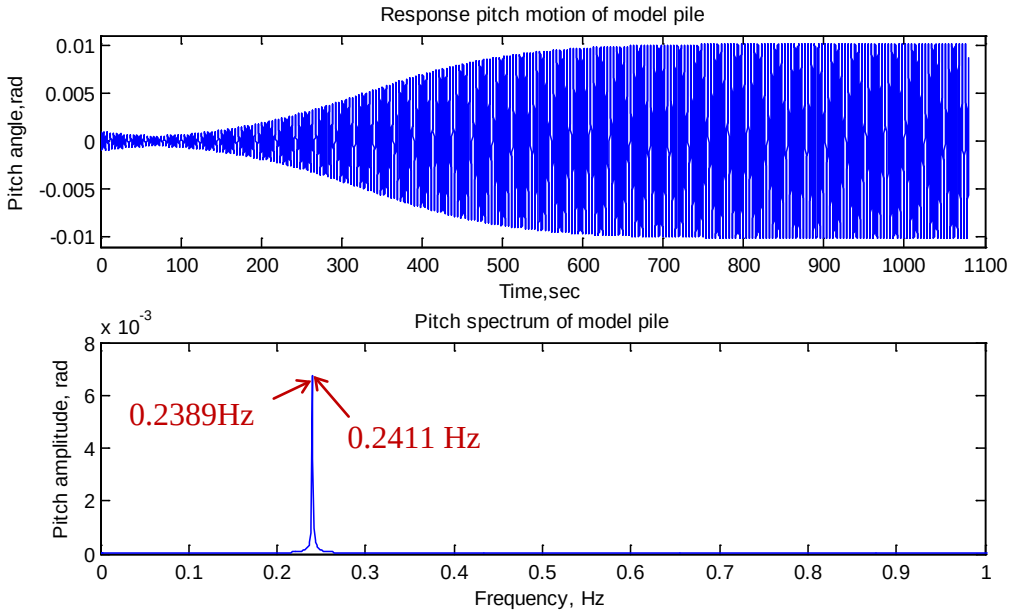

Fig. 95. The heave induced pitch motion at heave excitation frequency f = 0.480 Hz for the open end model: (a) Pitch angle of the model pile; (b) Pitch spectrum of the model pile.

5.5 Comparison of the #4 Valves Opening Model

5.5.1 Comparison of the heave motion

The specific parameters for the #4 opening model are listed in Table 22. For brevity, we drop out the comparisons of the simulations and measurements in time domain for the #4 opening model.

Table 22. # 4 valves opening model parameters for numerical simulations.

Model parameters	Notation	Value	Note
Length	L	3 ft (0.914 m)	
Outer diameter	D	6 in (15.24 cm)	
Wall thickness	t	0.25 in (0.64 cm)	
Opening area ratio (Perforation)	γ	14.90%	For the top cap
Normal added-mass coef.	$C_{a,n}$	1.2	
Normal drag coef.	$C_{d,n}$	1.0	
Axial added-mass coef.	$C_{a,t}$	0.84	From model test
Axial drag coef.	$C_{d,t}$	7.5	
Coef. of pitch damping term	$C_{D\beta}$	9.8236	Refer to Appendix B
Weight in air	W	16.0 lb (71.172 N)	
Weight in water	W'	9.6 lb (42.703 N)	
Weight of water inside pile plus water displaced by pile	W_0	36.8 lb (163.695 N)	
Buoyancy	F_B	6.729 lb (29.932 N)	
Moment of inertia in air	$I_{\beta p}$	1.5780 slug·ft^2 (2.139 kg/m^2)	Refer to Appendix B
Added moment of inertia in water	$I_{\beta a}$	4.1176 slug·ft^2 (5.583 kg/m^2)	Refer to Appendix B
Moment of inertia in water	I_{β}	5.6956 slug·ft^2 (7.722 kg/m^2)	
Gravity center from eye bolt	$O'G$	1.44 ft (0.439 m)	Including hanging bar height 2"
Buoyancy center from eye bolt	$O'B$	1.57 ft (0.479 m)	Including hanging bar height 2"
Heave natural frequency	f_n	0.5550 Hz	From model test
Pitch natural frequency	f_p	0.2400 Hz	Hand calculation

Table 23. Numerical results of heave motion for the # 4 valves opening model using the heave-pitch coupling scheme ($C_{a,t}$=0.84, $C_{d,t}$=7.5).

f (Hz)	ST1 (lb)	ST2 (lb)	ST2/ST1	SD3 (ft)	SD2 (ft)	SD2/SD3	SD2/SD1	SD3/SD1
0.3750	3.7012	3.6793	0.9941	0.2504	0.4492	1.7935	1.7968	1.0016
0.4000	4.7101	4.6884	0.9954	0.2505	0.5014	2.0021	2.0056	1.0020
0.4250	6.0580	6.0328	0.9958	0.2506	0.5684	2.2685	2.2736	1.0024
0.4500	7.8172	7.7962	0.9973	0.2506	0.6508	2.5966	2.6032	1.0024
0.4750	9.9929	9.9711	0.9978	0.2507	0.7409	2.9553	2.9636	1.0028
0.5000	12.2861	12.2766	0.9992	0.2507	0.8173	3.2601	3.2692	1.0028
0.5250	14.2738	14.2645	0.9993	0.2508	0.8577	3.4197	3.4308	1.0032
0.5500	15.5870	15.5855	0.9999	0.2509	0.8544	3.4056	3.4176	1.0036
0.5750	16.1373	16.1484	1.0007	0.2509	0.8133	3.2418	3.2532	1.0036
0.6000	15.9537	15.9789	1.0016	0.2509	0.7445	2.9671	2.9780	1.0036
0.6250	15.1576	15.1929	1.0023	0.2506	0.6595	2.6319	2.6380	1.0024
0.6500	14.1282	14.1510	1.0016	0.2513	0.5699	2.2684	2.2796	1.0052
0.6750	12.8893	12.9388	1.0038	0.2512	0.4863	1.9355	1.9452	1.0048
0.7000	11.7579	11.8132	1.0047	0.2514	0.4145	1.6487	1.6580	1.0056
0.7250	10.7777	10.8406	1.0058	0.2515	0.3556	1.4138	1.4224	1.0060
0.7500	9.9666	10.0369	1.0071	0.2516	0.3081	1.2245	1.2324	1.0064
0.7750	9.3044	9.3783	1.0079	0.2518	0.2698	1.0716	1.0792	1.0072
0.8000	8.7559	8.8343	1.0090	0.2519	0.2388	0.9480	0.9552	1.0076
0.8250	8.3195	8.3860	1.0080	0.2520	0.2132	0.8458	0.8528	1.0080

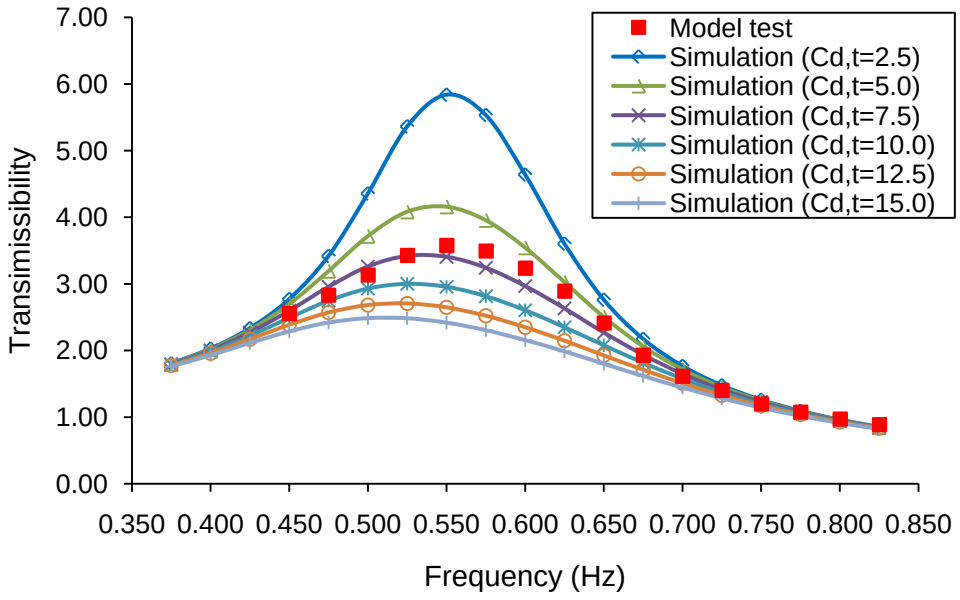

Fig. 96. Matching the heave amplitude transmissibility curves from the model tests by the simulations with different drag coefficients (heave-pitch coupling, $C_{a,t}$=0.84) for the #4 valves opening model pile.

The dynamics of the #4 opening model is different from the closed end model and the PS valves opening model. The slackening of cables/spring is not observed at all, and the damping effect due to the exchanging flow through the valves and vortices shed from the oscillation pile prohibited the heave motion of model pile. Fig. 96 presents the searching of the axial drag coefficient for the heave motion of the #4 opening model, and the axial drag coefficient for this case is roughly determined as $C_{d,t}$ =7.5. Table 23 presents the numerical results for the heave-pitch coupled motion ($C_{a,t}$ =0.84, $C_{d,t}$ =7.5) for the #4 opening model.

5.5.2 Comparison of the heave induced pitch motion

Table 24 summarizes the time domain results for the heave induced pitch motion for the #4 valves opening model simulations ($C_{a,t}$ =0.84, $C_{d,t}$ =7.5) based on the heave-pitch coupled motion scheme, and each columns have the same meaning as presented in the closed end model simulation. Fig. 97 shows satisfactory agreement in the comparison between the simulated pitch amplitude with measured pitch amplitude for the #4 valves opening model. Compared with the results of the heave induced pitch motion for the closed end model and the, the heave excitation frequency range for the heave induced pitch amplification is greatly narrowed to a very small region (0.465~0.475 Hz). Although the heave natural frequency is near above the twice of the pitch natural frequency for the #4 valves opening model, the heave amplitude of the model pile is relatively small due to a large heave damping when the heave excitation frequency is approaching one half of the pitch natural frequency. Since the value γ in Eqn. (3.63) is

quite close to zero, thus, the primary unstable region governed by the damped Mathieu equation is relatively narrow, as shown in Fig. 41. Note that the primary unstable region is less effected by the pitch damping coefficient μ in Eqn. (3.63), as discussed in the Chapter III.

Table 24. Numerical results of heave induced pitch motion for the #4 valves opening model simulations using the heave-pitch coupling scheme ($C_{a,t}$=0.84, $C_{d,t}$=7.5).

f (Hz)	f_β (Hz)	$f - f_\beta$ (Hz)	f_β/f	Pitch amplitude (rad)	β_{video} (rad)	β_{error} (rad)
0.3750	0.2333	0.1417	0.6221	0.0007	-	-
0.4000	0.2333	0.1667	0.5833	0.0008	-	-
0.4250	0.2333	0.1917	0.5489	0.0008	-	-
0.4500	0.2333	0.2167	0.5184	0.0008	-	-
0.4550	0.2333	0.2217	0.5127	0.0009	-	-
0.4600	0.2306	0.2294	0.5013	0.0015	-	-
0.4650	0.2333	0.2317	0.5017	0.0190	-	-
0.4700	0.2361	0.2339	0.5023	0.0200	-	-
0.4750	0.2361	0.2389	0.4971	0.0112	0.0175	0.0087
0.4800	0.2361	0.2439	0.4919	0.0005	-	-
0.4850	0.2361	0.2489	0.4868	0.0005	-	-
0.4900	0.2361	0.2539	0.4818	0.0006	-	-
0.4950	0.2333	0.2617	0.4713	0.0008	-	-
0.5000	0.2333	0.2667	0.4666	0.0008	-	-
0.5250	0.2333	0.2917	0.4444	0.0008	-	-
0.5500	0.2333	0.3167	0.4242	0.0008	0.0017	0.0017
0.5750	0.2333	0.3417	0.4057	0.0007	-	-
0.6000	0.2333	0.3667	0.3888	0.0007	-	-
0.6250	0.2333	0.3917	0.3733	0.0007	-	-
0.6500	0.2333	0.4167	0.3589	0.0007	-	-
0.6750	0.2333	0.4417	0.3456	0.0007	-	-
0.7000	0.2333	0.4667	0.3333	0.0007	0.0017	0.0017
0.7250	0.2333	0.4917	0.3218	0.0007	-	-
0.7500	0.2333	0.5167	0.3111	0.0007	-	-
0.7750	0.2333	0.5417	0.3010	0.0007	-	-
0.8000	0.2333	0.5667	0.2916	0.0007	-	-
0.8250	0.2333	0.5917	0.2828	0.0007	-	-

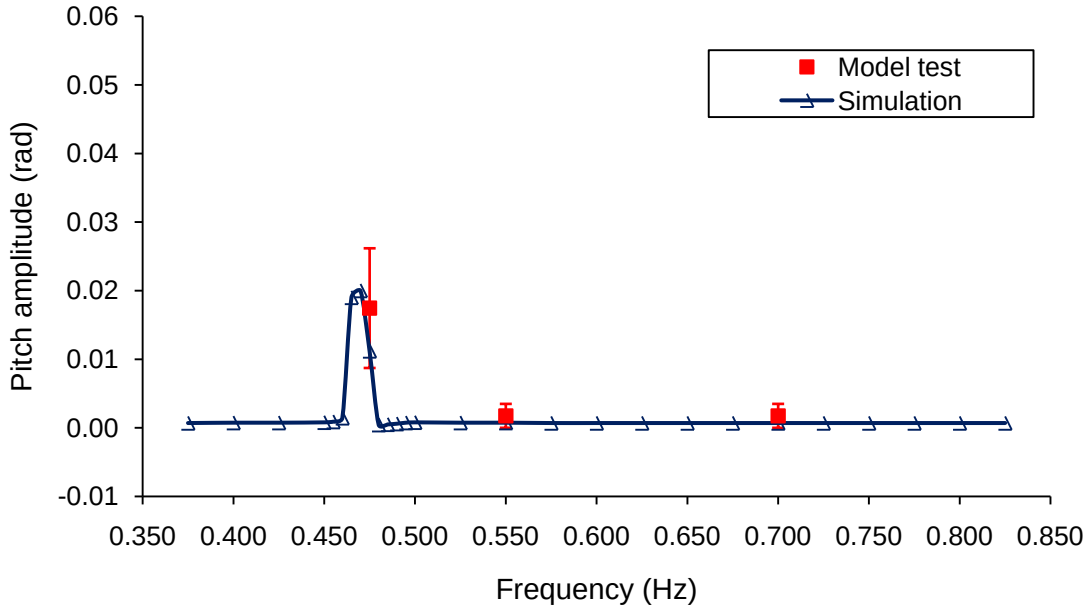

Fig. 97. Comparison of pitch amplitudes of the #4 valves opening model pile between simulations (heave-pitch coupling, $C_{a,t}$=0.84, $C_{d,t}$=7.5) and model tests.

5.6 Comparison of the #1, #2, #3, #4 Valves Opening Model

5.6.1 Comparison of the heave motion

The specific parameters for the #1, #2, #3, #4 opening model are listed in Table 25. For brevity, we drop out the comparisons of the simulations and measurements in time domain for the #1, #2, #3, #4 opening model.

Table 25. #1, #2, #3, #4 valves opening model parameters for numerical simulations.

Model parameters	Notation	Value	Note
Length	L	3 ft (0.914 m)	
Outer diameter	D	6 in (15.24 cm)	
Wall thickness	t	0.25 in (0.64 cm)	
Opening area ratio (Perforation)	γ	32.70%	For the top cap
Normal added-mass coef.	$C_{a,n}$	1.2	
Normal drag coef.	$C_{d,n}$	1.0	
Axial added-mass coef.	$C_{a,t}$	0.33	From model test
Axial drag coef.	$C_{d,t}$	7.5	
Coef. of pitch damping term	$C_{D\beta}$	9.8236	Refer to Appendix B
Weight in air	W	16.0 lb (71.172 N)	
Weight in water	W'	9.6 lb (42.703 N)	
Weight of water inside pile plus water displaced by pile	W_0	36.8 lb (163.695 N)	
Buoyancy	F_B	6.729 lb (29.932 N)	
Moment of inertia in air	$I_{\beta p}$	1.5780 slug·ft^2 (2.139 kg/m^2)	Refer to Appendix B
Added moment of inertia in water	$I_{\beta a}$	4.1176 slug·ft^2 (5.583 kg/m^2)	Refer to Appendix B
Moment of inertia in water	I_{β}	5.6956 slug·ft^2 (7.722 kg/m^2)	
Gravity center from eye bolt	$O'G$	1.44 ft (0.439 m)	Including hanging bar height 2"
Buoyancy center from eye bolt	$O'B$	1.57 ft (0.479 m)	Including hanging bar height 2"
Heave natural frequency	f_n	0.7100 Hz	From model test
Pitch natural frequency	f_p	0.2400 Hz	Hand calculation

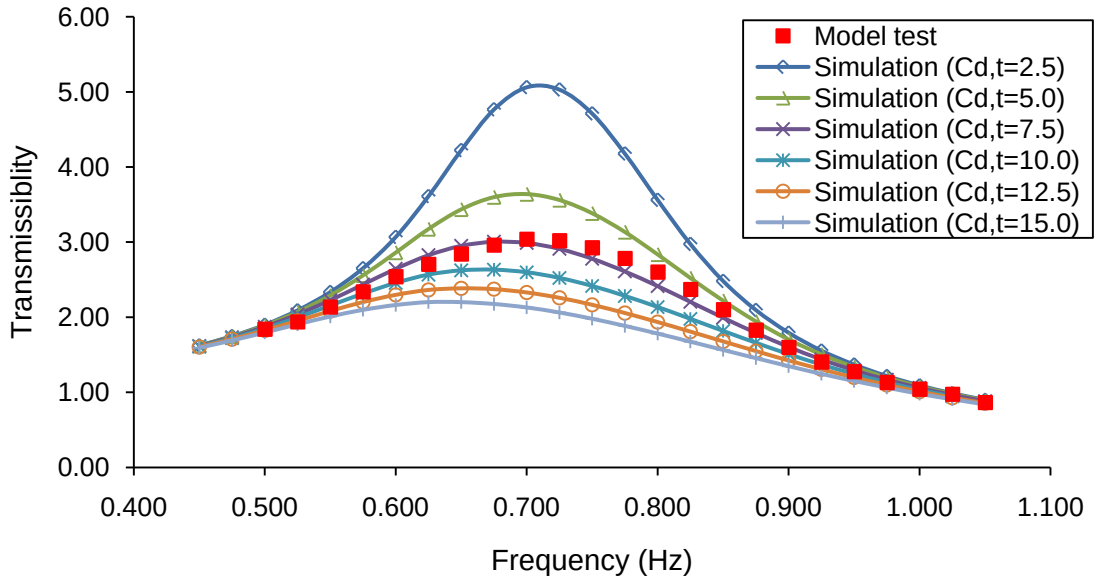

Fig. 98. Matching the heave amplitude transmissibility curves from the model tests by the simulations with different drag coefficients (heave-pitch coupling, $C_{a,t}$=0.33) for the #1, #2, #3, #4 valves opening model pile.

The dynamics of the #1, #2, #3, #4 opening model is different from the closed end model and the PS valves opening model. The slackening of cables/spring is not observed at all, and the damping effect due to the exchanging flow through the valves and vortices shed from the oscillation pile prohibited the heave motion of model pile. Fig. 98 presents the searching of the axial drag coefficient for the heave motion of the #1, #2, #3, #4 opening model, and The axial drag coefficient for this case is roughly determined as $C_{d,t}$ =7.5. Table 26 presents the time domain results for the heave-pitch coupled motion ($C_{a,t}$ =0.33, $C_{d,t}$ =7.5) for the #1, #2, #3, #4 opening model.

Table 26. Numerical results of heave motion for the #1, #2, #3, #4 valves opening model simulations using the heave-pitch coupling scheme ($C_{a,t}$ =0.33, $C_{d,t}$ =7.5).

f (Hz)	ST1 (lb)	ST2 (lb)	ST2/ST1	SD3 (ft)	SD2 (ft)	SD2/SD3	SD2/SD1	SD3/SD1
0.4500	2.9132	2.8807	0.9889	0.2506	0.4050	1.6161	1.6200	1.0024
0.4750	3.4877	3.4516	0.9897	0.2507	0.4345	1.7334	1.7380	1.0028
0.5000	4.1764	4.1377	0.9907	0.2507	0.4693	1.8718	1.8772	1.0028
0.5250	5.0412	4.9996	0.9917	0.2508	0.5110	2.0369	2.0440	1.0032
0.5500	6.0847	6.0404	0.9927	0.2509	0.5588	2.2269	2.2352	1.0036
0.5750	7.2978	7.2650	0.9955	0.2510	0.6113	2.4359	2.4452	1.0040
0.6000	8.7345	8.6846	0.9943	0.2511	0.6642	2.6453	2.6568	1.0044
0.6250	10.1081	10.0766	0.9969	0.2507	0.7086	2.8263	2.8344	1.0028
0.6500	11.4964	11.4725	0.9979	0.2513	0.7416	2.9508	2.9664	1.0052
0.6750	12.6654	12.6421	0.9982	0.2514	0.7554	3.0051	3.0216	1.0056
0.7000	13.5088	13.5086	1.0000	0.2515	0.7518	2.9896	3.0072	1.0060
0.7250	14.0751	14.0648	0.9993	0.2515	0.7320	2.9106	2.9280	1.0060
0.7500	14.3058	14.3086	1.0002	0.2516	0.6994	2.7796	2.7976	1.0064
0.7750	14.2377	14.2686	1.0022	0.2518	0.6571	2.6098	2.6284	1.0072
0.8000	13.9128	13.9714	1.0042	0.2519	0.6081	2.4146	2.4324	1.0076
0.8250	13.4337	13.4929	1.0044	0.2520	0.5556	2.2047	2.2224	1.0080
0.8500	12.8237	12.8860	1.0049	0.2522	0.5027	1.9936	2.0108	1.0088
0.8750	12.1261	12.2077	1.0067	0.2523	0.4520	1.7919	1.8080	1.0092
0.9000	11.4377	11.5299	1.0081	0.2525	0.4053	1.6050	1.6212	1.0100
0.9250	10.7848	10.8818	1.0090	0.2524	0.3630	1.4382	1.4520	1.0096
0.9500	10.2104	10.3055	1.0093	0.2527	0.3270	1.2940	1.3080	1.0108
0.9750	9.6683	9.7818	1.0117	0.2528	0.2951	1.1674	1.1804	1.0112
1.0000	9.1801	9.3045	1.0136	0.2523	0.2672	1.0589	1.0688	1.0092
1.0250	8.7938	8.9207	1.0144	0.2532	0.2439	0.9634	0.9756	1.0128
1.0500	8.4357	8.5697	1.0159	0.2533	0.2233	0.8817	0.8932	1.0132

5.6.2 Comparison of the heave induced pitch motion

Table 27 summarizes the numerical results for the heave induced pitch motion for the #1, #2, #3, #4 valves opening model simulations ($C_{a,t}$ =0.33, $C_{d,t}$ =7.5) based on the heave-pitch coupled motion scheme, and each columns have the same meaning as presented in the closed end model simulation. Fig. 99 shows satisfactory agreement in the comparison between the simulated pitch amplitude with measured pitch amplitude for the #1, #2, #3, #4 valves opening model. Compared with the results of the heave induced pitch motion for the closed end model and the, the heave excitation frequency range for the heave induced pitch amplification is greatly narrowed to a very small region (0.465~0.470 Hz). The heave natural frequency is far above the twice of the pitch natural frequency for the #1, #2, #3, #4 valves opening model, and the heave amplitude of the model pile is seriously damped when the heave excitation frequency is approaching one half of the pitch natural frequency. Since the value γ in Eqn. (3.63) is quite close to zero, thus, the primary unstable region (Fig. 41) governed by the damped Mathieu equation is relatively narrow. Note that the primary unstable region is less effected by the pitch damping coefficient μ in Eqn. (3.63), as discussed in the Chapter III.

Table 27. Numerical results of heave induced pitch motion for the #1, #2, #3, #4 valves opening model simulations using the heave-pitch coupling scheme ($C_{a,t}$=0.33, $C_{d,t}$=7.5).

f (Hz)	f_β (Hz)	$f - f_\beta$ (Hz)	f_β/f	Pitch amplitude (rad)	β_{video} (rad)	β_{error} (rad)
0.4500	0.2333	0.2167	0.5184	0.0007	0.0017	0.0017
0.4550	0.2333	0.2217	0.5127	0.0008	-	-
0.4600	0.2333	0.2267	0.5072	0.0009	-	-
0.4650	0.2333	0.2317	0.5017	0.0020	-	-
0.4700	0.2333	0.2367	0.4964	0.0030	-	-
0.4750	0.2333	0.2417	0.4912	0.0009	-	-
0.4800	0.2333	0.2467	0.4860	0.0009	-	-
0.4850	0.2333	0.2517	0.4810	0.0008	-	-
0.4900	0.2333	0.2567	0.4761	0.0008	-	-
0.4950	0.2333	0.2617	0.4713	0.0008	-	-
0.5000	0.2333	0.2667	0.4666	0.0007	-	-
0.5250	0.2333	0.2917	0.4444	0.0007	-	-
0.5500	0.2333	0.3167	0.4242	0.0007	-	-
0.5750	0.2333	0.3417	0.4057	0.0007	-	-
0.6000	0.2333	0.3667	0.3888	0.0007	-	-
0.6250	0.2333	0.3917	0.3733	0.0007	-	-
0.6500	0.2333	0.4167	0.3589	0.0007	-	-
0.6750	0.2333	0.4417	0.3456	0.0007	-	-
0.7000	0.2333	0.4667	0.3333	0.0007	-	-
0.7250	0.2333	0.4917	0.3218	0.0007	0.0017	0.0017
0.7500	0.2333	0.5167	0.3111	0.0007	-	-
0.7750	0.2333	0.5417	0.3010	0.0007	-	-
0.8000	0.2333	0.5667	0.2916	0.0007	-	-
0.8250	0.2333	0.5917	0.2828	0.0007	-	-
0.8500	0.2333	0.6167	0.2745	0.0007	0.0017	0.0017
0.8750	0.2333	0.6417	0.2666	0.0007	-	-
0.9000	0.2333	0.6667	0.2592	0.0007	-	-
0.9250	0.2333	0.6917	0.2522	0.0007	-	-
0.9500	0.2333	0.7167	0.2456	0.0007	-	-
0.9750	0.2333	0.7417	0.2393	0.0007	-	-
1.0000	0.2333	0.7667	0.2333	0.0007	-	-
1.0250	0.2333	0.7917	0.2276	0.0007	-	-
1.0500	0.2333	0.8167	0.2222	0.0007	-	-

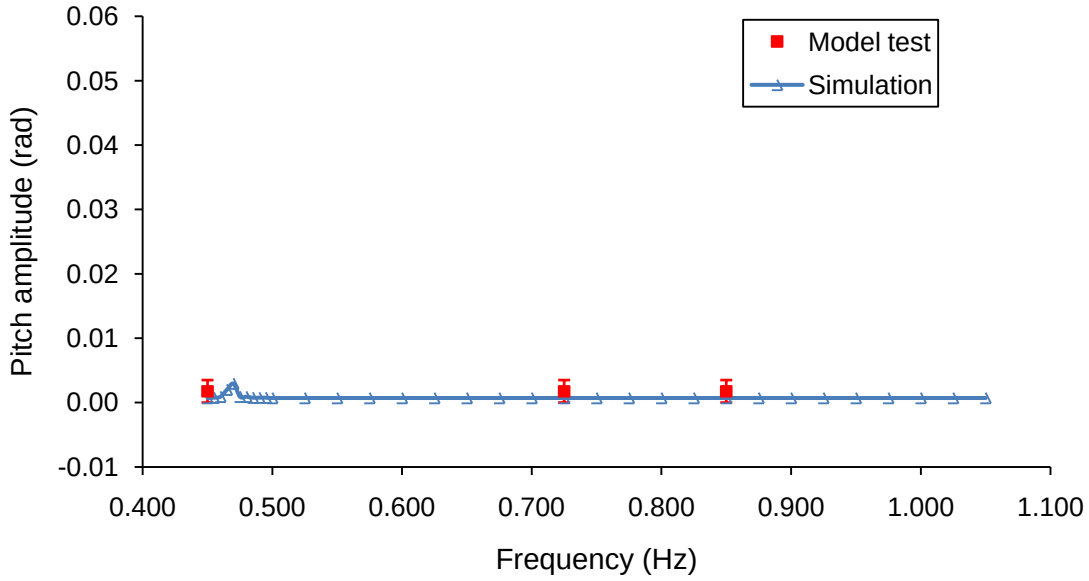

Fig. 99. Comparison of pitch amplitudes of the #1, #2, #3, #4 valves opening model pile between simulations (heave-pitch coupling, $C_{a,t}$ =0.33, $C_{d,t}$ =7.5) and model tests.

CHAPTER VI

CONCLUSIONS AND FUTURE WORK

Based on the experimental, analytic and numerical studies on the dynamics of a suction pile model oscillating in otherwise quiescent water, a few important conclusions have been derived, which may have important implications to the operation of lowering offshore equipments to the seafloor in deep water.

1. The numerical simulations based on the (heave-pitch) coupled motion scheme are in excellent agreement with the related measured heave and pitch and video records of the pile model tests in the range of realistic heave excitation frequencies, including near the related heave natural frequency of a pile-cable system during its lowering operation. The excellent agreement validates the numerical schemes, which in turn helps to understand the physics of lowering a pile-cable system, such as ‘slack’ in the cable and heave induce the pitch resonance.

2. It was observed that water always completely fills the inside of the pile during its oscillation regardless whether or not its cap has openings. However, the amount of water inside the pile cannot completely be accounted as the added mass except for the case of the closed end pile. Due to the openings at the cap, part of the water inside an oscillating pile flows through the openings and hence does not move at the same velocity and acceleration with the pile. The larger the opening ratio is, the more flow passes through the openings and less mass of water inside the pile moves with the pile. Hence, the total added mass of a pile reduces with the increase in the opening ratio of the cap.

Consequently, the natural frequency of a suction pile increases with the increase in the opening ratio. In general, total heave added mass of a pile includes part of water inside the pile as well as water outside the pile. The total added-mass coefficients of a cylindrical pile as a function of the opening ratio at its cap determined in this study are consistent with those recommended by DNV (ref).

3. The water inside a pile flows through the openings when the pile is oscillating, generating vortices above and below the openings at the cap, which increases the water resistance to the heave of the pile. Consequently, the resonance heave amplitudes for the partially open pile models are significantly smaller than those of either open or closed model. However, in order to significantly reduce the resonant heave amplitude the opening ratio has to be greater than 0.15. Increased damping that reduces resonant response would be viewed as a desirable feature when the ratio of the system natural period to the peak excitation period called beta ($\beta = T_n/T_p$) is less than the square root of 2. In the case of lowering relative small mass objects, such as Christmas trees for controlling oil and gas flow an under seafloor well, the natural period is likely in that range.

4. The greatest resonant heave amplitude was observed in the cases of open and closed (PS valve) models when the excitation frequency is closed to the related natural heave frequency. The large heave results in the ‘pushing up’ phenomenon when the pile model pushes up the spring and cable. The ‘pushing up’ by the pile may cause the cable slack and the related stiffness of the cable in its slack phase will be quite different from that of a taut cable, which is known as bi-linear stiffness of the cable.

5. The heave induced pitch resonance for a suction pile was observed during the test. This phenomenon can be explained in principle by a damped Mathieu equation. In the range of the characteristics of piles used for deep water anchoring, the dominant unstable region is located in the principle unstable region described by a Mathieu instability diagram. That is, when the heave excitation frequency is close to the twice of the pitch natural frequency, the pitch instability may occur. However, due to large damping to the pitch of a pile from the ambient water, the pitch of a pile can only be significantly amplified when its heave amplitude is also large enough. That is, at the same time the heave excitation frequency is close to the heave natural frequency, which results in the heave resonance. In summary, significant pitch of a pile induced by its heave may occur during its lowering process depending on two conditions. That is, 1) the pitch natural frequency is roughly one half of the heave natural frequency, and 2) the heave excitation frequency is approximately equal to the heave natural frequency. If only one of the two conditions is satisfied, no significant pitch resonance will occur.

In this study, it was assumed that the constant length of the lowering cable and the absence of ocean currents. Besides, the pile-cable system is only subjected to the regular heave excitation, which attempts to represent the motion of the surface vessel. However, in the real world, the excitation at the top of the system may be the irregular surge and heave motions, and the pile-cable system may be subjected to horizontal current forces near the surface. In order to simulate the prototype suction piles and compare with the field measurements, we should consider the irregular surge-heave combined motion as

the input to the pile-cable system, and add the effects of the lowering speed and the horizontal current forces to the system in the future study.

REFERENCES

Det Norske Veritas, 2000. DNV-RP-H103 Modelling and Analysis of Marine Operations. Det Norske Veritas, Høvik, Oslo, Norway.

Diab, B. and Tahan, N., 2005. Offshore installation, in: Chakrabarti, S.K. (Ed.) Handbook of Offshore Engineering, Volume II, Elsevier, London, pp. 1076-1078.

Driscoll, F.R., Lueck, R.G. and Nahon, M., 2000. Development and validation of a lumped-mass dynamics model of a deep-sea ROV system. Applied Ocean Research, 22, 169-182.

Goeller, J.E. and Laura, P.E., 1971. Analytical and experimental study of the dynamic response of segmented cable systems. Journal of Sound and Vibration, 18(3), 311-329.

Haslum, H.A. and Faltinsen, O.M., 1999. Alternative shape of spar platforms for use in hostile areas. In: Proceedings of the 31st Offshore Technology Conference, Houston, pp. 217-228, (OTC 10953).

Hennessey, C.M., Pearson, N.J. and Plaut, R.H., 2005. Experimental snap loading of synthetic ropes. Shock and Vibration, 12, 163-175.

Huang, L., Young, D., Zhang, J., Randall, R.E. and Wilde, B, 2010. Experimental study on suction pile heave resonance during lowering operations. In: Proceedings of 16th Offshore Symposium, Houston, TX, pp. C12-C22.

Huang, S. and Vassalos, D., 1993. A numerical method for predicting snap loading of marine cables. Applied Ocean Research, 15, 235-242.

Huang, Y.M, Krousgrill, C.M. and Bajaj, A.K., 1989. Dynamic behavior of offshore structures with bilinear stiffness. Journal of Fluids and Structures, 3, 405-422.

InterMoor Inc., 2010. Engineering services. < http://www.intermoor.com/ PageDisplay.asp?p1=21269 >.

Koo, B.J., Kim, M.H. and Randall R.E., 2004. Mathieu instability of a spar platform with mooring and risers. Ocean Engineering, 31, 2175-2208.

Liu, F.C., 1973. Snap loads in lifting and mooring cable systems induced by surface wave conditions. NCEL Technical Note N-1288, Port Hueneme, CA, Sept.

Milgram, J.H., Triantafyllou, M.S., Frim, F.C. and Anagnostou, G., 1988. Seakeeping and extreme tensions in offshore towing. Transactions of the Society of Naval Architects and Marine Engineers, 96, 35-70.

New Industries Inc., 2008. 9'-10" OD x 70' Long Suction Pile. < http:// www.newindustries.com/images/suction_pile.jpg>.

Niedzwecki, J.M. and Thampi, S.K., 1991. Snap loading of marine cable systems. Applied Ocean Research, 13(1), 2-11.

Rho, J.B., Choi, H.S., Lee, W.C., Shin, H.S. and Park, I.K., 2002. Heave and pitch motion of a spar platform with damping plate. In: Proceedings of the 12th International Offshore and Polar Engineering, Honolulu, HI, vol. 1, pp. 285-288.

Shin, H. 1991. Analysis of extreme tension in a snapping cable. In: Proc. of the First International Offshore and Polar Engineering Conference, Edinburgh, UK, vol. 2, pp. 216-221.

Yoshida K. and Oka, N., 1978. Snap loads in taut moored platforms. J. Soc. Naval Arch. Japan, 144, 205-213.

Zhang, L., Zou, J. and Huang, E.W., 2002. Mathieu instability evaluation for DDCV/SPAR and TLP tendon design. In: Proceedings of the 11th Offshore Symposium, Society of Naval Architect and Marine Engineering (SNAME), Houston, pp. 41-49.

Supplemental Sources Consulted

Baddour, R.E. and Raman-Nair, W., 2002. Marine tether dynamics: retrieval and deploying from a heave platform. Ocean Engineering, 29, 1633-1661.

Cao, P. and Zhang, J., 1996. Slow motion responses of compliant offshore structures. In: Proceedings of the Sixth International Offshore and Polar Engineering Conference, Los Angeles, vol. 1, pp. 296-303.

Chen, X., 2002. Studies on dynamic interaction between deep-water floating structures and their mooring/tendon systems. Ph.D. Dissertation, Civil Engineering Department, Texas A&M University, College Station, TX.

Plaut, R.H., Archilla, J.C. and Mays, T.W., 2000. Snap loads in mooring lines during large three-dimensional motions of a cylinder. Nonlinear Dynamics, 23, 271-284.

Rho, J.B., Choi, H.S., Lee, W.C., Shin, H.S. and Park, I.K., 2003. An experimental study for mooring effects on the stability of spar platform. In: Proceedings of the 13th International Offshore and Polar Engineering, vol. 6 (1), pp. 27-34.

Zhang, J., Randall, R.E., Huang, L. and Young, D, 2009. Testing of suction pile models. Experimental report to InterMoor Inc., Houston, TX.

APPENDIX A

OTHER MODEL TEST RESULTS

A.1 # 1 Valves Opening Model

Table 28 summarizes the time domain results of the tests conducted for the #1 valves opening model. Similarly, the largest heave transmissibility indicates that the resonance frequency is approximately equal to 0.505 Hz based on Fig. 100, and the largest *TR* is about 5.7 times of that at the actuator. Near the resonance frequency (0.505 Hz), the heave stroke of the upper sensors above the spring is slightly greater than that at the actuator, which is caused by the 'pushing up' of the pile model. The heave induced pitch resonance is also observed in this case at the frequency near the heave resonance, and the pitch amplitude is roughly equal to $2.5^\circ \pm 0.5^\circ$ $(0.0436\text{rad} \pm 0.0087\text{rad})$.

Table 28. Time domain results for the # 1 valves opening model tests.

f (Hz)	ST1 (lb)	ST2 (lb)	ST2/ST1	SD3 (ft)	SD2 (ft)	SD2/SD3	SD2/SD1	SD3/SD1
0.3751	4.6273	4.5116	0.9750	0.2435	0.4881	2.0045	1.9524	0.9740
0.4001	6.1477	6.0283	0.9806	0.2461	0.5846	2.3755	2.3384	0.9844
0.4251	8.6590	8.1443	0.9406	0.2481	0.7174	2.8916	2.8696	0.9924
0.4501	12.8246	11.8571	0.9246	0.2383	0.9569	4.0155	3.8276	0.9532
0.4751	16.2620	15.1309	0.9304	0.2346	1.0976	4.6786	4.3904	0.9384
0.5002	23.0039	22.5164	0.9788	0.2693	1.4160	5.2581	5.6640	1.0772
0.5252	21.7490	20.2802	0.9325	0.2242	1.2197	5.4402	4.8788	0.8968
0.5502	20.2950	18.9238	0.9324	0.2042	1.0410	5.0979	4.1640	0.8168
0.5752	18.5743	17.2869	0.9307	0.2152	0.8712	4.0483	3.4848	0.8608
0.6002	16.7236	15.7294	0.9405	0.2130	0.7175	3.3685	2.8700	0.8520
0.6252	11.8323	11.0182	0.9312	0.2187	0.4657	2.1294	1.8628	0.8748
0.6502	10.2456	9.7019	0.9469	0.2227	0.3831	1.7203	1.5324	0.8908
0.6752	9.0570	8.7036	0.9610	0.2234	0.3160	1.4145	1.2640	0.8936
0.7002	8.0646	7.6652	0.9505	0.2170	0.2605	1.2005	1.0420	0.8680

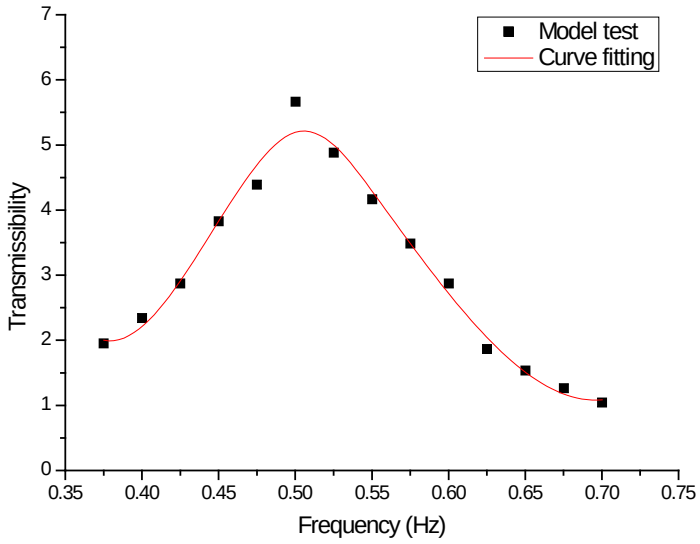

Fig. 100. Determining of the heave resonance frequency by the transmissibility curve for the # 1 valves opening model.

A.2 #2' Valves Opening Model

Table 29 summarizes the time domain results of the tests conducted for the #2' valves opening model. Similarly, the largest heave transmissibility indicates that the resonance frequency is approximately equal to 0.510 Hz based on Fig. 101, and the largest *TR* is about 5.1. Near the resonance frequency (0.510 Hz), the heave stroke of the upper sensors above the spring is slightly greater than that at the actuator, which is caused by the 'pushing up' of the pile model. The heave induced pitch resonance is also observed in this case at the frequency near the heave resonance, and the pitch amplitude is roughly equal to $2.5^\circ \pm 0.5^\circ$ (0.0436 rad ± 0.0087 rad).

Table 29. Time domain results for the #2' valves opening model tests.

f (Hz)	ST1 (lb)	ST2 (lb)	ST2/ST1	SD3 (ft)	SD2 (ft)	SD2/SD3	SD2/SD1	SD3/SD1
0.4501	10.2456	9.8204	0.9585	0.2454	0.8133	3.3142	3.2532	0.9816
0.4585	12.5606	11.9373	0.9504	0.2478	0.9187	3.7074	3.6748	0.9912
0.4751	14.5426	13.8529	0.9526	0.2457	1.1063	4.5026	4.4252	0.9828
0.4835	16.1956	15.3304	0.9466	0.2419	1.1665	4.8222	4.6660	0.9676
0.5002	19.6330	19.0031	0.9679	0.2619	1.2540	4.7881	5.0160	1.0476
0.5085	21.4173	20.4013	0.9526	0.2486	1.2833	5.1621	5.1332	0.9944
0.5252	21.0220	20.2811	0.9648	0.2152	1.2136	5.6394	4.8544	0.8608
0.5335	20.5590	19.8821	0.9671	0.2094	1.1386	5.4374	4.5544	0.8376
0.5502	19.6330	18.7636	0.9557	0.2138	1.0307	4.8209	4.1228	0.8552
0.5585	18.8396	18.3245	0.9727	0.2085	0.9555	4.5827	3.8220	0.8340
0.5752	18.0463	17.4464	0.9668	0.2101	0.8328	3.9638	3.3312	0.8404
0.5835	17.1203	16.6476	0.9724	0.2025	0.7632	3.7689	3.0528	0.8100
0.6002	16.1943	15.7294	0.9713	0.2053	0.6208	3.0239	2.4832	0.8212
0.6252	12.0300	11.6176	0.9657	0.2282	0.4968	2.1770	1.9872	0.9128

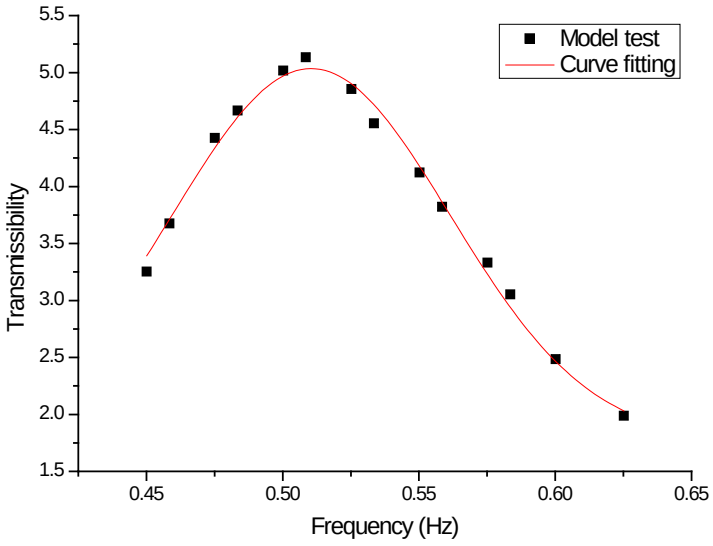

Fig. 101. Determining of the heave resonance frequency by the transmissibility curve for the # 2' valves opening model.

A.3 # 3 Valves Opening Model

Table 30 summarizes the time domain results of the tests conducted for the #3 valves opening model. Similarly, the largest heave transmissibility indicates that the resonance frequency is approximately equal to 0.540 Hz based on Fig. 102, and the largest *TR* is about 4.2. There is no 'pushing up' occur for this case throughout the testing frequencies. However, the heave induced pitch resonance is still observed in this case at the pitch natural frequency near the heave resonance, and the pitch amplitude is roughly equal to $1.0^\circ \pm 0.5^\circ$ $(0.0175\text{rad} \pm 0.0087\text{rad})$.

Table 30. Time domain results for the # 3 valves opening model tests.

f (Hz)	ST1 (lb)	ST2 (lb)	ST2/ST1	SD3 (ft)	SD2 (ft)	SD2/SD3	SD2/SD1	SD3/SD1
0.4501	9.5201	9.0425	0.9498	0.2455	0.6976	2.2732	2.7905	0.9820
0.4585	11.2055	10.6589	0.9512	0.2465	0.7670	2.4896	3.0680	0.9860
0.4751	12.5925	11.9172	0.9464	0.2431	0.8123	2.6723	3.2490	0.9724
0.4835	14.3775	13.7729	0.9579	0.2464	0.8779	2.8506	3.5115	0.9856
0.5002	15.3616	15.5938	1.0151	0.2397	0.9419	3.1436	3.7675	0.9588
0.5085	17.1206	16.3206	0.9533	0.2408	0.9975	3.3145	3.9900	0.9632
0.5252	18.6936	17.7183	0.9478	0.2383	1.0429	3.5010	4.1715	0.9532
0.5335	19.6204	18.5562	0.9458	0.2370	1.0479	3.5366	4.1915	0.9480
0.5502	20.0810	19.2830	0.9603	0.2374	1.0243	3.4521	4.0970	0.9496
0.5585	20.1740	19.1148	0.9475	0.2356	0.9773	3.3185	3.9090	0.9424
0.5752	19.4348	18.5562	0.9548	0.2337	0.9136	3.1275	3.6545	0.9348
0.5835	18.3240	17.5500	0.9578	0.2338	0.8334	2.8523	3.3335	0.9352
0.6002	17.4920	17.1585	0.9809	0.2317	0.7644	2.6398	3.0575	0.9268
0.6085	16.5672	15.9292	0.9615	0.2289	0.7005	2.4483	2.8020	0.9156
0.6252	15.7332	15.3145	0.9734	0.2280	0.6470	2.2701	2.5880	0.9120
0.6335	16.0629	15.6296	0.9730	0.2322	0.6045	2.0822	2.4180	0.9288
0.6502	15.3684	14.8521	0.9664	0.2253	0.5593	1.9859	2.2370	0.9012
0.6585	14.5745	14.0733	0.9656	0.2248	0.5118	1.8213	2.0470	0.8992
0.6752	13.8819	13.3547	0.9620	0.2246	0.4805	1.7117	1.9220	0.8984

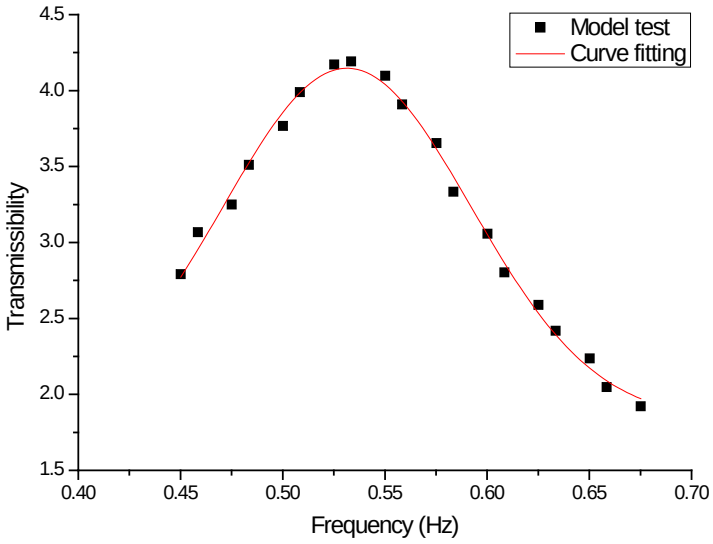

Fig. 102. Determining of the heave resonance frequency by the transmissibility curve for the # 3 valves opening model.

A.4 #1, #2, #3 Valves Opening Model

Table 31 summarizes the time domain results of the tests conducted for the #1, #2, #3 valves opening model. Similarly, the largest heave transmissibility indicates that the resonance frequency is approximately equal to 0.585 Hz based on Fig. 103, and the largest *TR* is about 3.3. There are no 'pushing up' and no heave induced pitch resonance observed in this case.

Table 31. Time domain results for the #1, #2, #3 valves opening model tests.

f (Hz)	ST1 (lb)	ST2 (lb)	ST2/ST1	SD3 (ft)	SD2 (ft)	SD2/SD3	SD2/SD1	SD3/SD1
0.5002	9.6691	10.3151	1.0668	0.2423	0.7347	3.0323	2.9389	0.9692
0.5252	11.6806	10.8479	0.9287	0.2377	0.7994	3.3629	3.1974	0.9508
0.5502	13.6895	12.7431	0.9309	0.2382	0.8254	3.4651	3.3015	0.9528
0.5752	15.3227	14.4877	0.9455	0.2353	0.8193	3.4819	3.2772	0.9412
0.6002	15.7055	15.0188	0.9563	0.2309	0.7898	3.4206	3.1593	0.9236
0.6252	15.6175	14.6017	0.9350	0.2251	0.7381	3.2788	2.9522	0.9004
0.6502	15.1713	14.1163	0.9305	0.2243	0.6835	3.0472	2.7339	0.8972
0.6752	14.3967	13.3719	0.9288	0.2261	0.5880	2.6006	2.3520	0.9044
0.7002	13.4320	12.8398	0.9559	0.2231	0.5221	2.3401	2.0883	0.8924
0.7252	12.5001	11.8811	0.9505	0.2160	0.4412	2.0428	1.7650	0.8640
0.7502	11.3110	10.9403	0.9672	0.2179	0.3736	1.7144	1.4942	0.8716
0.7752	10.7358	10.2467	0.9544	0.2136	0.3454	1.6170	1.3816	0.8544
0.8003	10.1606	9.5520	0.9401	0.2114	0.3075	1.4544	1.2298	0.8456
0.8253	9.6796	9.1465	0.9449	0.2072	0.2828	1.3649	1.1312	0.8288
0.8503	9.1064	8.5667	0.9407	0.2007	0.2571	1.2809	1.0283	0.8028
0.8753	8.5314	8.1625	0.9568	0.2196	0.2314	1.0541	0.9258	0.8782
0.9003	7.8600	7.6409	0.9721	0.2097	0.2034	0.9699	0.8136	0.8388
0.9253	7.4752	7.2367	0.9681	0.2189	0.1929	0.8813	0.7718	0.8757
0.9503	7.2848	6.8881	0.9455	0.2193	0.1771	0.8076	0.7084	0.8772
0.9753	6.9020	6.7731	0.9813	0.2194	0.1627	0.7414	0.6508	0.8778
1.0003	6.9020	7.7571	1.1239	0.2198	0.1499	0.6821	0.5997	0.8793

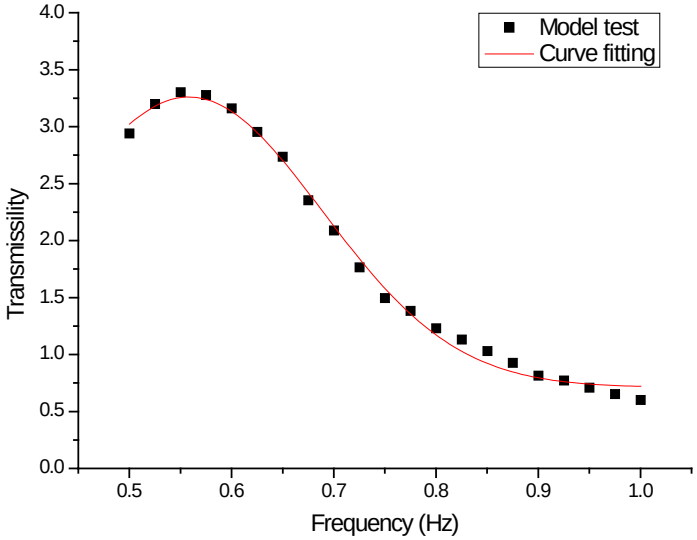

Fig. 103. Determining of the heave resonance frequency by the transmissibility curve for the #1, #2, #3 valves opening model.

A.5 #2, #4 Valves Opening Model

Table 32 summarizes the time domain results of the tests conducted for the #2, #4 valves opening model. Similarly, the largest heave transmissibility indicates that the resonance frequency is approximately equal to 0.610 Hz based on Fig. 104, and the largest *TR* is about 3.2. There are no 'pushing up' and no heave induced pitch resonance observed in this case.

Table 32. Time domain results for the #2, #4 valves opening model tests.

f (Hz)	ST1 (lb)	ST2 (lb)	ST2/ST1	SD3 (ft)	SD2 (ft)	SD2/SD3	SD2/SD1	SD3/SD1
0.5002	7.6627	8.7989	1.1483	0.2395	0.3832	2.7544	2.6387	0.9580
0.5252	8.9180	8.4199	0.9441	0.2385	0.3816	2.9410	2.8058	0.9540
0.5502	10.5488	9.7839	0.9275	0.2366	0.3786	3.1716	3.0016	0.9464
0.5752	12.4342	11.5300	0.9273	0.2362	0.3779	3.3287	3.1450	0.9448
0.6002	13.9416	13.5012	0.9684	0.2318	0.3709	3.4927	3.2384	0.9272
0.6252	15.0708	14.2593	0.9462	0.2285	0.3587	3.4238	3.1293	0.9140
0.6502	15.8270	14.5639	0.9202	0.2289	0.3434	3.2156	2.9442	0.9156
0.6752	15.8270	14.7161	0.9298	0.2269	0.3177	2.9357	2.6645	0.9076
0.7002	15.7010	14.5639	0.9276	0.2226	0.3005	2.6327	2.3441	0.8904
0.7252	15.1994	14.3355	0.9432	0.2188	0.2844	2.4063	2.1060	0.8752
0.7502	15.5724	14.7146	0.9449	0.2178	0.2723	2.1562	1.8785	0.8712
0.7752	14.3197	13.5029	0.9430	0.2125	0.2444	1.8974	1.6128	0.8500
0.8003	13.8155	12.9715	0.9389	0.2104	0.2314	1.6782	1.4124	0.8416
0.8253	13.3139	12.4403	0.9344	0.2037	0.2139	1.5351	1.2508	0.8148
0.8503	12.6863	11.7583	0.9269	0.2005	0.2005	1.3556	1.0872	0.8020
0.8753	11.9301	11.1509	0.9347	0.2195	0.1951	1.1230	0.9860	0.8780
0.9003	10.9269	10.3928	0.9511	0.2189	0.1885	0.9998	0.8752	0.8754
0.9253	10.5513	10.0882	0.9561	0.2191	0.1906	0.9509	0.8332	0.8762
0.9503	10.1732	9.8616	0.9694	0.2027	0.2027	0.9556	0.7748	0.8108
0.9753	9.6716	9.4808	0.9803	0.2128	0.2128	0.8285	0.7052	0.8512
1.0003	9.7977	11.2254	1.1457	0.2264	0.2264	0.6926	0.6272	0.9056
1.0253	9.1675	8.8751	0.9681	0.2223	0.2223	0.6694	0.5952	0.8892
1.0503	8.2878	7.9646	0.9610	0.2254	0.2254	0.5976	0.5388	0.9016
1.0753	7.9148	8.1153	1.0253	0.2242	0.2242	0.5642	0.5060	0.8968
1.1003	7.6627	7.2827	0.9504	0.2245	0.1128	0.5024	0.4512	0.8980
1.1254	7.0351	6.9037	0.9813	0.2237	0.1062	0.4747	0.4248	0.8948

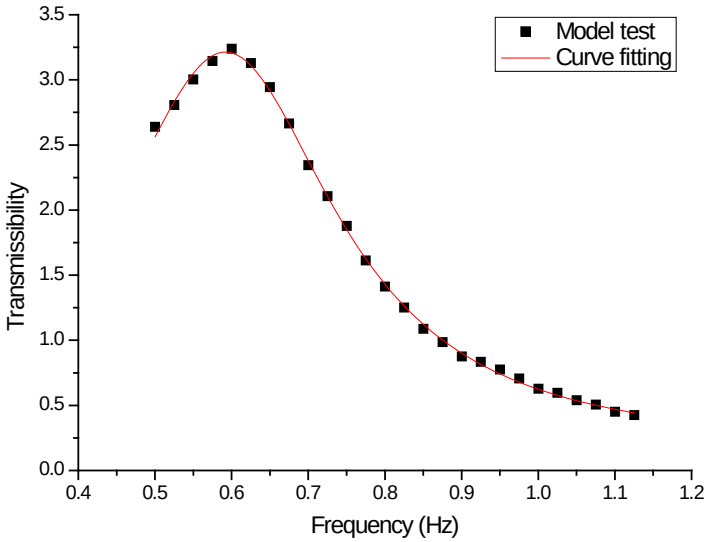

Fig. 104. Determining of the heave resonance frequency by the transmissibility curve for the #2, #4 valves opening model.

A.6 #1, #3, #4 Valves Opening Model

Table 33 summarizes the time domain results of the tests conducted for the #1, #3, #4 valves opening model. Similarly, the largest heave transmissibility indicates that the resonance frequency is approximately equal to 0.64 Hz based on Fig. 105, and the largest *TR* is about 3.1. There are no 'pushing up' and no heave induced pitch resonance observed in this case.

Table 33. Time domain results for the #1, #3, #4 valves opening model tests.

f (Hz)	ST1 (lb)	ST2 (lb)	ST2/ST1	SD3 (ft)	SD2 (ft)	SD2/SD3	SD2/SD1	SD3/SD1
0.5002	6.2814	8.1930	1.3043	0.2403	0.5892	2.4519	2.3568	0.9612
0.5252	7.2846	6.5991	0.9059	0.2381	0.6464	2.7148	2.5856	0.9524
0.5502	8.4164	7.7379	0.9194	0.2367	0.7036	2.9724	2.8142	0.9468
0.5752	9.9210	9.0258	0.9098	0.2354	0.7451	3.1654	2.9806	0.9416
0.6002	11.1790	10.8479	0.9704	0.2310	0.7706	3.3357	3.0822	0.9240
0.6252	12.6863	12.0612	0.9507	0.2294	0.7823	3.4100	3.1291	0.9176
0.6502	13.9416	12.7448	0.9142	0.2275	0.7760	3.4110	3.1040	0.9100
0.6752	14.4430	13.2728	0.9190	0.2288	0.7465	3.2626	2.9859	0.9152
0.7002	15.0708	13.8058	0.9161	0.2206	0.6839	3.1000	2.7354	0.8824
0.7252	14.9473	14.4117	0.9642	0.2194	0.6261	2.8537	2.5044	0.8776
0.7502	14.8213	14.2610	0.9622	0.2190	0.5612	2.5625	2.2448	0.8760
0.7752	14.5692	13.8043	0.9475	0.2146	0.5034	2.3456	2.0134	0.8584
0.8003	14.0676	13.3505	0.9490	0.2129	0.4498	2.1125	1.7990	0.8516
0.8253	13.5633	12.9700	0.9563	0.2065	0.4013	1.9432	1.6051	0.8260
0.8503	13.1879	12.8193	0.9721	0.2014	0.3388	1.6822	1.3552	0.8056
0.8753	12.5577	12.1357	0.9664	0.2194	0.3095	1.4107	1.2382	0.8777
0.9003	12.0587	11.3776	0.9435	0.2198	0.2806	1.2765	1.1224	0.8793
0.9253	11.5545	11.1494	0.9649	0.2002	0.2595	1.2960	1.0378	0.8008
0.9503	11.0529	10.9241	0.9883	0.2118	0.2422	1.1436	0.9689	0.8472
0.9753	10.2993	9.9361	0.9647	0.2132	0.2176	1.0205	0.8703	0.8528
1.0003	10.0472	11.6060	1.1551	0.2196	0.2050	0.9337	0.8202	0.8784
1.0253	9.2935	9.1018	0.9794	0.2241	0.1878	0.8379	0.7511	0.8964
1.0503	8.7919	8.7227	0.9921	0.2266	0.1658	0.7316	0.6631	0.9064

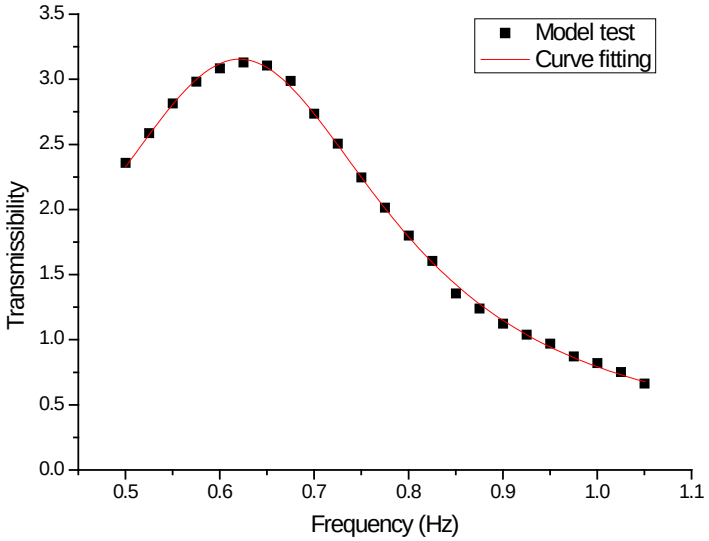

Fig. 105. Determining of the heave resonance frequency by the transmissibility curve for the #1, #3, #4 valves opening model.

APPENDIX B

STRIP THEORY FOR THE CALCULATIONS OF I_β AND $C_{D\beta}$

Strip Theory has been used to calculate hydrodynamic coefficients from Potential theory for the ship design and the seakeeping of surface vessels for over 50 years with great success. Stripe theory is a popular approximation of the 3-D Neumann-Kelvin Formulation for ships which are slender. The principle assumption is that:

$$\frac{B}{L}, \frac{T}{L} = O(\varepsilon), \varepsilon << 1 \tag{B.1}$$

where B is the maximum beam of the ship, T is the maximum draft of ship and L is the water line length of the ship.

For the calculations of the pitch hydrodynamic coefficients of the slender suction pile, we can also employ Strip Theory as an approximation of 2-D formulation for the surge-heave-pitch coupled motion. I_β is the total moment of inertia for the decoupled pitch motion of the model pile in water, which includes the moment of inertia $\left(I_{\beta p}\right)$ for the decoupled pitch motion in air and the added moment of inertia $\left(I_{\beta a}\right)$ for the decoupled pitch motion of the model pile in water,

$$I_\beta = I_{\beta p} + I_{\beta a} \tag{B.2}$$

The calculation of $I_{\beta p}$ is quite straightforward as follows,

$$I_{\beta p} = I_{AT} + I_{ST1} + I_{ST2} + I_{SC} \tag{B.3}$$

$$I_{AT} = \tfrac{1}{12} m_{AT} \left[3\left(r_2^2 + r_1^2\right) + L_{AT}^2 \right] + m_{AT} \left[t + a + L_{ST2} + L_{AT}/2 \right]^2 \tag{B.4}$$

$$I_{ST1} = \tfrac{1}{12} m_{ST1}\left[3\left(r_2^2 + r_1^2\right) + L_{ST1}^2\right] + m_{ST1}\left[L + a - L_{ST1}/2\right]^2 \quad \text{(B.5)}$$

$$I_{ST2} = \tfrac{1}{12} m_{ST2}\left[3\left(r_2^2 + r_1^2\right) + L_{ST2}^2\right] + m_{ST2}\left[t + a + L_{ST2}/2\right]^2 \quad \text{(B.6)}$$

$$I_{SC} = \tfrac{1}{12} m_{SC}\left[3\left(D/2\right)^2 + t^2\right] + m_{SC}\left[a + t/2\right]^2 \quad \text{(B.7)}$$

$$m_{AT} = \rho_{Acrylic} V_{AT} = \rho_{Acrylic} \pi\left(r_2^2 - r_1^2\right) L_{AT} \quad \text{(B.8)}$$

$$m_{ST1} = \rho_{Steel} V_{ST1} = \rho_{Steel} \pi\left(r_2^2 - r_1^2\right) L_{ST1} \quad \text{(B.9)}$$

$$m_{ST2} = \rho_{Steel} V_{ST2} = \rho_{Steel} \pi\left(r_2^2 - r_1^2\right) L_{ST2} \quad \text{(B.10)}$$

where I_{AT}, I_{ST1}, I_{ST2} and I_{SC} are the moments of inertia with respect to the *y*-axis through the origin O' for the four section of the model pile: Acrylic Tube (AT), Steel Tube 1 (ST1), Steel Tube 2 (ST2) and Steel Cap (SC) respectively; m_{AT}, m_{ST1}, m_{ST2} and m_{SC} are the mass of the four section of the model pile; V_{AT}, V_{ST1} and V_{ST2} are the volume of three tube sections; $\rho_{Acrylic}$ and ρ_{Steel} are the density of Acrylic and Steel; D, a, t, r_1, r_2, L_{AT}, L_{ST1} and L_{ST2} are the dimensions of the model piles shown in Fig. 106 and. Fig. 107 Note that the origin of the local coordinates moves to the GC of the model pile for calculating the hydrodynamic coefficients of the decoupled pitch motion.

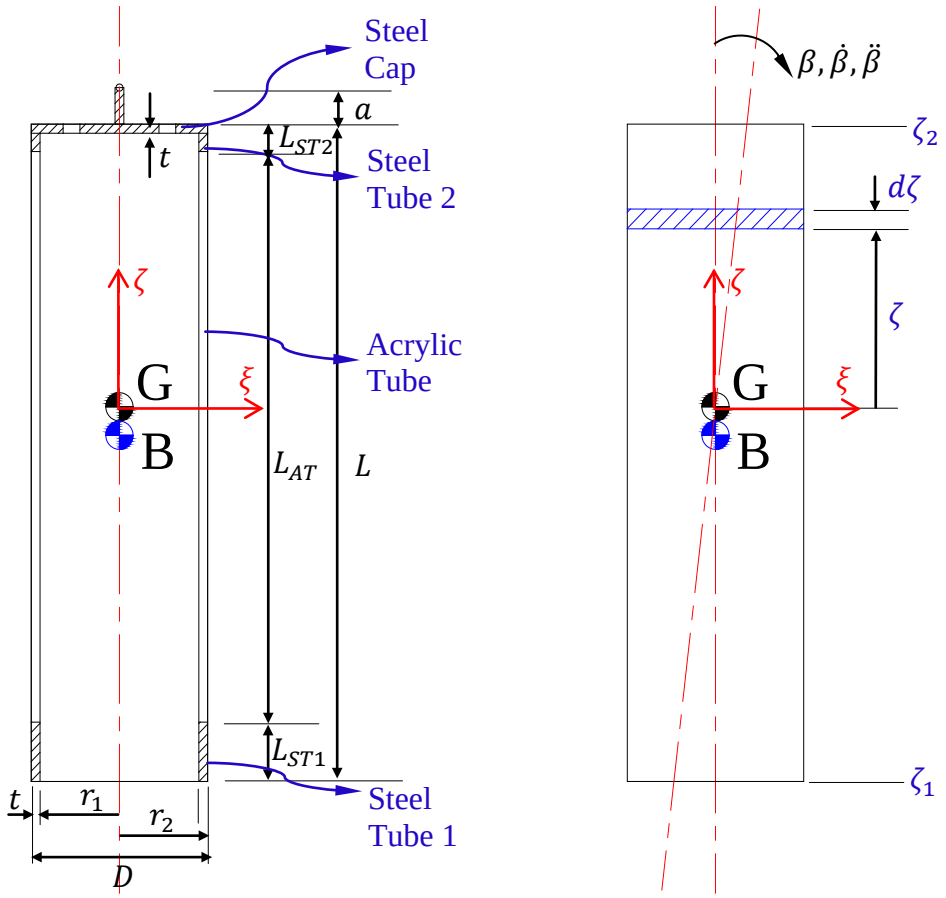

Fig. 106. Dimensions of the closed end model and stripped calculation of $I_{\beta a}$ and $C_{D\beta}$.

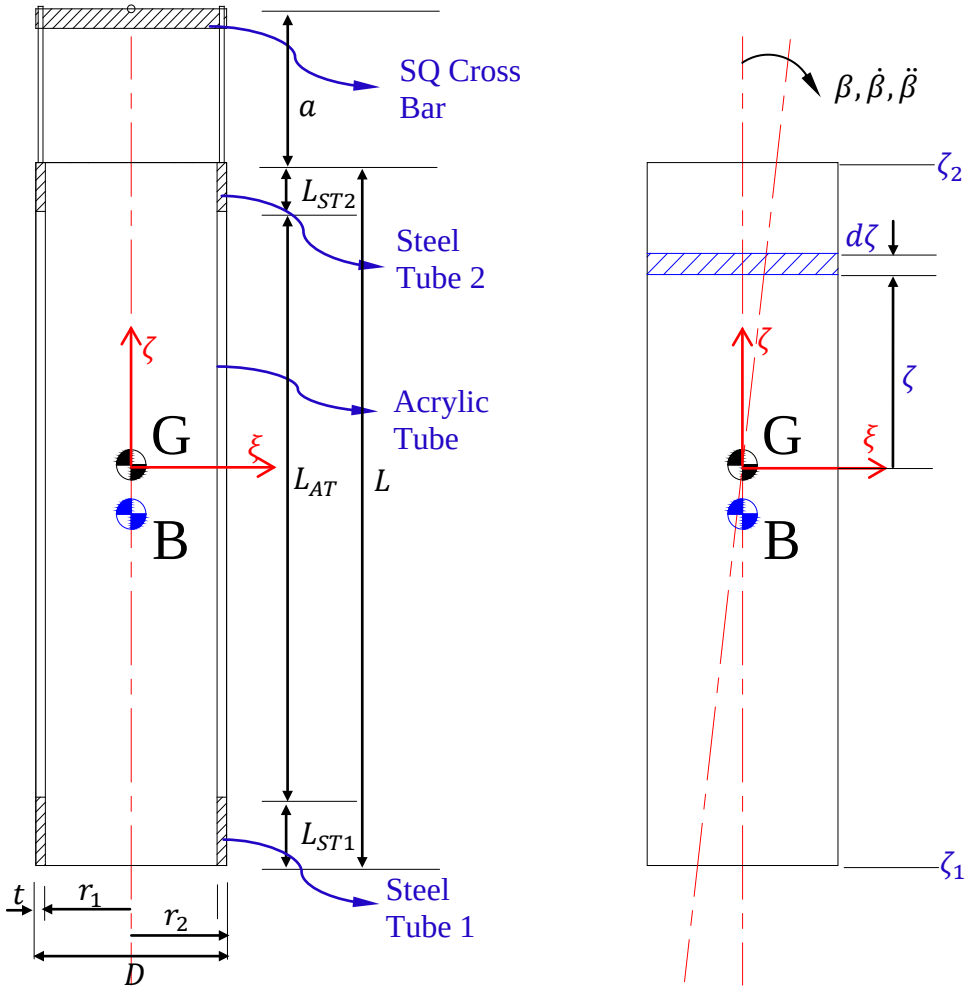

Fig. 107. Dimensions of the open end model and stripped calculation of $I_{\beta a}$ and $C_{D\beta}$.

The calculation of the added moment of inertia $\left(I_{\beta a}\right)$ for the decoupled pitch motion of the model pile in water is based on the Strip Theory as follows,

$$M_{\beta a}=\int_{\zeta_1}^{\zeta_2}\left(\frac{C_{a,n}m_0}{L}\right)\left(\ddot{\beta}\zeta\right)\zeta\,d\zeta=\frac{C_{a,n}m_0\ddot{\beta}}{L}\int_{\zeta_1}^{\zeta_2}\zeta^2 d\zeta=\frac{C_{a,n}m_0\ddot{\beta}}{3L}\left(\zeta_2^3-\zeta_1^3\right) \quad \text{(B.11)}$$

$$I_{\beta a}=\frac{M_{\beta a}}{\ddot{\beta}}=\frac{C_{a,n}m_0}{3L}\left(\zeta_2^3-\zeta_1^3\right) \quad \text{(B.12)}$$

The calculation of the coefficient $\left(C_{D\beta}\right)$ for the hydrodynamic damping moment term for the decoupled pitch motion of the model pile in water is also based on Strip Theory as follows,

$$\begin{aligned}M_{D\beta}&=\int_{\zeta_1}^{\zeta_2}\tfrac{1}{2}\rho C_{d,n}D\left|\dot{\beta}\zeta\right|\left(\dot{\beta}\zeta\right)\zeta\,d\zeta=\tfrac{1}{2}\rho C_{d,n}D\left|\dot{\beta}\right|\dot{\beta}\int_{\zeta_1}^{\zeta_2}\left|\zeta\right|\zeta^2 d\zeta\\&=\tfrac{1}{2}\rho C_{d,n}D\left|\dot{\beta}\right|\dot{\beta}\left\{\int_0^{\zeta_2}\zeta^3 d\zeta+\int_{\zeta_1}^{0}\left(-\zeta^3\right)d\zeta\right\}\\&=\tfrac{1}{8}\rho C_{d,n}D\left|\dot{\beta}\right|\dot{\beta}\left(\zeta_2^4+\zeta_1^4\right)\end{aligned} \quad \text{(B.13)}$$

$$C_{D\beta}=\frac{M_{D\beta}}{\left|\dot{\beta}\right|\dot{\beta}}=\tfrac{1}{8}\rho C_{d,n}D\left(\zeta_2^4+\zeta_1^4\right) \quad \text{(B.14)}$$

APPENDIX C

HILL'S INFINITE DETERMINANT METHOD

The Mathieu equation is a special case of the Hill's equation which is a linear second-order ordinary differential equation with a periodic coefficient. The standard form for the Hill's equation is as follows,

$$\frac{d^2\beta}{d\tau^2}+\left(\alpha+f\left(\tau\right)\right)\beta=0 \tag{C.1}$$

where $f\left(\tau\right)$ is a periodic function of τ. For the special case $f\left(\tau\right)=\gamma\cos\tau$, we have,

$$\frac{d^2\beta}{d\tau^2}+\left(\alpha+\gamma\cos\tau\right)\beta=0 \tag{C.2}$$

it is known as the Mathieu equation. If the damping term is added to the above equation,

$$\frac{d^2\beta}{d\tau^2}+\mu\frac{d\beta}{d\tau}+\left(\alpha+\gamma\cos\tau\right)\beta=0 \tag{C.3}$$

it is referred to as the damped Mathieu equation.

The damped Mathieu equation (C.3) cannot be solved explicitly. However, the transition curves between stability regions and instability regions can be obtained by the perturbation method and the Hill's infinite determinant method. Here, only the Hill's determinant method is employed to plot the damped Mathieu stability diagram.

The form of a periodic solution of period 2π is express by the trigonometric series as follows,

$$\beta\left(\tau\right)=a_0+\sum_{j=1}^{\infty}\left[a_j\cos\left(j\tau\right)+b_j\sin\left(j\tau\right)\right] \tag{C.4}$$

Substituting Eqn. (C.4) into the damped Mathieu equation (3.61), and utilizing the trigonometric identities

$$\begin{aligned}\cos(\tau)\cos(j\tau) &= \tfrac{1}{2}\left[\cos(j+1)\tau + \cos(j-1)\tau\right] \\ \cos(\tau)\sin(j\tau) &= \tfrac{1}{2}\left[\sin(j+1)\tau + \sin(j-1)\tau\right] \\ j &= 1, 2, \cdots\end{aligned} \tag{C.5}$$

we have

$$\begin{aligned}&\sum_{j=1}^{\infty}\left[-j^2 a_j \cos(j\tau) - j^2 b_j \sin(j\tau)\right] + \sum_{j=1}^{\infty}\left[-j\mu a_j \sin(j\tau) + j\mu b_j \cos(j\tau)\right] \\ &+ a_0(\alpha + \gamma\cos\tau) + \sum_{j=1}^{\infty}\left[\alpha a_j \cos(j\tau) + \alpha b_j \sin(j\tau)\right] \\ &+ \sum_{j=1}^{\infty}\frac{\gamma}{2} a_j\left[\cos(j+1)\tau + \cos(j-1)\tau\right] + \sum_{j=1}^{\infty}\frac{\gamma}{2} b_j\left[\sin(j+1)\tau + \sin(j-1)\tau\right] = 0\end{aligned} \tag{C.6}$$

Replacing $j+1$ and $j-1$ by m and n respectively in the last two summations,

$$\begin{aligned}&\alpha a_0 + \gamma\cos\tau + \sum_{j=1}^{\infty}\left[\left(\alpha - j^2\right)a_j + j\mu b_j\right]\cos(j\tau) + \sum_{j=1}^{\infty}\left[\left(\alpha - j^2\right)b_j - j\mu a_j\right]\sin(j\tau) \\ &+ \sum_{m=2}^{\infty}\frac{\gamma}{2} a_{m-1}\cos(m\tau) + \sum_{n=0}^{\infty}\frac{\gamma}{2} a_{n+1}\cos(n\tau) + \sum_{m=2}^{\infty}\frac{\gamma}{2} b_{m-1}\sin(m\tau) + \sum_{n=0}^{\infty}\frac{\gamma}{2} b_{n+1}\sin(n\tau) = 0\end{aligned} \tag{C.7}$$

The terms $\cos(j\tau)$ and $\sin(j\tau)$ are linearly independent functions so Eqn. (C.7) is true only if the coefficients of $\cos(j\tau)$ and $\sin(j\tau)$ are zero for all j. This yields the table of the coefficient equations below (Table 34),

Table 34. Coefficients of $\cos(j\tau)$ and $\sin(j\tau)$ terms for solutions of period 2π.

j	Coefficient of $\cos(j\tau)$	Coefficient of $\sin(j\tau)$
0	$\alpha a_0 + \frac{\gamma}{2} a_1 = 0$	-
1	$(\alpha - 1^2) a_1 + \gamma a_0 + \frac{\gamma}{2} a_2 + \mu b_1 = 0$	$(\alpha - 1^2) b_1 + \frac{\gamma}{2} b_2 - \mu a_1 = 0$
2	$(\alpha - 2^2) a_2 + \frac{\gamma}{2} a_1 + \frac{\gamma}{2} a_3 + 2\mu b_2 = 0$	$(\alpha - 2^2) b_2 + \frac{\gamma}{2} b_1 + \frac{\gamma}{2} b_3 - 2\mu a_2 = 0$
3	$(\alpha - 3^2) a_2 + \frac{\gamma}{2} a_2 + \frac{\gamma}{2} a_4 + 3\mu b_3 = 0$	$(\alpha - 3^2) b_3 + \frac{\gamma}{2} b_2 + \frac{\gamma}{2} b_4 - 2\mu a_3 = 0$
⋮	⋮	⋮
j	$(\alpha - j^2) a_2 + \frac{\gamma}{2} a_{j-1} + \frac{\gamma}{2} a_{j+1} + j\mu b_j = 0$	$(\alpha - j^2) b_j + \frac{\gamma}{2} b_{j-1} + \frac{\gamma}{2} b_{j+1} - j\mu a_j = 0$

Writing in the matrix form,

$$\underbrace{\begin{bmatrix}
\alpha & \gamma/2 & 0 & 0 & 0 & 0 & 0 & \cdots & 0 & 0 & \cdots \\
\gamma & (\alpha-1^2) & \mu & \gamma/2 & 0 & 0 & 0 & \cdots & 0 & 0 & \cdots \\
0 & -\mu & (\alpha-1^2) & 0 & \gamma/2 & 0 & 0 & \cdots & 0 & 0 & \cdots \\
0 & \gamma/2 & 0 & (\alpha-2^2) & 2\mu & \gamma/2 & 0 & \cdots & 0 & 0 & \cdots \\
0 & 0 & \gamma/2 & -2\mu & (\alpha-2^2) & 0 & \gamma/2 & \ddots & 0 & 0 & \cdots \\
0 & 0 & 0 & \gamma/2 & 0 & (\alpha-3^2) & 3\mu & \ddots & 0 & 0 & \cdots \\
0 & 0 & 0 & 0 & \gamma/2 & -3\mu & (\alpha-3^2) & \ddots & \gamma/2 & 0 & \cdots \\
\vdots & \vdots & \vdots & \vdots & \ddots & \ddots & \ddots & \ddots & 0 & \gamma/2 & \ddots \\
0 & 0 & 0 & 0 & 0 & 0 & \gamma/2 & 0 & (\alpha-j^2) & j\mu & \ddots \\
0 & 0 & 0 & 0 & 0 & 0 & 0 & \gamma/2 & -j\mu & (\alpha-j^2) & \ddots \\
\vdots & \vdots & \vdots & \vdots & \vdots & \vdots & \vdots & \ddots & \ddots & \ddots & \ddots
\end{bmatrix}}_{\mathbf{A}_1}
\underbrace{\begin{Bmatrix} a_0 \\ a_1 \\ b_1 \\ a_2 \\ b_2 \\ a_3 \\ b_3 \\ \vdots \\ a_j \\ b_j \\ \vdots \end{Bmatrix}}_{\mathbf{X}_1}
=
\underbrace{\begin{Bmatrix} 0 \\ 0 \\ 0 \\ 0 \\ 0 \\ 0 \\ 0 \\ \vdots \\ 0 \\ 0 \\ \vdots \end{Bmatrix}}_{\mathbf{0}}$$

(C.8)

The non-trivial solution to Eqn. (C.8) must exist physically, otherwise there is no motion to the vibration system described the damped Mathieu equation. The mathematical requirement for the existence of the non-trivial solution is that the infinite determinant of the coefficient matrix in Eqn. (C.8) must be zero,

$$\det(\mathbf{A}_1) = 0 \tag{C.9}$$

The form of a periodic solution of period 4π is express by the trigonometric series as follows,

$$\beta(\tau) = a_0 + \sum_{\substack{j=1 \\ j=2i-1}}^{\infty} \left[a_j \cos\left(\frac{j\tau}{2}\right) + b_j \sin\left(\frac{j\tau}{2}\right) \right] \tag{C.10}$$

where the summation is restricted to odd integers of j to exclude all 2π periodic terms. Substituting Eqn. (C.10) into the damped Mathieu equation (3.61), and utilizing the trigonometric identities

$$\begin{aligned} \cos(\tau)\cos\left(\frac{j\tau}{2}\right) &= \frac{1}{2}\left[\cos\left(\frac{j+2}{2}\right)\tau + \cos\left(\frac{j-2}{2}\right)\tau \right] \\ \cos(\tau)\sin\left(\frac{j\tau}{2}\right) &= \frac{1}{2}\left[\sin\left(\frac{j+2}{2}\right)\tau + \sin\left(\frac{j-2}{2}\right)\tau \right] \\ j &= 1,3,5,\cdots \end{aligned} \tag{C.11}$$

we have

$$\begin{aligned} &(\alpha + \gamma\cos\tau)a_0 + \sum_{\substack{j=1 \\ j=2i-1}}^{\infty} \left[-\left(\frac{j}{2}\right)^2 a_j \cos\left(\frac{j\tau}{2}\right) - \left(\frac{j}{2}\right)^2 b_j \sin\left(\frac{j\tau}{2}\right) \right] \\ &+ \sum_{\substack{j=1 \\ j=2i-1}}^{\infty} \left[-\left(\frac{j}{2}\right)\mu a_j \sin\left(\frac{j\tau}{2}\right) + \left(\frac{j}{2}\right)\mu b_j \cos\left(\frac{j\tau}{2}\right) \right] + \sum_{\substack{j=1 \\ j=2i-1}}^{\infty} \left[\alpha a_j \cos\left(\frac{j\tau}{2}\right) - \alpha b_j \sin\left(\frac{j\tau}{2}\right) \right] \\ &+ \sum_{\substack{j=1 \\ j=2i-1}}^{\infty} \frac{\gamma}{2} a_j \left[\cos\left(\frac{j+2}{2}\right)\tau + \cos\left(\frac{j-2}{2}\right)\tau \right] + \sum_{\substack{j=1 \\ j=2i-1}}^{\infty} \frac{\gamma}{2} b_j \left[\sin\left(\frac{j+2}{2}\right)\tau + \sin\left(\frac{j-2}{2}\right)\tau \right] = 0 \end{aligned} \tag{C.12}$$

Setting the coefficients of the linearly independent functions of τ to zero yields the table of the coefficient equations below (Table 35),

Table 35. Coefficients of $\cos\left(j\tau/2\right)$ and $\sin\left(j\tau/2\right)$ terms for solutions of period 4π.

j	Coefficient of $\cos\left(\frac{j\tau}{2}\right)$	Coefficient of $\sin\left(\frac{j\tau}{2}\right)$
1	$\frac{\gamma}{2}\left(a_1+a_3\right)+\left(\alpha-\left(\frac{1}{2}\right)^2\right)a_1+\frac{1}{2}\mu b_1=0$	$\frac{\gamma}{2}\left(-b_1+b_3\right)+\left(\alpha-\left(\frac{1}{2}\right)^2\right)b_1-\frac{1}{2}\mu a_1=0$
3	$\frac{\gamma}{2}\left(a_1+a_5\right)+\left(\alpha-\left(\frac{3}{2}\right)^2\right)a_3+\frac{3}{2}\mu b_3=0$	$\frac{\gamma}{2}\left(b_1+b_5\right)+\left(\alpha-\left(\frac{3}{2}\right)^2\right)b_3-\frac{3}{2}\mu a_3=0$
5	$\frac{\gamma}{2}\left(a_3+a_7\right)+\left(\alpha-\left(\frac{5}{2}\right)^2\right)a_5+\frac{5}{2}\mu b_5=0$	$\frac{\gamma}{2}\left(b_3+b_7\right)+\left(\alpha-\left(\frac{5}{2}\right)^2\right)b_5-\frac{5}{2}\mu a_5=0$
⋮	⋮	⋮
j	$\frac{\gamma}{2}\left(a_{j-2}+a_{j+2}\right)+\left(\alpha-\left(\frac{j}{2}\right)^2\right)a_j+\frac{j}{2}\mu b_j=0$	$\frac{\gamma}{2}\left(b_{j-2}+b_{j+2}\right)+\left(\alpha-\left(\frac{j}{2}\right)^2\right)b_j-\frac{j}{2}\mu a_j=0$

Writing in the matrix form,

$$\underbrace{\begin{bmatrix}
\alpha-(1/2)^2+\gamma/2 & \mu/2 & \gamma/2 & 0 & 0 & 0 & \cdots & 0 & 0 & \cdots \\
-\mu/2 & \alpha-(1/2)^2-\gamma/2 & 0 & \gamma/2 & 0 & 0 & \cdots & 0 & 0 & \cdots \\
\gamma/2 & 0 & \alpha-(3/2)^2 & 3\mu/2 & \gamma/2 & 0 & \cdots & 0 & 0 & \cdots \\
0 & \gamma/2 & -3\mu/2 & \alpha-(3/2)^2 & 0 & \gamma/2 & \ddots & 0 & 0 & \cdots \\
0 & 0 & \gamma/2 & 0 & \alpha-(5/2)^2 & 5\mu/2 & \ddots & 0 & 0 & \cdots \\
0 & 0 & 0 & \gamma/2 & -5\mu/2 & \alpha-(5/2)^2 & \ddots & \gamma/2 & 0 & \cdots \\
\vdots & \vdots & \vdots & \ddots & \ddots & \ddots & \ddots & 0 & \gamma/2 & \ddots \\
0 & 0 & 0 & 0 & 0 & \gamma/2 & 0 & \alpha-(j/2)^2 & j\mu/2 & \ddots \\
0 & 0 & 0 & 0 & 0 & 0 & \gamma/2 & -j\mu/2 & \alpha-(j/2)^2 & \ddots \\
\vdots & \vdots & \vdots & \vdots & \vdots & \vdots & \ddots & \ddots & \ddots & \ddots
\end{bmatrix}}_{\mathbf{A}_2}
\underbrace{\begin{Bmatrix} a_1 \\ b_1 \\ a_3 \\ b_3 \\ a_5 \\ b_5 \\ \vdots \\ a_j \\ b_j \\ \vdots \end{Bmatrix}}_{\mathbf{X}_2}
=
\underbrace{\begin{Bmatrix} 0 \\ 0 \\ 0 \\ 0 \\ 0 \\ 0 \\ 0 \\ 0 \\ 0 \\ 0 \end{Bmatrix}}_{\mathbf{0}}$$

(C.13)

The non-trivial solution to Eqn. (3.61) must exist physically, otherwise there is no motion to the vibration system described the damped Mathieu equation. The mathematical requirement for the existence of the non-trivial solution is that the infinite determinant of the coefficient matrix in Eqn. (C.13) must also be zero,

$$\det\left(\mathbf{A}_2\right)=0 \tag{5.5}$$

The whole chart of the damped Mathieu equation determined by the Hill's infinite determinant method is shown in Fig. 108.

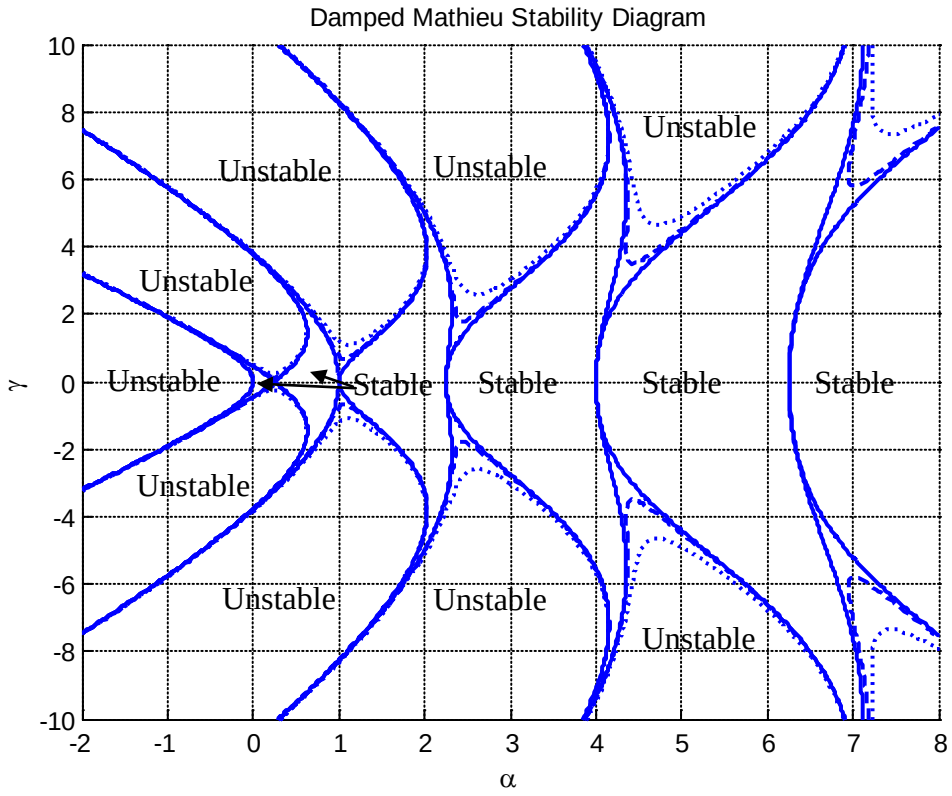

Fig. 108. The whole Mathieu stability diagram described by the damped Mathieu Equation: undamped $\mu = 0.0(-)$, damped $\mu = 0.1(---)$, and damped $\mu = 0.25(\cdots\cdots)$.

APPENDIX D

COMPARISON OF OTHER PARTIALLY OPEN END MODELS

D.1 Comparison of the #1 Valves Opening Model

D.1.1 Comparison of the heave motion

The specific parameters for the #1 valves opening model are listed in Table 36. For brevity, we drop out the time domain comparisons of the simulations and measurements for the #1 valves opening model.

The dynamics of the #1 valves opening model is quite similar to the closed end model and the PS valves opening model. Table 37 presents the time domain results of the heave-pitch coupled motion ($C_{a,t}$ =1.11, $C_{d,t}$ =2.5) for the #1 valves opening model. Fig. 109 presents the comparison between the simulations of the coupled motion scheme ($C_{a,t}$ =1.11, $C_{d,t}$ =2.5) and model tests for the #1 valves opening model.

Table 36. #1 valves opening model parameters for numerical simulations.

Model parameters	Notation	Value	Note
Length	L	3 ft (0.914 m)	
Outer diameter	D	6 in (15.24 cm)	
Wall thickness	t	0.25 in (0.64 cm)	
Opening area ratio (Perforation)	γ	0.90%	For the top cap
Normal added-mass coef.	$C_{a,n}$	1.2	
Normal drag coef.	$C_{d,n}$	1.0	
Axial added-mass coef.	$C_{a,t}$	1.11	From model test
Axial drag coef.	$C_{d,t}$	2.5	
Coef. of pitch damping term	$C_{D\beta}$	9.8236	Refer to Appendix B
Weight in air	W	16.0 lb (71.172 N)	
Weight in water	W'	9.6 lb (42.703 N)	
Weight of water inside pile plus water displaced by pile	W_0	36.8 lb (163.695 N)	
Buoyancy	F_B	6.729 lb (29.932 N)	
Moment of inertia in air	$I_{\beta p}$	1.5780 slug·ft^2 (2.139 kg/m^2)	Refer to Appendix B
Added moment of inertia in water	$I_{\beta a}$	4.1176 slug·ft^2 (5.583 kg/m^2)	Refer to Appendix B
Moment of inertia in water	I_{β}	5.6956 slug·ft^2 (7.722 kg/m^2)	
Gravity center from eye bolt	$O'G$	1.44 ft (0.439 m)	Including hanging bar height 2"
Buoyancy center from eye bolt	$O'B$	1.57 ft (0.479 m)	Including hanging bar height 2"
Heave natural frequency	f_n	0.5050 Hz	From model test
Pitch natural frequency	f_p	0.2400 Hz	Hand calculation

Table 37. Numerical results of heave motion for the #1 valves opening model simulations using the heave-pitch coupling scheme ($C_{a,t}$=1.11, $C_{d,t}$=2.5).

f (Hz)	ST1 (lb)	ST2 (lb)	ST2/ST1	SD3 (ft)	SD2 (ft)	SD2/SD3	SD2/SD1	SD3/SD1
0.3750	5.3532	5.3333	0.9963	0.2504	0.5444	2.1738	2.1776	1.0016
0.4000	7.2511	7.2276	0.9968	0.2505	0.6477	2.5859	2.5908	1.0020
0.4250	10.1919	10.1640	0.9973	0.2506	0.8055	3.2149	3.2220	1.0024
0.4500	14.9309	14.8969	0.9977	0.2507	1.0501	4.1895	4.2004	1.0028
0.4750	21.3930	21.3715	0.9990	0.2507	1.3437	5.3594	5.3748	1.0028
0.5000	26.4090	26.4025	0.9998	0.2507	1.4933	5.9563	5.9732	1.0028
0.5250	27.0906	27.1061	1.0006	0.2505	1.3927	5.5587	5.5708	1.0020
0.5500	23.8209	23.8499	1.0012	0.2514	1.1218	4.4623	4.4872	1.0056
0.5750	19.2800	19.3186	1.0020	0.2513	0.8347	3.3216	3.3388	1.0052
0.6000	15.7018	15.7432	1.0026	0.2511	0.6260	2.4932	2.5040	1.0044
0.6250	13.2743	13.3232	1.0037	0.2506	0.4872	1.9441	1.9488	1.0024
0.6500	11.6202	11.6736	1.0046	0.2513	0.3958	1.5755	1.5832	1.0052
0.6750	10.4319	10.4901	1.0056	0.2513	0.3299	1.3128	1.3196	1.0052
0.7000	9.5677	9.6207	1.0055	0.2514	0.2811	1.1180	1.1244	1.0056

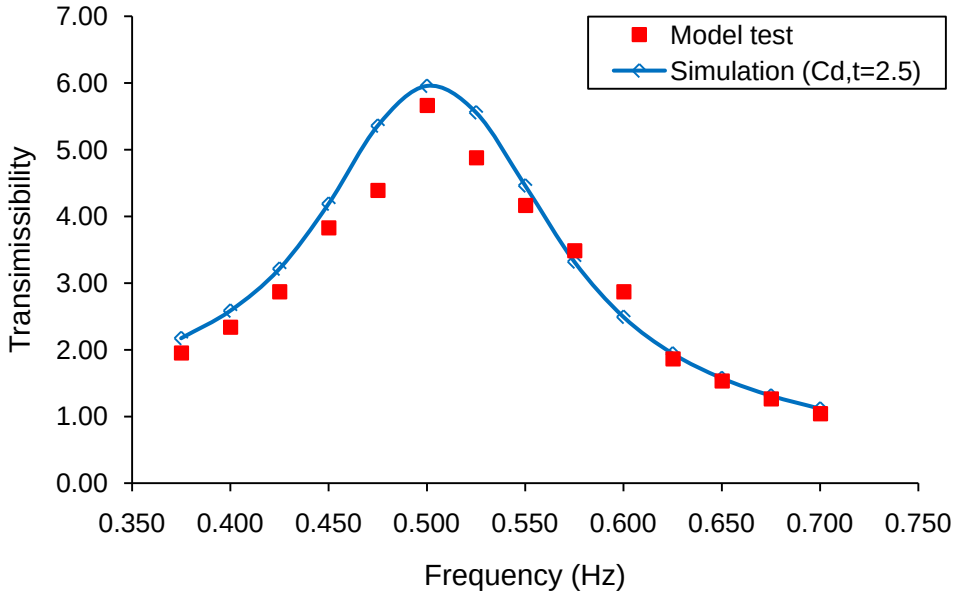

Fig. 109. Comparison of the heave amplitude transmissibility curves from simulations (heave-pitch coupling, $C_{a,t}$ =1.11, $C_{d,t}$ =2.5) for the #1 valves opening model.

D.1.2 Comparison of the heave induced pitch motion

Table 38 summarizes the time domain results of the heave induced pitch motion for the #1 valves opening model simulations ($C_{a,t}$ =1.11, $C_{d,t}$ =2.5) based on the heave-pitch coupled motion scheme, and each columns have the same meaning as presented in the closed end model simulation. Fig. 110 shows satisfactory agreement in the comparison between the simulated pitch amplitude with measured pitch amplitude for #1 valves opening model. The heave excitation frequency range for the heave induced pitch amplification is also quite broad (0.455~0.485 Hz) as for the closed end model.

Table 38. Numerical results of heave induced pitch motion for the # 1 valves opening model simulations using the heave-pitch coupling scheme ($C_{a,t}$=1.11, $C_{d,t}$=2.5).

f (Hz)	f_β (Hz)	$f - f_\beta$ (Hz)	f_β/f	Pitch amplitude (rad)	β_{video} (rad)	β_{error} (rad)
0.3750	0.2333	0.1417	0.6221	0.0008	-	-
0.4000	0.2333	0.1667	0.5833	0.0008	-	-
0.4250	0.2333	0.1917	0.5489	0.0009	-	-
0.4500	0.2306	0.2194	0.5124	0.0014	-	-
0.4550	0.2278	0.2272	0.5007	0.0060	-	-
0.4600	0.2306	0.2294	0.5013	0.0342	-	-
0.4650	0.2333	0.2317	0.5017	0.0429	-	-
0.4700	0.2361	0.2339	0.5023	0.0455	-	-
0.4750	0.2389	0.2361	0.5029	0.0434	0.0436	0.0087
0.4800	0.2389	0.2411	0.4977	0.0362	-	-
0.4850	0.2417	0.2433	0.4984	0.0196	-	-
0.4900	0.2389	0.2511	0.4876	0.0012	-	-
0.4950	0.2389	0.2561	0.4826	0.0009	-	-
0.5000	0.2389	0.2611	0.4778	0.0010	-	-
0.5250	0.2361	0.2889	0.4497	0.0008	-	-
0.5500	0.2361	0.3139	0.4293	0.0008	0.0017	0.0017
0.5750	0.2333	0.3417	0.4057	0.0008	-	-
0.6000	0.2333	0.3667	0.3888	0.0007	-	-
0.6250	0.2333	0.3917	0.3733	0.0007	-	-
0.6500	0.2333	0.4167	0.3589	0.0007	-	-
0.6750	0.2333	0.4417	0.3456	0.0007	-	-
0.7000	0.2333	0.4667	0.3333	0.0007	0.0017	0.0017

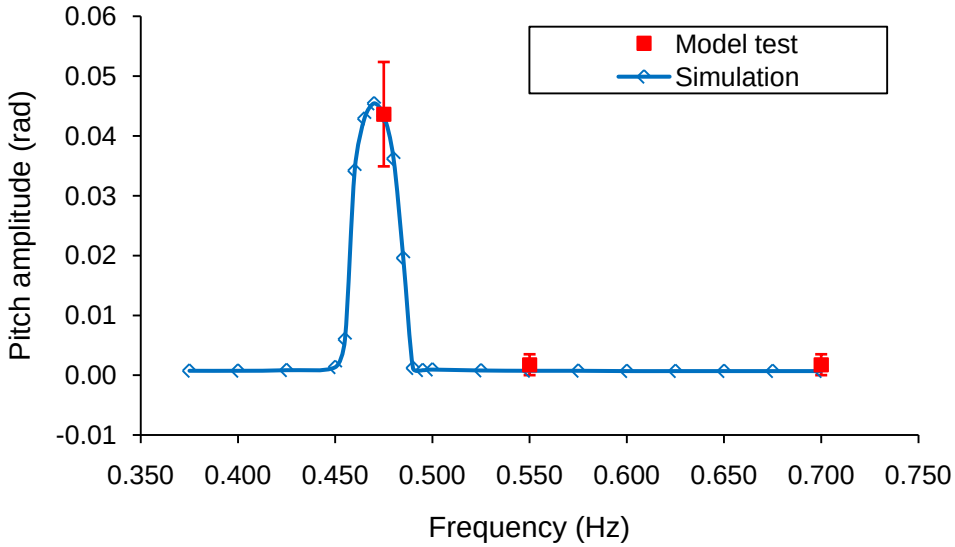

Fig. 110. Comparison of pitch amplitudes of the # 1 valves opening model pile between simulations (heave-pitch coupling, $C_{a,t}$=1.11, $C_{d,t}$=2.5) and model tests.

D.2 Comparison of the # 2' Valves Opening Model

D.2.1 Comparison of the heave motion

The specific parameters for the #2' valves opening model are listed in Table 39. For brevity, we drop out the time domain comparisons of the simulations and measurements for the #2' valves opening model.

The dynamics of the #2' valves opening model is quite similar to the closed end model and the PS valves opening model. Table 40 presents the time domain results of the heave-pitch coupled motion ($C_{a,t}$=1.08, $C_{d,t}$=3.0) for the #2' valves opening model. Fig. 111 presents the comparison between the simulations of the coupled motion scheme ($C_{a,t}$=1.08, $C_{d,t}$=3.0) and model tests for the #2' valves opening model.

Table 39. #2' valves opening model parameters for numerical simulations.

Model parameters	Notation	Value	Note
Length	L	3 ft (0.914 m)	
Outer diameter	D	6 in (15.24 cm)	
Wall thickness	t	0.25 in (0.64 cm)	
Opening area ratio (Perforation)	γ	3.70%	For the top cap
Normal added-mass coef.	$C_{a,n}$	1.2	
Normal drag coef.	$C_{d,n}$	1.0	
Axial added-mass coef.	$C_{a,t}$	1.08	From model test
Axial drag coef.	$C_{d,t}$	3.0	
Coef. of pitch damping term	$C_{D\beta}$	9.8236	Refer to Appendix B
Weight in air	W	16.0 lb (71.172 N)	
Weight in water	W'	9.6 lb (42.703 N)	
Weight of water inside pile plus water displaced by pile	W_0	36.8 lb (163.695 N)	
Buoyancy	F_B	6.729 lb (29.932 N)	
Moment of inertia in air	$I_{\beta p}$	1.5780 slug·ft^2 (2.139 kg/m^2)	Refer to Appendix B
Added moment of inertia in water	$I_{\beta a}$	4.1176 slug·ft^2 (5.583 kg/m^2)	Refer to Appendix B
Moment of inertia in water	I_{β}	5.6956 slug·ft^2 (7.722 kg/m^2)	
Gravity center from eye bolt	$O'G$	1.44 ft (0.439 m)	Including hanging bar height 2"
Buoyancy center from eye bolt	$O'B$	1.57 ft (0.479 m)	Including hanging bar height 2"
Heave natural frequency	f_n	0.5100 Hz	From model test
Pitch natural frequency	f_p	0.2400 Hz	Hand calculation

Table 40. Numerical results of heave motion for the #2' valves opening model simulations using the heave-pitch coupling scheme ($C_{a,t}$=1.08, $C_{d,t}$=3.0).

f (Hz)	ST1 (lb)	ST2 (lb)	ST2/ST1	SD3 (ft)	SD2 (ft)	SD2/SD3	SD2/SD1	SD3/SD1
0.3750	4.3620	4.3457	0.9963	0.2504	0.4525	1.8069	1.8098	1.0016
0.4000	5.8653	5.8453	0.9966	0.2505	0.5344	2.1333	2.1376	1.0020
0.4250	8.1629	8.1401	0.9972	0.2506	0.6580	2.6256	2.6319	1.0024
0.4500	11.8491	11.8241	0.9979	0.2507	0.8500	3.3905	3.4000	1.0028
0.4750	17.1662	17.1476	0.9989	0.2507	1.1008	4.3907	4.4030	1.0028
0.5000	21.9119	21.9016	0.9995	0.2507	1.2643	5.0430	5.0572	1.0028
0.5250	23.2807	23.2864	1.0002	0.2509	1.2193	4.8598	4.8773	1.0036
0.5500	21.0615	21.0848	1.0011	0.2513	1.0106	4.0213	4.0423	1.0052
0.5750	17.2286	17.2616	1.0019	0.2514	0.7601	3.0233	3.0403	1.0056
0.6000	13.9637	14.0009	1.0027	0.2511	0.5676	2.2606	2.2705	1.0044
0.6250	11.7109	11.7524	1.0035	0.2506	0.4389	1.7512	1.7554	1.0024
0.6500	10.1893	10.2346	1.0044	0.2513	0.3539	1.4081	1.4154	1.0052
0.6750	9.1034	9.1529	1.0054	0.2513	0.2935	1.1679	1.1740	1.0052
0.7000	8.3167	8.3618	1.0054	0.2514	0.2492	0.9913	0.9969	1.0056

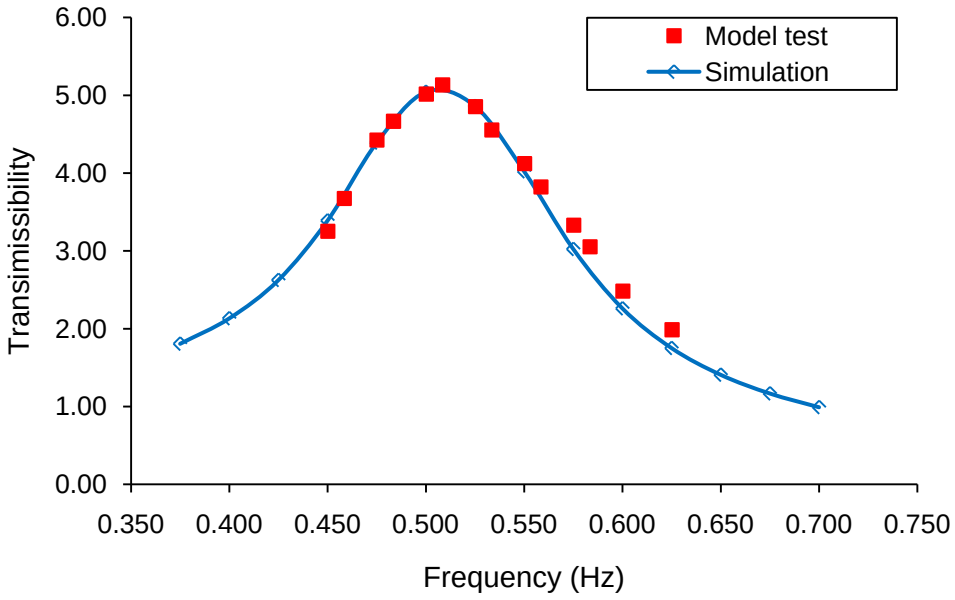

Fig. 111. Comparison of the heave amplitude transmissibility curves from simulations (heave-pitch coupling, $C_{a,t}$=1.08, $C_{d,t}$=3.0) for the #2' valves opening model.

D.2.2 Comparison of the heave induced pitch motion

Table 41 summarizes the time domain results of the heave induced pitch motion for the #2' valves opening model simulations ($C_{a,t}$ =1.08, $C_{d,t}$ =3.0) based on the heave-pitch coupled motion scheme, and each columns have the same meaning as presented in the closed end model simulation. Fig. 112 shows satisfactory agreement in the comparison between the simulated pitch amplitude with measured pitch amplitude for #2' valves opening model. The heave excitation frequency range for the heave induced pitch amplification is also quite broad (0.455~0.485 Hz) as for the closed end model.

Table 41. Numerical results of heave induced pitch motion for the #2' valves opening model simulations using the heave-pitch coupling scheme ($C_{a,t}$ =1.08, $C_{d,t}$ =3.0).

f (Hz)	f_β (Hz)	$f - f_\beta$ (Hz)	f_β/f	Pitch amplitude (rad)	β_{video} (rad)	β_{error} (rad)
0.3750	0.2333	0.1417	0.6221	0.0008	-	-
0.4000	0.2333	0.1667	0.5833	0.0008	-	-
0.4250	0.2333	0.1917	0.5489	0.0008	-	-
0.4500	0.2306	0.2194	0.5124	0.0010	-	-
0.4550	0.2306	0.2244	0.5068	0.0024	-	-
0.4600	0.2306	0.2294	0.5013	0.0309	-	-
0.4650	0.2333	0.2317	0.5017	0.0401	-	-
0.4700	0.2361	0.2339	0.5023	0.0427	-	-
0.4750	0.2389	0.2361	0.5029	0.0404	0.0436	0.0087
0.4800	0.2389	0.2411	0.4977	0.0327	-	-
0.4850	0.2417	0.2433	0.4984	0.0122	-	-
0.4900	0.2389	0.2511	0.4876	0.0005	-	-
0.4950	0.2389	0.2561	0.4826	0.0010	-	-
0.5000	0.2361	0.2639	0.4722	0.0010	-	-
0.5250	0.2361	0.2889	0.4497	0.0008	-	-
0.5500	0.2361	0.3139	0.4293	0.0008	0.0017	0.0017
0.5750	0.2333	0.3417	0.4057	0.0008	-	-
0.6000	0.2333	0.3667	0.3888	0.0007	-	-
0.6250	0.2333	0.3917	0.3733	0.0007	0.0017	0.0017
0.6500	0.2333	0.4167	0.3589	0.0007	-	-
0.6750	0.2333	0.4417	0.3456	0.0007	-	-
0.7000	0.2333	0.4667	0.3333	0.0007	-	-

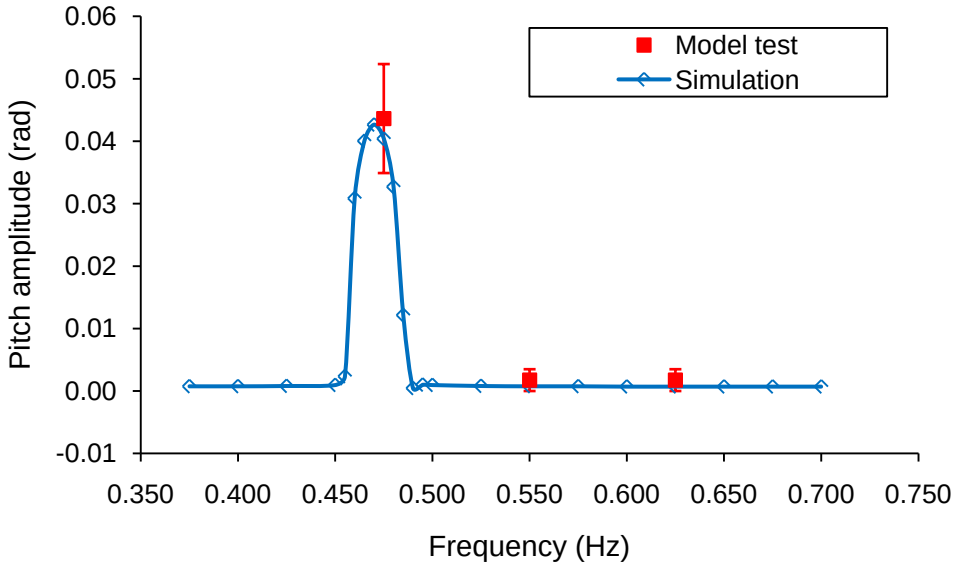

Fig. 112. Comparison of pitch amplitudes of the #2' valves opening model pile between simulations (heave-pitch coupling, $C_{a,t}$ =1.08, $C_{d,t}$ =3.0) and model tests.

D.3 Comparison of the #3 Valves Opening Model

D.3.1 Comparison of the heave motion

The specific parameters for the #3 valves opening model are listed in Table 42. For brevity, we drop out the time domain comparisons of the simulations and measurements for the #3 valves opening model. The dynamics of the #3 valves opening model is quite similar to the #4 valves opening model.

Table 43 presents the time domain results of the heave-pitch coupled motion (Ca,t =0.91, Cd,t =5.0) for the #3 valves opening model. Fig. 113 presents the comparison between the simulations of the coupled motion scheme (Ca,t =0.91, Cd,t =5.0) and model tests for the #3 valves opening model.

Table 42. #3 valves opening model parameters for numerical simulations.

Model parameters	Notation	Value	Note
Length	L	3 ft (0.914 m)	
Outer diameter	D	6 in (15.24 cm)	
Wall thickness	t	0.25 in (0.64 cm)	
Opening area ratio (Perforation)	γ	10.30%	For the top cap
Normal added-mass coef.	$C_{a,n}$	1.2	
Normal drag coef.	$C_{d,n}$	1.0	
Axial added-mass coef.	$C_{a,t}$	0.91	From model test
Axial drag coef.	$C_{d,t}$	5.0	
Coef. of pitch damping term	$C_{D\beta}$	9.8236	Refer to Appendix B
Weight in air	W	16.0 lb (71.172 N)	
Weight in water	W'	9.6 lb (42.703 N)	
Weight of water inside pile plus water displaced by pile	W_0	36.8 lb (163.695 N)	
Buoyancy	F_B	6.729 lb (29.932 N)	
Moment of inertia in air	$I_{\beta p}$	1.5780 slug·ft^2 (2.139 kg/m^2)	Refer to Appendix B
Added moment of inertia in water	$I_{\beta a}$	4.1176 slug·ft^2 (5.583 kg/m^2)	Refer to Appendix B
Moment of inertia in water	I_{β}	5.6956 slug·ft^2 (7.722 kg/m^2)	
Gravity center from eye bolt	$O'G$	1.44 ft (0.439 m)	Including hanging bar height 2"
Buoyancy center from eye bolt	$O'B$	1.57 ft (0.479 m)	Including hanging bar height 2"
Heave natural frequency	f_n	0.5400 Hz	From model test
Pitch natural frequency	f_p	0.2400 Hz	Hand calculation

Table 43. Numerical results of heave motion for the #3 valves opening model simulations using the heave-pitch coupling scheme ($C_{a,t}$=0.91, $C_{d,t}$=5.0).

f (Hz)	ST1 (lb)	ST2 (lb)	ST2/ST1	SD3 (ft)	SD2 (ft)	SD2/SD3	SD2/SD1	SD3/SD1
0.3750	4.0598	4.0397	0.9950	0.2504	0.4712	1.8814	1.8848	1.0016
0.4000	5.2471	5.2224	0.9953	0.2505	0.5342	2.1330	2.1368	1.0020
0.4250	6.8808	6.8545	0.9962	0.2506	0.6193	2.4718	2.4772	1.0024
0.4500	9.1640	9.1363	0.9970	0.2506	0.7324	2.9219	2.9296	1.0024
0.4750	12.1503	12.1256	0.9980	0.2507	0.8664	3.4556	3.4656	1.0028
0.5000	15.3707	15.3495	0.9986	0.2507	0.9830	3.9206	3.9320	1.0028
0.5250	17.9018	17.8962	0.9997	0.2508	1.0359	4.1301	4.1436	1.0032
0.5500	19.1426	19.1480	1.0003	0.2509	1.0116	4.0325	4.0464	1.0036
0.5750	19.0138	19.0371	1.0012	0.2510	0.9249	3.6842	3.6996	1.0040
0.6000	17.7827	17.8166	1.0019	0.2509	0.8002	3.1889	3.2008	1.0036
0.6250	15.9480	15.9918	1.0027	0.2506	0.6660	2.6572	2.6640	1.0024
0.6500	14.0930	14.1423	1.0035	0.2512	0.5470	2.1771	2.1880	1.0048
0.6750	12.4959	12.5522	1.0045	0.2513	0.4515	1.7971	1.8060	1.0052
0.7000	11.2503	11.3123	1.0055	0.2514	0.3787	1.5064	1.5148	1.0056

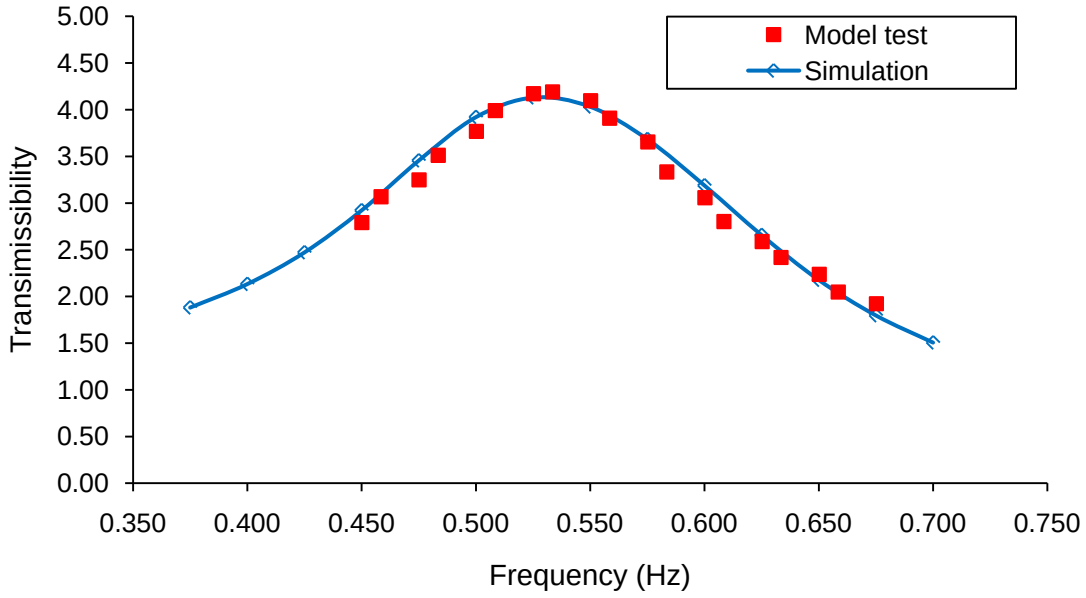

Fig. 113. Comparison of the heave amplitude transmissibility curves from simulations (heave-pitch coupling, $C_{a,t}$=0.91, $C_{d,t}$=5.0) for the #3 valves opening model.

D.3.2 Comparison of the heave induced pitch motion

Table 44 summarizes the time domain results of the heave induced pitch motion for the #3 valves opening model simulations ($C_{a,t}$=0.91, $C_{d,t}$=5.0) based on the heave-pitch coupled motion scheme, and each columns have the same meaning as presented in the closed end model simulation. Fig. 114 shows satisfactory agreement in the comparison between the simulated pitch amplitude with measured pitch amplitude for #3 valves opening model. The heave excitation frequency range for the heave induced pitch amplification is also quite narrow (0.460~0.480 Hz) as for #4 valves opening model.

Table 44. Numerical results of heave induced pitch motion for the #3 valves opening model simulations using the heave-pitch coupling scheme ($C_{a,t}$=0.91, $C_{d,t}$=5.0).

f (Hz)	f_β (Hz)	$f - f_\beta$ (Hz)	f_β/f	Pitch amplitude (rad)	β_{video} (rad)	β_{error} (rad)
0.3750	0.2333	0.1417	0.6221	0.0007	-	-
0.4000	0.2333	0.1667	0.5833	0.0008	-	-
0.4250	0.2333	0.1917	0.5489	0.0008	-	-
0.4500	0.2333	0.2167	0.5184	0.0010	-	-
0.4550	0.2333	0.2217	0.5127	0.0012	-	-
0.4600	0.2306	0.2294	0.5013	0.0071	-	-
0.4650	0.2333	0.2317	0.5017	0.0238	-	-
0.4700	0.2361	0.2339	0.5023	0.0253	-	-
0.4750	0.2361	0.2389	0.4971	0.0213	0.0262	0.0087
0.4800	0.2361	0.2439	0.4919	0.0016	-	-
0.4850	0.2361	0.2489	0.4868	0.0010	-	-
0.4900	0.2361	0.2539	0.4818	0.0009	-	-
0.4950	0.2361	0.2589	0.4770	0.0009	-	-
0.5000	0.2361	0.2639	0.4722	0.0008	-	-
0.5250	0.2361	0.2889	0.4497	0.0008	-	-
0.5500	0.2333	0.3167	0.4242	0.0008	0.0017	0.0017
0.5750	0.2333	0.3417	0.4057	0.0007	-	-
0.6000	0.2333	0.3667	0.3888	0.0007	-	-
0.6250	0.2333	0.3917	0.3733	0.0007	-	-
0.6500	0.2333	0.4167	0.3589	0.0007	-	-
0.6750	0.2333	0.4417	0.3456	0.0007	-	-
0.7000	0.2333	0.4667	0.3333	0.0007	0.0017	0.0017

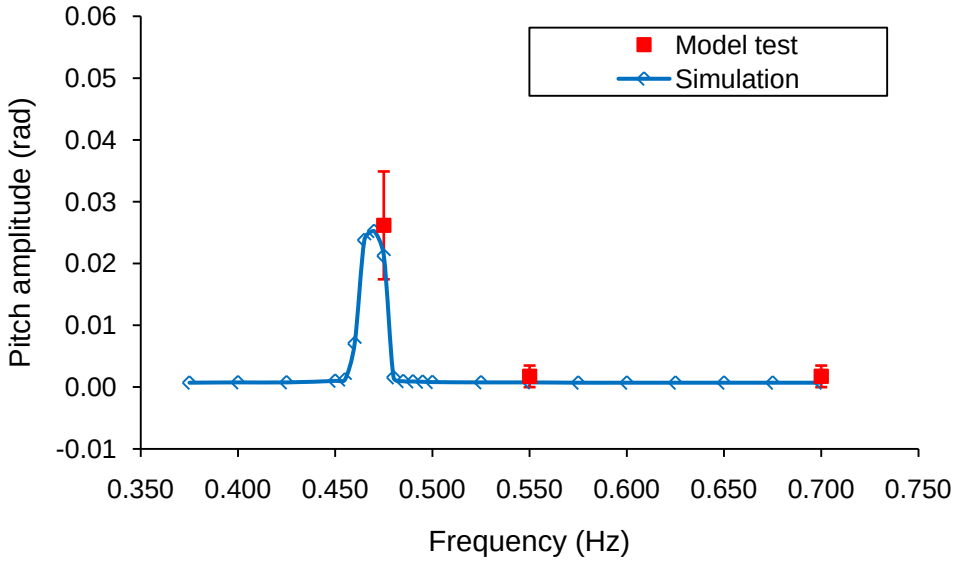

Fig. 114. Comparison of pitch amplitudes of the #3 valves opening model pile between simulations (heave-pitch coupling, $C_{a,t}$=0.91, $C_{d,t}$=5.0) and model tests.

D.4 Comparison of the #1, #2, #3 Valves Opening Model

D.4.1 Comparison of the heave motion

The specific parameters for the #1, #2, #3 valves opening model are listed in Table 45. For brevity, we drop out the time domain comparisons of the simulations and measurements for the #1, #2, #3 valves opening model.

The dynamics of the #1, #2, #3 valves opening model is quite similar to the #1, #2, #3, #4 valves opening model. Table 46 presents the time domain results of the heave-pitch coupled motion ($C_{a,t}$=0.71, $C_{d,t}$=7.5) for the #1, #2, #3 valves opening model. Fig. 115 presents the comparison between the simulations of the coupled motion scheme ($C_{a,t}$ =0.71, $C_{d,t}$=7.5) and model tests for the #1, #2, #3 valves opening model.

Table 45. #1, #2, #3 valves opening model parameters for numerical simulations.

Model parameters	Notation	Value	Note
Length	L	3 ft (0.914 m)	
Outer diameter	D	6 in (15.24 cm)	
Wall thickness	t	0.25 in (0.64 cm)	
Opening area ratio (Perforation)	γ	17.90%	For the top cap
Normal added-mass coef.	$C_{a,n}$	1.2	
Normal drag coef.	$C_{d,n}$	1.0	
Axial added-mass coef.	$C_{a,t}$	0.71	From model test
Axial drag coef.	$C_{d,t}$	7.5	
Coef. of pitch damping term	$C_{D\beta}$	9.8236	Refer to Appendix B
Weight in air	W	16.0 lb (71.172 N)	
Weight in water	W'	9.6 lb (42.703 N)	
Weight of water inside pile plus water displaced by pile	W_0	36.8 lb (163.695 N)	
Buoyancy	F_B	6.729 lb (29.932 N)	
Moment of inertia in air	$I_{\beta p}$	1.5780 slug·ft^2 (2.139 kg/m^2)	Refer to Appendix B
Added moment of inertia in water	$I_{\beta a}$	4.1176 slug·ft^2 (5.583 kg/m^2)	Refer to Appendix B
Moment of inertia in water	I_{β}	5.6956 slug·ft^2 (7.722 kg/m^2)	
Gravity center from eye bolt	$O'G$	1.44 ft (0.439 m)	Including hanging bar height 2"
Buoyancy center from eye bolt	$O'B$	1.57 ft (0.479 m)	Including hanging bar height 2"
Heave natural frequency	f_n	0.5850 Hz	From model test
Pitch natural frequency	f_p	0.2400 Hz	Hand calculation

Table 46. Numerical results of heave motion for the #1, #2, #3 valves opening model simulations using the heave-pitch coupling scheme ($C_{a,t}$=0.71, $C_{d,t}$=7.5).

f (Hz)	ST1 (lb)	ST2 (lb)	ST2/ST1	SD3 (ft)	SD2 (ft)	SD2/SD3	SD2/SD1	SD3/SD1
0.4500	6.1394	6.1093	0.9951	0.2506	0.5699	2.2738	2.2796	1.0024
0.4750	7.7867	7.7620	0.9968	0.2507	0.6451	2.5733	2.5804	1.0028
0.5000	9.7558	9.7343	0.9978	0.2507	0.7246	2.8897	2.8984	1.0028
0.5250	11.8186	11.8030	0.9987	0.2508	0.7910	3.1535	3.1640	1.0032
0.5500	13.6227	13.6112	0.9992	0.2509	0.8277	3.2987	3.3108	1.0036
0.5750	14.8984	14.8927	0.9996	0.2509	0.8288	3.3029	3.3152	1.0036
0.6000	15.5549	15.5546	1.0000	0.2510	0.7981	3.1796	3.1924	1.0040
0.6250	15.5647	15.5901	1.0016	0.2507	0.7431	2.9635	2.9724	1.0028
0.6500	15.1221	15.1552	1.0022	0.2512	0.6718	2.6742	2.6872	1.0048
0.6750	14.2670	14.3098	1.0030	0.2513	0.5930	2.3602	2.3720	1.0052
0.7000	13.2698	13.3090	1.0030	0.2514	0.5155	2.0504	2.0620	1.0056
0.7250	12.2007	12.2603	1.0049	0.2515	0.4451	1.7697	1.7804	1.0060
0.7500	11.2385	11.3041	1.0058	0.2516	0.3848	1.5295	1.5392	1.0064
0.7750	10.4086	10.4781	1.0067	0.2518	0.3349	1.3301	1.3396	1.0072
0.8000	9.7091	9.7860	1.0079	0.2519	0.2938	1.1667	1.1752	1.0076
0.8250	9.1379	9.2105	1.0080	0.2520	0.2601	1.0321	1.0404	1.0080
0.8500	8.6364	8.7211	1.0098	0.2521	0.2325	0.9219	0.9300	1.0084
0.8750	8.2137	8.3098	1.0117	0.2523	0.2092	0.8291	0.8368	1.0092
0.9000	7.8864	7.9724	1.0109	0.2528	0.1895	0.7497	0.7580	1.0112
0.9250	7.5742	7.6588	1.0112	0.2524	0.1726	0.6838	0.6904	1.0096
0.9500	7.3242	7.4146	1.0123	0.2527	0.1585	0.6271	0.6340	1.0108
0.9750	7.0832	7.1974	1.0161	0.2528	0.1459	0.5770	0.5836	1.0112
1.0000	6.8538	6.9857	1.0192	0.2523	0.1343	0.5324	0.5372	1.0092
1.0250	6.7226	6.8358	1.0168	0.2533	0.1255	0.4954	0.5020	1.0132
1.0500	6.5400	6.6794	1.0213	0.2533	0.1168	0.4611	0.4672	1.0132

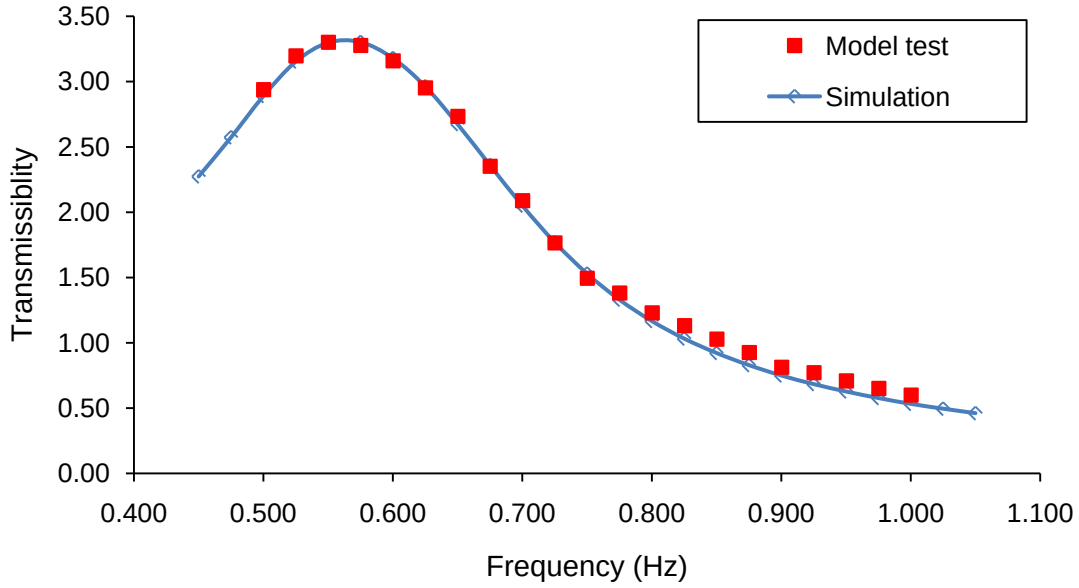

Fig. 115. Comparison of the heave amplitude transmissibility curves from simulations (heave-pitch coupling, $C_{a,t}$ =0.71, $C_{d,t}$ =7.5) for the #1, #2, #3 valves opening model.

D.4.2 Comparison of the heave induced pitch motion

Table 47 summarizes the time domain results of the heave induced pitch motion for the #1, #2, #3 valves opening model simulations ($C_{a,t}$ =0.71, $C_{d,t}$ =7.5) based on the heave-pitch coupled motion scheme, and each columns have the same meaning as presented in the closed end model simulation. Fig. 116 shows satisfactory agreement in the comparison between the simulated pitch amplitude with measured pitch amplitude for #1, #2, #3 valves opening model. The heave excitation frequency range for the heave induced pitch amplification is also quite narrow (0.460~0.480 Hz) as for #1, #2, #3, #4 valves opening model.

Table 47. Numerical results of heave induced pitch motion for the #1, #2, #3 valves opening model simulations using the heave-pitch coupling scheme ($C_{a,t}$=0.71, $C_{d,t}$=7.5).

f (Hz)	f_β (Hz)	$f - f_\beta$ (Hz)	f_β/f	Pitch amplitude (rad)	β_{video} (rad)	β_{error} (rad)
0.4500	0.2333	0.2167	0.5184	0.0007	-	-
0.4550	0.2333	0.2217	0.5127	0.0007	-	-
0.4600	0.2333	0.2267	0.5072	0.0007	-	-
0.4650	0.2333	0.2317	0.5017	0.0129	-	-
0.4700	0.2361	0.2339	0.5023	0.0104	-	-
0.4750	0.2361	0.2389	0.4971	0.0010	-	-
0.4800	0.2361	0.2439	0.4919	0.0009	-	-
0.4850	0.2333	0.2517	0.4810	0.0008	-	-
0.4900	0.2333	0.2567	0.4761	0.0007	-	-
0.4950	0.2333	0.2617	0.4713	0.0007	-	-
0.5000	0.2333	0.2667	0.4666	0.0008	0.0017	0.0017
0.5250	0.2333	0.2917	0.4444	0.0008	-	-
0.5500	0.2333	0.3167	0.4242	0.0008	-	-
0.5750	0.2333	0.3417	0.4057	0.0008	-	-
0.6000	0.2333	0.3667	0.3888	0.0008	0.0017	0.0017
0.6250	0.2333	0.3917	0.3733	0.0007	-	-
0.6500	0.2333	0.4167	0.3589	0.0007	-	-
0.6750	0.2333	0.4417	0.3456	0.0007	-	-
0.7000	0.2333	0.4667	0.3333	0.0007	0.0017	0.0017
0.7250	0.2333	0.4917	0.3218	0.0007	-	-
0.7500	0.2333	0.5167	0.3111	0.0007	-	-
0.7750	0.2333	0.5417	0.3010	0.0007	-	-
0.8000	0.2333	0.5667	0.2916	0.0007	-	-
0.8250	0.2333	0.5917	0.2828	0.0007	-	-
0.8500	0.2333	0.6167	0.2745	0.0007	-	-
0.8750	0.2333	0.6417	0.2666	0.0007	-	-
0.9000	0.2333	0.6667	0.2592	0.0007	-	-
0.9250	0.2333	0.6917	0.2522	0.0007	-	-
0.9500	0.2333	0.7167	0.2456	0.0007	-	-
0.9750	0.2333	0.7417	0.2393	0.0007	-	-
1.0000	0.2333	0.7667	0.2333	0.0007	-	-
1.0250	0.2333	0.7917	0.2276	0.0007	-	-
1.0500	0.2333	0.8167	0.2222	0.0007	-	-

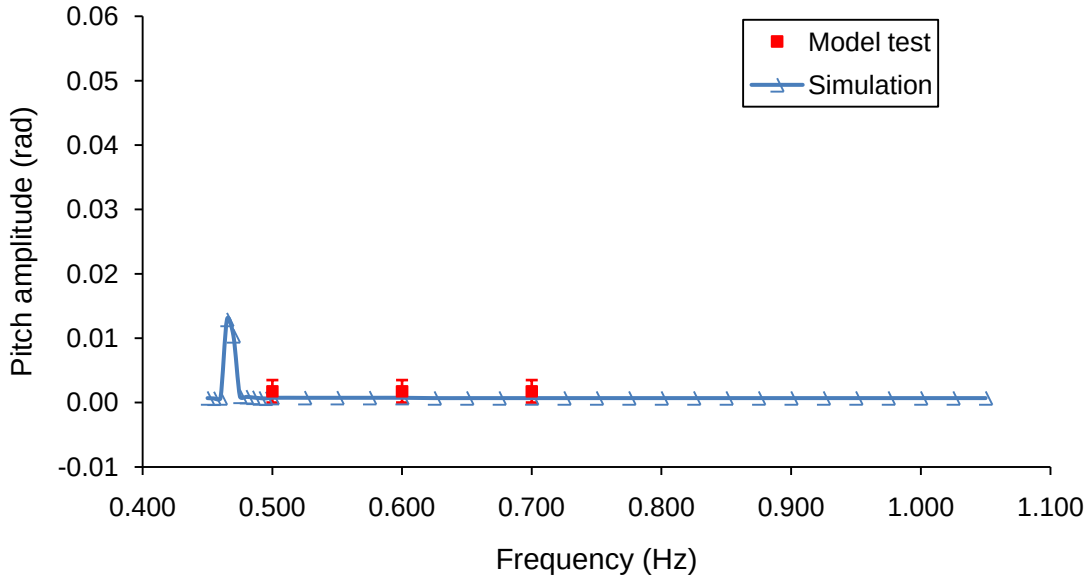

Fig. 116. Comparison of pitch amplitudes of the #1, #2, #3 valves opening model pile between simulations (heave-pitch coupling, $C_{a,t}$ =0.71, $C_{d,t}$ =7.5) and model tests.

D.5 Comparison of the #2, #4 Valves Opening Model

D.5.1 Comparison of the heave motion

The specific parameters for the #2, #4 valves opening model are listed in Table 48. For brevity, we drop out the time domain comparisons of the simulations and measurements for the #2, #4 valves opening model.

The dynamics of the #2, #4 valves opening model is quite similar to the #1, #2, #3, #4 valves opening model. Table 49 presents the time domain results of the heave-pitch coupled motion ($C_{a,t}$ =0.61, $C_{d,t}$ =7.5) for the #2, #4 valves opening model. Fig. 117 presents the comparison between the simulations of the coupled motion scheme ($C_{a,t}$ =0.61, $C_{d,t}$ =7.5) and model tests for the #2, #4 valves opening model.

Table 48. #2, #4 valves opening model parameters for numerical simulations.

Model parameters	Notation	Value	Note
Length	L	3 ft (0.914 m)	
Outer diameter	D	6 in (15.24 cm)	
Wall thickness	t	0.25 in (0.64 cm)	
Opening area ratio (Perforation)	γ	21.50%	For the top cap
Normal added-mass coef.	$C_{a,n}$	1.2	
Normal drag coef.	$C_{d,n}$	1.0	
Axial added-mass coef.	$C_{a,t}$	0.61	From model test
Axial drag coef.	$C_{d,t}$	7.5	
Coef. of pitch damping term	$C_{D\beta}$	9.8236	Refer to Appendix B
Weight in air	W	16.0 lb (71.172 N)	
Weight in water	W'	9.6 lb (42.703 N)	
Weight of water inside pile plus water displaced by pile	W_0	36.8 lb (163.695 N)	
Buoyancy	F_B	6.729 lb (29.932 N)	
Moment of inertia in air	$I_{\beta p}$	1.5780 slug·ft^2 (2.139 kg/m^2)	Refer to Appendix B
Added moment of inertia in water	$I_{\beta a}$	4.1176 slug·ft^2 (5.583 kg/m^2)	Refer to Appendix B
Moment of inertia in water	I_{β}	5.6956 slug·ft^2 (7.722 kg/m^2)	
Gravity center from eye bolt	$O'G$	1.44 ft (0.439 m)	Including hanging bar height 2"
Buoyancy center from eye bolt	$O'B$	1.57 ft (0.479 m)	Including hanging bar height 2"
Heave natural frequency	f_n	0.6100 Hz	From model test
Pitch natural frequency	f_p	0.2400 Hz	Hand calculation

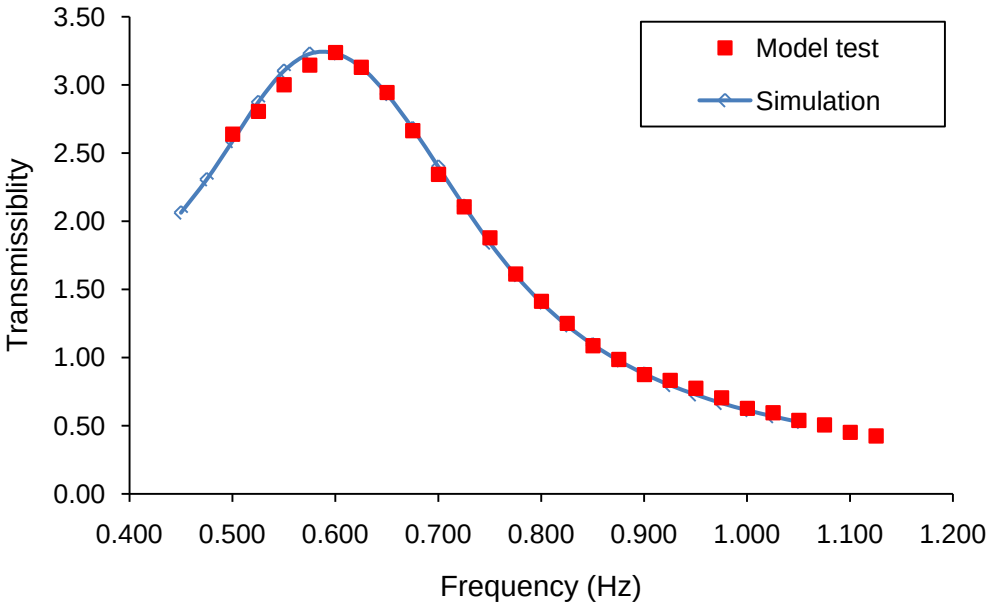

Fig. 117. Comparison of the heave amplitude transmissibility curves from simulations (heave-pitch coupling, $C_{a,t}$=0.61, $C_{d,t}$=7.5) for the #2, #4 valves opening model.

Table 49. Numerical results of heave motion for the #2, #4 valves opening model simulations using the heave-pitch coupling scheme ($C_{a,t}$ =0.61, $C_{d,t}$ =7.5).

f (Hz)	ST1 (lb)	ST2 (lb)	ST2/ST1	SD3 (ft)	SD2 (ft)	SD2/SD3	SD2/SD1	SD3/SD1
0.4500	5.0744	5.0450	0.9942	0.2506	0.5171	2.0633	2.0684	1.0024
0.4750	6.3544	6.3231	0.9951	0.2507	0.5783	2.3070	2.3132	1.0028
0.5000	7.9448	7.9154	0.9963	0.2507	0.6488	2.5874	2.5952	1.0028
0.5250	9.8190	9.7846	0.9965	0.2508	0.7207	2.8734	2.8828	1.0032
0.5500	11.6892	11.6674	0.9981	0.2509	0.7787	3.1034	3.1148	1.0036
0.5750	13.3319	13.3187	0.9990	0.2510	0.8103	3.2288	3.2412	1.0040
0.6000	14.5296	14.5289	1.0000	0.2510	0.8113	3.2319	3.2452	1.0040
0.6250	15.1793	15.1819	1.0002	0.2507	0.7848	3.1303	3.1392	1.0028
0.6500	15.3226	15.3358	1.0009	0.2512	0.7369	2.9333	2.9476	1.0048
0.6750	14.9759	15.0102	1.0023	0.2512	0.6739	2.6820	2.6956	1.0048
0.7000	14.3115	14.3528	1.0029	0.2514	0.6034	2.3999	2.4136	1.0056
0.7250	13.4082	13.4637	1.0041	0.2515	0.5313	2.1128	2.1252	1.0060
0.7500	12.4485	12.5112	1.0050	0.2516	0.4638	1.8429	1.8552	1.0064
0.7750	11.5282	11.5995	1.0062	0.2518	0.4043	1.6058	1.6172	1.0072
0.8000	10.7041	10.7820	1.0073	0.2518	0.3537	1.4045	1.4148	1.0072
0.8250	10.0107	10.0787	1.0068	0.2520	0.3115	1.2360	1.2460	1.0080
0.8500	9.3972	9.4821	1.0090	0.2521	0.2764	1.0961	1.1056	1.0084
0.8750	8.8806	8.9758	1.0107	0.2523	0.2471	0.9795	0.9884	1.0092
0.9000	8.4595	8.5503	1.0107	0.2525	0.2225	0.8813	0.8900	1.0100
0.9250	8.0936	8.1800	1.0107	0.2524	0.2015	0.7983	0.8060	1.0096
0.9500	7.7868	7.8746	1.0113	0.2527	0.1843	0.7292	0.7372	1.0108
0.9750	7.4932	7.6070	1.0152	0.2528	0.1686	0.6667	0.6744	1.0112
1.0000	7.2211	7.3530	1.0183	0.2523	0.1551	0.6146	0.6204	1.0092
1.0250	7.0282	7.1612	1.0189	0.2531	0.1442	0.5695	0.5768	1.0124
1.0500	6.8465	6.9859	1.0204	0.2533	0.1338	0.5282	0.5352	1.0132

D.5.2 Comparison of the heave induced pitch motion

Table 50 summarizes the time domain results of the heave induced pitch motion for the #2, #4 valves opening model simulations ($C_{a,t}$ =0.61, $C_{d,t}$ =7.5) based on the heave-pitch coupled motion scheme, and each columns have the same meaning as presented in the closed end model simulation. Fig. 118 shows satisfactory agreement in the comparison between the simulated pitch amplitude with measured pitch amplitude for #2, #4 valves opening model. The heave excitation frequency range for the heave

induced pitch amplification is also quite narrow (0.465~0.475 Hz) as for #1, #2, #3, #4 valves opening model.

Table 50. Numerical results of heave induced pitch motion for the #2, #4 valves opening model simulations using the heave-pitch coupling scheme ($C_{a,t}$ =0.61, $C_{d,t}$ =7.5).

f (Hz)	f_β (Hz)	$f - f_\beta$ (Hz)	f_β/f	Pitch amplitude (rad)	β_{video} (rad)	β_{error} (rad)
0.4500	0.2333	0.2167	0.5184	0.0007	-	-
0.4550	0.2333	0.2217	0.5127	0.0007	-	-
0.4600	0.2333	0.2267	0.5072	0.0008	-	-
0.4650	0.2333	0.2317	0.5017	0.0085	-	-
0.4700	0.2333	0.2367	0.4964	0.0075	-	-
0.4750	0.2361	0.2389	0.4971	0.0010	-	-
0.4800	0.2333	0.2467	0.4860	0.0008	-	-
0.4850	0.2333	0.2517	0.4810	0.0008	-	-
0.4900	0.2333	0.2567	0.4761	0.0008	-	-
0.4950	0.2333	0.2617	0.4713	0.0007	-	-
0.5000	0.2333	0.2667	0.4666	0.0007	-	-
0.5250	0.2333	0.2917	0.4444	0.0008	-	-
0.5500	0.2333	0.3167	0.4242	0.0008	-	-
0.5750	0.2333	0.3417	0.4057	0.0008	-	-
0.6000	0.2333	0.3667	0.3888	0.0007	0.0017	0.0017
0.6250	0.2333	0.3917	0.3733	0.0007	-	-
0.6500	0.2333	0.4167	0.3589	0.0007	-	-
0.6750	0.2333	0.4417	0.3456	0.0007	-	-
0.7000	0.2333	0.4667	0.3333	0.0007	-	-
0.7250	0.2333	0.4917	0.3218	0.0007	-	-
0.7500	0.2333	0.5167	0.3111	0.0007	0.0017	0.0017
0.7750	0.2333	0.5417	0.3010	0.0007	-	-
0.8000	0.2333	0.5667	0.2916	0.0007	-	-
0.8250	0.2333	0.5917	0.2828	0.0007	-	-
0.8500	0.2333	0.6167	0.2745	0.0007	-	-
0.8750	0.2333	0.6417	0.2666	0.0007	-	-
0.9000	0.2333	0.6667	0.2592	0.0007	0.0017	0.0017
0.9250	0.2333	0.6917	0.2522	0.0007	-	-
0.9500	0.2333	0.7167	0.2456	0.0007	-	-
0.9750	0.2333	0.7417	0.2393	0.0007	-	-
1.0000	0.2333	0.7667	0.2333	0.0007	-	-
1.0250	0.2333	0.7917	0.2276	0.0007	-	-
1.0500	0.2333	0.8167	0.2222	0.0007	-	-

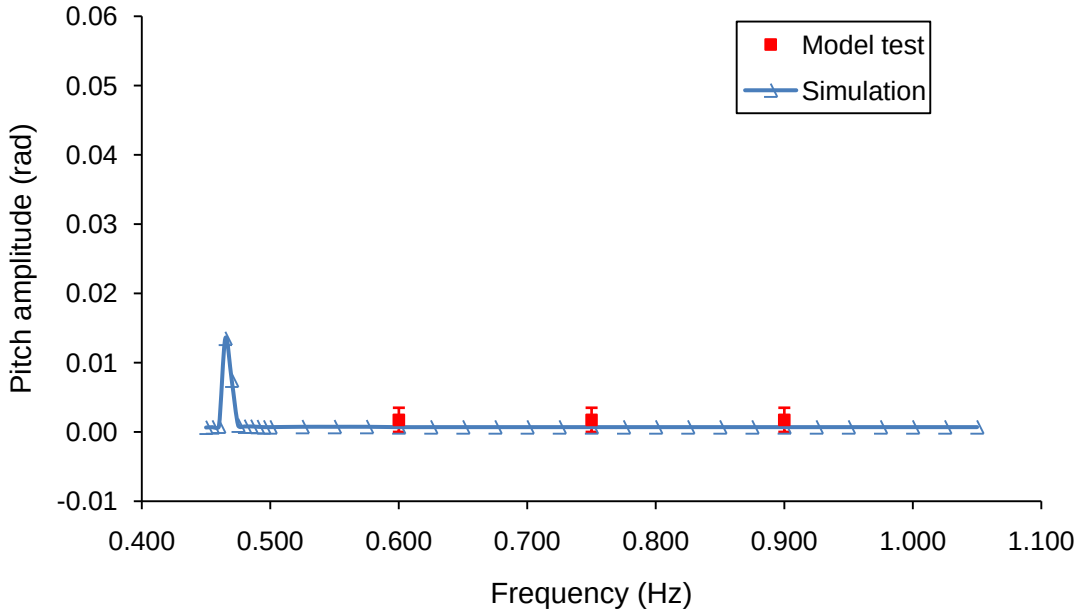

Fig. 118. Comparison of pitch amplitudes of the #2, #4 valves opening model pile between simulations (heave-pitch coupling, $C_{a,t}$ =0.61, $C_{d,t}$ =7.5) and model tests.

D.6 Comparison of the #1, #3, #4 Valves Opening Model

D.6.1 Comparison of the heave motion

The the specific parameters for the #1, #3, #4 valves opening model are listed in Table 51. For brevity, we drop out the time domain comparisons of the simulations and measurements for the #2, #4 valves opening model.

The dynamics of the #1, #3, #4 valves opening model is quite similar to the #1, #2, #3, #4 valves opening model. Table 52 presents the time domain results of the heave-pitch coupled motion ($C_{a,t}$ =0.51, $C_{d,t}$ =7.5) for the #1, #3, #4 valves opening model. Fig. 119 presents the comparison between the simulations of the coupled motion scheme ($C_{a,t}$ =0.51, $C_{d,t}$ =7.5) and model tests for the #1, #3, #4 valves opening model.

Table 51. #1, #3, #4 valves opening model parameters for numerical simulations.

Model parameters	Notation	Value	Note
Length	L	3 ft (0.914 m)	
Outer diameter	D	6 in (15.24 cm)	
Wall thickness	t	0.25 in (0.64 cm)	
Opening area ratio (Perforation)	γ	26.10%	For the top cap
Normal added-mass coef.	$C_{a,n}$	1.2	
Normal drag coef.	$C_{d,n}$	1.0	
Axial added-mass coef.	$C_{a,t}$	0.51	From model test
Axial drag coef.	$C_{d,t}$	7.5	
Coef. of pitch damping term	$C_{D\beta}$	9.8236	Refer to Appendix B
Weight in air	W	16.0 lb (71.172 N)	
Weight in water	W'	9.6 lb (42.703 N)	
Weight of water inside pile plus water displaced by pile	W_0	36.8 lb (163.695 N)	
Buoyancy	F_B	6.729 lb (29.932 N)	
Moment of inertia in air	$I_{\beta p}$	1.5780 slug·ft^2 (2.139 kg/m^2)	Refer to Appendix B
Added moment of inertia in water	$I_{\beta a}$	4.1176 slug·ft^2 (5.583 kg/m^2)	Refer to Appendix B
Moment of inertia in water	I_{β}	5.6956 slug·ft^2 (7.722 kg/m^2)	
Gravity center from eye bolt	$O'G$	1.44 ft (0.439 m)	Including hanging bar height 2"
Buoyancy center from eye bolt	$O'B$	1.57 ft (0.479 m)	Including hanging bar height 2"
Heave natural frequency	f_n	0.6400 Hz	From model test
Pitch natural frequency	f_p	0.2400 Hz	Hand calculation

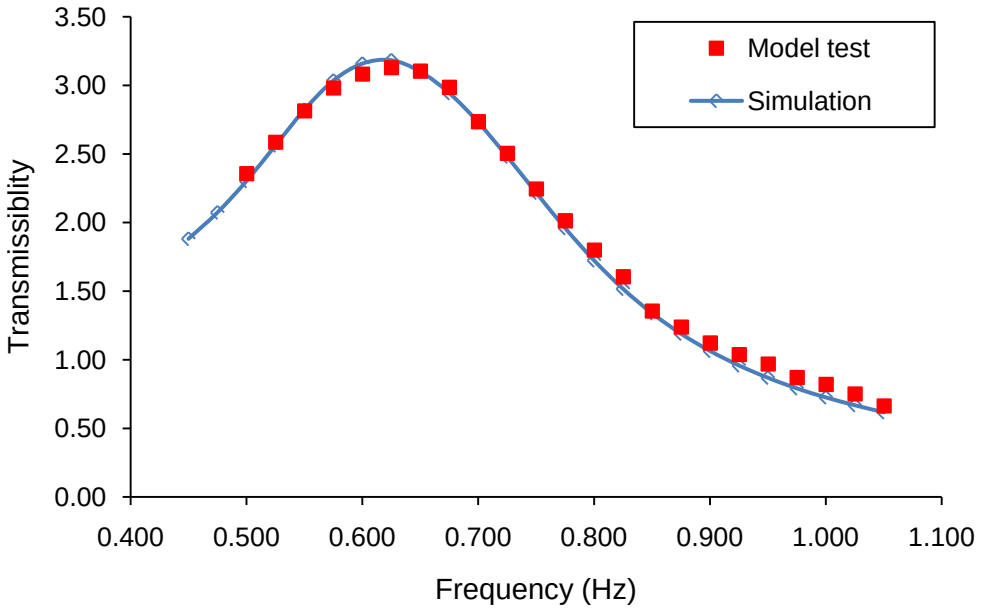

Fig. 119. Comparison of the heave amplitude transmissibility curves from simulations (heave-pitch coupling, $C_{a,t}$=0.51, $C_{d,t}$=7.5) for the #1, #3, #4 valves opening model.

Table 52. Numerical results of heave motion for the #1, #3, #4 valves opening model simulations using the heave-pitch coupling scheme ($C_{a,t}$ =0.51, $C_{d,t}$ =7.5).

f (Hz)	ST1 (lb)	ST2 (lb)	ST2/ST1	SD3 (ft)	SD2 (ft)	SD2/SD3	SD2/SD1	SD3/SD1
0.4500	4.1770	4.1449	0.9923	0.2506	0.4716	1.8816	1.8864	1.0024
0.4750	5.1512	5.1187	0.9937	0.2507	0.5198	2.0734	2.0792	1.0028
0.5000	6.3559	6.3279	0.9956	0.2507	0.5773	2.3025	2.3092	1.0028
0.5250	7.8645	7.8350	0.9963	0.2508	0.6426	2.5618	2.5704	1.0032
0.5500	9.6008	9.5616	0.9959	0.2509	0.7080	2.8216	2.8320	1.0036
0.5750	11.3202	11.2932	0.9976	0.2510	0.7616	3.0345	3.0464	1.0040
0.6000	12.8664	12.8524	0.9989	0.2511	0.7929	3.1583	3.1716	1.0044
0.6250	14.0666	14.0567	0.9993	0.2507	0.7980	3.1829	3.1920	1.0028
0.6500	14.7700	14.7757	1.0004	0.2512	0.7789	3.1003	3.1156	1.0048
0.6750	15.0356	15.0582	1.0015	0.2512	0.7397	2.9440	2.9588	1.0048
0.7000	14.9031	14.9357	1.0022	0.2514	0.6866	2.7308	2.7464	1.0056
0.7250	14.4207	14.4635	1.0030	0.2515	0.6240	2.4808	2.4960	1.0060
0.7500	13.6892	13.7436	1.0040	0.2516	0.5582	2.2181	2.2328	1.0064
0.7750	12.8402	12.9087	1.0053	0.2518	0.4935	1.9597	1.9740	1.0072
0.8000	11.9650	12.0401	1.0063	0.2518	0.4342	1.7242	1.7368	1.0072
0.8250	11.1494	11.2316	1.0074	0.2520	0.3822	1.5166	1.5288	1.0080
0.8500	10.4209	10.5099	1.0085	0.2521	0.3377	1.3395	1.3508	1.0084
0.8750	9.7899	9.8841	1.0096	0.2523	0.3002	1.1900	1.2008	1.0092
0.9000	9.2685	9.3460	1.0084	0.2525	0.2688	1.0646	1.0752	1.0100
0.9250	8.8022	8.8894	1.0099	0.2524	0.2420	0.9586	0.9680	1.0096
0.9500	8.4146	8.5030	1.0105	0.2527	0.2196	0.8690	0.8784	1.0108
0.9750	8.0462	8.1595	1.0141	0.2528	0.2001	0.7913	0.8004	1.0112
1.0000	7.7129	7.8448	1.0171	0.2523	0.1831	0.7257	0.7324	1.0092
1.0250	7.4745	7.6075	1.0178	0.2531	0.1693	0.6689	0.6772	1.0124
1.0500	7.2520	7.3918	1.0193	0.2533	0.1563	0.6169	0.6252	1.0132

D.6.2 Comparison of the heave induced pitch motion

Table 53 summarizes the time domain results of the heave induced pitch motion for the #1, #3, #4 valves opening model simulations ($C_{a,t}$ =0.51, $C_{d,t}$ =7.5) based on the heave-pitch coupled motion scheme, and each columns have the same meaning as presented in the closed end model simulation. Fig. 120 shows satisfactory agreement in the comparison between the simulated pitch amplitude with measured pitch amplitude for #1, #3, #4 valves opening model. The heave excitation frequency range for the heave

induced pitch amplification is also quite narrow (0.465~0.470 Hz) as for #1, #2, #3, #4 valves opening model.

Table 53. Numerical results of heave induced pitch motion for the #1, #3, #4 valves opening model simulations using the heave-pitch coupling scheme ($C_{a,t}$=0.51, $C_{d,t}$=7.5).

f (Hz)	f_β (Hz)	$f - f_\beta$ (Hz)	f_β/f	Pitch amplitude (rad)	β_{video} (rad)	β_{error} (rad)
0.4500	0.2333	0.2167	0.5184	0.0007	-	-
0.4550	0.2333	0.2217	0.5127	0.0008	-	-
0.4600	0.2333	0.2267	0.5072	0.0009	-	-
0.4650	0.2333	0.2317	0.5017	0.0051	-	-
0.4700	0.2333	0.2367	0.4964	0.0084	-	-
0.4750	0.2333	0.2417	0.4912	0.0006	-	-
0.4800	0.2333	0.2467	0.4860	0.0007	-	-
0.4850	0.2333	0.2517	0.4810	0.0008	-	-
0.4900	0.2333	0.2567	0.4761	0.0008	-	-
0.4950	0.2333	0.2617	0.4713	0.0008	-	-
0.5000	0.2333	0.2667	0.4666	0.0007	-	-
0.5250	0.2333	0.2917	0.4444	0.0008	-	-
0.5500	0.2333	0.3167	0.4242	0.0008	-	-
0.5750	0.2333	0.3417	0.4057	0.0007	-	-
0.6000	0.2333	0.3667	0.3888	0.0007	0.0017	0.0017
0.6250	0.2333	0.3917	0.3733	0.0008	-	-
0.6500	0.2333	0.4167	0.3589	0.0007	-	-
0.6750	0.2333	0.4417	0.3456	0.0007	-	-
0.7000	0.2333	0.4667	0.3333	0.0007	-	-
0.7250	0.2333	0.4917	0.3218	0.0007	-	-
0.7500	0.2333	0.5167	0.3111	0.0007	0.0017	0.0017
0.7750	0.2333	0.5417	0.3010	0.0007	-	-
0.8000	0.2333	0.5667	0.2916	0.0007	-	-
0.8250	0.2333	0.5917	0.2828	0.0007	-	-
0.8500	0.2333	0.6167	0.2745	0.0007	-	-
0.8750	0.2333	0.6417	0.2666	0.0007	-	-
0.9000	0.2333	0.6667	0.2592	0.0007	0.0017	0.0017
0.9250	0.2333	0.6917	0.2522	0.0007	-	-
0.9500	0.2333	0.7167	0.2456	0.0007	-	-
0.9750	0.2333	0.7417	0.2393	0.0007	-	-
1.0000	0.2333	0.7667	0.2333	0.0007	-	-
1.0250	0.2333	0.7917	0.2276	0.0007	-	-
1.0500	0.2333	0.8167	0.2222	0.0007	-	-

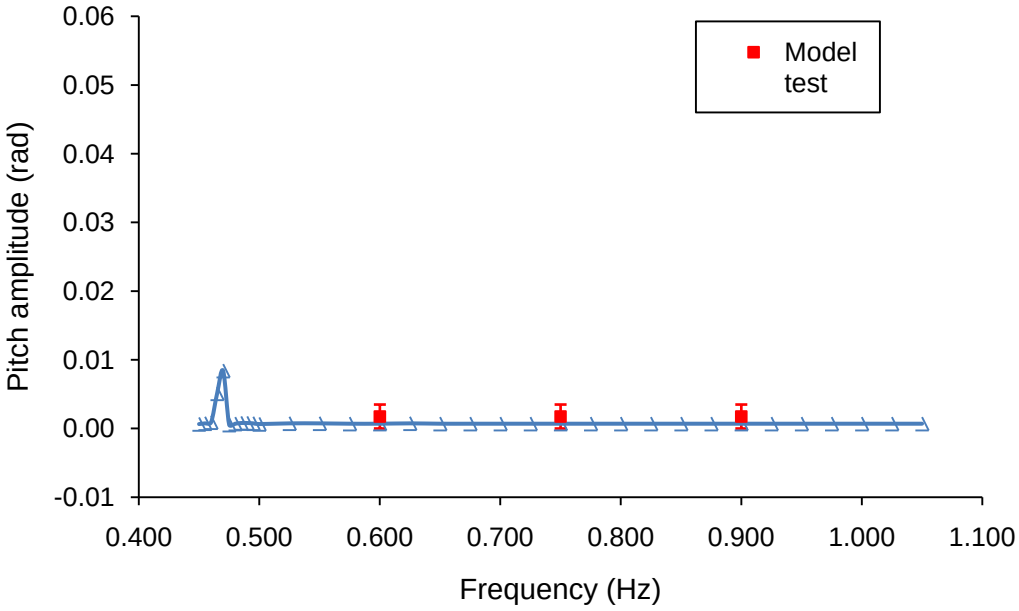

Fig. 120. Comparison of pitch amplitudes of the #1, #3, #4 valves opening model pile between simulations (heave-pitch coupling, $C_{a,t}$=0.51, $C_{d,t}$=7.5) and model tests.

VITA

Liqing Huang received his 5-year dual B.S. degrees in Civil Engineering and Theoretical & Applied Mechanics from Harbin Institute of Technology in July 2008. He entered the Ocean Engineering Program at Texas A&M University in September 2008. His research interests include dynamic analysis of marine cables, mooring lines, risers and their interactions with submerged and floating structures, wave mechanics, CFD, FEM, and so on.

Mr. Huang can be reached at Marintek USA Inc., 2603 Augusta Dr., #200, Houston, TX 77057. His email is liqing.huang@marintekusa.com.